



Alternative Fuels in Cement Production

Larsen, Morten Boberg; Dam-Johansen, Kim; Jensen, Lars Skaarup; Glarborg, Peter; Jappe Frandsen, Flemming

Publication date:
2007

Document Version
Publisher's PDF, also known as Version of record

[Link back to DTU Orbit](#)

Citation (APA):
Larsen, M. B., Dam-Johansen, K., Jensen, L. S., Glarborg, P., & Frandsen, F. (2007). Alternative Fuels in Cement Production. Technical University of Denmark, Department of Chemical and Biochemical Engineering.

DTU Library

Technical Information Center of Denmark

General rights

Copyright and moral rights for the publications made accessible in the public portal are retained by the authors and/or other copyright owners and it is a condition of accessing publications that users recognise and abide by the legal requirements associated with these rights.

- Users may download and print one copy of any publication from the public portal for the purpose of private study or research.
- You may not further distribute the material or use it for any profit-making activity or commercial gain
- You may freely distribute the URL identifying the publication in the public portal

If you believe that this document breaches copyright please contact us providing details, and we will remove access to the work immediately and investigate your claim.

Technical University of Denmark
Department of Chemical Engineering

ALTERNATIVE FUELS IN CEMENT PRODUCTION

Morten Boberg Larsen

2007

Research & Development

FLSmidth A/S

Copyright © Morten Boberg Larsen, 2007
ISBN 978-87-91435-49-8

Printed by Book Partner, Nørhaven Digital
Copenhagen, Denmark

Preface

This PhD project has been carried out in cooperation with the CHEC research group at the Department of Chemical Engineering at the Technical University of Denmark (DTU) and the Research and Development Department of FLSmidth. The project is partly supported by the Industrial PhD programme of the Danish Ministry of Science, Technology and Innovation.

First of all, I would like to thank my supervisors Kim Dam-Johansen (CHEC), Lars Skaarup Jensen (FLSmidth), Peter Glarborg (CHEC) and Flemming Frandsen (CHEC) for excellent supervision regarding different matters within this project. Also special thanks to Alexander Helm, Lars Skaarup Jensen and Henrik Wassard from FLSmidth for their support regarding the measurements on an industrial scale, and to the M.Sc students Lars Schultz and Morten Linde Hansen, who have contributed to some of the experimental results presented in this thesis. Thanks to all the other people at FLSmidth or DTU, not mentioned here, who have also been involved in this project.

I would also like to thank my colleagues at FLSmidth and CHEC for providing a pleasant environment, and special thanks to FLSmidth for making it possible for me to visit three different cement plants during this study and for having provided good working conditions to undertake this study.

Morten Boberg Larsen

Abstract

The substitution of alternative for fossil fuels in cement production has increased significantly in the last decade. Of these new alternative fuels, solid state fuels presently account for the largest part, and in particular, meat and bone meal, plastics and tyre derived fuels (TDF) accounted for the most significant alternative fuel energy contributors in the German cement industry. Solid alternative fuels are typically high in volatile content and they may differ significantly in physical and chemical properties compared to traditional solid fossil fuels. From the process point of view, considering a modern kiln system for cement production, the use of alternative fuels mainly influences 1) kiln process stability (may accelerate build up of blockages preventing gas and/or solids flow), 2) cement clinker quality, 3) emissions, and 4) decreased production capacity. Kiln process stability in particular is influenced by insufficient carbon burnout in the calciner system, which results in reducing conditions in the material inlet of the rotary kiln and consequently an increased tendency to form deposits induced by sticky eutectic melts. Clinker quality is mainly affected by minor components from the fuel ashes or from carbon dropping into the material charge of the rotary kiln. As regards the presently most used solid alternative fuels, phosphorous from meat and bone meal or zinc from TDF are the main components to consider with respect to clinker chemistry. The emissions seem not to have been affected by the alternative fuels used up until now. However, caution should be taken with regard to emissions of CO when using alternative fuels.

As alternative solid fuels are typically high in volatile content, the devolatilization stage in the combustion process is responsible for a large part of the fuel heating value. In addition, the devolatilization time of alternative fuels cannot be neglected in kiln system process analyses, as these fuels are typically in the cm-size with devolatilization times in the order of minutes. The devolatilization characteristics of large particles of tyre rubber were investigated in two experimental setups with the emphasis being on devolatilization rates and times, and the results were analysed using mathematical modelling. During devolatilization, the large TDF particles formed a crackling char layer, which was seen to be removed depending on whether external mechanical interaction was present or not. Both pathways were investigated experimentally and a significantly shorter devolatilization time was observed in the situation where the char layer was removed. In addition, the experiments showed a significant effect of particle size on devolatilization time, where increased particle size increased the devolatilization time. Model analyses demonstrated that the overall devolatilization kinetics of large particles of tyre rubber is mainly controlled by heat transfer and intrinsic pyrolysis kinetics, whereas mass transfer has negligible influence. The models developed are used to predict devolatilization conversion times for tyre rubber as a function of relevant parameters. The devolatilization rates of other alternative fuels are also expected to be controlled by conversion pathway, heat transfer and intrinsic kinetics.

The char combustion stage has a decisive influence on the fuel carbon burnout in cement kiln systems. The oxidation kinetics of a char from TDF was investigated experimentally and by mathematical modelling. Experiments were performed in a fixed bed reactor under well

defined conditions, where small particles (102-212 μ m) of TDF were combusted at 750-850°C at up to 10 vol.% O₂. The effluent of the reactor was analysed for CO and CO₂, and used to derive conversion against time. The experimental data demonstrated that mass transfer was important within the investigated temperature range of 750-850°C, and a mathematical model for intra-particle diffusion and reaction was developed in order to analyse the data. A reaction expression for the intrinsic kinetics of TDF char oxidation was proposed and comparison with literature data showed fair agreement. For larger TDF char particles with realistic sizes up to 7 mm, it was demonstrated that they are converted according to a shrinking particle mechanism, and based on this observation a model was developed in order to explain the controlling factors for TDF char combustion under conditions relevant to cement kiln systems. It was demonstrated that external mass transfer was the rate limiting parameter, as the kinetics are sufficiently faster than external mass transfer. The intrinsic kinetics of other typical alternative fuels is demonstrated to be comparable or faster than intrinsic TDF char oxidation kinetics. Consequently, the char oxidation stage for large particles of other alternative fuels is also expected to be controlled by mass transfer, under conditions relevant to cement kiln systems.

A comparison between the mechanisms behind the devolatilization and char combustion stages for large alternative solid fuel particles indicates that the devolatilization kinetics are mainly controlled by heat transfer and intrinsic kinetics, whereas char oxidation kinetics are mainly controlled by mass transfer, under conditions relevant to cement kiln systems.

Measurements at two industrial HOTDISC's using TDF indicate that up to about 75% fuel conversion takes place before discharge into the subsequent calciner. Model analyses of the measurements, using the previously developed sub-models for devolatilization and char oxidation rates, explain that devolatilization takes place in the HOTDISC whereas char oxidation takes place both in the HOTDISC and in the calciner system.

Resume (In Danish)

Substitutionen af fossilt med alternativt brændsel i cement produktionen er steget betydeligt i den sidste dekade. Af disse nye alternative brændsler, udgør de faste brændsler p.t. den største andel, hvor kød- og benmel, plastic og dæk i særdeleshed har været de alternative brændsler der har bidraget med mest alternativ brændsels energi til den tyske cement industri. De nye alternative brændsler er typisk karakteriseret ved et højt indhold af flygtige bestanddele og adskiller sig typisk fra traditionelle fossile fast stof brændsler ved at have anderledes fysiske og kemiske egenskaber. For et moderne ovn system til cement produktion, kan anvendelsen af alternative brændsler primært influere 1) ovn system stabiliteten (kan accelerere dannelsen af belægninger/påbagninger og derved øge modstanden mod gas og faststof strømning), 2) cement klinker kvaliteten, 3) emissioner og 4) nedsat produktionskapacitet. Ovn stabiliteten er i særdeleshed influeret af uforbrændt kulstof i kalcinator systemet, som kan resultere i reducerende betingelser i materiale indløbet af roter ovnen og derved en øget tendens til at danne belægninger induceret af klistrende eutektiske smelter. Klinker kvaliteten er primært påvirket af mindre forekommende komponenter i asken fra brændslet, eller fra uforbrændt kulstof fra flammen i roter-ovnen, som falder ned i materialet af roter-ovnen. Zink og fosfor, fra de p.t. mest anvendte brændsler af dæk og kød- og benmel respektive, udgør de vigtige komponenter med hensyn til at undgå cement kvalitets problemer. Indtil nu er emissionerne ved anvendelsen af alternative brændsler uændrede i forhold til anvendelsen af fossile brændsler. Forsigtighed bør dog udvises med hensyn til CO emissioner ved anvendelsen af alternative brændsler.

Da alternative brændsler typisk har et højt indhold af flygtige komponenter, er disse ansvarlig for en betydelig del af brændslets brændværdi. Derudover kan tiden for afgivelsen af flygtige komponenter fra alternative brændsler ikke negligeres i proces analyser af ovn systemet, da disse brændsler typisk er i cm-størrelsen med en tid for afgivelsen af flygtige komponenter i størrelsesordenen af minutter. Frigivelses-karakteristikken af flygtige komponenter blev undersøgt for dæk gummi i to eksperimentelle opstillinger med hovedvægt på omsætningshastigheder og tider. De eksperimentelle resultater blev analyseret ved anvendelse af matematisk modellering. Under frigivelsen af de flygtige komponenter fra dæk gummi, dannes et krakelerende kokslag, som observeredes at blive fjernet i afhængighed af om tilstrækkelig ekstern mekanisk påvirkning var til stede eller ej. Begge omsætningsmekanismer blev undersøgt eksperimentelt og en signifikant kortere omsætningstid blev observeret i det tilfælde hvor kokslaget blev fjernet. Derudover blev en betydelig effekt af partikelstørrelse på frigivelsestid observeret, hvor større partikelstørrelser øgede tiden. Model analyser demonstrerede at frigivelses-kinetikken for store partikler af dækgummi primært er kontrolleret af varme transport og indre kinetik, hvorimod masse transport ikke har nogen betydelig indflydelse. De udviklede modeller er anvendt til at forudsige tiden for frigivelse af flygtige komponenter fra dækgummi som funktion af relevante parametre. Hastigheden hvormed flygtige bestanddele frigives fra andre faste alternative brændsler forventes også primært at være kontrolleret af omsætningsvej, varmetransport og indre kinetik.

Koks forbrændings trinnet har væsentlig betydning for omsætningen af kulstof i cement ovn systemer. Den indre oxidationskinetik af koks fra dæk gummi blev undersøgt eksperimentelt og ved anvendelse af matematisk modellering. Eksperimenter blev udført i en fixed bed reaktor under veldefinerede betingelser, hvor små partikler (102-212 μ m) blev omsat ved 750-850 °C i en gas med op til 10 vol.% O₂. De eksperimentelle data demonstrerede at stof transport er betydelig for omsætningen ved de undersøgte temperaturer mellem 750 og 850 °C, og en matematisk model for diffusion og reaktion i partiklen blev udviklet for at analysere de eksperimentelle data. Et reaktionsudtryk for den indre dæk gummi koks oxidations kinetik blev foreslået og sammenligning med litteratur data viste god overensstemmelse. For større dæk gummi koks partikler med realistiske størrelser på op til 7 mm, blev det demonstreret at de omsættes som en skrumpende partikel model, og med basis i denne observation blev en matematisk model udviklet for at undersøge kontrollerende faktorer for omsætningen af dæk koks ved betingelser relevante for cement ovn systemer. Det blev demonstreret at masse transport er den hastigheds begrænsende parameter, fordi den indre koks oxidations kinetik er betydeligt hurtigere end stof transporten. Koksomsætningen for store partikler af andre alternative brændsler er også forventet at være kontrolleret af stof transport, da den indre kinetik for disse er vist at være sammenlignelig med eller hurtigere end den indre dæk koks kinetik.

En sammenligning mellem mekanismerne for frigivelsen af flygtige komponenter og koks forbrændingen for store alternative faste brændselspartikler, indikerer at førstnævnte primært er kontrolleret af varmetransport og indre kinetik, hvorimod koks oxidationen primært er kontrolleret af stof transport, ved betingelser relevante for cement ovn systemer.

Målinger på to industrielle HOTDISC's, der anvender dæk som brændsel, indikerer at op til ca. 75 % brændselsomsætning finder sted, før afkast til det efterfølgende kalcinator system finder sted. Model analyser af målinger, ved anvendelse af tidligere udviklede under modeller for frigivelsen af flygtige komponenter og koks forbrænding, forklarer at frigivelse af flygtige komponenter finder sted i HOTDISC'en mens koks forbrænding finder sted både i HOTDISC'en og kalcinator systemet.

Table of Contents

Chapter 1 - Introduction.....	1
1.1 Background.....	1
1.2 Structure.....	2
1.3 Objectives.....	3
1.4 References.....	4
Chapter 2 – Cement Chemistry and Production.....	5
2.1 Historical Perspective.....	5
2.2 Cement Chemistry.....	6
2.2.1 Raw Materials.....	6
2.2.2 Calcination.....	7
2.2.3 Clinker Reactions.....	7
2.3 Overview of a Modern Cement Production Plant.....	9
2.3.1 Preparation of Raw Materials.....	9
2.3.2 Pyro Processing.....	9
2.3.3 Clinker Processing.....	10
2.4 Review of the Kiln System.....	11
2.4.1 Rotary Kiln.....	11
2.4.2 Preheater.....	12
2.4.3 Calciner Systems.....	13
2.5 Conclusions on Chapter 2.....	18
2.6 References.....	19
Chapter 3 – Alternative Fuels in Cement Production.....	21
3.1 Alternative Fuel Types and Amounts.....	21
3.1.1 Types of Alternative Fuels.....	21
3.1.2 Quantification of Alternative Fuels in Cement Production.....	22
3.1.3 Fuel Analyses.....	26
3.2 Use of Alternative Fuels in Cement Production.....	29
3.2.1 Small Particles, Gaseous Fuels or Liquid Droplets.....	32
3.2.2 Extensional Equipment for Large Fuel Particles.....	33
3.3 Effects of other Components on Processing and Chemistry.....	38
3.3.1 Alkali, Sulphur and Chlorine.....	38
3.3.2 Effects of Minor Components on Cement Chemistry and Quality.....	41
3.4 Emissions.....	42
3.4.1 Legislation.....	42
3.4.2 Effect of Alternative Fuels on Emissions.....	42
3.5 Conclusions on Chapter 3.....	47
3.6 References.....	48

Chapter 4 – Devolatilization of Large Solid Fuel Particles	53
4.1 Introduction to Solid Fuel Combustion.....	54
4.1.1 Heating and Drying.....	54
4.1.2 Devolatilization	54
4.1.3 Char Conversion	56
4.1.4 Solid Fuel Conversion Pathways	56
4.2 Literature Study on Devolatilization Kinetics of Large Particles	58
4.2.1 Tyre Derived Fuel (TDF).....	58
4.2.2 Plastics	60
4.2.3 Meat and Bone Meal.....	61
4.2.4 Conclusions on Literature Study.....	62
4.3 Experimental	63
4.3.1 Pre-experimental Considerations	63
4.3.2 Fuel Samples.....	64
4.3.3 Flame Devolatilization Experiments.....	64
4.3.4 Macro TGA Experimental Setup	67
4.3.5 Conclusions	69
4.4 Experimental Results	70
4.4.1 Results of Flame Devolatilization Experiments.....	70
4.4.2 Results of Macro-TGA Experiments	72
4.4.3 Conclusions on Experimental Investigations.....	76
4.5 Model Analyses of Tyre Rubber Devolatilization	77
4.5.1 Devolatilization Model A: Nusselt Shrinking Core Model	78
4.5.2 Devolatilization Model B.....	80
4.5.3 Devolatilization Model C.....	82
4.5.4 Model Parameters - Physical and Chemical Properties of Tyre Rubber.....	83
4.5.5 Comparison of Model A, B and C with Flaming Devolatilization Exp. Results	86
4.5.6 Comparison of Model A and B with Experimental Macro-TGA Results	88
4.5.7 The Effect of Steel Wires on the Devolatilization Rate	91
4.5.8 Modeling Devolatilization Times of Whole and Shredded Car Tyres.....	95
4.5.9 Tyres with Other Tread Thicknesses	97
4.5.10 Conclusions on Modeling Investigations.....	98
4.6 Influencing Factors and Implications.....	99
4.7 Other Alternative Fuels.....	101
4.8 Conclusions on Chapter 4	102
4.9 References.....	103
Chapter 5 - Char Combustion.....	107
5.1 Literature Study on Char Conversion	107
5.1.1 TDF Chars	108
5.1.2. MBM Chars	108
5.2 Experimental and Model Analysis of Intrinsic TDF Char Oxidation Kinetics	109
5.2.1 Pre-experimental considerations.....	109
5.2.2 Materials	110
5.2.3 Experimental Setup and Procedure.....	110
5.2.4 Interpretation of combustion kinetics	116
5.2.5 Results of model analyses.....	118
5.2.6 Comparison of Estimated Intrinsic Kinetics with Literature data.....	119
5.2.7 Conclusions	120

5.3 Modeling TDF Char Combustion in the Kiln System	121
5.3.1 Pre Modeling Considerations.....	121
5.3.2 Single Particle Model for TDF char combustion.....	126
5.3.3 Analysis of Single Particle Model	127
5.3.4 In-Line-Calciner Model	129
5.3.5 Conclusions	136
5.4 Chars from Other Alternative Fuels.....	137
5.4.1 Intrinsic Kinetics.....	137
5.4.2 Structural Changes and Effect of Particle Size	139
5.4.3 Oxidizer Bulk Concentration	139
5.4.4 Mass Transfer Rates	139
5.4.5 Particle Residence Time	140
5.4.6 Conclusions	140
5.5 Conclusions on Chapter 5	141
5.6 References.....	142

Chapter 6 - Analyses of Industrial Scale HOTDISCs..... 145

6.1 Model for Conversion of Whole and Shredded Tyres in the HOTDISC.....	145
6.1.1 Devolatilization.....	147
6.1.2 Char Oxidation	149
6.1.3 Calcination.....	152
6.1.4 Gas Phase Calculations.....	153
6.1.5 Solution Procedure.....	154
6.1.6 Results of Model Calculations	155
6.1.7 Conclusions on Model Investigations.....	156
6.2 Plant Measurements and Analyses.....	157
6.2.1 Procedures for Measurements.....	157
6.2.2 Analysis Method of Plant Measurement Data	159
6.2.3 Uncertainties	162
6.2.4 Results of Plant Measurements.....	162
6.2.5 Conclusion on Plant Measurements and Analyses.....	164
6.3 Comparison of Measured and Modelled Fuel Conversion	165
6.3.1 HOTDISC at Plant A	165
6.3.2 HOTDISC at Plant B	166
6.3.3 Discussion of Discrepancies between Modelled and Measured Fuel Conversion.....	166
6.3.4 Conclusions on Comparison between Modelled and Measured Data.....	167
6.4 Use of Other Alternative Fuels in the HOTDISC.....	168
6.4.1 Liquids.....	168
6.4.2 Paper and Cardboard.....	168
6.4.3 Plastics	169
6.4.4 Refuse Derived Fuel	169
6.4.5 Meat and Bone Meal.....	169
6.5 Conclusions on Chapter 6	169
6.6 References.....	170

Chapter 7 – Final Conclusions	171
7.1 Concluding Trends.....	171
7.2 Suggestions for Further Work.....	172
 Appendixes	 175
Appendix A: Solution of Devolatilization Model A and C	176
Appendix B: Determination of External Heat Transfer Coefficients	180
Appendix C: Sensitivity Analysis on Devolatilization Model B	184
Appendix D: Instantaneous Air Excess Ratio.....	187
Appendix E: Uncertainties on Estimated Degree of Fuel conversion	188

Paper A

Devolatilization characteristics of large particles of tyre rubber under combustion conditions. Published in FUEL, 85, 1335-1345, 2006.

Paper B

Kinetics of tyre char oxidation under combustion conditions. In press, FUEL, 2007.

List of Symbols

Roman nomenclature

a	Absorbivity	-
A	Pre exponential factor	1/s
A	Area	m ²
A	Specific outer surface area	m ² /kg
A	Discretization matrice	-
B	Discretization matrice	-
C	Concentration	mol/m ³ or mol/cm ³
c _p	Specific heat capacity	J/kg/K
D	Diffusion coefficient	m ² /s
D	Diameter	m or mm
E	Normalised residence time distribution	-
E	Activation energy	J/mol
F	View factor	-
FC	Fixed Carbon	wt.% or kg/kg
Gr	Grasshoff number	-
h	Heat transfer coefficient	W/m ² /K
H	Enthalpy	J/mol or J/kg
h	Height	m
k	Thermal conductivity	W/m/K
k	Rate constant	1/s
k _g	Convective mass transfer coefficient	m/s
K	Calcination rate	-
L	Length	m
m	Mass	kg or g
m _v	Volatile flux	kg/m ² /s
m _f	Secondary fuel feed rate	kg/s
M _{w(i)}	Molecular weight of specie i	kg/mol
n _{char}	Char carbon load on Hotdisc	mol/m ² /s
n	Molar flow	mol/s
Nu	Nusselt number	-
p	Pressure	Pa
p	Jacobi polynomial	-
Pr	Prandtl number	-
Q	Volumetric flow	Nm ³ /h
r	Radius (or distance to symmetry line for slab)	m
r	Surface reaction rate	mol/m ² /s
R	Volumetric reaction rate	1/s
Re	Reynolds number	-
R _g	Universal gas constant	8.314 J/mol/K
s	Shape factor (0=slab, 1=cylinder and 2=sphere)	-
Sh	Sherwood number	-
Sc	Schmidth number	-
t	Time	s
T	Temperature	°C or K
u	Transformed dimensionless position (u=x ²)	-
v	Velocity	m/s
V	Initial volatile content	wt.% or kg/kg

x	Mass fraction based on initial sample mass ($= \frac{m_i(t)}{\sum m_{i,0}}$)	kg/kg
x	Dimensionless position	-
X	Conversion	-
y	Molar fraction	mol/mol

Greek Nomenclature

α	Molar content of C in fuel or volatiles	mol/kg
β	Molar content of H in fuel or volatiles	mol/kg
χ	Molar content of N in fuel or volatiles	mol/kg
δ	Molar content of S in fuel or volatiles	mol/kg
ε	Molar content of O in fuel or volatiles	mol/kg
ε	Emissivity	-
ϕ	Molar content of H ₂ O in fuel or volatiles	mol/kg
γ	Dimensionless activation energy	-
η	Dimensionless position	-
λ	Air excess ratio	-
μ	Weighting factor	-
σ	Stefan Boltzmanns Constant	$5.72 \cdot 10^{-8} \text{ W/m}^2/\text{K}^4$
τ	Residence time	s or dimensionless
θ	Dimensionless temperature	-
ρ	Density	kg/m ³ or mol/m ³
ρ	Reflectivity (1- ε)	-
Θ	Effective Hotdisc angle	°
Π	Char combustion product distribution	mol C / mol O ₂

Subscripts

c	Core or carbon
conv	Convective
D	Devolatilization
eff	Effective
eq	Equivalent
g	Gas
H	Hydraulic
i	index number
local	Local conditions
min	Minimum stoichiometric air consumption
p	Particle
rad	Radiative
Surf	Surface
tert	Tertiary air
vf	Virgin fuel
0	Initial
∞	Surroundings

Chapter 1 - Introduction

1.1 Background

Despite the fact that modern efficient cement production plants consume less energy than 20-30 years ago, the energy usage is still about 700 kcal per kg cement clinker produced, equivalent to 60-130 kg coal per tonnes of cement clinker produced (depending on coal heating value) [1,2]. According to figures from the Independent Cement Producers Association, the fuel cost per tonne of clinker produced is about 6.0 US\$, corresponding to about 38% of the total cement clinker production costs [3].

Since the oil crises in the 70's, most cement producers have implemented several technological improvements to lower fuel costs per produced tonne of cement. Traditionally, cement production has mainly depended on fossil fuel resources (oil, coal and gas). In the last decade however, the utilization of alternative fuels^a, as a substitute for fossil fuels, has increased significantly. This increase has been most prominent in the developed countries, because in the developing countries 1) alternative fuels are not sufficiently available, mainly due to lack of infrastructure for collecting the fuels, and 2) the legal framework promoting increased substitution rates of alternative fuels is not in place [4,5].

The significant progress made in the last decade regarding utilization of alternative fuels in cement production, has partly been driven by the EC directive 1999/31/EC [6] which banned landfill of combustible wastes. In addition, alternative fuels are typically cheaper than fossil fuels, and cement producers may even be paid to receive the alternative fuels.

Besides the above mentioned driving forces, the following major advantages are also achieved utilizing alternative fuels in cement production:

- 1) *Fossil fuel resources are saved*
- 2) *No solid residues are produced^b, since ashes from the alternative fuels are incorporated into the cement clinker.*
- 3) *Flame temperatures of up to 2000°C and high residence times provide good conditions for destruction of organic compounds.*
- 4) *Alternative fuels may be CO₂ neutral.*

However, with the introduction of alternative fuels in high substitution rates, new issues have arisen:

^aIn this thesis "alternative fuels" is used as a term designating all non-fossil fuels except petcoke. By-product, secondary, waste or replacement fuel are often used as synonyms for alternative fuels.

^b An exception is a possible higher by-pass dust production (see also chapter 3).

- 1) *What are the combustion kinetics of the various alternative fuels, and how should existing/new combustion equipment be altered/developed to obtain the desired fuel conversion?*
- 2) *How is the quality of the cement clinker affected by using alternative fuels?*
- 3) *How does the use of alternative fuels influence kiln process stability and production capacity?*
- 4) *How is the stack emission of NO_x , SO_2 , acidic gasses, trace metals, unburnt hydrocarbons, CO and dioxins/furans influenced by the use of alternative fuels?*
- 5) *How are the alternative fuels transported, stored, handled and delivered?*

The main technical subject of this thesis is to understand the combustion steps of alternative fuels, identifying rate determining parameters and quantifying how these are influenced by relevant parameters. This is discussed thoroughly in chapters 4 and 5. It is demonstrated in chapter 3 that tyre derived fuel (TDF), meat and bone meal, plastics and waste oils are presently the most important alternative fuels in the German cement industry. The emphasis is on qualitative and quantitative characterisation of the combustion steps when using TDF in cement production. The emphasis on TDF is mainly due to the fact that the starting point for this work has been a characterisation of FLSmidth's HOTDISC with respect to prevailing combustion mechanisms. The reference fuel for the HOTDISC is TDF. However, analogies, with origin in experiments and mathematical models are drawn to other fuels, which enable prediction of the combustion kinetics of these fuels.

Cement quality may be affected by minor components introduced with the alternative fuels. This is briefly reviewed in section 3.3 of this thesis. The effect of alternative fuel utilization on the kiln stability is also reviewed briefly in section 3.3. The emissions of gaseous compounds when using alternative fuels are reviewed briefly in section 3.4. For the emissions of NO_x and SO_2 from the cement production particular attention should be paid to the works of Jensen [7] and Hansen [8], respectively. The issues related to the storing, handling and stable delivery of alternative fuels are beyond the scope of this thesis.

1.2 Structure

Chapter 2 of this thesis provides background information regarding the modern process of cement production. The emphasis is on the kiln system, as this is where the alternative fuels are combusted.

Chapter 3 reviews different issues regarding utilization of alternative fuels in cement production. It further describes how the combustion characteristics, and in particular the carbon burnout of the alternative fuels in the calciner system and/or rotary kiln are important, in order to ensure the desired cement clinker quality and stable kiln system operation.

Chapter 4 discusses the devolatilization of large fuel particles. The emphasis is on tyre rubber, investigating the effect of particle size, temperature, steel wires and conversion pathway on overall devolatilization kinetics. Experiments under controlled conditions are described and analysed using mathematical modelling. The chapter starts out with an introduction to basic principles of solid fuel combustion.

Char oxidation is the topic of chapter 5. Tyre rubber char is the starting point of the investigations including experimental investigations under well defined conditions and mathematical analyses. The results of the analyses of the controlled experiments are applied in mathematical models, in order to simulate burnout of realistically sized tyre chars in a modern In-Line-Calcliner.

Chapter 6 describes and analyses plant measurements at two industrial scale HOTDISCs in order to determine fuel burnout of alternative fuels on the HOTDISC. The analyses are further accomplished using mathematical modelling and results derived from chapter 4 and 5.

Chapter 7 contains the overall conclusions regarding combustion of alternative fuels utilised in modern cement production plants. Suggestions for further work are made.

1.3 Objectives

The main objective of this thesis is to provide scientifically based knowledge regarding combustion mechanisms of alternative fuels applied in cement production. This is achieved through experimental investigations on a laboratory and industrial scale coupled with mathematical modelling analyses.

The knowledge can and has been used to redesign existing combustion equipment, or to develop new equipment in order to achieve the best possible conditions for alternative fuel utilization, considering the restrictions set by kiln process stability and cement clinker quality. In addition, the knowledge is used to produce a scientifically based framework to identify the most important alternative fuel characteristics, in order to 1) predict where in the kiln system the specific fuel should be used, and 2) identify what type of combustion equipment that is the most appropriate.

This thesis has been written to be applied both by the cement production industry and related companies, as well as on academic level.

1.4 References

¹ Chandelle, J.M.; Alternative Fuels: The “Valorisation” of waste in the cement industry; Cement International, 4, 50-60, 2003.

² Dry Process Kiln Systems; Available from FLSmidth.com.

³ News & Analysis, The Independent Cement Producers Association; Issue 3, December, 2005.

⁴ Scheuer, A.; Utilization of Alternative Fuels and Raw Materials in the Cement Industry; Cement International, 1, 48-66, 2003.

⁵ Hoidalén, O.; An Alternative Approach; International Cement Review, 40-44, August 2006.

⁶ EC Directive 1999/31/EC available from www.europa.eu.int.

⁷ Jensen, L.S.; NO_x from cement production – Reduction from primary measures; PhD Thesis, Department of Chemical Engineering, DTU, Denmark, 1999

⁸ Hansen, J.P.; SO₂ emissions from cement Production; PhD Thesis, Dept. of Chem. Eng., Technical University of Denmark, 2003

Chapter 2 – Cement Chemistry and Production

Chapter 2 seeks to provide sufficient insight into the chemical and process aspects of modern cement production systems required to understand the implications of alternative fuel usage on cement production. With regard to processing, the main emphasis is on the kiln system, as this is where the alternative fuels are combusted.

Initially, a short historical perspective of cement and production processes is provided, and then fundamental cement chemistry is treated followed by an overview of the modern cement production plant. Finally, more detailed descriptions of modern kiln systems are provided.

2.1 Historical Perspective

Since ancient times, burnt limestone (mortar) has been used as a binder material for constructions [1,2]. Mortar, however, is not durable and burning of limestone with impurities was discovered to result in a much more durable paste. The main type of cement that is used today is termed *Portland cement* and is based on a burned mixture of limestone, sand and clay.

During the last 150 years, the production processes used for Portland cement production have moved from shaft kiln units with production capacities of about 7 tonnes cement clinker per day to modern production plants with a production capacity of up to 12000 tonnes cement clinker per day. The development has mainly been driven by a desire to attain a lower specific energy consumption per mass of cement clinker produced. Initially, the shaft kilns were replaced by long rotary kilns fed with a wet slurry resulting in a specific heat consumption of about 1400-1500 kcal/kg clinker. A long rotary kiln fed with dry raw materials reduced the specific energy consumption to about 1075 kcal/kg clinker, as the evaporation of water from the slurry was avoided [3]. Further developments led to a separation of the processes involved in cement clinker production in order to improve energy efficiency. The modern kiln system of today consists of separate processes including raw material pre-heating, a pre-calcination unit for calcination of limestone, and a rotary kiln for the final cement clinker burning. The specific energy consumption of a modern process is about 700 kcal/kg clinker. The next major development is to replace fossil with alternative fuels in order to achieve the advantages outlined in chapter 1.

2.2 Cement Chemistry

Portland cement is a hydraulic binder that sets and hardens by chemical interaction with water and is capable of doing so under water with the purpose of holding solid particles together in a coherent mass [4]. Portland cement is manufactured from Portland cement clinker that is mixed and interground with gypsum. The names as well as the chemical composition of the main constituents of Portland cement clinker appear from Table 2-1. Belite and alite are responsible for the late and early strength giving properties respectively, whereas ferrite and aluminates form melt phases during cement clinker burning, which accelerates cement clinker formation (see also section 2.2.3). The components of $2\text{CaO}\cdot\text{SiO}_2$ and $3\text{CaO}\cdot\text{SiO}_2$ are polymorphs and may exhibit different crystal structures. The names alite and belite denote the components with the desired crystal structure.

<i>Name</i>	<i>Chemical composition</i>
<i>Belite</i>	$2\text{CaO}\cdot\text{SiO}_2$
<i>Alite</i>	$3\text{CaO}\cdot\text{SiO}_2$
<i>Ferrite</i>	$4\text{CaO}\cdot\text{Al}_2\text{O}_3\cdot\text{Fe}_2\text{O}_3$
<i>Aluminate</i>	$3\text{CaO}\cdot\text{Al}_2\text{O}_3$

Table 2-1: Main constituents of Portland Cement clinker.

According to Hewlett [4], the Portland cement product should possess the following physical characteristics:

- a) *The product should not expand significantly during hydration causing cracks.*
- b) *When ground with gypsum, the final product should yield a specific surface area of 300-350 m²/kg.*
- c) *Develop a 28 day strength of 50-65 N/mm² when tested according to method EN 196-1.*

The above criteria are usually met when the clinker contains:

- a) *<3 wt.% free CaO*
- b) *<5 wt. % MgO*
- c) *70-80 wt.% alite and belite of which more than 60wt.% should be alite*

Alkali sulphates up to 3 wt.% and other minor components may also be accepted in the clinker.

2.2.1 Raw Materials

The typical raw materials used for the production of Portland cement clinker are naturally occurring limestone, clay, sand or by-products from other industries (e.g. coal fly-ash). Limestone is the source of calcium whereas clay and sand are the sources of silicates,

aluminum as well as iron. Raw materials may also derive from waste materials [5]. The components of the raw meal mixture and the fuel ash should match the desired clinker chemistry. For instance, when utilizing tires with steel reinforcements as a fuel, the amount of iron in the raw material mixture should be adjusted accordingly. However, in the production of white cement, the iron content of the raw materials and fuels is relatively lower and care should therefore be exerted using tyre derived fuels containing steel wires [4].

The raw materials are heated up to 1450°C in the kiln system (see section 2.3.2), which results in chemical and physical processes that form the components of the Portland cement clinker.

2.2.2 Calcination

Calcination is the first major chemical step in the thermal treatment of the raw materials, in which calcium carbonate decomposes into its oxide and carbon dioxide as shown in equation (2-1):



This is the most endothermic reaction in modern cement production plants consuming about 58% of the fired energy. The equilibrium temperature of this reaction is about 700-900°C (depended on CO₂ partial pressure), and as a consequence CaCO₃ decomposes to CaO in this temperature range and above (see also Figure 2-1). In addition, as the calcination reaction is very endothermic and its rate generally is faster than the rate of heat release from combustion (due to the small particle size), calcination may be used to control the temperature in different parts of the kiln system (see also section 2.4).

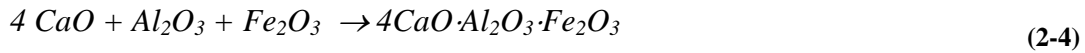
2.2.3 Clinker Reactions

Clinker reactions occur at temperatures between about 700°C and 1450°C forming the cement clinker product (see also Figure 2-1). The reaction scheme forming the final clinker constituents involves intermediate compounds, and the clinker reactions may be affected by minor compounds (see also sections 3.2 and 3.3). The overview given here emphasizes the overall clinker reactions as well as other important chemical reactions. A detailed overview of the chemistry, phase relations etc. is provided by Hewlett [4], Bye [7] or Taylor [8].

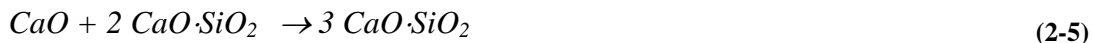
From about 700°C the formation of belite from CaO and SiO₂ takes place according to (2-2). Correspondingly, the silicate source quartz is observed to be consumed in Figure 2-1.



From about 900°C, the solid compounds of aluminate (abbreviated C₃A) and ferrite (abbreviated C₄AF) are formed according to:



At temperatures above about 1300°C, aluminate and ferrite form a melt phase acting as a media for increased diffusive transport, and consequently increased reactivity of alite crystal formation from lime and belite according to (2-5).



The amount of melt and its viscosity have significant influence on the alite formation and may be influenced by changing the chemical composition of the feed. Decreased viscosity may accelerate the dissociation rate of belite and lime as well as increase its diffusion rate through the liquid phase and hence increase reactivity of alite formation [4]. Simultaneously, under the action of the rotary kiln (to be introduced in section 2.3), clinker nodules are produced in the cm size. Rapid cooling produces the final product. However, if the cooling rate is not sufficient, alite may dissolve into the liquid phase and appear as secondary belite and free lime. This is unwanted since secondary belite does not possess the same strength giving properties as alite and belite [4,7].

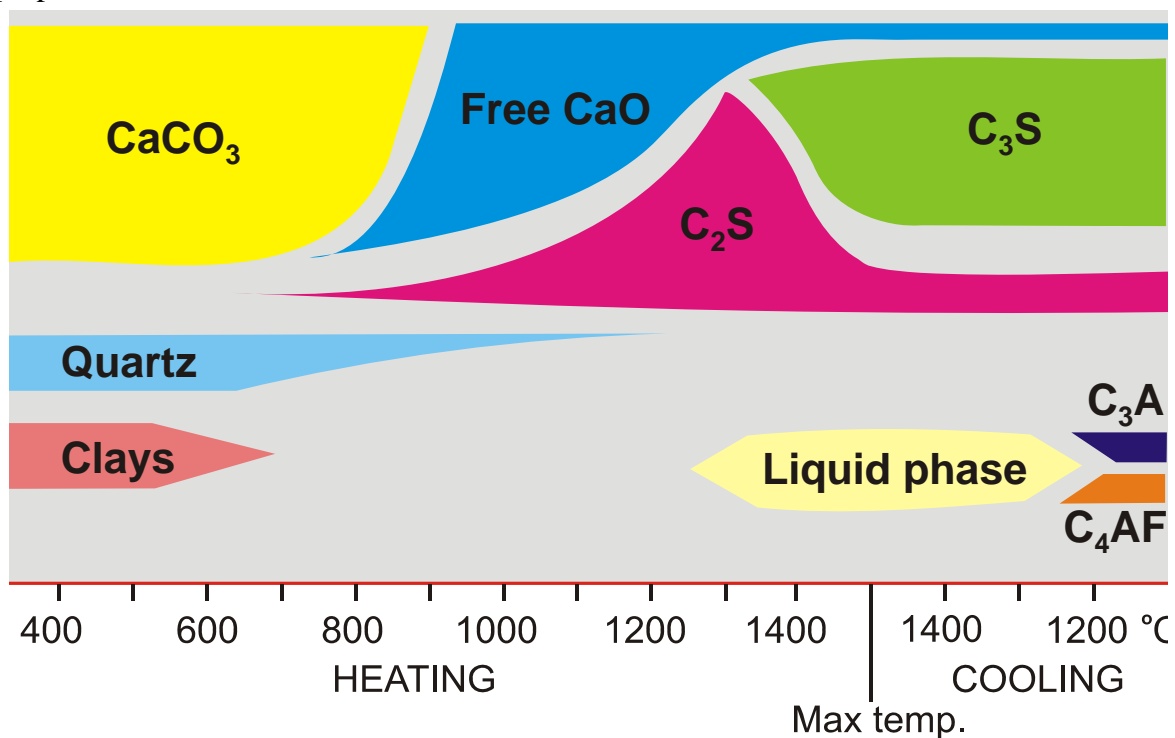


Figure 2-1: Phases present at different temperatures during cement clinker production. Abbreviations are: C=CaO, A=Al₂O₃, S=SiO₂ and F=Fe₂O₃. From [9].

2.3 Overview of a Modern Cement Production Plant

The production process may be divided into three parts including: 1) preparation of raw materials, 2) pyro-processing and 3) clinker processing, storage and shipment. In the following sections, a brief description of each part is provided. In section 2.4, a more detailed description of the kiln system is provided, due to its importance regarding interpretation of combustion mechanisms of alternative fuels in cement production.

2.3.1 Preparation of Raw Materials

Initially, the raw materials are crushed to a particle size of about 25-100 mm [2] and stored in separate storages according to their content of limestone, silicates, iron and alumina. This enables a continuous delivery of raw materials to the raw mill, with a composition matching the desired product, because different amounts of raw material may be retrieved from each storage. The particle size of the raw material mixture is further reduced to about 90 wt.% smaller than 90 μ m, with a mass based average particle size of about 40 μ m. This is done in the raw material mill where the raw materials are also dried by hot flue gasses from the kiln system [2]. The fineness of the raw material is mainly determined by how fine grinding of different constituents is required to reach a desired burnability [4]. The produced raw material mixture ready for production is stored in a silo.

2.3.2 Pyro Processing

Pyro processing involves the preheating of raw materials, calcination, clinker reactions as well as cooling. A flow sheet of a modern kiln system for cement production is shown in Figure 2-2. Raw materials are admitted to the preheater and heated counter current by direct contact with the hot flue gasses. The preheated raw material is then admitted to the calciner system where decomposition of CaCO_3 takes place. The energy needed for the endothermic calcination is supplied by combustion of the fuel added in preheated air. The calcined raw material is admitted to the rotary kiln, where the remaining clinker reactions as well as nodulisation take place. Fuel and preheated air are admitted to the rotary kiln in order to heat the reacting materials to a temperature where the clinker reactions take place. Finally, the clinker is cooled by air in the clinker cooler, producing a preheated combustion air that is used in the rotary kiln and in the calciner system. The flue gas from the rotary kiln may be passed directed through the calciner (1) or bypassed (2), i.e. In-line-calciner (ILC) or Separate-line-calciner (SLC) system respectively.

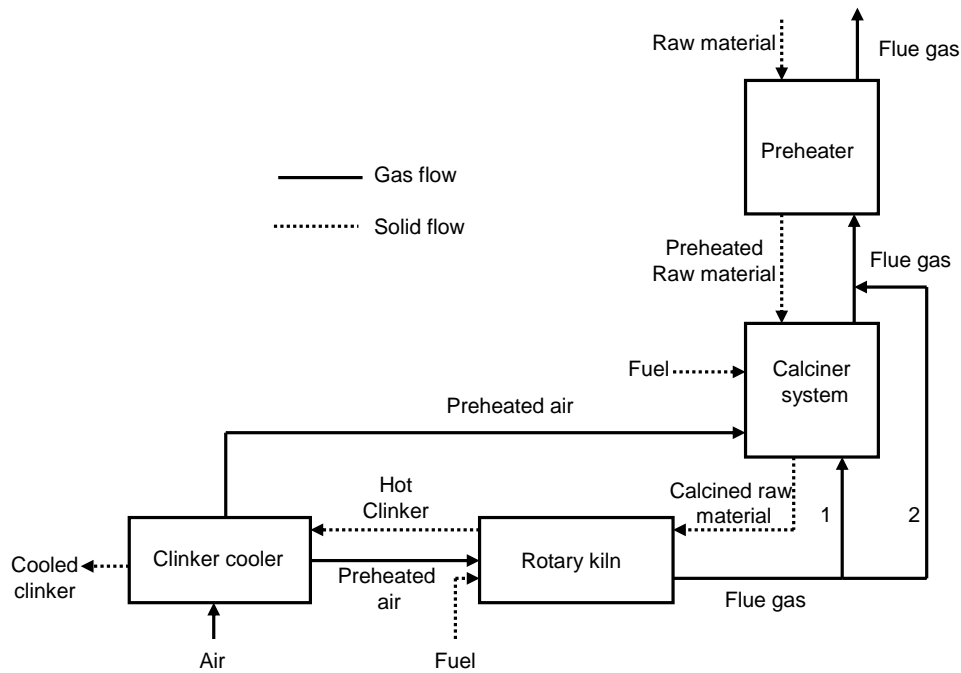


Figure 2-2: Flow diagram of modern kiln system for cement production.

A more detailed view of the preheater, calciner system and rotary kiln is provided in section 2.4, due to their relevance to understanding the implications of alternative fuel utilization.

The aims of the clinker cooler are to 1) recuperate as much of the heat from the clinker as possible and transfer it to the combustion air, and 2) to cool the clinker sufficiently fast to minimize secondary belite formation. In modern systems, this is usually accomplished in cross current grate coolers. Cement clinker at this stage typically has a particle size of 20-50 mm.

2.3.3 Clinker Processing

The clinker is stored in a clinker silo before being mixed and interground with a few percent of gypsum (to control hydration rate of the final cement product). Additives, such as coal fly-ash, sand or raw material may also be added at this stage. The additives may exhibit pozzolanic properties, whereby they actually contribute positively to the cement's strength giving properties. Size reduction of the cement clinker at this stage is accomplished by using a cement mill installation that frequently includes a separator and a roller press. The cement product of a sufficient fineness is transported to a cement silo from which it is distributed over land or by sea.

2.4 Review of the Kiln System

As alternative fuels are applied in the rotary kiln or the calciner system, a review of them is provided here. A brief description of a typical modern preheater is described, as this is important when interpreting certain types of emissions and overall process stability (see also chapter 3). Temperatures, O₂-levels and residence times in the different parts of the kiln system are provided as they are important to interpret combustion. The aims of this section are to 1) draw attention to important features of the kiln system with regard to combustion, and 2) to introduce nomenclature for the easier interpretation of results and discussions in later chapters.

2.4.1 Rotary Kiln

The aim of the rotary kiln is to create an environment promoting the chemical clinker reactions as well as nodulisation. The aims of the rotary kiln burner are 1) to provide heat for the clinker reactions to take place, 2) to ensure sufficient fuel burnout in order to reduce impact on clinker quality (see also section 3.2), and 3) to reduce emissions. The flame of the rotary kiln burner should be short and intense close to the burner tip in order to achieve rapid heat up and cooling of the material charge to increase alite formation reactivity and to minimize formation of secondary belite [10,11,12].



Figure 2-3: View inside the rotary kiln along the burner. At the bottom of the picture, the cement clinker is seen to leave the rotary kiln.

The typical rotary kiln burner is of the non-premixed type [13], where fuel(s) and transport air are delivered somewhere in the center of the burner, while the remaining combustion air is mixed gradually into this fuel stream. Swirl is usually applied to achieve better mixing, but this increases flame divergence. The remaining combustion air is withdrawn from the cement clinker cooler. As a consequence of the high temperature and the non-premixed combustion, mass transfer (char combustion) or mixing (gaseous combustion) is usually the main rate determining parameter of the combustion process [13].

Temperatures

The material temperature in the rotary kiln is up to about 1450°C in order to ensure sufficient alite formation. Consequently, the gas temperature in the rotary kiln must be significantly higher in order to produce a driving force for heat transfer between gas (flame) and material

charge. Typically, gas temperatures in the rotary kiln vary from a gas inlet temperature of 850-1100°C and up to 1700-2000°C [2,7] in the hottest parts of the flame and then decreasing to about 900-1100°C in the rotary kiln gas outlet. The temperature profile varies in the axial direction (distance from burner) and radial direction, and mainly depends on fuel properties as well as burner type and its adjustment. In the radial direction, steep temperature gradients exist as a consequence of the diffusion flame.

Oxygen Levels

Subsequent to clinker cooling, the preheated air (still) has an oxygen concentration of about 21 vol.% equalling atmospheric air. In the rotary kiln, the oxygen level decreases as the combustion proceeds to approximately 3-5 vol.% at the rotary kiln gas outlet. The axial and radial oxygen concentration in the flame is mainly dependent on the fuel properties and fluid dynamics.

Residence Times

Preheated raw materials are admitted at the material kiln inlet. The residence time for solid material travelling downwards through the rotary kiln is typically 10-30 minutes [14,15] and influenced by the kiln inclination, length and rotational speed [16]. The average gas residence time in the rotary kiln is typically in the range of 5-10 seconds and is mainly dependent on kiln size, degree of filling in the kiln as well as temperature distribution, due to the fact that the gas density is dependent on temperature and hence its velocity through the kiln.

2.4.2 Preheater

In modern systems, preheating of raw materials takes place counter current in direct contact with the flue gas. A multi stage cyclone preheater is applied for this purpose (see also Figure 2-4). The raw material mixture is fed to the process in the hotter flue gas stream between 2nd and 1st cyclone stage, where heat exchange with the gas takes place followed by a subsequent gas solid separation in the 1st stage cyclone. The gas that leaves the 1st stage is conveyed through the raw mill and the filter/electrostatic precipitator to the stack. The solids are conveyed to the gas between 3rd and 2nd stage where they experience the same heat exchange followed by separation of the gas and solids. Due to the suspension of particles in the upward gas stream in the duct between two cyclones, efficient heating of the solid raw materials is achieved (i.e. high heat transfer rate).

In the preheater section, the oxygen concentration is almost constant and is only slightly affected by consumption in for instance 1) reactions between pyrite (FeS_2) in raw materials and oxygen (see also section 3.4), 2) recarbonation of CaO forming CaCO_3 , 3) consumption of organic C in raw materials see also section 3.4), or 4) small amounts of atmospheric air entrained into the preheater.

Strauss et al. [15] have established the solid residence time in a single preheater stage to be about 10 seconds, whereas the gas residence time is approximately 1-2 seconds.

2.4.3 Calciner Systems

The aims of the calciner system are to:

- 1) *Decompose CaCO_3 to CaO (Calcination)*
- 2) *Convert the fuel sufficiently (see also sections 3.2 and 3.3)*
- 3) *Reduce emissions (see also section 2.4)*

and for this purpose, the following categories of modern calciner systems are typically applied:

- 1) *In-line-calciner (ILC)*
- 2) *Separate-line-calciner (SLC)*
- 3) *Extensional equipment designed for difficult fuels not applicable to 1) and 2)*

Category 3) equipment is typically combined with 1) or 2). In this thesis, the focus is on the ILC system and its combination with 3), as this was the starting point with the HOTDISC, and these systems are therefore described most thoroughly. Brief descriptions of the SLC systems are provided. Systems of category 3) are described in section 3.2.

2.4.3.1 ILC System

Figure 2-4 provides an overview of a typical modern ILC system and its position relative to the cyclone preheater, the rotary kiln and the cooler. The ILC system is mainly characterised by the fact that the flue gas coming from the rotary kiln is led directly through the calciner (see also Figure 2-2). In the ILC system, a part of the preheated air, produced during clinker cooling, is bypassed the rotary kiln and is led directly to the calciner. This minimises the amount of gas flow through the rotary kiln and hence rotary kiln size reduction. In addition, good conditions for reduction of NO_x produced in the rotary kiln are achieved (to be described later in this section). Systems without a tertiary air duct are denoted ILC-E, where E denotes excess air through the rotary kiln compared to the ILC system with a tertiary air duct.

The combustion characteristics of solid fuel particles and liquid droplets in the ILC are significantly different than in the rotary kiln, because they burn in suspension imaging single particle behavior. The temperatures are lower in the ILC than in the flame of the rotary kiln and the chemical reaction kinetics are therefore more important than in the rotary kiln (see also chapters 4 and 5). The suspension type burning ensures good external mass and heat transfer. Utilization of gaseous fuels in the ILC needs mixing of fuel and oxidizer and is mainly influenced by turbulence and chemical kinetics. Combustion of volatile gasses from

solid fuels is similar to gaseous fuel combustion. In addition, modern systems may be equipped with a duct in order to mix regions of incompletely combusted gasses with oxygen rich regions eliminating CO by oxidation [17].

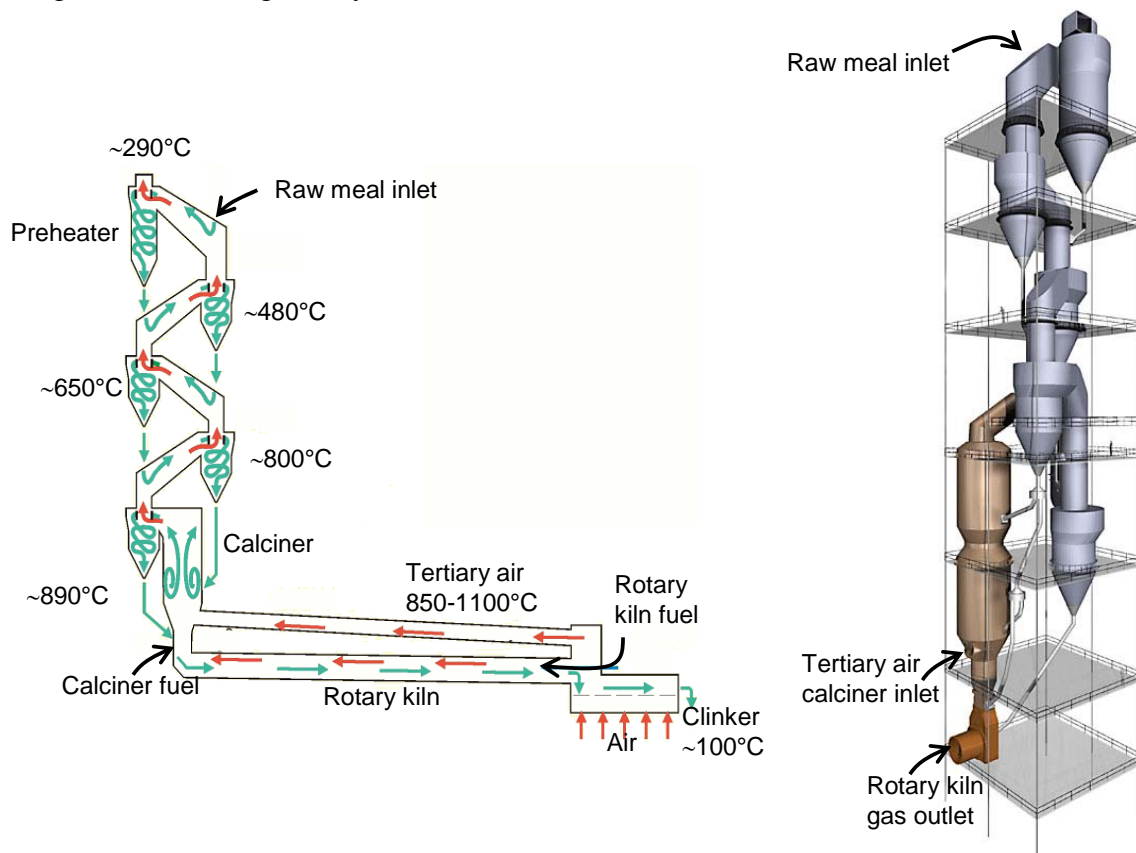


Figure 2-4: Modern In-Line-Calciner (ILC) and preheater system in 2D view and the preheater and calciner in 3D view.

Temperatures

The temperatures in modern calciner systems range from a lower value of 800-900°C and up to 1150-1200°C. The lower value reflects the equilibrium temperature of the CaCO_3 decomposition, and the higher value is set by the initiation of melt formation of raw material particles that may cause blockages in the calciner.

A high temperature oxidation zone may be promoted in order to increase fuel reaction rates, and is achieved by admitting non-calcined raw material from the preheater to positions higher up in the calciner than the fuel is admitted. Consequently, CaCO_3 will not be available in sufficient amounts to consume the energy released from the combustion process (see Figure 2-4 and Figure 2-5). A high temperature region also provides enhanced reduction of NO_x formed in the rotary kiln under the reducing conditions prevailing in the region between the calciner fuel and tertiary air admission (see also Figure 2-5) [18].

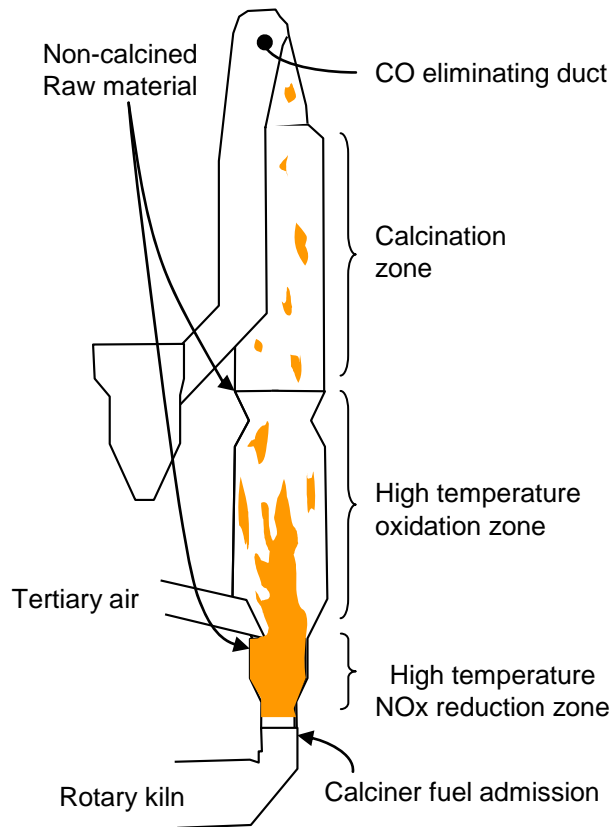


Figure 2-5: Different zones in the modern In-Line-Calciner.

Oxygen Levels

In the lower part of the calciner, the oxygen level is low because fuel is admitted without its combustion air (see Figure 2-5). Tertiary air is admitted to the calciner further up. The oxygen level in the calciner decreases from 21 Vol.% at this point and up through the calciner to about 3 vol.% in the lowermost cyclone. This decrease is due to O_2 being consumed in the combustion process and gaseous CO_2 from calcination producing a higher gas flow and consequently a dilution of oxygen. The distribution of O_2 throughout the calciner is mainly determined by fuel properties and fluid dynamics.

Residence Times

In modern ILC calciner systems, the average gas residence time is typically in the order of 3-4 seconds.

However, suspended raw material particles with sizes of about $5\text{-}13\mu\text{m}$ have been demonstrated to have a residence time about four times the gas residence time, despite the fact that these small particles have a terminal velocity of a few mm/s, which is significantly lower than the upward average gas velocity ($\sim 8\text{m/s}$). The higher solid residence time is attributed to the high concentration of particles, causing them to form clusters/aggregates with significantly higher terminal settling velocity than the gas, falling some length in the calciner.

Eventually, the clusters split up into single particles which are carried upwards while they form new clusters and the process is repeated. Consequently, particles caught in clusters/aggregates must travel the same distance more than once and their passage through the calciner is hindered [19].

Giddings et al. [20] performed CFD simulations of an ILC system and found that particle concentrations were higher along the outer wall than in the middle of the calciner. However, they did not include micro flow structures, e.g. the tendency of the small particles to form aggregates/clusters.

2.4.3.2 SLC Systems

In the Separate-Line-Calciner system, flue gasses from the rotary kiln are bypassed the calciner (see also Figure 2-2).

In the SLC-D(owndraught) system (see Figure 2-6), fuel is added at the top whereas tertiary air with suspended raw material particles are introduced tangentially. Consequently, the fuel burns as a downward directed diffusion flame in the centre, and the raw material particles are transported to the wall and downward by the centrifugal and gravitational force. This distribution of raw material along the wall ensures a high flame temperature as well as cooling of the refractory wall. In addition, combustion takes place in a region of higher O₂ concentration than in the ILC system, as the flue gas from the kiln is not mixed until after the calciner. However, the downward direction may result in a lower solid fuel residence time than in the ILC or SLC (see later). In addition, the convective mass and heat transfer rates between particle and gas may be smaller than in the ILC or SLC, due to particles being entrained with the gas in the SLC-D compared to the suspension type burning in the SLC or ILC.

Overall, the high temperature and the high oxidizer level provide good conditions for combustion, but the downward direction lowers the solid residence time and the entrained particle behaviour lowers mass and heat transfer from gas to fuel particle.

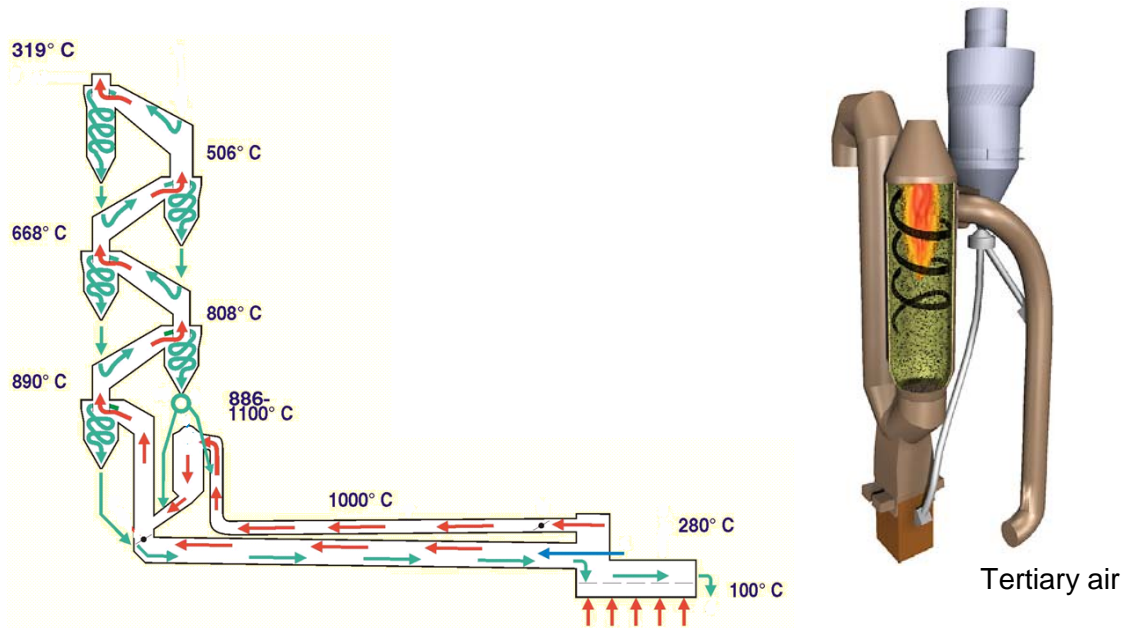


Figure 2-6: SLC-Downdraft calciner and its position relative to the rotary kiln and the preheater.

In the SLC system (see Figure 2-7), the calciner design and consequently combustion characteristics are similar to the ILC system, except that combustion of the calciner fuel takes place in a region of higher O_2 concentration than in the ILC.

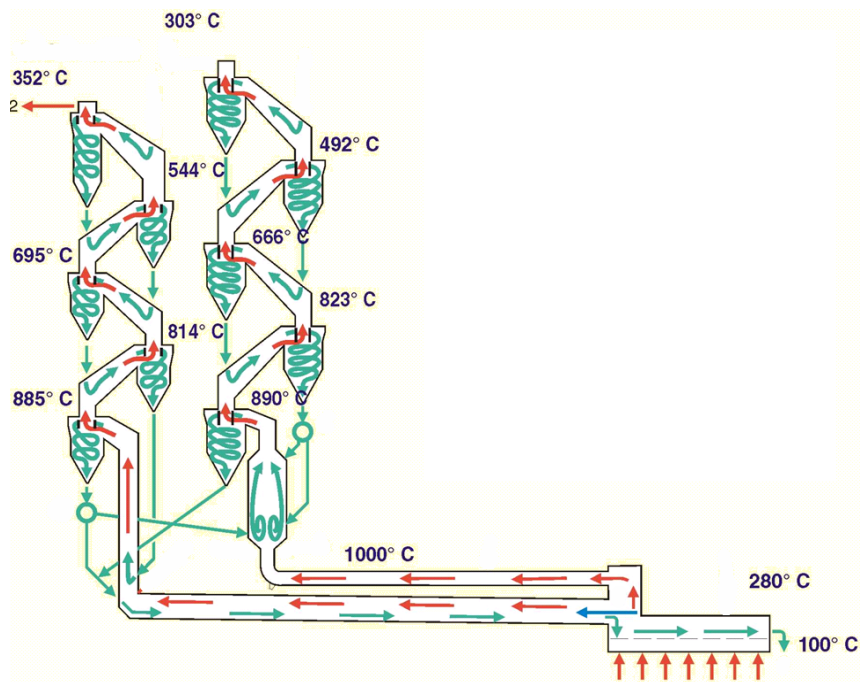


Figure 2-7: SLC calciner and its position relative to the rotary kiln and the preheaters.

2.5 Conclusions on Chapter 2

Production of Portland cement clinker requires the right proportions of limestone, silicates as well as sources of aluminium and iron in order to produce a cement product with the desired properties. The main strength giving properties are the di- and tricalcium silicates of alite and belite, respectively.

In the production, raw materials are initially reduced in particle size, preheated and burnt in the kiln system in order to produce cement clinker. The cooled clinker is mixed and interground with gypsum in order to produce the final cement product.

Two main types of calciner systems are described in this section, namely the in-line-calciner and the separate-line-calciner, and differences with regard to combustion characteristics were identified. The main emphasis is on the ILC system, as this together with the HOTDISC is the basis for the presented in later chapters.

Temperature as well as oxygen levels range in the kiln system from about 290°C-2000°C and from ~3-21 vol.% respectively. The solid and gas residence times vary in all parts of the kiln system.

2.6 References

- ¹ Larsen, J.B.; F.L.Smith & CO's technological development in the twentieth century; Master Thesis, University of Southern Denmark; August 2001 (In Danish).
- ² Cementfabrikken (In Danish); FLSmith & CO; January 1981.
- ³ Jensen, L.S., Thomsen, K.; Emissions, Fuel Diversity and Energy Efficiency Driving the Development of FLSmith's Kiln Systems; Proceedings of Dansk Kemi-ingeniør Konference, Technical University of Denmark, 24.-26. of may, 2004.
- ⁴ Hewlett, P.C. (Editor); Lea's Chemistry of Cement and Concrete (4th ed); Elsevier Butterworth Heinemann, 2004. ISBN 0-7506-6256-5.
- ⁵ Scheuer, A.; Utilization of Alternative Fuels and Raw Materials in the Cement Industry; Cement International, 1, 48-66, 2003.
- ⁶ HSC Chemistry Database v.5.11; Outokumpu Research; November 2002
- ⁷ Bye, G.C.; Portland Cement, 2nd ed; Thomas Telford, London, 1999. ISBN 0-7277-2766-4.
- ⁸ Taylor, H.F.W.; The Chemistry of Cements; Academic Press, London, 1964.
- ⁹ The International Cement Production Seminar, Vol.2, Chapter 17; FLSmith & CO, May 2002.
- ¹⁰ Retallack, D.; Minor heart surgery; Cement Environmental Handbook, 127-132, 2003.
- ¹¹ Ohlsen, I.; Burner Technology; Innovation for Sustainability - VIth Colloquia of Managers and Technicians of Cement Plants, 133-146, Valencia, Spain, 1-3 March, 2006.
- ¹² Vaccaro, M.; Boosting Alternative Fuel Firing; World Cement, 85-90, August, 2006.
- ¹³ Smith, I.; Co-Utilisation of coal and other fuels in cement kilns; IEA Clean Coal Centre, August 2003. ISBN 92-9029-386-1.
- ¹⁴ The International Cement Production Seminar, Vol.1, Chapter 11; FLSmith & CO, May 2002.
- ¹⁵ Strauss, F., Steinbiss, E., Wolter, A.; Messung der Verweilzeiten in Zementbrannanlagen mit Hilfe von Radionukliden; ZKG International, 9, 1987.
- ¹⁶ Niessen, R.W.; Combustion and Incineration Processes, 3rd ed.; Marcel Dekker, Inc., New York, 2002. ISBN 0-8247-0629-3.
- ¹⁷ Happ, K.R., Jensen, L.S.; Leading the way; World Cement, 67-72, June 2006.
- ¹⁸ Jensen, L.S., Shenk, R.E.; Fulfilling Emission Guarantees; World Cement, 87-94, December 2005.
- ¹⁹ Hundebøl, S., Kumar, S.; Retention time of particles in calciners of the cement industry; ZKG International, 8, 422-425, 1987.
- ²⁰ Giddings, D., Eastwick, C.N., Pickering S.J. and Simmons, K.; Computational Fluid Dynamics applied to a Cement Precalciner; Proc. Inst. Mech. Eng., Vol. 214 Part A, 269-240, 2000.

Chapter 3 – Alternative Fuels in Cement Production

This chapter reviews issues regarding the utilization of alternative fuels in cement production. Section 3.1 reviews the types and amounts of alternative fuels in cement production as well as fuel analyses of the most important fuels. Section 3.2 discusses where and how alternative fuels are applied. The influence on cement quality as well as the process stability of alternative fuel utilization is reviewed in section 3.3. Finally, section 3.4 assesses the influences of alternative fuel utilization on emissions. The emphases of this chapter are combustion process and chemistry-related issues rather than extensional equipment for handling, storing or transporting of alternative fuels, as well as infrastructure-related issues, outside the cement plant.

3.1 Alternative Fuel Types and Amounts

3.1.1 Types of Alternative Fuels

Many types of alternative fuels are applied, ranging from hazardous to non-hazardous, and they may be in the gaseous, liquid or solid state. Figure 3-1 lists different alternative fuels used in cement production. The list is not complete; however, it demonstrates the diversity with regard to physical properties as well as composition that may be expected among the different fuels. The size of the groups may be regarded as an approximate indicator of the amounts currently used, i.e. solid fuels are the most important, whereas gaseous fuels are rare.

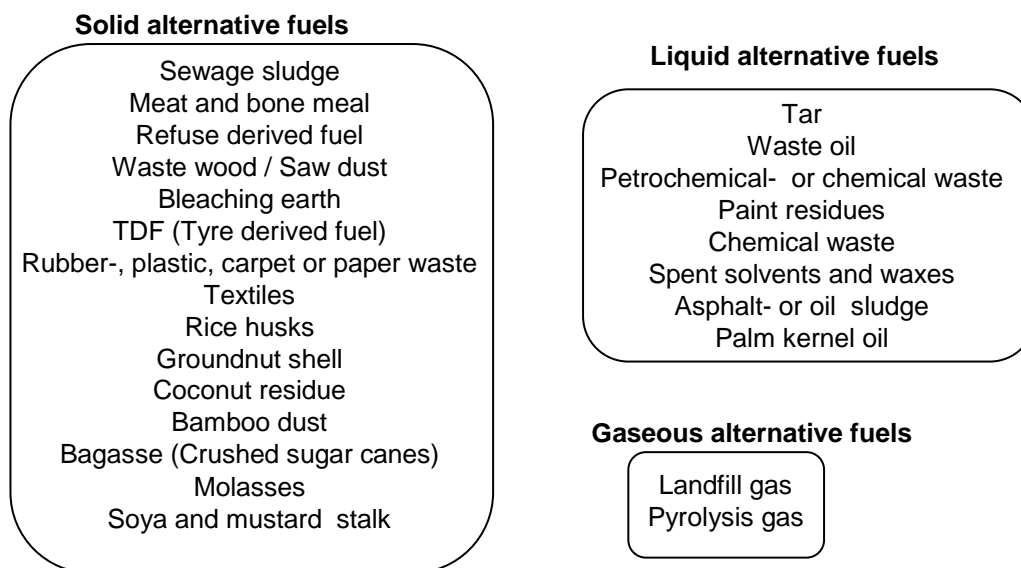


Figure 3-1: Alternative fuels used in cement production (partly from [1,2,3]).

3.1.2 Quantification of Alternative Fuels in Cement Production

Utilization of alternative fuels in cement production, as described in chapter 1, is mainly practised in the developed countries. Consequently, more detailed statistical information is available for these countries compared to the limited information from developing countries. The discussion here is therefore mainly based on data from developed countries.

3.1.2.1 Alternative Fuel Substitution Rates

The overall substitution rate of alternative fuels for fossil fuels varied inside the European Union from 0-4 energy-% in 1999-2001 for countries such as Ireland, Portugal, Poland, Finland, Denmark and Great Britain to a fuel substitution rate of 72 energy-% in the Netherlands. In between, Germany, Belgium, Austria, Switzerland and France had an overall alternative fuel substitution rate of about 30 energy-% [4,5]. In USA and Canada in 2002, the alternative fuel substitution rate was about 26 and 15 energy-%, respectively [6]. In 2003, Holcim, operating 34 cement plants all over Europe, achieved an overall fuel substitution rate of 21.8 weight-% with 8.1 weight-% liquid fuels and 13.7 weight-% solid fuels [7].

As demonstrated, the substitution rates of alternative fuels vary significantly between the different countries. Detailed data regarding the utilization of alternative fuels in cement production is mainly available in Germany. These data are therefore presented and analyzed here (collected raw data presented in Table 3-1). In Figure 3-2, the alternative fuel substitution rate from 1999-2004 in Germany is shown on an energy basis. The first set of data is derived from the literature [8,9,10] and the second data set is calculated using equation (3-1) with data of Table 3-1, the heating values of Table 3-2, as well as the total energy consumption in the German cement industry in each year derived from [8 and 9].

$$Energy\% = \frac{\sum_{Fuel\ types} [Absolute\ amount\ of\ alternative\ fuel] \cdot [heating\ value]}{[Total\ fuel\ energy\ consumption\ in\ German\ cement\ industry]} \quad (3-1)$$

The results of Figure 3-2 are clear and show a significant increase in the use of alternative fuels from a substitution rate of about 23 energy-% in 1999 to 42-49 energy-% in 2004, depending on the method applied. The corresponding increase in alternative fuel substitution rate is about 4-5 energy-% per year. A few German plants were able to achieve fuel substitution rates of up to 90 energy-% in 2003 [4].

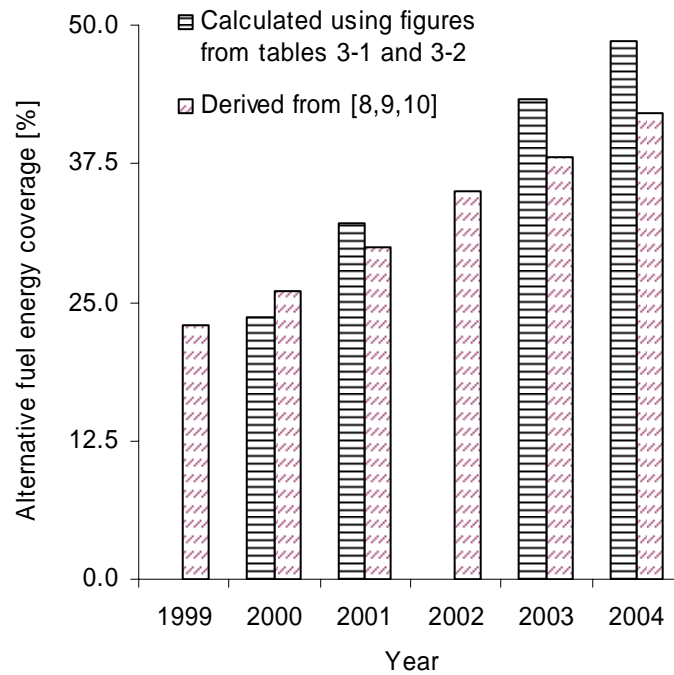


Figure 3-2: Alternative fuel substitution rate in the German cement industry from 1999-2004.

The method described here is seen to yield a slightly higher fuel substitution rate than that reported in the references of [8,9,10]. This is due to the fact that the literature data are based on a different heating value for plastics of 22 MJ/kg compared to the value of 45.3 MJ/kg applied here. The latter is valid for common plastics, whereas the value of 22MJ/kg applied in the literature is only valid for Poly-vinyl-chloride (see Table 3-2). Independent of method, the trends are unambiguous showing a significant increase in alternative fuel substitution rate in the years examined.

3.1.2.2 Amounts of Alternative Fuels

The absolute amounts of various alternative fuels as well as their proportionate shares in the German cement industry from 2000 to 2004, are shown graphically in Figure 3-3. The total amounts are observed to increase from about 1069000 to 2042000 tonnes from 2000 to 2004, in accordance with the increasing alternative fuel substitution rate.

The absolute amount of TDF as alternative fuel remained almost constant from 2000 to 2003 followed by a slight increase in 2004; however with increased overall alternative fuel substitution rates, the relative share of TDF is observed to decrease from about 23 to 14% from 2000 to 2004. Waste oils and wood as alternative fuel decreased in absolute amounts and relative level, whereas plastics increased in both share and amount. The utilization of meat and bone meal showed an increasing share up to 26% in 2003, and this increase was driven by the BSE crisis (mad cow disease) [5,10]. The share of meat and bone meal, however, dropped in 2004, but the absolute amount remained at 2003 level.

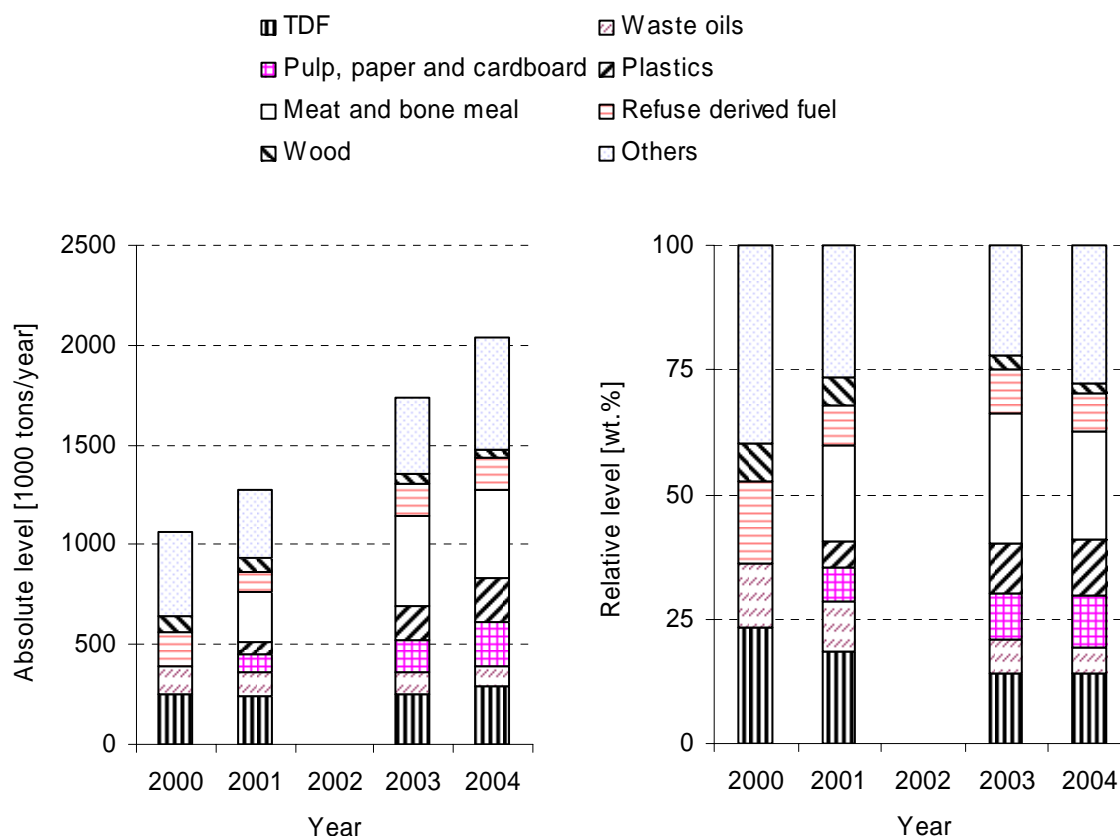


Figure 3-3: Absolute and relative levels of alternative fuels used in the German cement industry from 2000 to 2004. Others include: Sewage sludge, Bleaching Earth, Solvents, oil sludge, Textile Industry waste, Packaging materials and other undefined fuels (see also Table 3-1).

<i>Alternative fuel type</i>	<i>2000</i>	<i>2001</i>	<i>2003</i>	<i>2004</i>
<i>Reference</i>	[8]	[8]	[9]	[9]
<i>TDF</i>	248	237	247	290
<i>Waste oils</i>	140	128	116	100
<i>Pulp, paper and cardboard</i>		84	156	218
<i>Plastics</i>		67	177	229
<i>Packaging materials</i>	372 ^a	12	9	13
<i>Textile industry waste</i>		5	15	2
<i>Others</i>		250	269	401
<i>Meat and bone meal</i>		245	452	439
<i>Refuse derived fuel</i>	176 ^a	102	155	157
<i>Oil sludge/Organic dist.</i>		8	17	20
<i>Residues</i>				
<i>Wood</i>	79	72	48	42
<i>Solvents</i>	31	33	48	72
<i>Bleaching earth</i>	23	29	20	11
<i>Sewage sludge</i>	N.A.	N.A	4	48
Total	1069	1272	1733	2042

Table 3-1: Amounts of alternative fuels used in 1000 tonnes/year in the German cement industry in 2000, 2001, 2003 and 2004 as well as their relative share. a) lumped in the original reference for the year 2000.

3.1.2.3 Energy Contribution of the Applied Alternative Fuels

As the alternative fuels deliver energy to the cement production process rather than mass, an analysis of the energy contribution of each alternative fuel is made in this section, using the previously presented data on the German cement industry as a starting point. The absolute energy amount delivered with each particular fuel type may be predicted by multiplication of the amount with its respective heating value (see equation (3-2)). The results of this calculation as well as the relative proportions of the fuel types are shown in Figure 3-4. Strikingly, the absolute amount of energy delivered as well as the share of plastics, waste oils and TDF have increased significantly compared to mass basis. This is a consequence of their relatively higher heating values, compared to for instance meat and bone meal, whose energy share has dropped slightly compared to mass basis (see also Table 3-2). For this reason, all other fuels examined are also seen to drop in relative amount of energy delivered compared to mass basis.

The alternative fuels of plastics, waste oils, meat and bone meal and TDF are the most important alternative energy contributors, covering about 67-68 energy-% of the total amount of energy supplied with alternative fuels in 2001 and 2003 increasing to about 71 energy-% in 2004. The group “others” covered about 19 energy% in 2004.

$$Fired\ energy = \sum [Absolute\ amount\ of\ alternative\ fuel] \cdot [heating\ value] \quad (3-2)$$

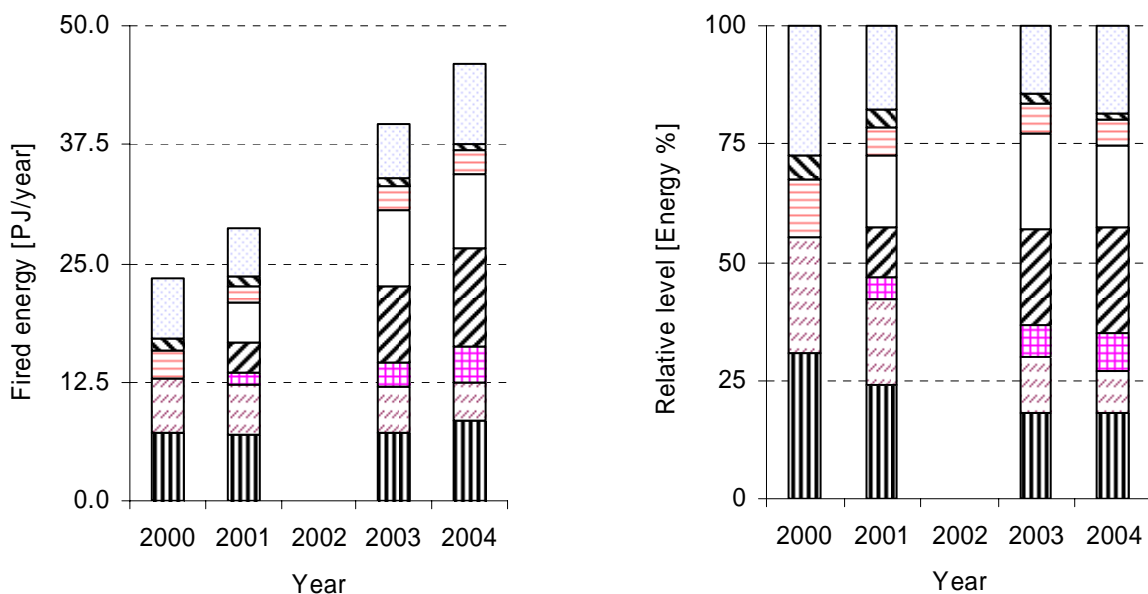


Figure 3-4: Total and relative energy contribution from alternative fuels in the German cement industry from 2000 to 2004. The heating values used are obtained from Table 3-2, except the group “others” where it is assumed to be 15 MJ/kg and the absolute amounts are obtained from Table 3-1. Captions identical to Figure 3-3.

In the French cement industry the relative amount of meat and bone meal as alternative fuel accounted for about 24 energy-% corresponding to 350,000 tonnes per year in 2001 [5]. Finally, even though no significant quantities of sewage sludge were used in the German cement industry, it was used as alternative fuel in Great Britain, Japan and the Netherlands, with substitution rates of up to 35% in the Netherlands [6].

3.1.3 Fuel Analyses

In this section, fuel analyses of the presently most widely used alternative fuels in the German cement industry are presented (see Table 3-2). The values reported are approximate and may deviate depending on local conditions, water contents in the fuels received, etc. The values, however, reflect the diversity among the common fuels utilized in cement production. The most important properties with regard to utilization in a cement kiln system which can be obtained from a fuel analysis are:

- 1) *The heating value, which influences the flame temperature and shape in the rotary kiln burner (see also section 3.2).*
- 2) *The water content, which influences the kiln systems' clinker production capacity (see also section 3.2).*
- 3) *The content of minor components, which may interfere with the cement chemistry and may cause kiln system instabilities (see also section 3.3).*

In addition, the proportion between volatile and char fractions is important, as well as physical and chemical properties, as they influence the combustion characteristics of the fuel (see also chapters 4, 5, 6 and 7).

The highest heating values are observed for plastics in the range of 42-47 MJ/kg, except for PVC which has a heating value of 22.8 MJ/kg. TDF has a heating value of about 29 MJ/kg which is similar to conventional coals traditionally used in cement production, being about 30-35 MJ/kg [11]. For wood, paper, cardboard, refuse derived fuels and meat and bone meal the heating values are around 14-20 MJ/kg. A significant difference exists in the heating values of the most widely applied alternative fuels in cement production.

Plastics and waste oils have the highest volatile content with absolute levels of about 95-100 wt. %. Wood, paper, meat and bone meal, refuse derived fuel and TDF also have a significant volatile content in the range of about 70-90 wt. %. For all the alternative fuels examined, the volatile content is higher than traditional coals used in cement production, being about 5-40 wt. % [11]. The char content of the alternative fuels examined is up to 24 wt.% for TDF, this being the alternative fuel with the highest char content. The other fuels, except plastics and waste oils have a char content of 4-15 wt.%.

From the ultimate analysis, the chlorine and sulphur level in particular should be noted for process reasons as will be described in section 3.3. The chlorine level is very high in poly-vinyl-chloride due to the element being a main part of that particular polymer type. Refuse derived fuel and meat and bone meal have a chlorine content of about 0.5-1.3 wt.%. The chlorine content of refuse derived fuel may be attributed to small amounts of poly-vinyl-chloride and other chlorine containing contaminants. Sulphur is most dominant in TDF, MBM and waste oils. Other important elements with regard to cement chemistry not shown in Table 3-2, are phosphorous and zinc. Bone meal contains about 3-4 wt.% phosphorous [6,12] while TDF contains about 1-2 wt.% zinc [6,13,14,15] (see also section 3.3). Finally, the iron content varies between 12 and 25 wt.% for car tyres and truck tyres, respectively [13].

However, if the water content of the fuel is known, the ultimate and proximate values of Table 3-2 may be recalculated according to the actual water content using equation (3-3).

$$wt.\%_{as\ received} = \frac{100\% - wt.\% H_2O_{as\ received}}{100\%} \cdot wt.\%_{dry} \quad (3-3)$$

Processed commercial and industrial waste may also partly be automobile shredder residues, plastic wastes of automobile manufacturing with fuel analyses given by Kobayashi et al. [22] or carpet wastes with fuel analyses given by Reallf [16]. Fuel analyses for a number of sewage water sludges are provided by Niessen [17]. Significant deviations in these fuel analyses are observed, for example the reported volatile and carbon contents varied between 41.5-83 wt.% and 26.3-50wt.%, respectively.

	Proximate analysis			Ultimate analysis						Heating value		Reference
	VM ^a	FC ^b	Ash	C	H	N	S	Cl	O ^c	LHV/HHV		
Wood	70-85	10-15	0,3-6	48-52	5,2-6,1	0,11-0,7	<0,1	<0,01	~42	/15,6	6, 18,19	
Cardboard	84,7	6,9	8,4	48,6	6,2	0,11	0,13	N.A.	44,96	/16,9	20	
Recycled paper	73,6	6,2	20,2	N.A.	N.A.	N.A.	N.A.	N.A.	N.A	/13,6		
Newspaper	88,5	10,5	1,0	52,1	5,9	0,11	~0	N.A.	41,86	/19,3		
Poly-Ethylene	100	~0	~0	85,7-86,1	13-14,2	~0	~0	N.A.	0,9	40-46/46,5		
Poly-Propylene	100	~0	~0	86,1	13,7	N.A.	N.A.	N.A.	0,2	40-46/46,4	20,21	
Poly-Styrene	99,8	0,2	~0	92,7	7,9	N.A.	N.A.	N.A.	~0	39,7-46/42,1		
Poly-Vinyl-chloride	94,8	4,8	0,4	41,4	5,3	~0	~0	47,7	5,83	18,8/22,8		
RDF ^d	71-81	4,4-14	14,1-15,3	44,3-46,9	5,6-6,8	0,85	0,17-0,25	0,7-1,3	33-40,8	14-18,5/	22,23,24	
TDF ^e	54	23	22,7	64,1	5,6	0,45	1,4	0,15	5,6	/26,9	f	
MBM ^f	65-74	7,2-10,6	18,4-28,3	42,1-47,8	5,8-6,7	7,5-10,5	~0,7	0,2-0,5	15,3-20,5	16,2-19,5/	6,12, 25,26	
Waste Oils	100	~0	~0	86,0	12,0	~0	2,0	<0,1	~0	/40-42	23,27	

Table 3-2: Fuel analyses and heating values of common alternative fuels used in cement production in dry wt.% and MJ/kg as received. Notes are : a) Volatile matter, b) Fixed carbon (char), c) Calculated by difference, d) RDF = Refuse derived fuel, e) TDF=Tyre Derived Fuel (car tyre), f) measured using BS1016-1018 and ISO1928 and f) MBM = Meat and bone meal.

3.2 Use of Alternative Fuels in Cement Production

This section starts out with an identification of limitations associated with the use of alternative fuels, as limitations are the determining factors for redesign/development of existing/new equipment as well as an overall understanding of the use of alternative fuels in cement production. This is followed by a description of equipment for the use of alternative fuels. The aim of this section is to provide insight into the important issues when using alternative fuels in cement production.

When considering use of a new alternative fuel in cement clinker production, the most important parameters determining applicability with regard to combustion are:

- 1) *Will the reactivity and/or heating value of the alternative fuel cause problems with the desired flame formation in the rotary kiln?*
- 2) *Will the use of alternative fuels affect emissions?*
- 3) *Will the water content reduce cement clinker production capacity?*
- 4) *To what extent will the minor components affect the cement chemistry and kiln operational stability?*
- 5) *Can sufficient burnout of the fuels be achieved in order to prevent*
 - a. *Kiln operational instabilities?*
 - b. *Decreased cement clinker quality?*

Re 1) see sections 2.4 and 3.2.1.1. **Re 2)** see section 3.4.

Re 3) A higher water content may increase the flue gas amount and consequently decrease the production capacity of the cement kiln. Krennbauer [28] performed process calculations for six different fuel mixtures used in a conventional 4-stage preheater, in order to investigate the effect of fuel moisture on production capacity. The author reports a decay in production capacity of up to 23% at constant gas flow, when using fuel mixtures with a moisture content of 4.5 and 28.3 wt.% (as fired) in the rotary kiln burner and calciner, respectively.

Re 4) Nearly all elements from the fuel ashes or in-organics are incorporated into the cement clinker. The chemical input via the alternative fuels must therefore be controlled in order to achieve the desired cement quality. For many alternative fuels this does not pose any problem. However, when using e.g. meat and bone meal or TDF, the increased input of phosphorous or zinc, respectively, may disturb the clinker chemistry. If PVC or other chlorine contaminated fuel is used, the chlorine may cause process disturbances with build ups in the calciner and/or cyclones. Further information is given in section 3.3.

Re 5) Burnout in the kiln system is important in order to avoid (see also Figure 3-5):

- a) *unburnt carbon in the lowermost cyclone in the case of incomplete combustion in the calciner system and*

b) unburnt carbon dropping into the material charge from the burner of the rotary kiln

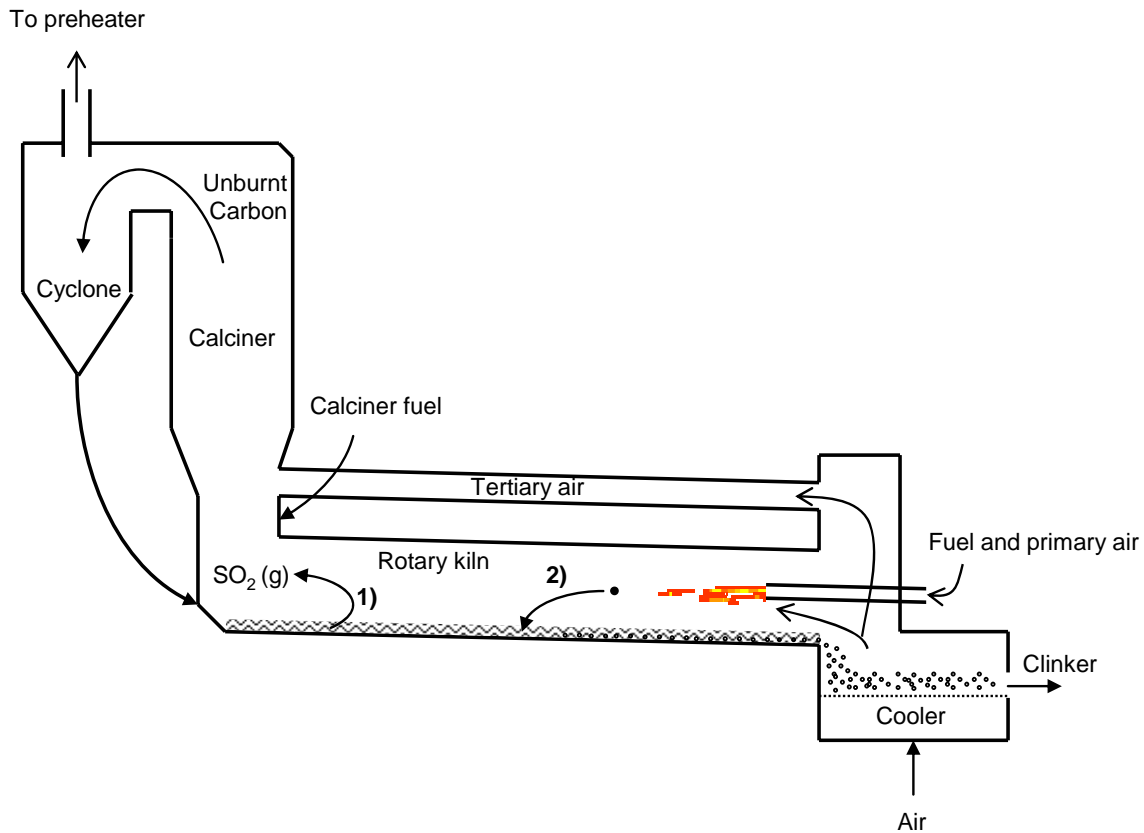


Figure 3-5: Illustration showing the points in the ILC kiln system where unburnt carbon mainly interferes with the process. For the sake of clarity specific additions of alternative fuels are not shown.

The reason for a) is that unburnt carbon in the material to the rotary kiln feed may create reducing conditions in the material inlet of the rotary kiln resulting in increased release of sulphur dioxide and thereby accelerating problems with material build ups that prevent the flows of solids and gas (see also section 3.3).

The reason for b) is that fuel particles that not are sufficiently converted in the rotary kiln, may drop into the clinker bed and induce reducing conditions resulting in decreasing cement quality and release of sulphuric oxide gases from the material charge [29]. Under reducing conditions, the Fe_2O_3 in the clinker bed may be reduced to FeO . The Fe^{2+} -ions of FeO may then both replace Ca^{2+} -ions in alite or promote decomposition of alite during cooling. Under reducing conditions the FeO may go into solid solution with belite and accelerate formation of secondary belite [30]. In addition, due to higher terminal settling velocity compared to small particles, large particles utilized in the rotary kiln burner may drop into the clinker bed near the material exit, resulting in ashes increasing the amount of free lime in the clinker bed with decreasing cement quality as a result [31,32].

Liquid and gaseous fuels may be injected through nozzles directly into the rotary kiln or calciner system, as these fuels are considered to be easily combusted because they have no char content. For solid fuels, however, the utilization is further complicated by the fact that the particle size and its physical shape differ among the various fuel types, and it may not be feasible to reduce the particle size, in order to produce a homogenous fuel with regard to particle size. In particular, TDF with steel reinforcement causes difficulties with regard to size reduction. The energy costs when producing smaller TDF particle sizes are high (see Table 3-3). For instance, when producing shreds of 5cm·5cm, the energy cost is about 28 euro/tonne, which is higher than the negative cost received for the fuel. Even though a relatively large amount of energy is used, the particle size is still large compared to coal particle sizes typically used in the rotary kiln burner or calciner (the exact particle size (distribution) depends on combustion temperature and coal char reactivity – typically, not more than 4-8 wt.% of the particles may exceed 90µm for a coal with 10 wt.% volatiles [33]). In addition, cryogenic grinding of tires is reported to be 3 to 5 times more expensive than the cost of coal grinding [34].

<i>Particle size</i> [cm·cm]	<i>Energy expenditure</i>		<i>Energy cost^b</i> [Euro/ton]	<i>Revenue^c</i> [Euro]
	[MJ/tire]	[MJ/kg tire] ^a		
Coarse shred	0.5	~0	~0	20
5·5	2.6	0.4	~28	-8
2.5·2.5	15.8	2.4	~167	-147
0.6·1.3	37-53	5.7-8.15	396 to 567	-376 to -547

Table 3-3: Energy expenditure of shredding and milling in order to reduce the particle size of tyre rubber [35]. a) calculated values based on a tyre weight of 6.5 kg corresponding to a passenger car tyre, b) assumed energy cost of 0.25 euro/kWh, c) calculated from an assumed TDF fuel price of -20 euro/tonne (negative cost) disregarding maintenance of machinery, etc.

As outlined above, solid fuels are typically the most difficult due to their higher physical inhomogeneity and content of char compared to liquid and gaseous fuels. These fuels therefore require greater consideration in terms of where and how in the kiln system they should be applied, compared to liquid or gaseous fuels.

In general, small particles, gaseous fuels or droplets with combustion conversion times in the order of seconds should be utilized in the rotary kiln burner or in the calciner system. Large alternative fuel particles may need special equipment in order to ensure sufficient burnout of them. The remaining part of section 3.2 reviews the use of small and large solid fuel particles in cement production and gives a brief description of the use of gaseous and liquid fuels in the rotary kiln burner.

3.2.1 Small Particles, Gaseous Fuels or Liquid Droplets

3.2.1.1 Rotary Kiln Burner

A multiple channel burner for several types of alternative fuels is typically used to comply with differences in the solid state or other physical parameters of the various fuels [36,37] (see also section 2.4). An example of such a burner is shown in Figure 3-6.

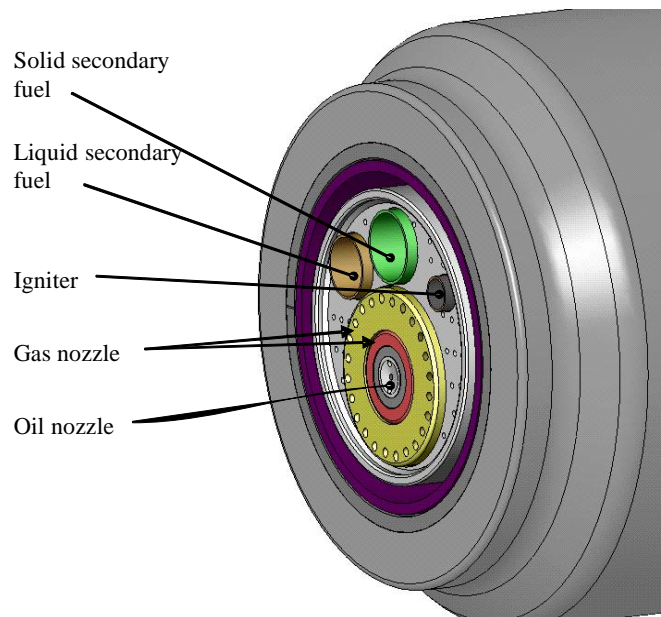


Figure 3-6: Burner tip of the DUOFLEX burner from FLSmidth and the position of fuel supply channels for different fuels (from [36]).

Among the commonly reported concerns regarding use of alternative fuels in the rotary kiln burner are the possible lowering of flame temperature and lengthening of flame compared to coal dust firing [4,6,29], because lower heating values and higher water contents typically are associated with alternative fuels. In addition, large solid fuel particles may be less reactive than traditional fuels and consequently lengthen the flame and/or lower its temperature. The lower flame temperature may result in reduced clinker quality, if the solids in the rotary kiln do not achieve a sufficiently high temperature for the clinker reactions to proceed. A longer flame length is usually more divergent resulting in reducing conditions in the clinker bed and reduced refractory life.

3.2.1.2 Calciner System

The use of alternative fuels in the different calciner systems is very flexible, as long as the overall process fulfills the aims outlined in section 2.4.3. In the three calciner systems described there is high flexibility with regard to temperature, O₂ concentration as well as mass and heat transfer characteristics between gas and solid. In addition in the ILC or SLC, the abrasion of raw material particles on solid fuel particles may increase the fuel burnout rate (see also chapters 4 and 5).

In an ILC system, the gas residence time is typically 3-4 seconds, while the residence time of raw material and fine solid fuel particles is about four times higher (see also section 2.4). However, Giugliano et al. [38] have shown that particle gas interaction also has to be taken into account in order to estimate the residence time of larger alternative fuel particles in the centimeter size. They made model simulations of the behaviour of a shredded tyre rubber particle inside the calciner including gravity, drag force and upward gas velocity and concluded that the residence time of a shredded tyre rubber piece averaged 40 seconds. They also concluded that this time was sufficient to ensure complete devolatilization of shredded tyre particles inside the calciner. However, the authors did not consider clustering of small particles in the calciner or conversion pathway of the TDF particles in their simulations (see also chapters 4 and 5).

3.2.2 Extensional Equipment for Large Fuel Particles

This section describes extensional equipment for utilization of large fuel particles. The equipment described may function as a preparation unit that preprocesses fuel before being admitted to the calciner or may function as a combustion chamber or a combination.

3.2.2.1 HOTDISC

The HOTDISC unit from FLSmidth is a rotating hearth furnace designed to convert large fuel particles within calciner systems for cement production. It is described by Keefe and Shenk [39], Haugom et al. [40], Christensen [41] and Kvitvik [42]. Figure 3-7 shows the HOTDISC as well as its position in an ILC. The HOTDISC has a rotating disc inside a chamber on which solid fuel particles are exposed to preheated air from the clinker cooler (tertiary air). The residence time of the solid fuel particles on the disc is typically 20-40 minutes controlled by the disc rotational speed. However, the gas residence time is only about 1 second. The temperature inside the HOTDISC is controlled using non-calcined raw material, which is typically added from the second lowermost cyclone stage. This cooling effect is needed to avoid overheating of refractory above the maximum service temperature, because the tertiary air already has a temperature of 850-1100°C when entering the HOTDISC.

The HOTDISC chamber is flanged to the calciner delivering ashes, possible unburnt alternative fuel and meal to the gas rising from the rotary kiln as shown in the right part of Figure 3-7. Depending on particle shape, density and size, the individual particle may be carried up into the calciner or fall down into the rotary kiln. The solids are discharged from the disc to the remaining kiln system by a scraper.

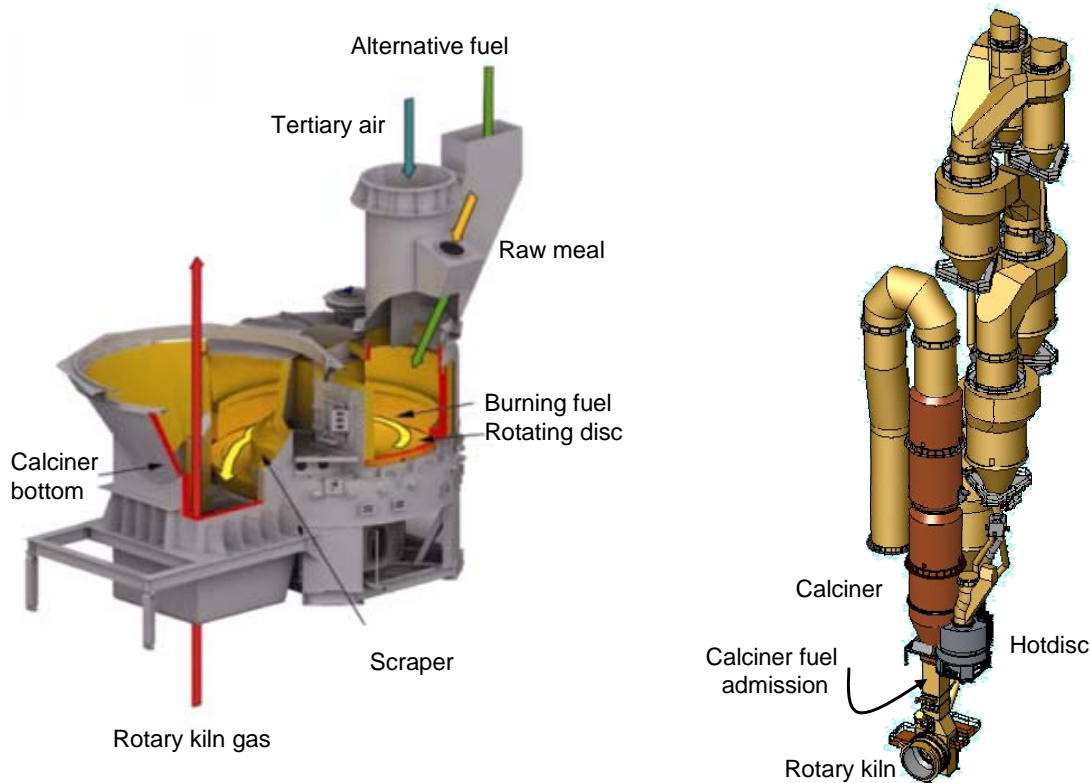


Figure 3-7: HOTDISC unit for large alternative fuel particles (left) and its typical position flanged onto the ILC (right).

Four HOTDISC units are now in operation at typical calciner fuel substitution rates up to approximately 50 Energy-%. Shredded and whole tyres, plastic materials, wood and refuse derived fuel have mainly been applied as alternative fuels.

3.2.2.2 Circulating Fluidized Bed Gasifier (CFBG)

At Rüdersdorf Cement Works in Germany, a circulating fluidized bed gasifier (CFBG) has been utilized for alternative fuels since 1995. It is described by Drebelhof [43], Wirthwein [44] and in [45]. The CFBG fulfills two purposes: 1) to produce gaseous fuel for the calcination process and 2) to produce raw material for cement production.

The area in which Rüdersdorf is situated does not have sufficient amounts of raw materials containing silicates. However, plenty of residual brown coal ash is available from the German power plants and that may therefore be used as a substitute raw material to provide silicates. The power plant ashes, however, contain a few percent of carbon that may oxidize in the upper preheater stages releasing CO and/or unburnt hydrocarbons (see also section 3.4). Pretreatment of the ash in the CFBG may reduce the carbon content and consequently eliminate these emissions. In addition, the CFBG is reported able to gasify solid fuel with particle sizes of up to 50mm.

Figure 3-8 gives an outline of the kiln system and the CFBG at Rüdersdorf cement works. A maximum of 10t/h of alternative fuels and 5-15 t/h power plant ashes are fed to the circulating bed gasifier. If no ashes are fed to the CFBG, up to 25 t/h of alternative fuel may be added. The products of the CFBG are synthesis gas and ashes which are directed to the calciner and raw mill, where they are used as fuel and raw material, respectively. About 50,000 Nm³/h of synthesis gas with heating values between 3000-5000 KJ/Nm³ and 20 t/h of ashes with a carbon content below 1.5 wt.% are produced. The heating value of the synthesis gas produced is mainly dependent on the alternative fuel type. For three alternative fuels of paper and plastic the composition was reported to consist of 4-13 vol.% CO, 1.6-3.7 vol.% CH₄, 3.7-10 vol.% H₂ and 11.5-29.1 vol.% H₂O. The water stems mainly from the moisture of the alternative fuel.

During normal operation, the alternative fuels substitute about 75% of the calciner fuel and consequently about 45% of the total fuel for the kiln system.

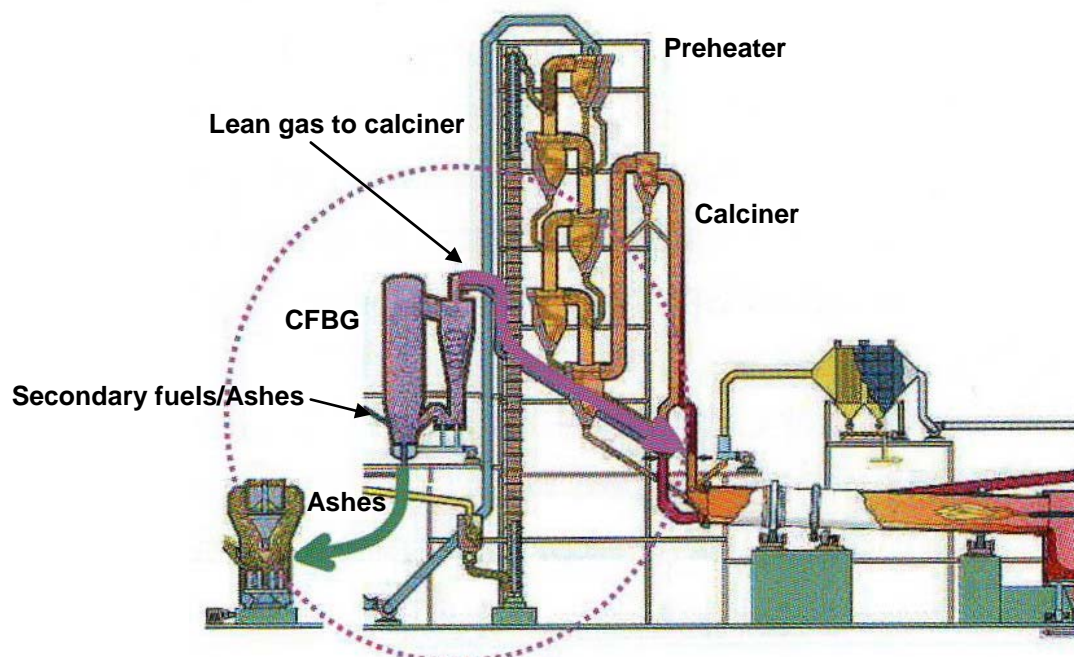


Figure 3-8: Kiln system and circulating fluidised bed gasifier at Rüdersdorf Cement Works (from [43]).

3.2.2.3 Pre-Combustion Chamber

The Pre-Combustion Chamber (PCC) is designed to convert large fuel particles of wood and TDF into a gaseous and solid fuel used in the calciner system. The PCC is described by Schmidthals, Rose and Werner [14, 46, 47 and 48] and is shown in Figure 3-9. In the PCC, thermal conversion of large fuel particles takes place under sub-stoichiometric conditions producing a lean gas that is used as a gaseous fuel in the calciner system. The remaining solids are metered and used as a solid fuel in the calciner system. In the case of the utilization

of whole tires, the steel residue formed is separated from the fine char residues and transported to the lower part of the calciner system.

The preheated air to initiate and maintain the pyrolysis of the large fuel particles in the PCC has an inlet temperature of about 500°C, and is produced by cooling part of the preheated tertiary air with atmospheric air. Only part of the tertiary air is used because the pyrolysis process operates under sub-stoichiometric conditions, with an overall excess air ratio of about 0.2, i.e. five times as much fuel as under stoichiometric conditions. The gas produced is reported to have a heating value of about 5.0 MJ/Nm³ and a temperature of about 850°C. The solid residues have a temperature of about 500°C.

To the author's knowledge, two PCCs have currently been installed with nominal capacities of about 3-5 tonnes/h

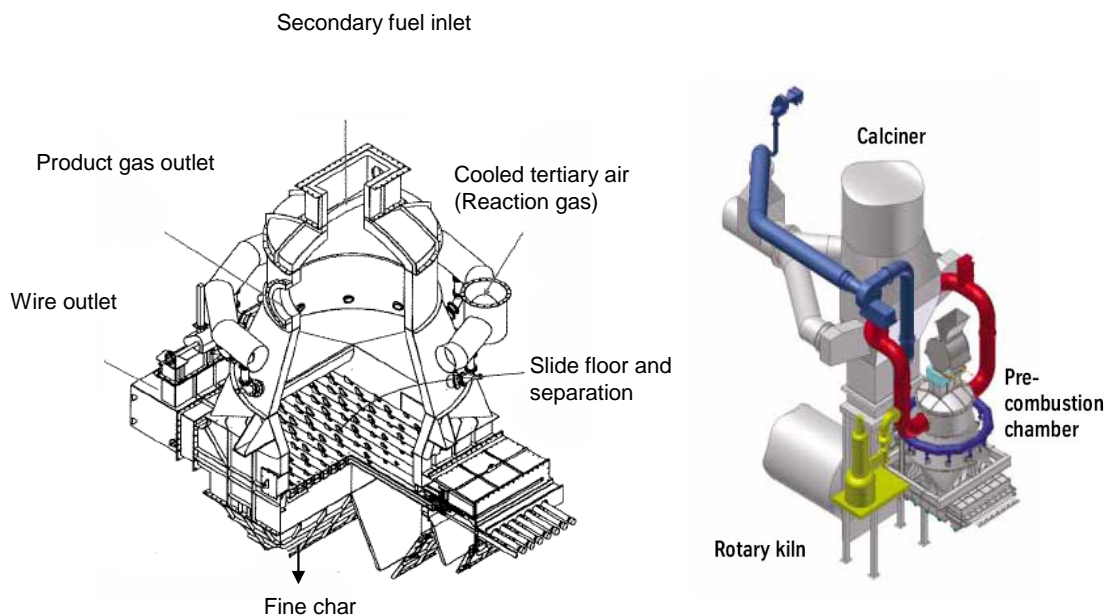


Figure 3-9: Pre-Combustion Chamber for large solid fuel particles in cement production. To the left is shown a detailed view and to the right its position on the calciner system (From [49]).

3.2.2.4 Pyrorotor

The Pyrorotor is presented by Streit [50]. It consists of a rotary kiln that is flanged in between the ILC system and the tertiary air duct as depicted in Figure 3-10. Alternative fuel particles with sizes up to 1 meter may be introduced in the upper end of the Pyrorotor and converted during their downward movement caused by the rotation. Meal may be admitted together with the fuel in order to control the temperature. The author is not aware of any Pyrorotor currently having been installed.

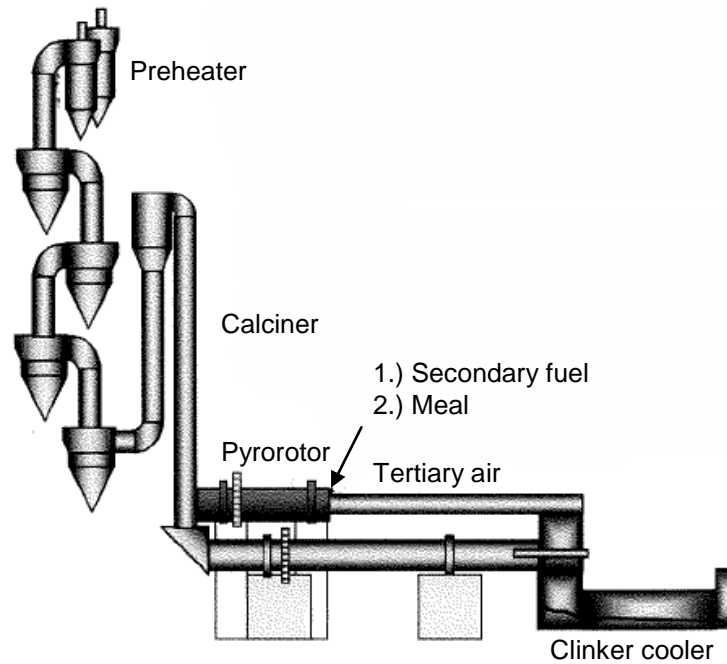


Figure 3-10: Pyrorotor for large fuel particles in cement production (from [50]).

3.2.2.5 Refuse Energy Gasifier

The Refuse Energy Gasifier (REG) was developed by Taiheiyo Engineering Corporation and described by Saito et al. [51]. The REG is a fluidized bed gasifier for whole tyres operated parallel to the conventional kiln system for gasification. The produced lean gas is used as a gaseous fuel in the calciner system or rotary kiln burner. The steel wires from the tyre reinforcement are discharged at the bottom. The energy recovery from the fluidized bed gasifier is reported to be approximately 95%, which means that only 5% of the original heating value of the tyre is lost. This high efficiency is also in agreement with the rather high heating value of the produced gas, which is reported to be about 19 MJ/Nm^3 compared to the heating value of the gas produced in the circulating fluidized bed at Rüdersdorf and in the pre-combustion chamber.

To the author's knowledge, two REGs were reported to operate well with tyre capacities of 300-400 kg/h and 500-800 kg/h producing lean gas to obtain overall fuel substitution rates of 5-7% in the rotary kiln burner and 11-18% in the calciner system, respectively.

3.3 Effects of other Components on Processing and Chemistry

One of the major issues when utilizing alternative fuels in cement production has been to understand the effect of other components introduced with the alternative fuels on the stability of the kiln system and the effect on clinker quality. Unfortunately, it is not always possible to isolate the effect of one component, and the effects should rather be seen as a whole. Therefore, an overview, mainly based on the texts of Hewlett [31], Bye [52] and Taylor [53], is provided here in order to illustrate important phenomena regarding minor components. In section 3.3.1 the effects of the common components of S, K, Na and Cl on cement quality and process stability are described. In section 3.3.2, the effects of minor components on cement chemistry and quality are briefly commented.

A modern kiln system for cement production shows a special recirculation behaviour, where components may evaporate from the solid phase in the hot burning zone of the rotary kiln, or somewhere else in the kiln system, dependent on its volatility, and condense on the solid material in the colder parts of the kiln system, e.g. preheater stages. The component is subsequently brought along with the solid stream until it eventually re-evaporates, and the cycle is established. At steady state operation, equilibrium between the solid phase and its gaseous counterparts is established and elements are removed with the flue gas, clinker or bypass (see section 3.3.1.2), in the same amount as introduced with the fuel and raw materials. Due to this circulation of some components, the concentration of them may be up to 50 times the input concentration in the kiln system [54]. Very volatile compounds may not condense in the preheater stages and may be transported to the raw material mill and flue gas cleaning system.

3.3.1 Alkali, Sulphur and Chlorine

Sodium (Na) and potassium (K) are the alkali metals normally found in cement production and they are typically introduced with the raw materials or fuels. Alkalis play an important role with respect to binding sulphur in the clinker. The alkali equivalent is used to describe the amount of alkali present in the clinker product (denoted $\text{Na}_2\text{O}_{\text{equivalent}}$ in cement literature, even though the alkalis are usually not bound as oxides in the clinker):

$$\text{Na}_2\text{O}_{\text{equivalent}} = 0.658 \cdot \text{wt.}\% \text{K}_2\text{O} + \text{wt.}\% \text{Na}_2\text{O} \quad (3-4)$$

Sulphur is mainly introduced with the fuels but may also be introduced via raw materials. Sulphides, organic sulphur and pyrite in the raw materials are oxidized to SO_2 (g) in the upper preheater stages and the sulphur therefore only reaches the calciner system or kiln if absorbed in the limestone. Sulphates however are more prone to be carried to the calciner system and kiln due to their relatively lower volatility. Chlorine may be introduced to the kiln system as impurities in the raw material or via the fuel. The input of chlorine via the fuel is frequently

the most important contributor, and in particular with alternative fuels containing PVC or other chlorine contaminated fuels.

Sulphur and alkali may react forming alkali sulphates in the form of K_2SO_4 , Na_2SO_4 , $Na_2SO_4 \cdot 3K_2SO_4$ (aphtitalite) and $2CaSO_4 \cdot K_2SO_4$ (langbeinite). Sulphates are generally less volatile than their respective oxides and are therefore retained in the solid state. Under reducing conditions, the alkali sulphates, however, may decompose to their respective oxide or other components and gasses (SO_2 and SO_3).

3.3.1.1 Cement Quality

High levels of alkali in the final cement product may influence its properties in different ways and detailed descriptions of these phenomena as well as references may be found in reference [31]. For instance, in the presence of moisture, high levels of alkali may produce a gel that may expand and produce cracks in the final construction application, and consequently, lower the strength.

The alkali level in the clinker may be maintained using careful selection of raw materials and fuels. The right proportion between sulphur and alkali in the kiln system ensures that alkalis are bound as sulphate and consequently removed from the system with the clinker, due to the low volatility of the alkali sulphates. In kiln-systems equipped with a by-pass (see section 3.3.1.2) a deliberate addition of chloride may be used to remove alkali from the clinker, because alkali chlorides are more volatile than their respective sulphates. Chlorine addition may be accomplished via calcium chloride addition, chlorinated solvents or other alternative fuels containing chlorine.

3.3.1.2 Influence on Kiln System Stability

The proportions of alkali, sulphur and chlorine influence the process stability of the kiln system. Inappropriate chemistry of these components may form blockages in the preheater cyclones and the calciner system or so-called rings in the rotary kiln. Blockages may restrict or prevent the flow of solid and/or gasses and consequently severely disrupt the overall process.

If deficient sulphur is present, alkalis may not be removed in sufficiently quantities with the clinker as sulphates. Instead they may evaporate in the burning zone and form alkali carbonates that condenses in the preheater stages and potentially causes cyclone blockages.

Excess sulphur evaporates in the burning zone and form eutectic mixtures with alkali salts with melting points as low as $800^\circ C$. This partly melted material is sticky causing dust or particles in the system to collide and adhere to each other giving rise to blockages in the connection between the rotary kiln and calciner or in the calciner. As described earlier, the

volatilisation of sulphur may be accelerated if reducing conditions exist in the clinker bed. This may for instance be induced via the entry of unburnt carbon into the clinker bed from either the lowermost cyclone caused by insufficient burnout in the calciner and/or unburnt fuel from the rotary kiln burner. Chlorine in the system may moreover interfere with the sulphur-alkali system and reduce the eutectic melting points by as much as 100°C and therefore accelerate problems with blockages even more.

Excess sulphur may furthermore form sulphate-spurrite ((CaO·SiO₂)₂·CaSO₄) with a melting point of about 1200°C that potentially may induce ring formations in the rotary kiln. Ring formation primarily inhibits material flows and secondly gas flow in the rotary kiln may be prevented. The sticky solid material may, under the action of the rotary kiln, further form a sphere of solid material with diameters of up to 2 meters, which potentially may block the entire rotary kiln or create other severe mechanical damages

It should be clear that the effect of sulphur and alkali is intimately linked and it is possible to remove both components as alkali salts with the clinker under the right circumstances. It should furthermore be clear that the sulfur volatilization, and consequently process stability, is linked to the burnout in the rotary kiln as well as in the calciner.

A by-pass system may be used to control the level of chlorine, sulphur and/or alkali in the kiln system. The most frequent reason for using a bypass is to control the chlorine in the kiln system and the clinker.

It should be remembered that the concentration of gaseous chlorine is several times higher than in the in- and output levels, due to the high recirculation in the kiln system. A considerable amount of chlorine may therefore be removed, extracting only part of the gas. In order to achieve the highest chlorine extraction, the gas temperature should be as high as possible and the gas extraction is therefore typically performed at the gas outlet of the rotary kiln (see Figure 3-11). The gas temperature is higher in the flame of the rotary kiln than in the gas outlet, but, due to lack of accessibility, it is not possible to extract gas from this point. Once the kiln flue gas is extracted, the chloride is removed using quench cooling of the extracted gas, forcing the chlorides to condense.

The removal efficiency of chlorine is relatively good for even small bypass ratios. For the particular by-pass system described by Sutou et. al. [55], a chlorine removal efficiency of about 90% of the input is achieved with a by-pass ratio of only 5% (percentage of rotary kiln gas extracted). They also report that chlorine is mainly found in the fine crystals with about 80% of the extracted chlorine in the crystals with a particle size below about 5 µm.

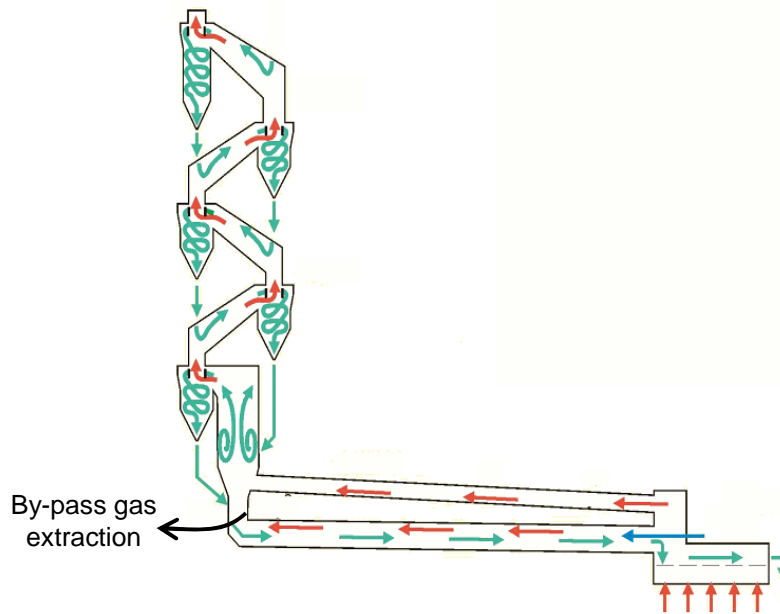


Figure 3-11: Position of by-pass gas extraction in kiln system with an ILC type calciner. By-pass extraction position is similar in SLC systems.

3.3.2 Effects of Minor Components on Cement Chemistry and Quality

This section briefly reviews the effects of minor components introduced with the alternative fuels on cement chemistry. More detailed information may be obtained from the original references.

Based on the analyses in section 3.1 identifying the presently most important alternative fuels in the German cement industry, zinc and phosphorus are the most important, because they are introduced with the steel reinforcement in the TDF and with meat and bone meal. Furthermore, a series of other components may be introduced to the kiln system, particularly with the application of mixed alternative fuels, such as refuse derived fuel.

Zinc in amounts of 0.01-0.2 wt.% in the clinker may increase the reactivity of alite causing possible setting problems [31]. Norcini et al. [56] reported that the ZnO level in the clinker increased from 0.005 wt.% with no tyre utilization to 0.02 wt.% for 15-20% total fuel substitution with tyres. Giugliano et al. [38] further reported that the compression strength development, as well as free lime, did not change when using up to 36% total fuel substitution rate of tyres over a lengthy period, instead of petcoke firing.

Phosphorus is normally found in the clinker in concentrations of 0.03-0.22 wt.% P_2O_5 . Higher levels favor belite in the clinker at the expense of alite. Minor amounts of fluorine, however, may prevent this and promote production of alite. With more than 1wt. % P_2O_5 in the clinker, the alite content is reported to decrease with 10 wt. % for each additional wt. % of P_2O_5 [31,57,58,59].

The normal level of *fluorine* in clinker ranges from 0.01-0.15 wt.% F. Above this level, strength reductions of the final product are to be expected. Despite decreasing the cement strength, fluorine is reported to reduce the viscosity of the melt in the rotary kiln and consequently increase alite formation (see also section 2.2.4) or act as a mineraliser promoting alite-formation. In addition, fluorine in cement clinker tends to give a yellow color [31,60].

Magnesium in up to 5 wt. % MgO may also decrease the viscosity of the melt in the rotary kiln material charge and consequently increase alite formation reactivity. Excessive amounts above 5wt.% MgO, however, may induce crystallization of periclase that may have adverse effect on the soundness^a. Periclase formation is enhanced during slow cooling [31].

Lead in the clinker is typically in the range of 0.001-0.02 wt.% (as PbO), but may increase to 0.02-0.04 wt.% PbO when using alternative fuels. As long as the concentration is below 0.1 wt% no setting and/or hardening problems are to be expected [31].

3.4 Emissions

This section reviews issues regarding gaseous emissions when using alternative fuels in cement production. Generally, noise from cement plants and pollutant of water are also recognized as emissions [61], but they are not treated here, as gaseous emissions are considered to be the most important.

3.4.1 Legislation

Cement plants located in the European Union which use alternative fuels are subject to the regulations of directive 2000/76/EC [62]. The emission limits stipulated in this directive are shown in Table 3-4. No CO emission levels are specified, because they are set by the local authorities.

3.4.2 Effect of Alternative Fuels on Emissions

In modern kiln systems, the SO₂ emission originates mainly from oxidation of pyrites, FeS or organic sulphur in the upper preheater stages, whereas SO₂ originating from the fuel is re-adsorbed on the limestone in the preheater stages [63]. However, if a by-pass is installed, SO₂ emissions originating from the fuel may be expected from here. Since SO₂ emissions mainly are affected by the raw materials they are not treated further here. In addition, dust emission is not treated, because this may be considered independent of fuel type, except for its composition that may be enriched in trace elements.

^a Cement is said to be unsound if it expands excessively during hydration producing cracks in the final product.

<i>Pollutant</i>	<i>Concentration limit</i>	<i>Unit</i>
Total dust	30	mg/Nm ³ @ 10 vol.% O ₂ dry gas
HCl	10	do
HF	1	do
NO _x	800 ^a / 500 ^b	do
Cd + Tl	0.05	do
Hg	0.05	do
Sb+As+Pb+Co+Cr+Cu+Mn+Ni+V	0.5	do
Dioxins and furans	0.1	TEQ ^c /Nm ³ @ 10 vol.% O ₂ dry gas
SO ₂	50 ^d	mg/Nm ³ @ 10 vol.% O ₂ dry gas
TOC	10 ^d	do

Table 3-4: Emission limits for cement plants using alternative fuels in the European Union. a) Existing plants, b) new plants c) TEQ=Toxic Equivalents (see Table 3-5), d) Exemptions may be authorised by the competent authority in cases where SO₂ and TOC do not result from the incineration of waste.

3.4.2.1 HCl and HF

The increasing use of alternative fuel may introduce mainly chlorine into the kiln system with the fuels. Cement kilns, however, operate under alkaline conditions, where chlorine and fluorine are bound as salts rather than acidic gasses of HCl and HF and this typically ensures negligible emission of these compounds from cement kilns compared to municipal solid waste incinerators [64]. HCl and HF emission through the bypass gas poses a special risk.

3.4.2.2 NO_x

Emission of NO_x from cement production originates mainly from fuel and thermal NO_x. A detailed description of the different formation and reduction mechanisms in cement production is given by Jensen [11]. A number of investigations have been made in order to address the effect of co-firing alternative fuels on NO_x emission. Increasing amounts of alternative fuels in the calciner is usually associated with reduction of NO_x emissions.

In the rotary kiln, the application of alternative fuels usually reduces NO_x formation compared to plain coal firing. It is reported to be a consequence of the lower flame temperature associated with alternative fuels (see also section 3.2) and consequently minimized lower thermal NO_x formation [7]. In addition, alternative fuels typically have a higher volatile content and are therefore more prone to local NO_x reduction via reburning reactions (see also section 2.4). Sewage sludge, however, is reported to increase NO_x formation in the flame [57] compared to plain coal firing.

In two out of three cases [10,65,66], meat and bone meal fired into the calciner is reported to decrease NO_x emission by up to about 60% compared to operation without alternative fuels despite the fact that meat and bone meal has a high N-content (see also Table 3-2). The NO_x reduction is attributed to the relatively higher volatile content of meat and bone meal and hence higher NO_x reduction potential [10]. Tyre chips admitted to the calciner below the admission of tertiary air are reported to decrease the NO_x emission by up to 40% [38,67].

Whole tyres at a calciner fuel substitution rate of 40 energy-% fired into the HOTDISC are reported to decrease the NO_x emission by about 15% compared to plain petcoke firing in the calciner [68]. Polypropylene and polyethylene-tere-phtalatate at fuel substitution rates of up to 15% were reported to decrease the NO_x emission by 21% and 37%, respectively [69]. Finally, refuse derived fuel is reported to decrease the NO_x emission when fired into the calciner [66].

3.4.2.3 Trace Elements

The components As, Cr, Cu, Mn, Ni and V are primarily incorporated into the clinker and only below 0.1 % of the input results in gaseous emissions [6]. Incorporation of these elements in the cement results in no leaching from the final product, due to their being incorporated into the crystal phase during cement hydration [4,70].

The semi volatile components of Sb, Cd and Pb are mainly volatilized in the burning zone and effectively re-adsorbed on the particles in the preheater and returned to the process. Consequently, no stack emissions of these components are observed [6], however, they may be extracted in the by-pass and collected with the solid particles.

Mercury and partly thallium are the most relevant to consider with regard to emissions from cement production due to their high volatility [6,71,72]. Thallium is removed from the kiln system via dust escaping with the gas in the upper preheater stage or the by-pass dust. Thallium in the preheater dust is captured in the raw mill or in the main kiln system filter, and is returned to the preheater or clinker grinding. Mercury is highly volatile and evaporates in the upper preheater stages and is therefore only removed with the preheater dust. If the temperature in the raw mill and particle filter of the flue gas cleaning system is sufficiently low, mercury may re-condense on the solid particles and be transferred back to the preheater and re-evaporate in the upper preheater stages. This results in cycles between the raw mill / particle filter and the upper preheater stages. The gas temperature in the particulate filter of the flue gas cleaning system should be below 130°C in order to ensure negligible mercury emissions [64]. Emissions of mercury may be prevented by using activated carbon [6] and/or by extracting dust from the main kiln system filter and admitting it to the cement mill, when the raw mill is turned off [70], or other methods. The latter is a consequence of the higher concentration of mercury obtained in the dust from the main filter when no adsorption takes place in the raw mill. The main mercury input to the kiln system is frequently with the raw materials [73]. However, care should be exerted with fuels containing relatively high amounts of Hg, e.g. municipal solid waste of refuse derived fuel with a Hg content of <15 and 1-10 ppm respectively [74].

3.4.2.4 Dioxins and Furans

Dioxin and furans denote polychlorinated dibenzo-para-dioxins or polychlorinated dibenzofurans respectively (See Figure 3-12), where 75 and 135 isomers of the two compounds may be formed, respectively. The toxicity is restricted to isomers with four or more chlorine atoms positioned at 2, 3, 7 and 8 yielding a total of 17 toxic isomers (see Table 3-5). Measurement of dioxins and furans may be done using a Gas-Chromatograph equipped with a high resolution mass spectrometer. This technique, however, is very difficult and should only be carried out by experts [75].



Figure 3-12: Molecular structures of polychlorinated dibenzo-p-dioxins (left) and dibenzofurans (right). $X=0$ to 4, $Y=0$ to 4 and $X+Y \geq 1$. (From [75])

Two mechanisms have been proposed to account for dioxin and furan formation in combustion systems. The homogeneous gas phase route takes place at temperatures of 500-800°C with reactions between gaseous precursors containing chlorine, hydrogen and carbon. Radicals formed in the combustion process may enhance these formation reactions. The maximum net dioxin/furan production rate is around 600°C. The heterogeneous route takes place at temperatures of 200-400°C either from solid carbon (de Novo reaction), or chloro-phenols and chloro-benzenes. Under catalytic action of metals in the solid this produces dioxins or furans [75]. For both mechanisms, the dioxin/furan net formation may be reduced using rapid cooling through the temperature regions of high net production rates and limit the presence of solid or gaseous precursors and catalysts.

With regard to emissions of dioxins and furans from cement kiln systems using alternative fuels, Lang [7] reports emissions one order of magnitude below the limit set by the authorities of 0.1 TEQ/Nm³, both with and without utilization of sewage water sludge. Pech and Douillet [5] also report an emission level of dioxins/furans below the allowed limit, when utilizing meat and bone meal in the rotary kiln burner. They report that 10-15% of fuel substitution in the rotary kiln with meat and bone meal reduced the emission of dioxins/furans compared to coal firing. Oerter [76] and Bolwerk [64] also report dioxin/furan emissions below the allowed limit when using alternative fuels. Generally, the emission of dioxins and furans is seen to be insignificant in agreement with [75].

	<i>Compound</i>	<i>Toxic Equivalence Factor</i>
2,3,7,8	— Tetrachlorodibenzodioxin (TCDD)	1
1,2,3,7,8	— Pentachlorodibenzodioxin (PeCDD)	0,5
1,2,3,4,7,8	— Hexachlorodibenzodioxin (HxCDD)	0,1
1,2,3,6,7,8	— Hexachlorodibenzodioxin (HxCDD)	0,1
1,2,3,7,8,9	— Hexachlorodibenzodioxin (HxCDD)	0,1
1,2,3,4,6,7,8	— Heptachlorodibenzodioxin (HpCDD)	0,01
	— Octachlorodibenzodioxin (OCDD)	0,001
2,3,7,8	— Tetrachlorodibenzofuran (TCDF)	0,1
2,3,4,7,8	— Pentachlorodibenzofuran (PeCDF)	0,5
1,2,3,7,8	— Pentachlorodibenzofuran (PeCDF)	0,05
1,2,3,4,7,8	— Hexachlorodibenzofuran (HxCDF)	0,1
1,2,3,6,7,8	— Hexachlorodibenzofuran (HxCDF)	0,1
1,2,3,7,8,9	— Hexachlorodibenzofuran (HxCDF)	0,1
2,3,4,6,7,8	— Hexachlorodibenzofuran (HxCDF)	0,1
1,2,3,4,6,7,8	— Heptachlorodibenzofuran (HpCDF)	0,01
1,2,3,4,7,8,9	— Heptachlorodibenzofuran (HpCDF)	0,01
	— Octachlorodibenzofuran (OCDF)	0,001

Table 3-5: The 17 toxic dioxins and furans as well as their toxic equivalence factor.

3.4.2.5 TOC – Total Organic Carbon

Organic compounds emitted with the flue gas stem mainly from carbonaceous matter in the raw material volatilised in the upper preheater stages [4,6,77], or secondarily from incomplete combustion of the fuel in the calciner [78].

Organic carbon emissions from the carbonaceous matter in the raw material are formed because the temperature in the upper preheater stages is sufficiently high to volatilize and/or partially oxidize the carbon, but not sufficiently high for complete carbon oxidation forming CO₂ and H₂O at the available residence time.

Organic carbon emissions from the calciner are mainly due to incomplete combustion of the fuels applied in the calciner, forming mainly CO that is transported with the gas up through the preheater stages. Experiments based on using tyre chips in the calciner with calciner fuel substitution rates of up to 80%, showed no significant changes in CO or total organic carbon emission compared to plain petcoke firing [38]. Whole tyres at a calciner fuel substitution rate of 40 energy-% utilized in the HOTDISC are reported to decrease the CO stack emission by 20% compared to 100% utilization of a medium volatile coal in the calciner [68].

3.5 Conclusions on Chapter 3

The use of alternative fuels in cement production has increased significantly in the last decade. The physical and chemical properties as well as the solid state of the different fuels vary significantly and hence influence their application. TDF, waste oils, plastic and meat and bone meal are the most important alternative energy carriers covering up to 71 % of the total energy supplied by alternative fuels in the German cement industry in 2003-2004.

Alternative fuels may be applied in the rotary kiln burner, calciner system or in extensional equipment that is specially designed for large solid fuel particles. Sufficient burnout in the calciner system or rotary kiln is important in order to preserve cement quality as well as stable kiln system operation. Gaseous and liquid alternative fuels are more easily combusted than solid fuels, due to the liquid and gaseous fuels having no slow burning char content.

Alkali, sulphur and in particular chlorine have major influence on the stability of the kiln system. This is due to the fact that they accelerate the deposit formation in the rotary kiln, in the calciner as well as in the preheater and consequently disrupt kiln system operation. Phosphorus and zinc, from meat and bone meal and TDF respectively, are the minor components of concern with regard to influence on cement clinker quality of alternative fuel use.

The gaseous emissions when using alternative fuels seems not to be affected compared to conventional fossil fuel firing. It has even been reported that the application of alternative fuels has led to decreased emissions. Care should be taken when considering alternative fuels in cement production with regard to CO emissions.

3.6 References

- ¹ Liebl, P., Gerger, W.; Nutzen und Grenzen beim Einfluss von Sekundär; ZKG International, 46, 1993.
- ² Pandey, S.P., Tiwari, A.K.; The use of agricultural by-products as alternative fuels; ZKG-International, Vol. 55, No.2, 68-75, 2002.
- ³ Hoidalén, O.; An Alternative Approach; International Cement Review, 40-44, August 2006
- ⁴ Scheuer, A.; Utilization of Alternative Fuels and Raw Materials in the Cement Industry; Cement International, 1, 48-66, 2003.
- ⁵ Pech, M., Douillet, G; Operation Experience in co-Incineration of Animal Meals in Cement Kilns; VDZ Congress, 352-356, 2002.
- ⁶ Smith, I.; Co-Utilisation of coal and other fuels in cement kilns; IEA Clean Coal Centre, August 2003. ISBN 92-9029-386-1.
- ⁷ Lang, Th.A.; Use of Alternative Fuels and Raw Materials at Holcim Cement Plants in Europe; Cement International, 4, 62-70, 2003.
- ⁸ Umweltdaten der deutschen, Verein Deutscher Zementwerke, Düsseldorf, Available from www.vdz-online.de, 2002.
- ⁹ Umweltdaten der deutschen, Verein Deutscher Zementwerke, Düsseldorf, Available from www.vdz-online.de, 2004.
- ¹⁰ Schneider, M. (Chief Executive Manager); VDZ (German Cement Works Association); Activity Report 2003-2005; May, 2005.
- ¹¹ Jensen, L.S.; NO_x from cement production – Reduction from primary measures; PhD Thesis, Department of Chemical Engineering, DTU, Denmark, 1999. ISBN 87-90142-55-1.
- ¹² Aho, M. Ferrer, E.; Importance of coal ash composition in protecting the boiler against chlorine deposition during combustion of chlorine-rich biomass; Fuel, 84, 201-212, 2005.
- ¹³ Jannerup, H.E., Rydeng, P., Jensen, C.D.; Whole Tires – Tire Chips; Available from FLSmidth, 2005
- ¹⁴ Schmidthals, H.; Luftvergasung von Altreifen zur integrierten stofflichen und energetischen Nutzung im Klinkerbrennprozess; PhD Thesis, Fakultät der Maschinenbau, Ruhr Universität Bochum, 2001.
- ¹⁵ Avenell, C.S., Sainz-Daz, A.I., Griffiths, A.J.; Solid waste pyrolysis in a pilot scale batch pyrolyser; Fuel, Vol. 75, 1167-1171, 1996.
- ¹⁶ Reallf, J.M, Lemieux, P., Lucero, S, Mulholland, J. and Smith, P.B.; Characterization of Transient Puff Emissions from the Burning of Carpet Waste Charges in a Rotary Kiln Combustor; IEEE Conference, 212-228, 2005.
- ¹⁷ Niessen, W.R.; Combustion and Incineration Processes, 3rd edition; Marcel Dekker, New York, 2002. ISBN 0-8247-0629-3.
- ¹⁸ Van Lith, S.; Release of Elements During Wood Firing on A Grate; PhD Thesis; Department of Chem. Eng, Technical University of Denmark, December 2000.
- ¹⁹ Stenseng, M.; Pyrolysis and Combustion of Biomass; PhD Thesis, Department of Chem. Eng, Technical University of Denmark, October 2005. ISBN 87-90142-65-9.
- ²⁰ Sørum, L.; Environmental Aspects of Municipal Solid Waste Combustion; PhD Thesis, NTNU, Norway, 2000. ISBN 82-79841202

- ²¹Bech, N.; Forbrænding – teori og praksis, bind 2. Polyteknisk forlag, Odense, Denmark, 2004 (In danish). ISBN 87-502-0765-2.
- ²²Kobyashi, N., Itaya, Y., Piao, G., Mori, S., Kondo, M., Hamai, M. and Yamaguchi, M.; The behaviour of flue gas from RDF combustion in a fluidized bed; *Powder Technology*, 151, 87-95, 2005.
- ²³Axelsen, E.P.; Theoretical and experimental studies on combustion of alternative fuels in cement kilns; PhD Thesis, Telemark University College, Norway, 2002. ISBN 82-471-5485-4.
- ²⁴Tokheim, L.A.; An Alternative Solution; *World Cement*, 57-63, November 2005.
- ²⁵Ayllon, M., Gea, G., Murillo, M.B., Sanchez, J.L. and Arauzo, J.; Kinetic study of meat and bone meal pyrolysis: an evaluation and comparison of different possible kinetic models; *J. Anal. Appl. Pyrolysis*, 74, 445-453, 2005.
- ²⁶Kääntee, U., Zevenhoven, R., Backman, R., Hupa, M.; Cement manufacturing using alternative fuels and the advantages of process modelling; *Fuel Processing Technology*, 85, 293-301, 2004.
- ²⁷Jannerup, H.E., Rydeng, P., Jensen, C.D.; Hazardous Waste ; Available from FLSmidth, 2005.
- ²⁸Krennbauer, F.; Alternative fuels and their influence on the cement burning process; *ZKG-International*, 5, 63-71, 2006.
- ²⁹Vaccaro, M.; Burning Alternative Fuels in Rotary Cement Kilns; *IEEE*, 127-136, 2006.
- ³⁰Suzukawa, Y. and Sasaki, T., *Sy.*, Washington, I, 83, 1960.
- ³¹Hewlett, P.C. (editor); *Lea's Chemistry of Cement and Concrete* (4th ed); Elsevier Butterworth Heinemann, 2004. ISBN 0-7506-6256-5.
- ³²Personal communication: Peter Green Andersen, FLSmidth , 4/1-2006.
- ³³Roy, G.R.; *Petcoke Combustion Characteristics*; *World Cement*, April 2002.
- ³⁴Atal, A., Levendis, Y.A.; Comparison of the combustion behaviour of pulverized waste tyres and coal; *Fuel*, Vol.74, 1570-1581, 1995.
- ³⁵Schrama, H., Blumenthal, H., Weatherhead, E.C.; A survey of tire burning technology for the cement industry; *IEEE cement industry technical conference* (San Juan, Puerto Rico), p.283-206, 1995.
- ³⁶Ohlsen, I.; *Burner Technology; Innovation for Sustainability - VIth Colloquia of Managers and Technicians of Cement Plants*,133-146, Valencia, Spain, 1-3 March, 2006.
- ³⁷Gemmer, M., Schnerider, W.; Development status of a modern rotary-kiln burner; *ZKG International*, No.8, 40-46, 2006.
- ³⁸Giugliano, M., Gernuschi, S., Ghezzi, U., Grosso, M.; Experimental Evaluation of Waste Tires Utilization in Cement Kilns; *Jour. of the Air & Waste management Association*; 49,1405-1414,1999.
- ³⁹Keefe, B.P., Shenk, R.E.; An innovative solution for waste utilization; *IEEE Cement Industry Technical Conference*, 197-206, 2003.
- ⁴⁰Haugom, J.O., Kvitvik, A.O. and Christensen, K.P.; HOTDISC installation at Norcem Kjøpsvik: Project realization and operational experience; *VDZ Congress*, Düsseldorf, 348-351, 2002.
- ⁴¹Christensen, N.A.; Hot disc Reactor; *Innovation for Sustainability - VIth Colloquia of Managers and Technicians of Cement Plants*,191-206, Valencia, Spain, 1-3 March, 2006.
- ⁴²Kvitvik, A.; HOTDISC installation; *World Cement*, 35, 69-74, 2004.

- ⁴³ Drebelhoff, S., Scharf, K.-F.; Preparation and utilization of waste materials in a fluidized-bed gasifier of a cement kiln; *Cement International*, 2, 56-63, 2003.
- ⁴⁴ R. Wirthwein, K.-F. Scharf, P. Scur, S. Drebelhoff; Operating experience gained with a fluidized-bed gasifier using waste materials for lean gas making; *ZKG International*, No.1, 61-69, 2002.
- ⁴⁵ Rüdersdorf – the first 30 months; *International Cement Review*, July, 1998, 49-58
- ⁴⁶ Schmidthals, H.; The Pre-Combustion Chamber for Alternative Fuels – Development Status of a new Technology; *IEEE-IAS/PCA Cement Industry Technical Conference*, 207-218, 2003.
- ⁴⁷ Schmidthals, H., Rose, D.; Investigations into the Thermal Utilization of Alternative Fuels in Lump Form in the cement Burning Process; *ZKG International*, 54, 180-188, 2001.
- ⁴⁸ Werner, V., Rose, D.; Progress in the Gasification of Coarse Alternative Fuels in the Cement Industry; *VDZ Congress*, 344-347, 2002.
- ⁴⁹ Forum – Technische mitteilungen ThyssenKrupp, English edition, December 2002. ISSN 1438-9754.
- ⁵⁰ Streit, N.; A Modular Calciner Concept – The Right Solution for any Kind of Fuel; Presented at the ECRA Seminar : Experience with Precalciner Kilns, Bernburg, November, 2004.
- ⁵¹ Saito, I., Sakae, K., Ogiri, T., Ueda, Y.; Effective Use of waste tyres by gasification in cement plant; *World Cement*, 264-269, September 1987.
- ⁵² Bye, G.C.; *Portland Cement*, 2nd ed; Thomas Telford, London, 1999. ISBN 0-7277-2766-4
- ⁵³ Taylor, H.F.W.; *The Chemistry of Cements*, 2nd ed.; Thomas Telford, London, 1997. ISBN 0-7277-2592-0.
- ⁵⁴ Thomsen, K.; *International Cement Production Seminar – lecture notes on Behaviour of Volatile Matter*; FLSmidth , May, 2002.
- ⁵⁵ Sutou, K., Harada and H., Ueno, N.; Concentration is the Key; *International Cement Review*, 36-41, June 1999.
- ⁵⁶ Norcini, M., Tassistro, N., Quaresima, R., Scoccia, G., Volpe, R.; Use of Chopped tyres as auxiliary fuel in clinker kilns: Industrial experience at the Cagnano Amiterno cement works. *Proceedings of the 6th NCB international Seminar on cement and building materials*, Vol.3, 24-274, Nov 1998.
- ⁵⁷ Greco, R.; Combustion of Unusual Fuels; *World Cement*, 33-38, February 2006.
- ⁵⁸ Clark, M.; Phase Equilibria; *International Cement Review*, 55-56, June, 2002.
- ⁵⁹ Clark, M.; From Waste to Fuel; *International Cement Review*, 46-47, October 2005.
- ⁶⁰ Peiquan, L., Changfa, L., Muzhen, S., Baoshan, L., Guangmin, L., Wenmin, G., Yongfan, C.; Research and application of composite mineralizer in rotary kiln; 9th *International Congress on the Chemistry of Cement*, New Delhi.; National Council for Cement and Building Materials, vol.2, theme I-C, 393-398, 1992.
- ⁶¹ Clark, M.; Zero Emissions; *International Cement Review*, 45-46, October 2006.
- ⁶² EC Directive 2000/76/EC available from www.europa.eu.int.
- ⁶³ Hansen, J.P.; SO₂ emissions from cement Production; PhD Thesis, Dept. of Chem. Eng., Technical University of Denmark, 2003. ISBN 87-90142-96-9.
- ⁶⁴ Bolwerk, R.; Waste Management and Environmental Protection by the use of Waste Fuels in the Cement Production; *VDZ Congress*, 380-383, 2002.
- ⁶⁵ Scur, S.; NO_x reduction in the cement industry; *VDZ Congress*, 479-483, 2002.

- ⁶⁶ Axelsen, E.P. Tokheim, L.A., Bjerketvedz, D.; Investigation of NO_x reduction during the combustion of alternative fuels; ZKG International, 4, 54-63, 2003.
- ⁶⁷ Syverud, T., Thomasson, A., Gautestad, T.; Utilization of chipped car tyres for reducing NO_x emissions in a precalciner kiln; World Cement, 39-43, 1994.
- ⁶⁸ Jensen, L.S., Shenk, R.E.; Fulfilling Emission Guarantees; World Cement, 87-94, December 2005.
- ⁶⁹ Tokheim, L.A., Bjerketvedt, D., Husum, I., Hoidalen, O.; NO_x reduction in a precalciner kiln using plastic as reburning fuel; ZKG International, 1, 12-23, 1998.
- ⁷⁰ Wanzura, F., Wendt, B.; Influence of the use of Alternative Materials on the Levels of Heavy metals in Portland cement Clinkers and Cements; ZKG International, 10, 53-60, 2003.
- ⁷¹ Willitsch, F., Sturm, G.; Use and preparation of alternative fuels for the cement industry; Cement plant environmental handbook, 151-157, 2003.
- ⁷² Willitsch, F.W., Sturm, G.; From waste to fuel; International Cement Review, 59-62, March 2003.
- ⁷³ Richards, J.; Capabilities and Limitations of Available Control Techniques for Mercury Emissions From Cement Kilns. Portland Cement Association, 2005.
- ⁷⁴ Zevenhoven, R., Kilpinen, P.; Chapter 8 in CONTROL OF POLLUTANTS IN FLUE GASES AND FUEL GASES; Available from <http://www.abo.fi/~rzevenho/gasbook.html>, 2001
- ⁷⁵ Stanmore, B.R.; Review article : The formation of dioxin in combustion systems; Combustion and Flame, 136, 398-427, 2004.
- ⁷⁶ Oerter, M.; Effects of the use of Alternative Fuels on Emission in Clinker Production. VDZ Congress, 368-371, 2002.
- ⁷⁷ Sidu, S., Kasti, N., Edwards, P. and Dellinger, B.; Hazardous air pollutants formation from reactions of raw meal organics in cement kilns; Chemosphere, 42, 499-506, 2001.
- ⁷⁸ Cembureau; Best Available Techniques for the Cement Industry; Available from www.cembureau.be, December 1999

Chapter 4 – Devolatilization of Large Solid Fuel Particles

With increasing substitution rates of alternative fuels, the size of fuel particles that are to be combusted in the kiln system typically also increases. However, limited knowledge is available regarding devolatilization of these large solid fuel particles, as focus historically has been on devolatilization of small coal particles under conditions pertinent to suspension firing – an area which is also well exploited. Devolatilization of alternative solid fuel particles is important, as alternative fuels typically contain a significantly higher amount of volatiles compared to coals (see also section 3.1). Consequently, a high proportion of the heating value of the alternative fuels is released during combustion of volatile products.

In chapter 3 it was shown that TDF, plastics and MBM currently are the most important solid alternative fuels in the German cement industry, and devolatilization of these fuels is therefore of primary interest. The main emphasis of the detailed investigation in this chapter will be on devolatilization of large particles of TDF, because 1) TDF is difficult to produce as small tyre fuel particles with rapid burnout characteristics (see also section 3.2), 2) TDF has an irregular shape containing steel wires, and 3) TDF is used as a reference alternative fuel in the HOTDISC, which was the starting point of this work. In addition, MBM and plastics are typically introduced to the kiln as smaller particles than tyre rubber and therefore more easily combusted than TDF. The emphasis is on mass loss rates and conversion times due to the fact that the heat release rate is closely correlated with the mass loss rate and that the conversion time is an important parameter to be able to predict sufficient residence time for fuel burnout to prevent reduced clinker quality and kiln operational problems (see also section 3.2).

The experimental results from the macro-TGA setup in this chapter were obtained from a Master's degree project carried out parallel with this PhD study [1]. In addition, the development of devolatilization model C presented in this chapter has been in cooperation with Niels Bech from the Department of Chemical Engineering at the Technical University of Denmark.

Initially, a brief introduction to solid fuel combustion phenomena is presented followed by a literature study of devolatilization of large particles of TDF, plastics and MBM. The remaining part of the chapter contains experimental investigations of devolatilization of large TDF-particles as well as analyses of them using mathematical modelling.

4.1 Introduction to Solid Fuel Combustion

The combustion of a solid fuel particle may be divided into 4 stages: Heating, drying, pyrolysis/devolatilization and char combustion (see also Figure 4-1).

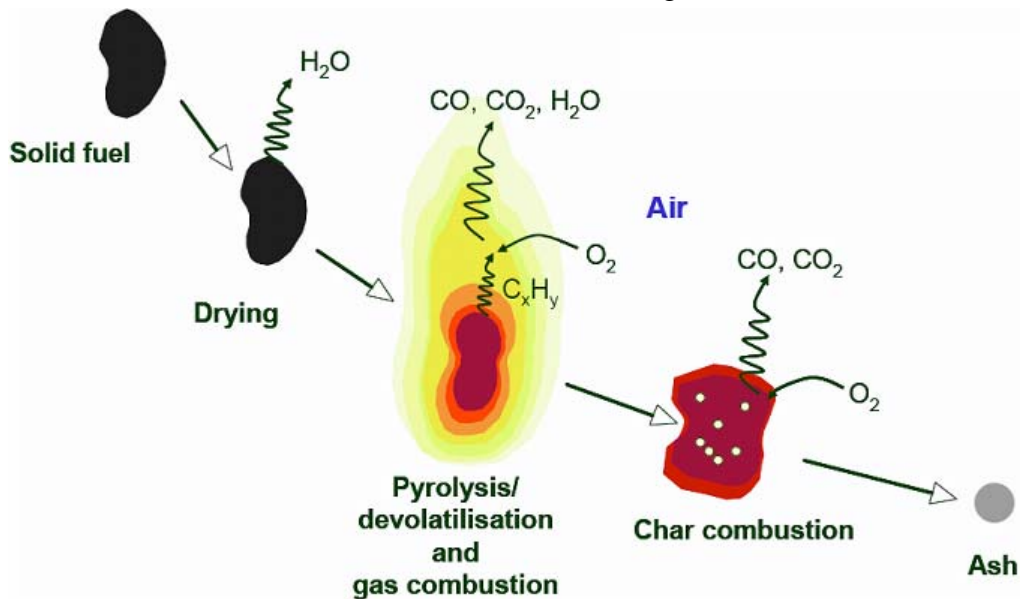


Figure 4-1: Stages involved in the combustion of a solid fuel particle [2].

4.1.1 Heating and Drying

The heating is the first stage and occurs after injection of the solid fuel particles into the combustion chamber. Upon heating to about 100°C , the moisture is evaporated and transported through the outer particle volume and away from the particle surface. Consequently, the particle is dried.

4.1.2 Devolatilization

The terms pyrolysis and devolatilization indicate the release of volatiles without or with oxidising atmosphere, respectively. The description in this section provides a background for the processes most often encountered in solid fuel devolatilization of large particles, where the virgin fuel particle retains its original shape and size. However, some solid fuels may not produce/retain a char layer (see also section 4.1.4), and the description of the steps in the devolatilization process should therefore be adjusted accordingly.

For solid fuel particles, where the char layer is retained during devolatilization, several physical and chemical processes influence the devolatilization process (see Figure 4-2). The devolatilization process is initiated by external heating. Heat is consequently transported into the material by conduction through the char, reacting and virgin fuel layers, where radiative heat transfer may have a role in the char and reacting layers. In the reacting layer, volatiles are released, and as a consequence of the volatile production, an outward mass transport

through the particle is induced. Independent pyrolysis reactions may be endo- or exothermic, where the latter may increase the intra-particle temperature locally and consequently conduct heat both in- and outwards. The outward mass-flow may cool the hotter solid when the cooler mass flows from the interior. In an oxidizing atmosphere, the devolatilization products may ignite in a flame front above the outer surface, enhancing the external heat transfer to the surface. In this case the visibility of the flame is due to radiation from intermediate soot particles, formed during the combustion of volatile products. The physics and reactions associated with the volatile release may cause structural changes of the remaining solid, denoted char.

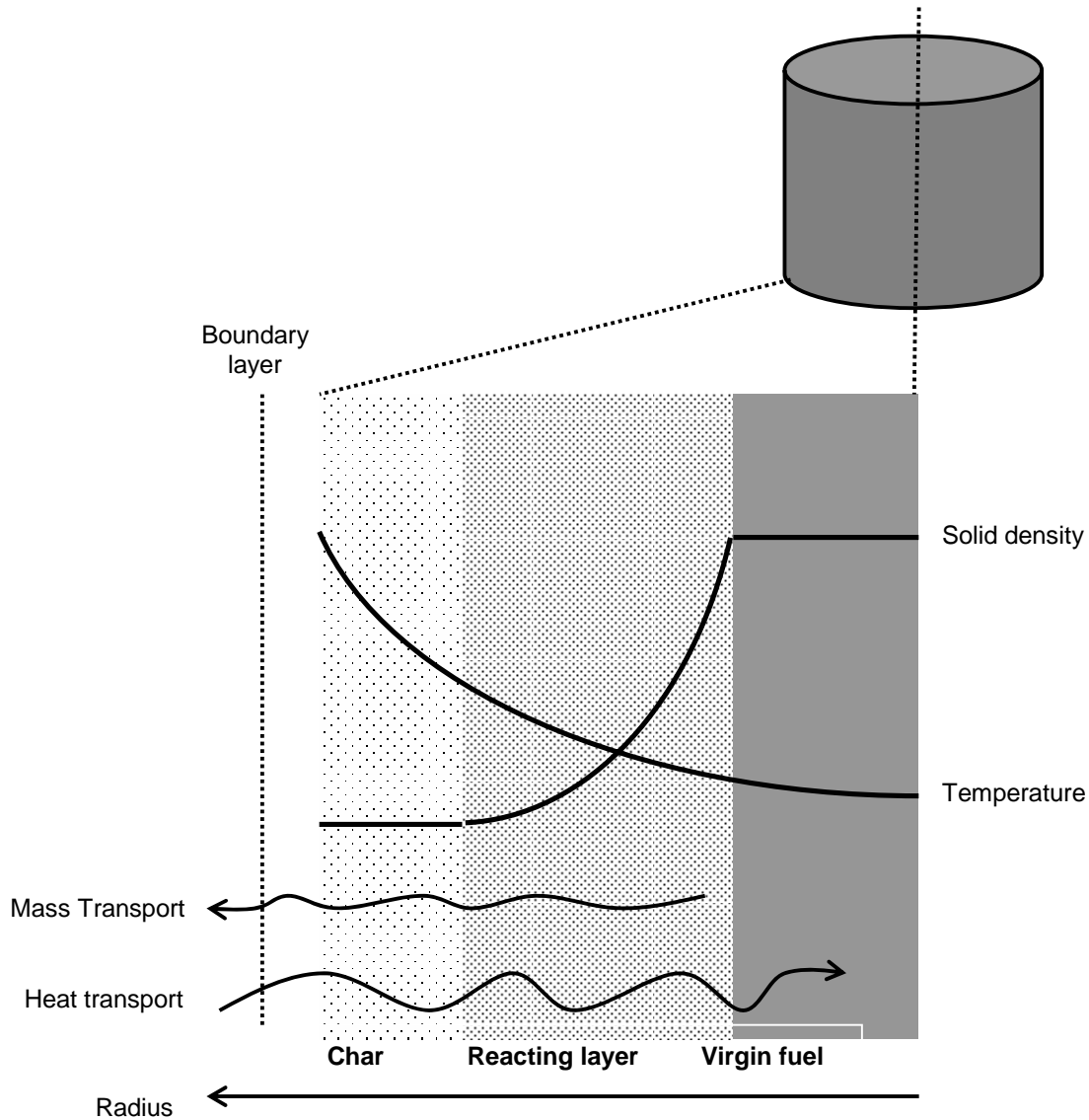


Figure 4-2: Radial cross section of partially devolatilized solid fuel particle in cylinder geometry (end effects ignored resembling the infinite long cylinder).

4.1.3 Char Conversion

The remaining char is a solid rich in carbon. In the char conversion stage, oxygen is transported from the surrounding gas through the boundary layer to the solid fuel outer surface and eventually further into the particle matrix via pore diffusion. Oxygen is adsorbed onto the surface of the solid matrix, where it reacts with solid carbon and desorbs as gaseous combustion products. The products are transported to the surface and further through the boundary layer. Char oxidation may be assumed to start when the release of volatiles is finished, because the flame formed during the combustion of volatiles may effectively prevent oxygen transport to the surface of the char. Ash is the remaining product after char combustion.

4.1.4 Solid Fuel Conversion Pathways

In addition to the overall description of steps in solid fuel combustion provided previously, a description regarding typically encountered solid fuel conversion pathways is provided here. This is important in order to interpret the differences in fuel conversion reaction kinetics of various solid fuels.

Figure 4-3 shows different reaction paths encountered during devolatilization and char combustion in solid fuel conversion. Reaction path A illustrates the direct volatilisation of gasses from the solid fuel. Reaction paths B and C show formation of intermediate products of liquid and tar formed during devolatilization. Reaction path D shows the evaporation of them. For devolatilization through reaction path I, the particle shrinks during devolatilization with or without simultaneous production of smaller char particles (indicated by dotted arrows). Reaction path K illustrates the reshaping of particles during heating. If oxidizer is present, the gas produced from the devolatilization steps is combusted in the gas phase.

Subsequent to devolatilization, or parallel to pathway I, the char combustion may follow different pathways. In pathway F, the char fragments into smaller char particles. In pathway G, the particle is converted according to a shrinking particle mechanism, and in pathway H, the char particle is converted as a constant size. For reaction pathway H, an unreacted shrinking core (H1) or a progressive conversion model (H2) may be adequate to describe the combustion process [3]. Finally, the agglomeration of char may cause larger particles as shown in path J.

It is necessary to evaluate which path the particle follows during devolatilization, because faster volatilisation is expected for a particle following pathway I than for example E. With regard to utilization of alternative fuels in cement production, the char oxidation is the last step in the combustion process, and mainly governs the degree of fuel conversion obtained in the calciner system or rotary kiln (incomplete devolatilization may also influence fuel burnout). The size of a char particle is an important parameter with regard to conversion time and it is therefore necessary to characterize the char formation/combustion mechanisms according to Figure 4-3 for alternative fuels that are to be used in cement production. For

instance, if the initial fuel particle crackles during pathways F or I, less time is needed for char conversion than if pathway H or J is responsible.

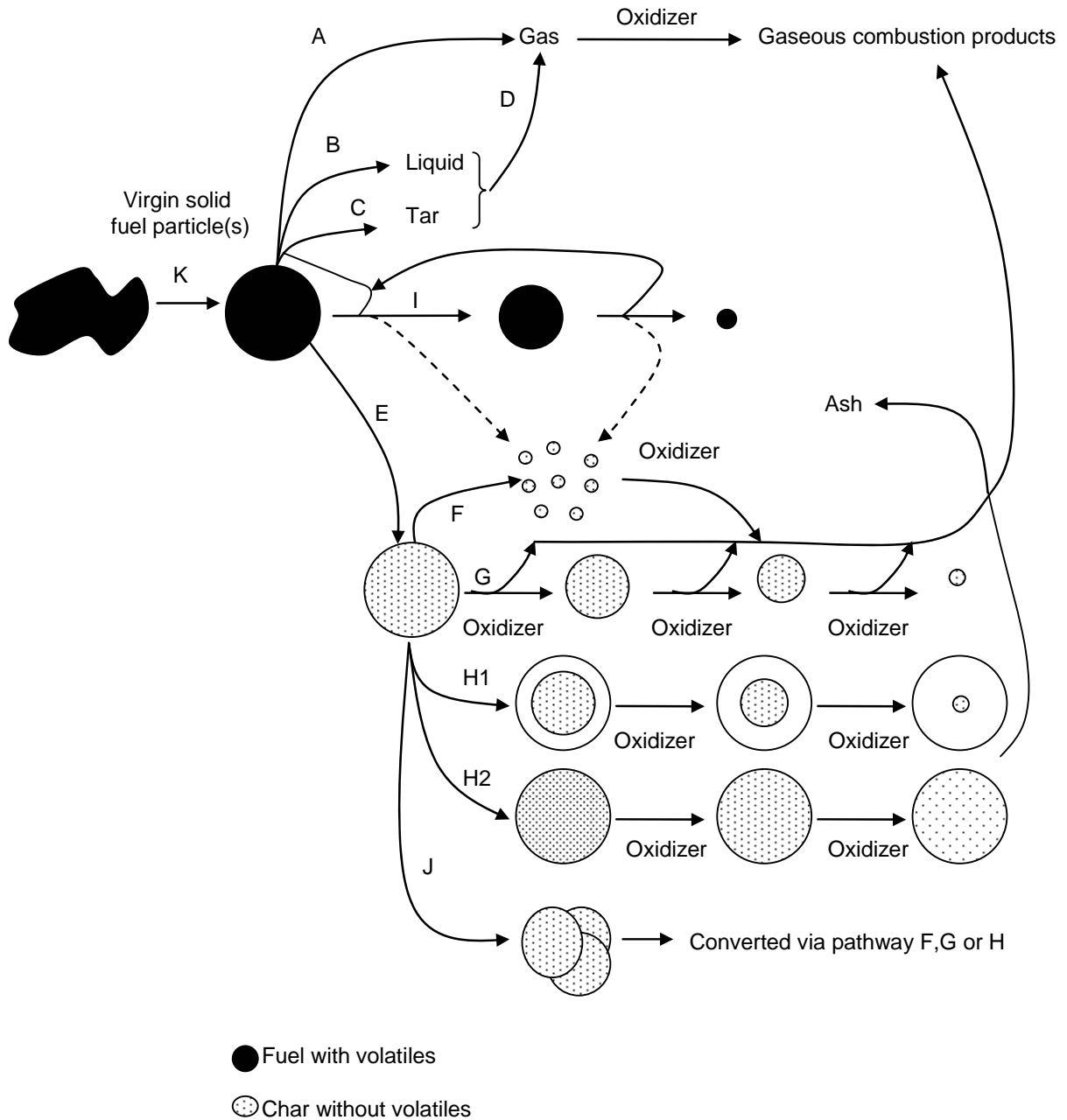


Figure 4-3: Main reaction pathways involved in the combustion process of a solid fuel particle.

4.2 Literature Study on Devolatilization Kinetics of Large Particles

The aim of this section is to provide an insight into the literature regarding devolatilization of TDF, MBM and plastics. The emphasis is on devolatilization characteristics of large particles.

4.2.1 Tyre Derived Fuel (TDF)

Most investigations of devolatilization of tyre rubber are performed in micro-TGA on small samples in order to determine the kinetics and reaction mechanisms [4,5,6,7] for the decomposition pattern, to identify and quantify the rubber polymers in the tyre [8] or to characterize the fractional yield and composition of oil, gas, char [9,10,11]. Physical and chemical properties of TDF as well as a micro-TGA investigation of TDF pyrolysis are provided in section 4.5.4. Studies regarding large tyre rubber particles are complicated, due to the difficulties in selecting a representative sample. This is due to tyres being a composite material containing steel, rubber and different kinds of overlays (see Figure 4-4).

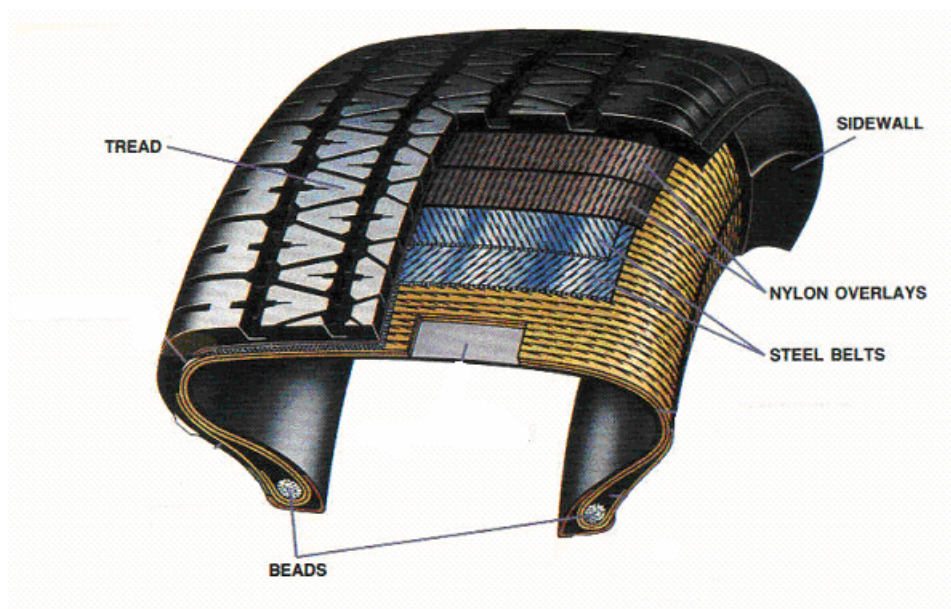


Figure 4-4: Cross section of a tyre (From www.energymanagertraining.com)

Different approaches are taken in the literature to the quantification of devolatilization times of large particles of tyre rubber. Giddings et al. [12] performed devolatilization experiments with chopped pieces of tyre rubber placed on a perforated tray, where air at 900°C was flowing from beneath. They reported a time of devolatilization of approximately 120 seconds as indicated by the extinction of a flame. The mass of the specimen was about 7 gram, but no exact geometry was reported. Schmidhals [13] reports experimental observations, where the devolatilization of chopped pieces of tyre rubber in the cm size (no exact geometry reported) was completed in approximately 10 minutes, at 650°C, in atmospheric air, while the devolatilization time increased to about 20 minutes in an inert atmosphere of nitrogen. Bouvier et al. [14] performed macro-TGA experiments with cubes of tyre rubber in a preheated oven at 433 and 590°C in inert atmosphere and found that the devolatilization time

increased with particle size and decreasing temperature. Yang et al. [15] investigated devolatilization of a tyre rubber-cylinder with a diameter of 40 mm and a length of 60 mm, at a temperature of 510°C, under vacuum, and from this study the time for devolatilization was observed to be approximately 50 minutes. A comparison of the reported devolatilization times of tyre rubber particles is shown in Figure 4-5. It is noted that Rodriguez et. al. [11] also performed devolatilization experiments with tyre particles in the cm size; however the focus of this study was not on conversion time.

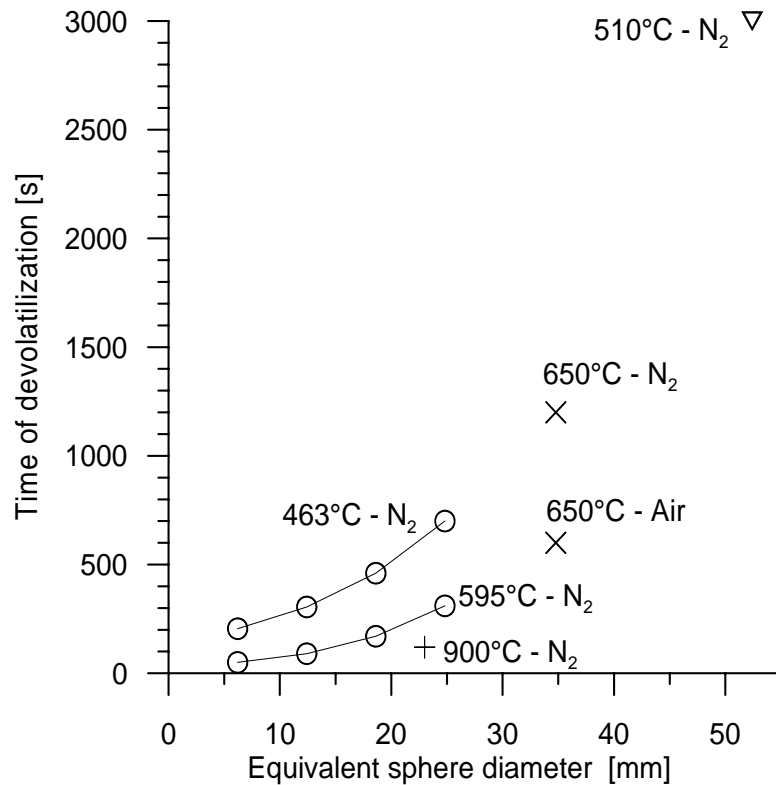


Figure 4-5: Comparison of devolatilization times for large particles of tyre rubber from the literature with temperature as discrete variable. The captions are: (O) Bouvier et al. [14], (∇) Yang et al. [15], (+) Giddings et al. [12] and (X) Schmidthals [13].

It is difficult to extract precise data for the devolatilization time of large particles of tyre rubber from the reported literature data. However, it is observed that an increase of particle size increases the devolatilization time and increasing surrounding temperature decreases the devolatilization time. Furthermore, the results from Schmidthals [13] indicate that an oxidative atmosphere may increase the rate of devolatilization, conceivably due to an enhanced external heat transfer caused by radiation from the enveloping flame from combustion of the volatiles. This is in agreement with Senneca et al. [16] who observed a shift in the mass-loss towards lower temperatures for micro TGA experiments with high volatile fuels in an oxidative atmosphere. However, from the study of Senneca et al. it is not possible to separate the role of simultaneous char oxidation and devolatilization.

4.2.2 Plastics

Sørnum et al. [17] performed micro-TGA studies of high- and low density poly-ethylene (PE), poly-propylene (PP), poly-styrene (PS) and PVC at a heating rate of 10°C/min in inert atmosphere obtaining the normalized mass loss curves shown in Figure 4-6. All investigated plastics, except PVC, show a volatile content of about 100 wt.% in accordance with the fuel analyses presented in table 3-2. PVC shows a char and ash content of about 10 wt.%, which is slightly higher than the values of table 3-2. PVC plastic is observed to start decomposing around 250°C and up to 500°C with a plateau around about 350-400°C. The other plastics are observed to decompose in a narrow temperature interval of about 50°C.

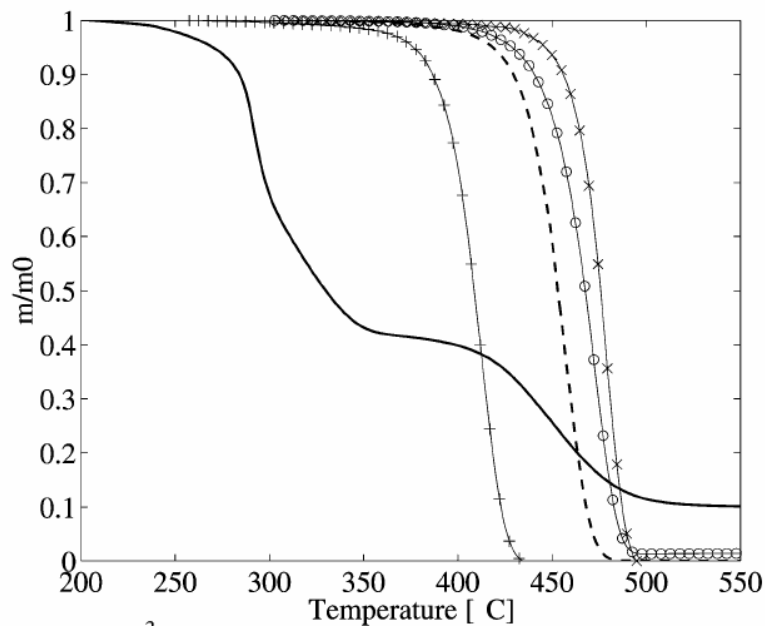


Figure 4-6: Normalized mass loss of different plastics obtained in micro-TGA at 10°C and inert atmosphere (from [17]). Captions are: HDPE (X-X-X), LDPE (O-O-O), PP (- - -), PS(+++-+) and PVC (full line).

Micro-TGA results provide information regarding decomposition temperatures, and intrinsic kinetic models for the pyrolysis reactions may also be derived. However, TGA curves do not provide information regarding structural changes nor mass and heat transport effects that may be expected for large particles. Zevenhoven et al. [18] used in-situ video recordings to study combustion characteristics of large plastic particles at temperatures of 750-950°C at 2-12 Vol.% O₂. They reported that plastic sheets were reshaped to spherical particles upon heating, and during devolatilization, the products evaporated from the outer surface and combusted in a flame front around the particle (pathway K and I of Figure 4-3), resembling liquid fuel combustion. They correlated the experimental data with a well described droplet combustion model [19,20] and obtained values of the transfer number at 7 Vol. % Oxygen. At 850°C and 7 Vol.%, the time of devolatilization for thin sheets of PP, PS, HDPE, LDPE were reported to be about 10 seconds, whereas PVC showed a slightly lower value in agreement with its higher pyrolysis reactivity (see Figure 4-6). The time of combustion for PVC, however, was prolonged to about 30 seconds due to its char content.

Franke et al. [21] investigated devolatilization rates in bubbling fluidized bed combustion and devolatilization times for cylindrical pellets ($\varnothing=10\text{mm}$ and length= 10mm) of PE and PP. Devolatilization times may be derived from their work: 65-100 seconds for PE dependent on external heat transfer and about 65 seconds for PP at 670°C at 6 Vol.% O_2 . The decomposition of PP was only investigated at one external heat transfer rate.

Di Blasi [22] investigated pyrolysis of large poly-ethylene particles, using a mathematical model including intra-particle pyrolysis decomposition as well as mass and heat transfer. In addition, the author modelled the shrinking of the outer particle surface, in agreement with the experimental observation of Zevenhoven et al. [18]. Modelled conversion time of a solid PE slab (0.5 cm to symmetry line) may be extracted from the work: about 150 seconds at 1000°C increasing to 220 seconds at 900°C .

Pyrolysis/devolatilization investigations of mixtures of sheets of plastic and papers have also attracted attention, because these components are the main contents of RDF. The study of Salvador et al. [23] investigated the effect of different mixtures of PE and cardboard and packing degree on devolatilization reactivity of large particles in an experimental macro-TGA setup. The main conclusions from their work with regard to reactivity are: 1) the devolatilization time was proportional with the particle density and 2) the devolatilization time decreased with the content of PE.

4.2.3 Meat and Bone Meal

The thermal decomposition of small particles of meat and bone meal (MBM) in micro-TGA reactors, has been investigated by Conesa et al. [24], Ayllon et al. [25] and Skodras et al. [26]. Skodras et al. report mass loss up to 500°C , which will be demonstrated to be insufficient to describe MBM decomposition. Conesa et al. and Ayllon et al. fitted the experimental data to three independent parallel decomposition reactions (see also section 4.5.4), and the results of their kinetic model together with experimental data obtained in this work are shown in Figure 4-7. It is seen that the three independent investigations agree relatively well up to about 400°C . At higher temperatures good agreement exists between the laboratory data of this study and the model of Ayllon et al. The difference between them seems only to be a shift in temperature of about 20°C . From the mass loss curves it should be noted that the main pyrolysis takes place at temperatures in the range of about 200 to 450°C . However, losses of about 8-15 wt.% of the initial mass take place at higher temperatures up to about 800°C . Consequently, the devolatilization of MBM particles needs higher particle temperatures than for instance the plastics to achieve complete devolatilization (see also Figure 4-6), and small particles^a of MBM are therefore considered less reactive during devolatilization than small particles^a of plastic as well as TDF (see also Figure 4-22).

^a Sufficiently small to be controlled by kinetics

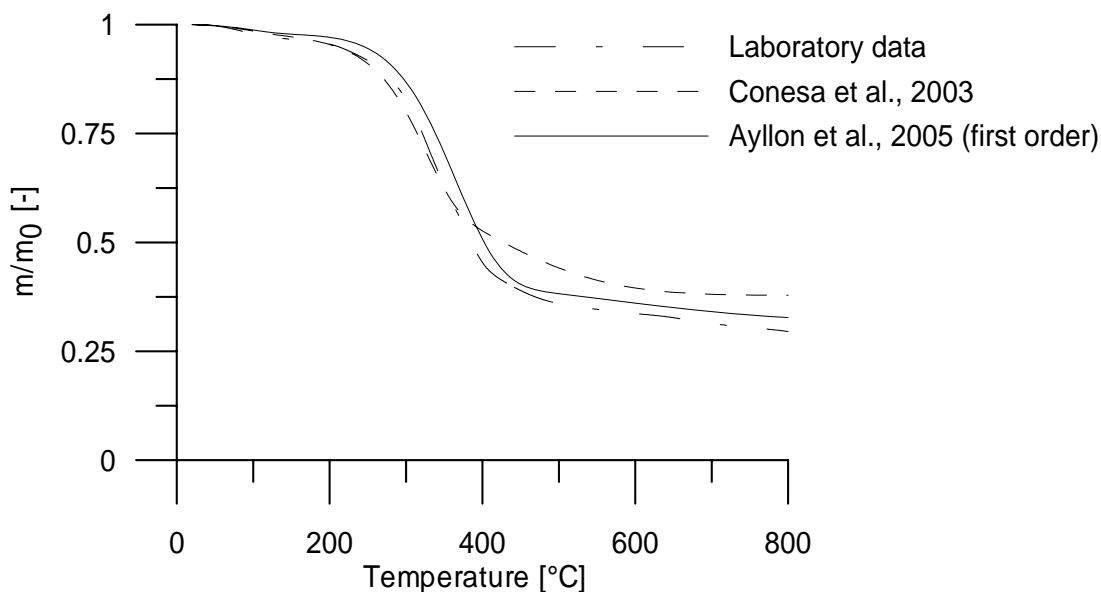


Figure 4-7: Scaled mass loss against temperature for MBM. Results based on kinetic scheme of Conesa et al. [24], the first order scheme of Ayllon et al. [25] and experimental data obtained at 10°C/min in micro-TGA for an MBM obtained from a German cement plant.

Ayllon et al. [27] investigated decomposition of a bed of MBM particles in a fixed bed reactor with emphasis on product distributions and char characterization. To the author's knowledge, no studies are available in the open literature regarding decomposition kinetics of particles of MBM in realistic sizes.

4.2.4 Conclusions on Literature Study

The literature study regarding devolatilization of large particles of TDF, plastics and MBM revealed that several micro-TGA studies for the decomposition of each fuel exist. However, from these studies, the devolatilization rates of large particles is not easily established, as large particles may also be controlled by heat and mass transfer. In addition, micro-TGA investigations do not provide information regarding conversion pathways.

The effect of particle size and temperature on the rate of devolatilization of large tyre rubber particles is not clear in the literature. Moreover, the effect of steel wires on devolatilization rates has not been addressed. For plastics, the literature study revealed that sheets are reshaped during heating forming spherical droplets that burn like liquid fuels. No studies regarding decomposition of realistically sized particles of MBM are available.

4.3 Experimental

As revealed in the literature study, information regarding devolatilization of large particles under combustion conditions is limited. This section describes the experimental setups applied in order to investigate the devolatilization rate of large particles of tyre rubber. This is preceded by a discussion of the pre-experimental considerations.

4.3.1 Pre-experimental Considerations

Devolatilization of large particles of TDF may follow pathway E or I of Figure 4-3, where pathway I results in a simultaneous production of smaller char fragments. However, mechanical action must be exerted in order to remove the char layer produced during devolatilization, and pathway I is therefore not an inevitable result of the devolatilization process. The experimental investigations are to resemble TDF particles converted through conversion pathway E or I and preferably yield the effect of:

- 1) *Particle size*
- 2) *Surrounding temperature and*
- 3) *Presence of steel wires*

on the devolatilization rate and time. In addition, experimental data is to be obtained for model validation purposes.

Initially, no dedicated experimental setup was available for studying devolatilization of large particles with regard to devolatilization mass loss and time. In order to quantify the devolatilization conversion rate or time, four experimental methodologies were initially considered.

- 1) *Inject the large rubber particle into a preheated oven in oxidizing atmosphere and subsequently measure the continuous CO/CO₂ signal. Integration of the signal should then yield conversion against time that may be converted to a devolatilization conversion.*
- 2) *Inject a large tyre rubber particle into a preheated oven in inert atmosphere with thermocouples placed in the centre. The devolatilization is then assumed finished, when the particle centre reaches a predefined temperature, e.g. obtained from micro-TGA.*
- 3) *Inject a large tyre rubber particle into a preheated oven in oxidizing atmosphere and subsequently observe the flame produced during combustion of volatiles. The extinction of the flame depicts the devolatilization time.*
- 4) *Inject a large tyre rubber into a preheated oven in inert atmosphere and measure the continuous mass loss.*

Methodology 1) was rejected due to the uncertainties with regard to separation of simultaneous char oxidation and combustion of volatile gasses. In addition, at low

temperatures, incomplete oxidation of volatiles may disturb successful data interpretation. Methodology 2) was also rejected, due to the fact that it is difficult to determine a pyrolysis temperature, as some pyrolysis reactions may be endo- or exothermic and therefore influence the centre temperature of the particle (actually proved to be the case for devolatilization of large TDF particles - see section 4.5). In addition, it is difficult to place a thermocouple precisely in the centre. Methodology 3) was selected even though it is only possible to establish the devolatilization time and not the mass loss rate. Methodology 4) was also selected due to the fact that it both gives mass loss rate and devolatilization time.

The geometry of the investigated samples should preferably resemble one-dimensional geometries, because this eases data interpretation, and a sphere is consequently the best choice. However, it is difficult to produce a sphere of the tested materials due to the elasticity of the tyre rubber.

4.3.2 Fuel Samples

The tested fuel samples were to resemble large particles of tyre rubber used in the kiln system, and in particular the HOTDISC. However, since tyre is an inhomogeneous material, containing tread and steel it is unsuitable for systematic experiments, due to the difficulties in producing identical samples. Consequently, new tyre rubber from the wearing face of a truck tyre without tread and steel wires was obtained from *PointS*, Denmark, and used for the experiments. The tyre rubber was cut into cylindrical or rectangular shapes (dependent on experimental setup). A proximate and ultimate analysis of the tyre rubber is shown in Table 4-1.

		<i>Unit</i>	<i>Truck tyre rubber</i>
Proximate analysis	Moisture	wt.%	1.2
	Volatiles	wt.%	64.1
	Ash	wt.%	5.0
	Fixed C (Calculated)	wt.%	29.7
Ultimate analysis	C	wt.%	82.0
	H	wt.%	6.71
	S	wt.%	1.35
	N	wt.%	0.32
	O (Calculated)	wt.%	3.42
Lower heating value		MJ/kg	35.0

Table 4-1: Proximate and ultimate analysis and lower heating value for the tested tyre rubber. Determined according to British Standard Methods (BS 1016-1018) and the heating value was determined using ISO 1928 standards.

4.3.3 Flame Devolatilization Experiments

In this study, rectangular blocks of solid truck tyre rubber with different heights are made and placed in a specially designed holder as shown in Figure 4-8. The solid fuel sample is insulated on the side walls and bottom. The tyre rubber sample is therefore only susceptible to

external heating from the upper side and heat transfer inside the rubber particle is ideally only governing in the vertical direction, i.e. one dimensional heat transport. Furthermore, the upper surface of the tyre rubber block is kept parallel to the top surface of the insulation by varying the height of the insulation at the bottom, in order not to change the gas flow profile around the sample holder when changing the height of the sample.

For the investigation of conversion pathway I, the side walls of the sample holder are simply moved, as this allows the gas flow to remove the char layer continuously. However, this also allows heating from the sidewalls and consequently not entirely 1-dimensional heating.

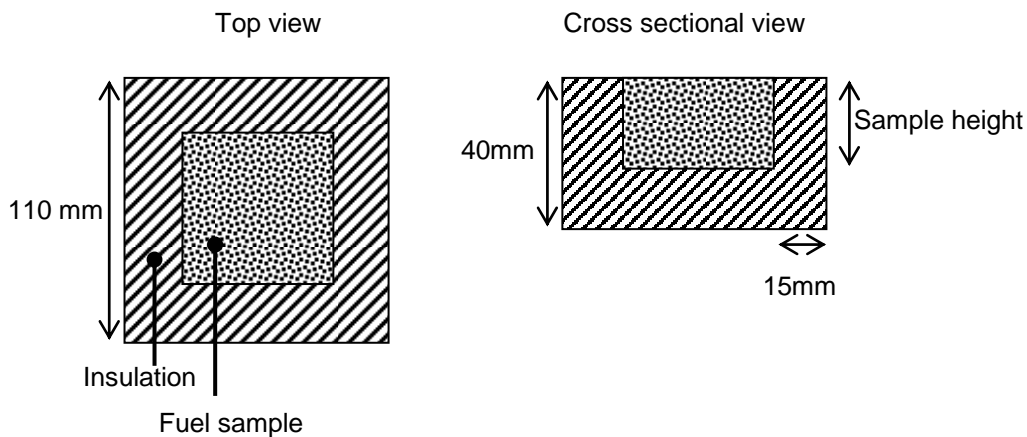


Figure 4-8: Schematic drawing of holder used for devolatilization experiments of large TDF particles converted via conversion pathway E. The side walls are removed when investigating conversion through pathway I.

The holder with the fuel sample is then immersed into a preheated reaction chamber and hot combustion gas is passed around the holder and the sample as shown in Figure 4-9. Inside the reaction chamber, a thermocouple and a gas measurement probe are placed to measure the temperature and O_2 concentration continuously. At the top of the reaction chamber is placed a hole for insertion and rejection of fuel samples which is sealed by an air-tight viewing glass allowing visual observation of the solid fuel sample during the experiment. The hot gas is produced by an oil furnace, and the temperature may therefore be controlled by varying the oil flow to the furnace. However, due to the fact that more oil produces more flue gas, the linear gas velocity through the channel also changes as shown in Table 4-2.

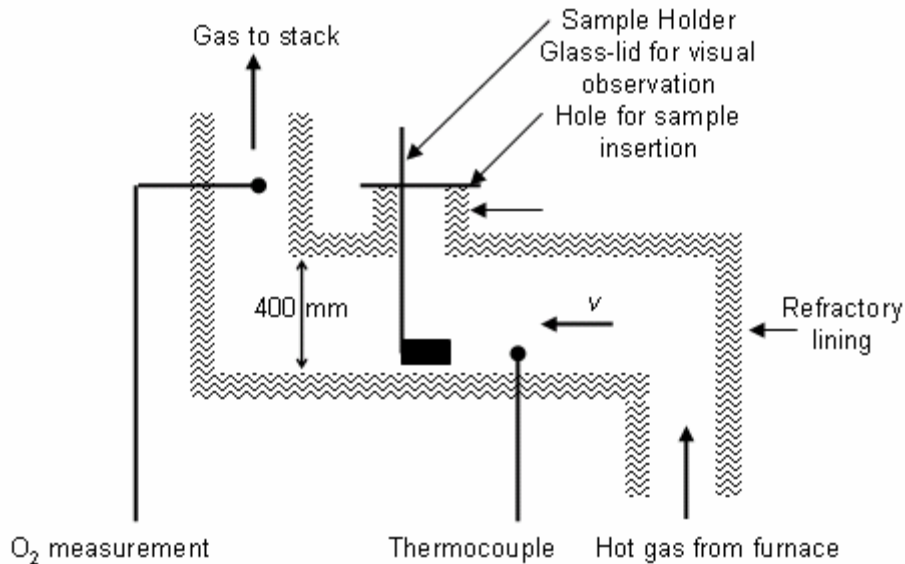


Figure 4-9: Overview of system used for preliminary devolatilization experiments (Not to scale).

<i>Temperature</i>	<i>Linear gas velocity</i>
805°C	~2.2 m/s
955°C	~6.1 m/s

Table 4-2: Linear gas velocities in reaction chamber as a function of temperature.

In the preparation of each experiment, the tyre rubber sample is placed in the sample holder and immersed into the chamber (see Figure 4-9) and the glass lid is closed again. The sample is then observed during the volatilisation of gasses indicated by a flame above the sample. The time when the devolatilization stops (i.e. extinction of the flame) is logged and in the following referred to as the time of devolatilization. The holder is drawn out of the reaction chamber and cooled carefully before the next sample is prepared.

The reaction chamber is insulated with 200 mm of refractory lining to minimize heat losses and due to this large mass of insulation, steady state temperature conditions are obtained after approximately 12 hours. Therefore, changes in operation conditions are not easily obtained. Despite these difficulties, however, this experimental setup was selected for the flame devolatilization experiments, because its conditions came closest to those of an industrial HOTDISC.

A special experiment was designed in order to investigate the effect of steel wires on devolatilization time. Stainless steel wires with a diameter of 1.5 mm were placed vertically into the rubber sample as shown in Figure 4-10. The population density of the wires was approximately 4 wires per cm². The same experimental procedure as described above was used and the devolatilization time was derived.

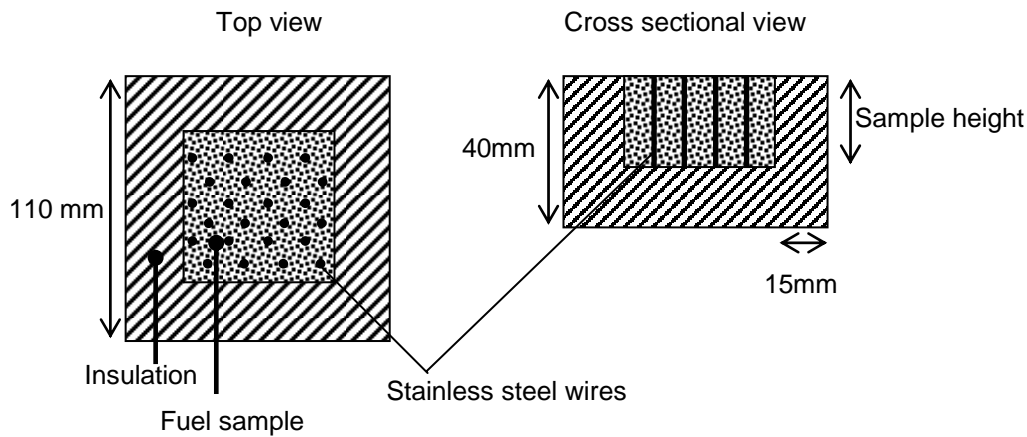


Figure 4-10: Illustration of solid fuel with wires of stainless steel inserted (not to scale).

4.3.4 Macro TGA Experimental Setup

This experimental setup was designed particularly for studying devolatilization rates and times of large alternative solid fuel particles.

In this experimental setup, the fuel samples are placed on a specially designed cylindrical sample holder and immersed into a preheated tubular reactor and the weight loss of the sample is measured continuously (macro-TGA). For all experimental investigations, a high length to diameter ratio is sought in order to approach one dimensional radial heating and consequently ease later data interpretation. To investigate conversion pathway E, a sample holder with a stainless steel mesh surrounding the tyre rubber sample is used (see left part of Figure 4-11). The purpose of the net is to retain the outer particle position and to retain the char layer during the devolatilization process and thereby ensure well defined conditions. When investigating conversion pathway I, the surrounding mesh is removed allowing the char to fall off continuously during devolatilization (see right part of Figure 4-11).



Figure 4-11: Sample holders used for devolatilization investigation of large particles in the Macro TGA setup ($\varnothing=18$ shown). Not to scale.

The Macro-TGA setup used for the experiments is shown in Figure 4-12. It consists of a vertical cylindrical reactor with four electrical heating elements. A valve and a Mass Flow Controller (MFC) are used for addition of a well defined flow of pure N_2 to the bottom of the reactor. All experimental

results herein are obtained with a gas flow of 17.5 Nl/min. Preheating of the gas takes place in the bottom of the reactor and experimental temperature measurements in the centre of the reactor for different set point temperatures of the heating elements indicate the temperature experienced by the sample in the reactor.

Each experiment is initiated by immersing the sample holder with tyre rubber particles into the preheated reactor under continuous gas flow, i.e. the particle experiences the same conditions as under combustion conditions, except for the significantly lower gas velocity around the sample. A precision balance measures the weight of the sample, and a data acquisition program records the signal on a computer for subsequent data interpretation.

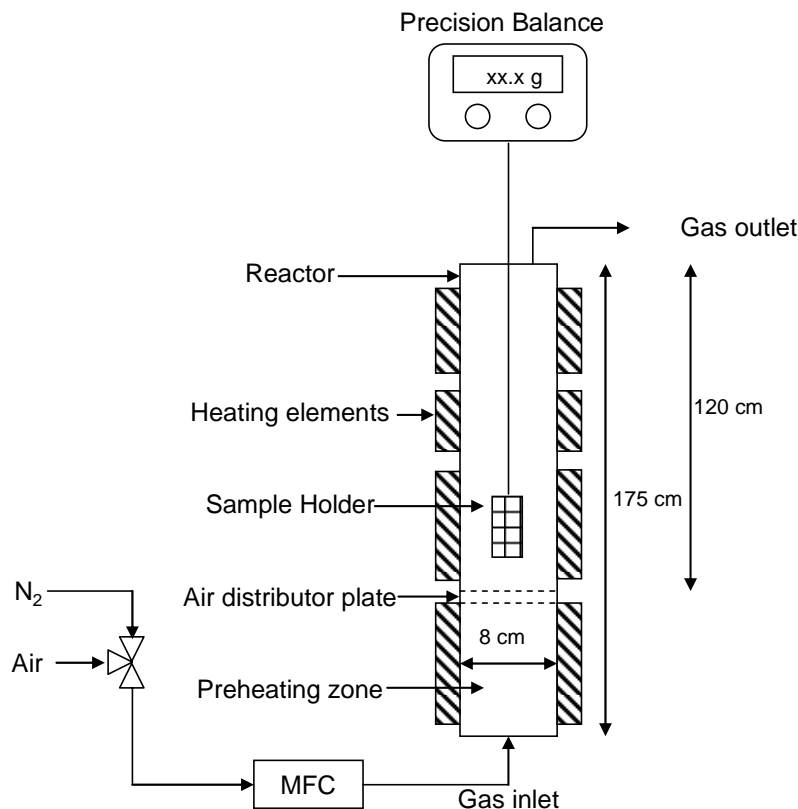


Figure 4-12: Experimental macro-TGA setup

For the experiments with surrounding mesh, temperature profiles in the tyre rubber were measured during the devolatilization process for later model validation purposes. Thermocouples were placed in the axial direction at the centre of the cylindrical particle, i.e. $r=0$, and at the halfway distance between the surface and the centre, i.e. $r=\frac{1}{2}R_0$ (see Figure 4-13). The signal from the temperature measurements as a function of time was then logged on a computer during an experiment. Mass-loss measurements were not made simultaneously with measuring the transient temperature profiles, because the thermocouples could disturb the mass-loss measurement.

Steel wires were inserted in the tyre rubber particles with diameters of 14 and 22 mm and their devolatilization mass losses were investigated at 840°C with a surrounding mesh. The

steel wires ($\text{Ø}1.6 \text{ mm}$) were placed in the radial direction with an axial distance of 7 mm (see Figure 4-13). No temperature measurements were made with the inclusion of wires.

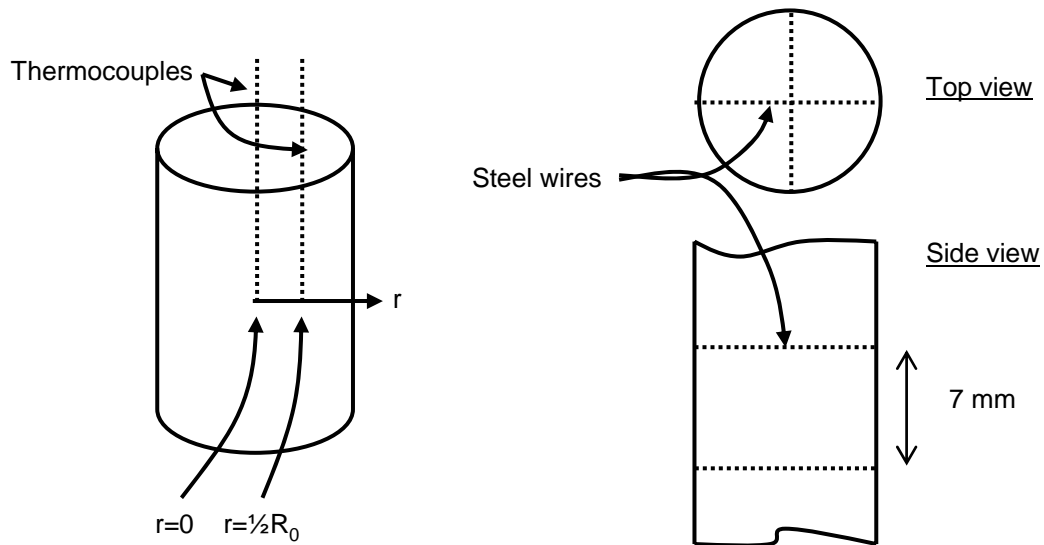


Figure 4-13: Positions of thermocouples (left) and wires (right) in the tyre rubber cylinders.

4.3.5 Conclusions

Two different experimental methods are employed in order to investigate the devolatilization rate/time of large particles of tyre rubber. In the flaming devolatilization setup, the devolatilization time is the parameter measured, whereas also the mass loss may be measured in the macro-TGA setup. Both experimental setups simulate conditions experienced by a large tyre rubber particle upon injection into a preheated combustion chamber.

4.4 Experimental Results

In this section, the experimental results are presented and analysed. Initially, the results of the flame devolatilization experiments are presented and analysed followed by the data obtained in the macro-TGA setup and an analysis of the data.

4.4.1 Results of Flame Devolatilization Experiments

These sections contain the results obtained using methodology 3) of section 4.3.1.

4.4.1.1 Tyre Rubber without Steel Wires

The results of the flame devolatilization experiments without steel wires and for the two types of sample holder are shown in Figure 4-14, as devolatilization time against height. Initially, it is observed that a successful double determination for each particle size, sample holder type and temperature verifies the experimental results.

Effect of sample size

A significant effect of sample height on the devolatilization time is observed for both tested temperatures and both type of sample holders. For the insulated experiments (with side walls) and a height of 20 mm, the devolatilization time is observed to be about 750 seconds for both investigated temperatures. It drops to about 100 seconds for a height of 5 mm. For the non-insulated experiments (without sidewalls) and a temperature of 955°C, the devolatilization time is observed to be about 300 seconds for a height of 20mm, dropping to about 100 seconds for a height of 5mm.

Effect of temperature

For the insulated experiments, no significant effect on devolatilization time is observed for the investigated temperature and particle size range. The devolatilization time is only slightly higher at 805°C for particle sizes above 10mm. For the non-insulated experiments a slight effect of the temperature on the devolatilization time is observed, where a higher temperature yields a lower conversion time. However, this may also be due to a significantly higher gas velocity around the sample at 955°C than at 805°C (see Table 4-2), and consequently a higher mechanical interaction on the char layer and a higher convective heat transfer coefficient.

Effect of sample holder

For larger particle sizes, a significant effect of the sample holder type on the devolatilization time is observed. For a height of 5 mm the devolatilization time is similar in the two tested experimental sample holders, whereas for a height of 20mm the devolatilization time is about 750 seconds with insulation and about 300 seconds without insulation at 955°C. The experimental results show a significant effect of sample holder type, indicating that devolatilization of large tyre rubber particles via conversion pathway I accelerates the devolatilization rate compared to conversion via pathway E. However, as mentioned earlier, heating of the sidewalls distort this conclusion somewhat.

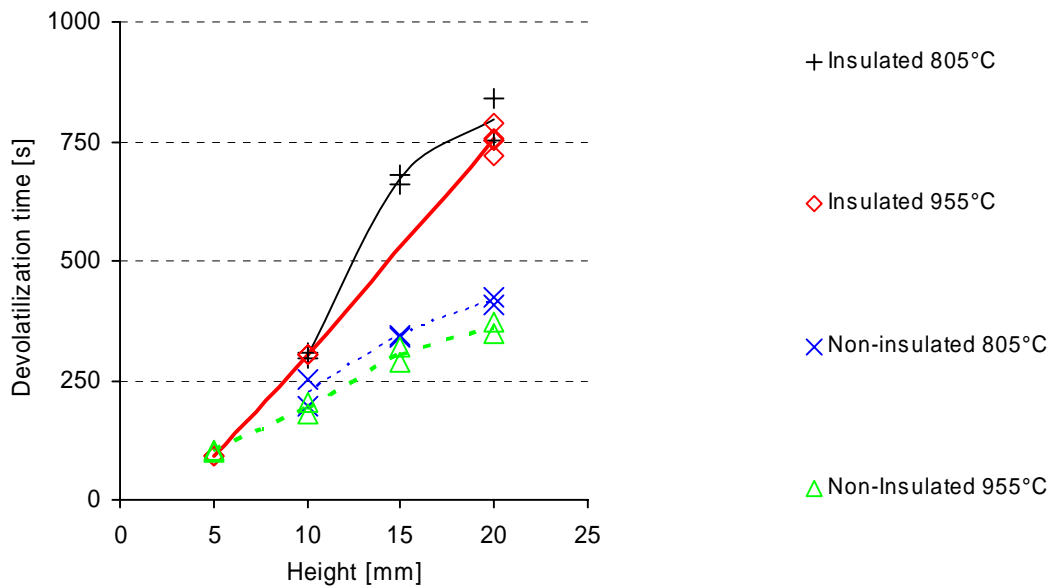


Figure 4-14: Results of flame devolatilization experiments. Insulated and non-insulated refer to experiments with and without sidewalls. Lines connecting average values inserted for clarity.

4.4.1.2 Tyre Rubber with Steel Wires

The effect of steel wires inserted into the tyre rubber on devolatilization time is clear from Figure 4-15. Again, double determinations verify the experimental results. It is observed, that the devolatilization time decreases from about 750 to 488 seconds upon inclusion of steel wires. This corresponds to a decrease of 35% and hence a significant effect of steel wires on devolatilization is observed.

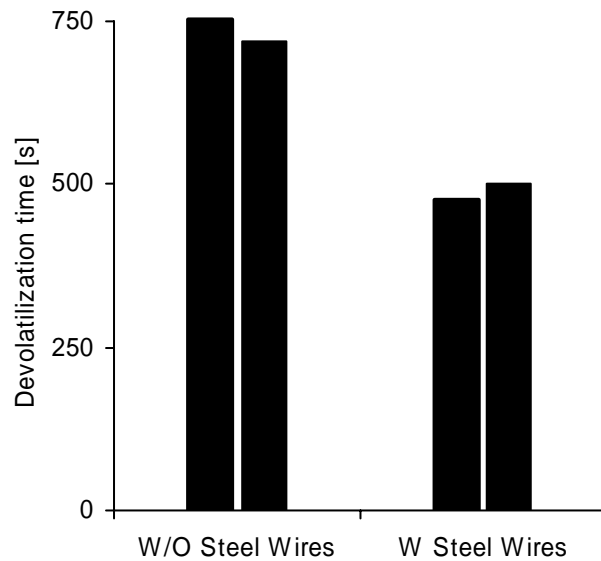


Figure 4-15: Measured devolatilization times with and without steel wires at 955°C and a height of 20mm in the flame devolatilization setup (insulated experiments).

4.4.2 Results of Macro-TGA Experiments

These sections contain the experimental results of methodology 4) of section 4.3.1.

4.4.2.1 Results with a Net Surrounding the Sample – Without Steel Wires

Figure 4-16 shows the experimental scale mass-loss, obtained with a net surrounding the tyre rubber particle during devolatilization, for four different cylindrical particle sizes of tyre rubber at different temperatures in inert atmosphere. The discontinuities observed in the experimental mass-loss curves are a consequence of the balance which has a minimum signal response of ± 0.1 g. Since the weight of a rubber sample can be down to 2 g, a small variation in the scale readout may cause significant changes in the calculated scale mass-loss. For the larger particles, the discontinuity diminishes because the particles have larger masses. The ultimate mass-loss observed in the macro-TGA experiments is observed to be approximately 0.65 and independent of particle size, i.e. a volatile content of approximately 65 wt.% which is in agreement with the proximate analysis (see Table 4-1). For the 7.5 mm particle, the ultimate mass-loss is observed to vary in the range 0.50 - 0.70, with a temperature of 840°C yielding the highest amount of volatiles and these variations are attributed to experimental uncertainties for the small sample masses. If the devolatilization time is defined as the time when the first derivative of the scaled mass-loss curve against time approaches zero, the effect of the surrounding temperature on devolatilization time is seen to be very significant for all particle diameters. For a particle with a

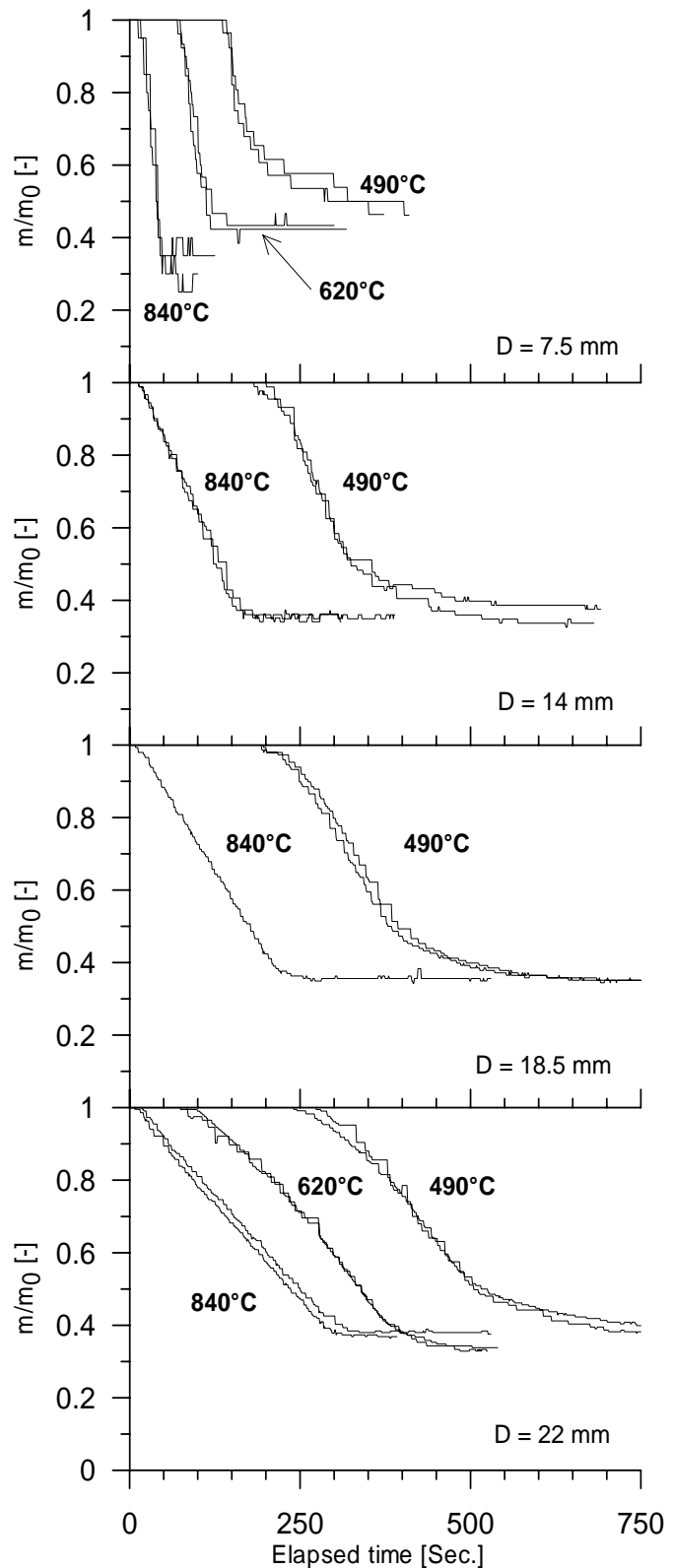


Figure 4-16: Experimental derived mass-loss against time of cylindrical tyre rubber particles surrounded by net in the sample holder.

diameter of 22 mm, the devolatilization time is observed to increase from approximately 300 seconds for a surrounding temperature of 840°C to approximately 400 seconds at 620°C and approximately 750 seconds at 490°C. The effect of particle size on the time of devolatilization is also significant. At 840°C, the time of devolatilization is observed to increase from approximately 75 to 300 seconds when increasing the particle diameter from 7.5 mm to 22mm. The shape of the mass-loss vs. time is observed to behave similarly. For the temperature of 840°C, the shape of the mass-loss curve is seen to be close to a straight line for all sizes, whereas the shape for the results at 490°C is seen to be more curved, and this behaviour is especially pronounced towards the end of the devolatilization process. Apparently each particle size yields approximately the same slope of the mass loss against time independent of temperature.

Figure 4-17 shows the measured temperature profiles at the particle centre and halfway between the centre and the particle surface during devolatilization for two particle sizes and surrounding temperatures of 490°C and 840°C. The graphs to the left show results for particles with a diameter of 14 mm and the graphs to the right represent particles with a diameter of 22 mm. It is observed that a higher surrounding temperature causes the intra-particle temperature to rise faster, and for all four conditions, the temperature asymptotically approaches the surrounding temperature with increasing time. The effect of size and surrounding temperature is also recognized in the temperature measurements via the penetration time, i.e. how long time it takes before the thermocouple in the centre registers the external heat flux. For both particle sizes, it is observed that increasing the surrounding temperature decreases the penetration time. For increasing particle size, at constant surrounding temperature, the penetration time increases. A temperature difference is observed between the two measurement positions for all sizes and surrounding temperatures, demonstrating a presence of an intra-particle temperature gradient. Finally, an interesting observation from all the transient temperature measurements is the temperature rise initiating when the local temperature approaches 400°C. This temperature rise is especially pronounced at the centre of the particle.

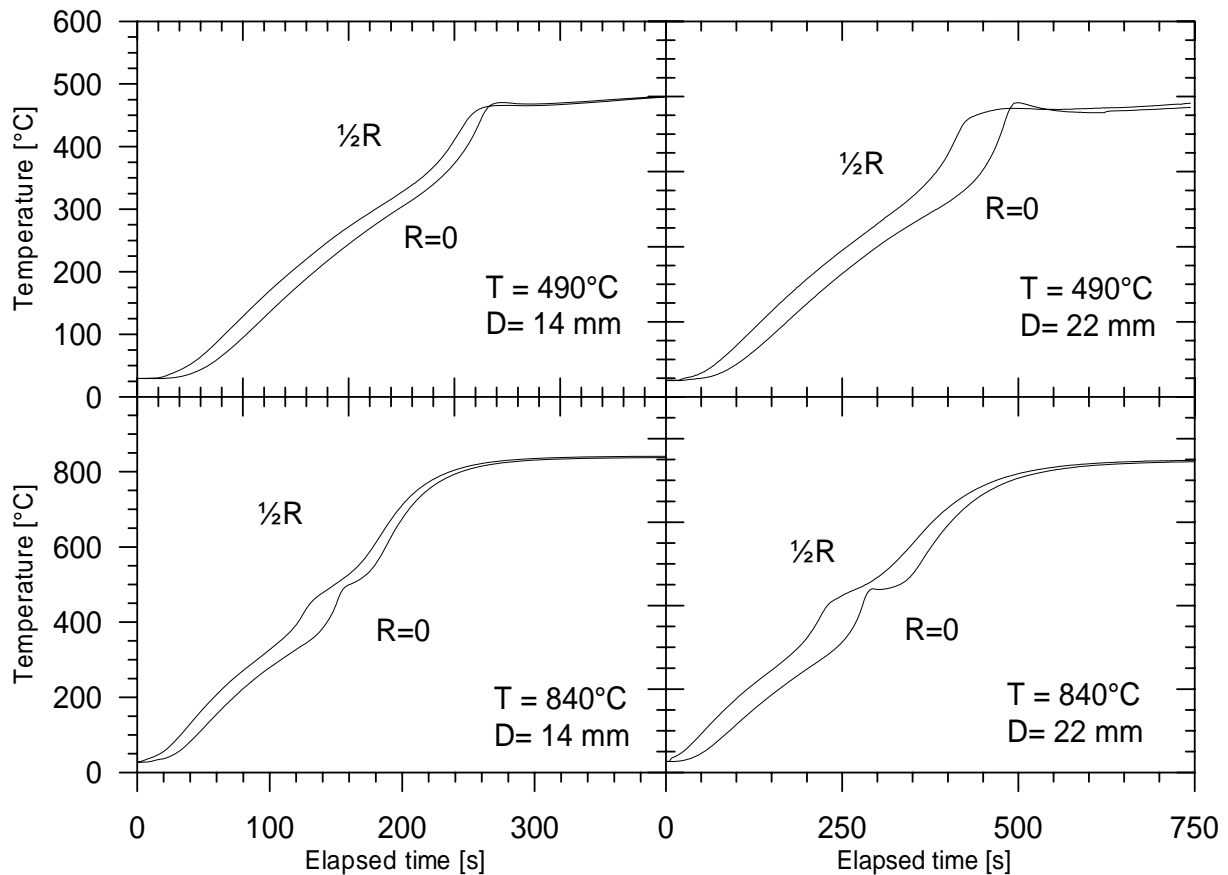


Figure 4-17: Measured transient temperature profiles during devolatilization of tyre rubber at the positions at $r=0$ and $r=\frac{1}{2}R_0$.

4.4.2.2 Results with a Net Surrounding the Sample – With Steel Wires

In order to investigate the effect of steel wires on devolatilization mass loss rate and time, experiments were made with tyre rubber cylinders with diameters of 14 and 22mm at 840°C (see also Figure 4-13). The results of these experiments are shown in Figure 4-18 together with the corresponding results without steel wires. Firstly, double determinations are observed to verify the experimental results. It is observed that the initial mass loss is faster without steel wires and this effect is most distinct at the particle diameter of 22 mm. As time progresses the mass loss rate with steel wires increases compared to without steel wires. This results in lower devolatilization time for the particles with steel wires. Inclusion of steel wires for the particle size of 14 mm lowers the devolatilization time from about 176 to 146 seconds, i.e. a decrease of about 17%. For a particle with a diameter of 22 mm, the devolatilization time is reduced from about 331 to 291 seconds corresponding to 12%. In the flame devolatilization experiments, a 35 % decrease in devolatilization time was observed, i.e. significantly higher.

The mechanism for the observed initial slower mass loss and the later fast mass loss for the particles with inclusion of steel wires is given in section 4.5.7 as well as an examination of the differences observed in decrease of devolatilization time.

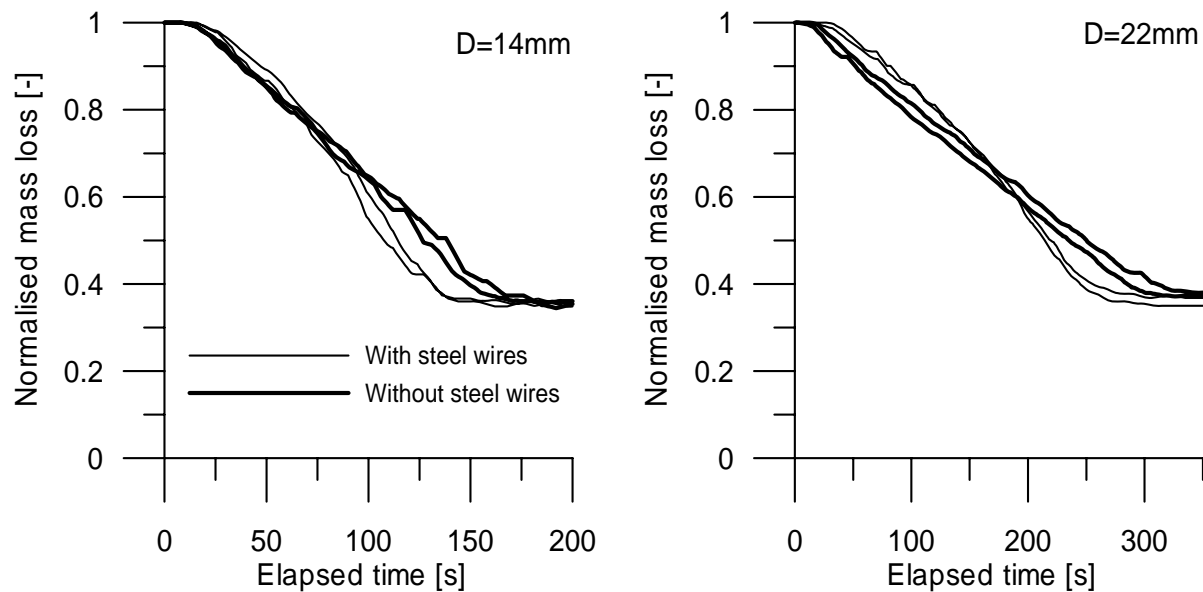


Figure 4-18: Experimental mass loss results of tyre rubber with and without steel wires at 840°C (normalised by rubber mass).

4.4.2.3 Results without a Net Surrounding the Sample – Without Steel Wires

The experimental results for two particle sizes of 14 and 22mm with and without the surrounding net at 840°C are shown in Figure 4-19. For experiments without net, larger discontinuities are observed than with net. This is due to 1) the mass of the net not stabilising the recorded weight as much as with the net, and 2) a consequence of the possibility of particles being able to break off and thereby influence the recorded mass loss (see also Figure 4-11).

For the 22mm particles, the mass loss rate is slightly higher without than with the net, up to a mass loss of about 57% ($m/m_0=0.43$). At this point the mass drops drastically for the sample without the net, indicating that large char fragments are removed from the sample discontinuously. After about 300 seconds, the mass of the 22 mm particles remains almost constant throughout. A similar trend is observed for the 14 mm particles, except that the drastic loss of char fragments initiates at a lower mass loss of about 30% ($m/m_0=0.70$). It drops to a mass loss of about 88% ($m/m_0=0.12$).

The results of these investigations show evidence of pathway I. However, they do not provide reliable mass loss rates, as a non continuous char removal process was seen to dominate, where larger char fragments seem to fall off. Experimental data obtained at a temperature of 480°C reveals the same trend (not shown).

The removal of large char fragments is attributed to the sample geometry, a high length to diameter ratio being aimed at, and consequently there is greater susceptibility to collapsing than at a lower length to diameter ratio. This is also verified by the experimental data, which shows that the 14mm particle collapses earlier than the 22 mm particle.

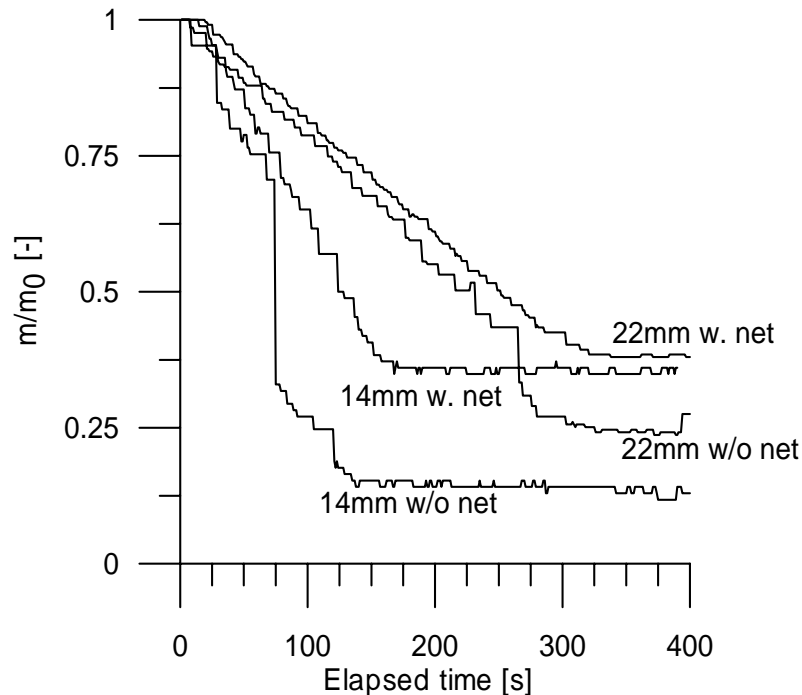


Figure 4-19: Experimental macro-TGA results for 14 and 22 mm cylinders with or without surrounding net obtained at 840°C.

4.4.3 Conclusions on Experimental Investigations

Experiments in the flaming devolatilization setup demonstrated a significant effect of particle size on devolatilization time, an increased particle size leading to increased devolatilization time. For devolatilization pathway E, no significant effect of surrounding temperature on devolatilization time in the temperature range of 805-955°C was found in this experimental setup. However, the measured devolatilization time through pathway I (crackling) was influenced by temperature. Inclusion of steel wires in tyre rubber converted via pathway E decreased the devolatilization time by 35% compared to without steel wires for a height of 20mm. Finally, devolatilization via conversion pathway I showed a significantly lower devolatilization time for larger particle sizes than these particles converted via pathway E. For smaller particles, the two conversion pathways yielded the same results.

In the experimental macro-TGA setup, the effect of particle size and surrounding temperature on the rate of devolatilization was observed to be significant, i.e. larger particle diameters and lower temperatures increased the devolatilization time. Furthermore, the effect of steel wires on the devolatilization time was found to be significant with a decrease in devolatilization time by 12 and 17% for the 22 and 14mm particle, respectively. Finally, investigating the effect of devolatilization pathway proved the existence of conversion pathway I, but this experimental setup was found inadequate to quantify devolatilization rates/times, as the particles collapsed during the experiments due to their relatively high length to diameter ratio.

4.5 Model Analyses of Tyre Rubber Devolatilization

The aims of this section are to develop and verify mathematical models for devolatilization mass loss behaviour of large particles of tyre rubber with and without steel wires. The models are to be used for analyses of TDF devolatilization rates under conditions similar to cement kiln systems.

Two models are developed to analyse the experimental data for devolatilization conversion via pathway E, and one model is developed for investigation of pathway I. As the macro-TGA did not yield reliable data regarding pathway I and the data of the flaming devolatilization setup was susceptible to heating at the sides, it was not possible to validate the model for this pathway.

Several mathematical models for the devolatilization of large particles with char layers have been published (reaction pathway E of Figure 4-3); however most of these models concern the devolatilization of biomass or coal. To the author's knowledge only Yang et al. [15] consider modelling of devolatilization of large tyre rubber particles. Mathematical models for the devolatilization of large particles include coupled, non-linear, ordinary and partial differential equations. The solution approaches found in the literature may be divided into three classes:

- 1) Via suitable assumptions and reductions of the original equations, the resulting equation(s) may be solved analytically, e.g. see Kanury [28].*
- 2) Integral models [29] where heat transfer is assumed to be the rate controlling parameter and the spatial transient temperature profile is assumed to be a known function, e.g. polynomial or linear, which upon substitution into the original partial differential equation reduces to a system of ordinary differential equations [30,31,32].*
- 3) Solution of ordinary- and partial differential equations via finite approximation methods [33,34].*

In the models presented in this work, heat transfer and chemical reaction kinetics are assumed to be the rate controlling parameters for the devolatilization process, whereas resistance to mass transport is assumed to be negligible. In the literature, these assumptions are also successfully used in the modelling of devolatilization mass-loss rates and conversion times by Chern and Hayhurst [35], Adesanya and Pham [36] and Wildegger-Gaissmaier and Agarwall [37] in their modelling of coal devolatilization and by Galgano and Di Blasi to model devolatilization of both dry [31] and wet [32] biomass. Grønli and Melaan [34] argue that the internal mass transfer during the devolatilization has negligible influence on the spatial temperature profile for biomass. The mass transport influences the residence time distribution of outflowing pyrolysis products and consequently influences the secondary pyrolysis reactions.

4.5.1 Devolatilization Model A: Nusselt Shrinking Core Model ³⁸

This model simulates devolatilization conversion via pathway E. The virgin fuel is assumed to decompose instantaneously to char and volatiles once it reaches a predefined devolatilization temperature, T_D (See Figure 4-20). It is further assumed that:

- 1) *The volatile products are transported through the char layer without heat exchange with the hotter char.*
- 2) *The conductivity, specific heat capacity as well as density of the char and virgin fuel layers are assumed to be identical and constant.*
- 3) *The particle does not swell, i.e. the outer position of the surface remains constant.*
- 4) *The devolatilization process is energy neutral*

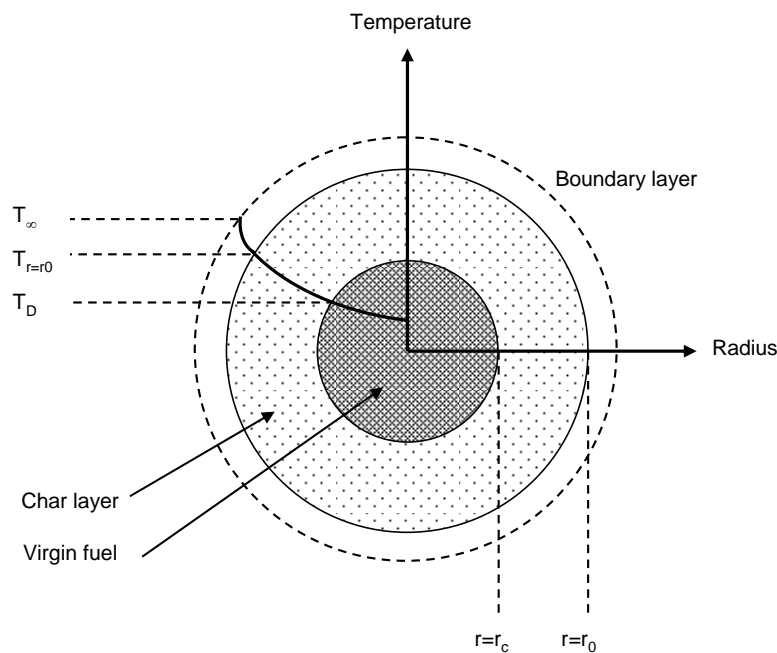


Figure 4-20: Partially devolatilized sphere (or cylinder axial view) and nomenclature in Nusselt shrinking core model for devolatilization.

With these assumptions, the resulting devolatilization model is reduced to derivation of the transient spatial temperature profile through the particle. Subsequently, the position of the unreacted core with a predefined devolatilization temperature is tracked, and from its position, the devolatilization conversion may be derived. The transient temperature distribution in the solid may be described by the following partial differential equation [39]:

$$\rho \cdot c_p \frac{\partial T}{\partial t} = \frac{1}{r^s} \frac{\partial}{\partial r} \left(k \cdot r^s \frac{\partial T}{\partial r} \right) \quad (4-1)$$

where s is the shape factor ($s=0$ for plate, $s=1$ for cylinder and $s=2$ for sphere), ρ is the density, c_p is the specific solid heat capacity and k is the thermal conductivity. If they are assumed constant, (4-1) may be rewritten as:

$$\frac{\partial T}{\partial t} = \frac{k}{\rho c_p} \frac{1}{r^s} \frac{\partial}{\partial r} \left(r^s \frac{\partial T}{\partial r} \right) \quad (4-2)$$

The initial (IC) and boundary (BC) conditions for the partial differential equation are:

$$\text{IC1 : } T(t = 0, r) = T_0 \quad (4-3)$$

$$\text{BC1: } k \frac{\partial T}{\partial r} \Big|_{r=r_0} = h_{\text{eff}} (T_\infty - T_{r=r_0}) \quad (4-4)$$

$$\text{BC2: } \frac{\partial T}{\partial r} \Big|_{r=0} = 0 \quad (4-5)$$

IC1 states that the initial spatial temperature profile is uniform, BC1 states that heat transferred to the external surface is transported into the material by conduction and finally BC2 states that the particle is symmetric around the particle centre. The effective heat transfer coefficient may include both radiation and convection.

The model is made dimensionless and solved numerically using orthogonal collocation (see appendix A) and the devolatilization temperature is subsequently tracked for each time step, using linear interpolation between the node values of the collocation procedure. The devolatilization conversion (4-6) and scaled mass loss (4-7), for comparison with experimental results, may then be derived from the position of the core, r_c , and the volatile content, V :

$$X(t) = 1 - \left(\frac{r_c(t)}{r_0} \right)^{s+1} \quad (4-6)$$

$$\frac{m(t)}{m_0} = 1 - X(t) \cdot V \quad (4-7)$$

The Nusselt model of devolatilization is based on a series of assumptions that causes the model to deviate from real solids undergoing devolatilization:

- 1) *Single pyrolysis reactions are not infinitely fast, but their rate is usually dependent on temperature and concentration.*
- 2) *More than one reaction may often be responsible for the solid decomposition.*
- 3) *Independent pyrolysis reactions may be endo- or exothermic.*
- 4) *Decomposition of the solid may alter the physical properties of the solid.*
- 5) *Outward volatile flux may cool the hotter char matrix.*

4.5.2 Devolatilization Model B

In this model (conversion pathway E), the solid matrix is assumed to consist of constant char and ash fractions as well as a varying volatile part made of up to 3 subfractions. The reaction scheme for the devolatilization process is assumed to consist of up to 3 independent parallel reactions where the solid is volatilised forming gas in a single step according to (4-8). The gas produced during the solid decomposition of the different fractions is assumed to behave identically and to have same specific heat capacity.



The solid is assumed to decompose according to the following first order volumetric Arrhenius decomposition rate:

$$R_i = \frac{dx_i}{dt} = -A_i \exp\left(-\frac{E_i}{R_g T}\right) x_i, \quad i = 1, 3 \quad (4-9)$$

where x_i is the mass fraction of the volatile component, i , based on initial mass (see nomenclature). Because the temperature may vary with position in the large particle, the rate of decomposition may differ in the particle centre from a position closer to the surface. Therefore an energy balance is needed to account for the temperature variation. If the outflow of volatile gasses is in thermal equilibrium with the surrounding solid, the complete energy balance with heat transport in one direction becomes:

$$\left(\rho_{solid} c_{p,solid} + \rho_{gas} c_{p,gas}\right) \frac{\partial T}{\partial t} + c_{p,v} m_v \frac{\partial T}{\partial r} - \frac{1}{r} \frac{\partial}{\partial r} \left(k \cdot r^s \frac{\partial T}{\partial r}\right) - \rho_{vf} \sum_{i=1}^3 R_i \Delta H_i = 0 \quad (4-10)$$

The first term represents accumulation of energy, the second term convective outward transport of energy, the third term conduction of energy and the fourth term heat effects of reactions. A reduction of (4-10) may safely be performed acknowledging that $\rho_{solid} c_{p,solid} \gg \rho_{gas} c_{p,gas}$ which yields:

$$\rho_{solid} c_{p,solid} \frac{\partial T}{\partial t} + c_{p,v} m_v \frac{\partial T}{\partial r} - \frac{1}{r} \frac{\partial}{\partial r} \left(k \cdot r^s \frac{\partial T}{\partial r}\right) - \rho_{vf} \sum_{i=1}^N R_i \Delta H_i = 0 \quad (4-11)$$

The initial and boundary conditions for (4-11) are identical to those of model A (see (4-3) to (4-5)). The outflow of volatiles accumulates towards the particle surface, since volatiles released closer to the particle centre flow towards the particle surface where decomposition reactions may further contribute to the volatile flux. A differential mass balance yields:

$$-\frac{d}{dr}(r^s \cdot m_v) = r^s \rho_{vf} \sum_{i=1}^3 R_i \quad (4-12)$$

Upon integration the volatile flux at a given position, r' , is:

$$m_v(r') = -\rho_{vf} \left(\frac{1}{r'}\right)^s \sum_{i=1}^3 \int_0^{r'} r^s \cdot R_i dr \quad (4-13)$$

During the progress of the devolatilization, the physical structure of the solid changes, and therefore, the thermal conductivity and the specific heat capacity also change. In order to describe the change of physical parameters, a local devolatilization conversion is introduced:

$$X_{local}(r) = 1 - \frac{\rho(r) - (1-V)\rho_{vf}}{V\rho_{vf}} \quad (4-14)$$

and from the local devolatilization conversion, the effective thermal conductivity and effective heat capacity of solid is obtained:

$$k(r) = (1 - X_{local})k_{vf} + X_{local}k_{char} \quad (4-15)$$

$$c_{p,solid}(r) = (1 - X_{local})c_{p,vf} + X_{local}c_{p,char} \quad (4-16)$$

The total devolatilization conversion, X , is determined from (4-17) and the scaled mass loss for experimental validation is derived using (4-7).

$$X(t) = 1 - \frac{\text{mass of volatiles at } t}{\text{mass of volatiles at } t = 0} = 1 - \frac{2^s \int_0^{r_0} r^s (\rho(r) - (1-V)\rho_{vf}) dr}{r_0^{s+1} V \rho_{vf}} \quad (4-17)$$

Equation (4-11) is discretized and solved together with the remaining equations using an implicit finite difference method. The obtained solution was tested and found to be independent of applied spatial discretization points and time step.

4.5.3 Devolatilization Model C

This model simulates the shrinking particle during devolatilization (devolatilization pathway I) and may be the situation 1) when the char layer is removed continuously and hence exposes a fresh virgin fuel layer, or 2) for a solid fuel where the volatile content approaches 100% and the particle shrinks during devolatilization due to surface volatilisation, e.g. plastic. In this model, it is assumed that the outer surface constitutes an infinitely thin reaction front surrounded by virgin fuel at the particle side and devolatilization products at the other side. Consequently, it constitutes a limiting case for TDF devolatilization as the char removal is not expected to follow a thin front, but rather a front of a few mm, as the formed char particles are in the mm size (see also section 5.3)

Mathematically, this model is to solve the transient temperature profile through the particle accounting for the coupled movement of the surface. The assumptions in this model are:

- 1) *A single pyrolysis reaction is responsible for the surface decomposition and its rate may be described with a first order Arrhenius rate expression.*
- 2) *The physical properties are assumed constant at all intra-particle positions and identical to that of the virgin fuel.*

An expression for the movement of the surface is obtained by setting up a shell balance for the particle to obtain the differential equation:

$$\frac{d}{dr}(r^s v) + r^s R = 0 \quad (4-18)$$

Here v is the velocity of the retracting surface and R is the volumetric rate of reaction. Integration within limits and substituting R with the following Arrhenius first order expression gives:

$$\frac{dr_{surf}(t)}{dt} = -\frac{1}{r_{surf}^s} \int_0^{r_{surf}} r^s R dr \quad (4-19)$$

The heat transport model for the virgin fuel particle is identical to that of models A and B, except for boundary condition BC1*, that has to be evaluated at the moving outer particle surface. In addition, the initial condition accounts for the initial position of the retracting surface. The conversion is at all times determined using equation (4-6) with with $r_c=r_{surf}$.

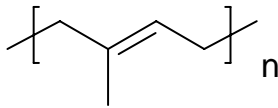
$$\text{IC2 : } r_{surf}(t=0) = r_0 \quad (4-20)$$

$$\text{BC1* : } k \frac{\partial T}{\partial r} \Big|_{r=r_{surf}} = h_{eff} (T^\infty - T_{r_{surf}}) \quad (4-21)$$

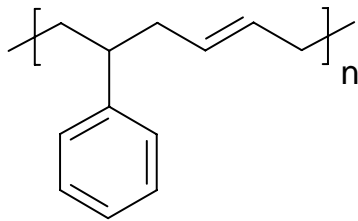
The solution is accomplished using orthogonal collocation (see appendix A) and complicated by the moving outer particle surface.

4.5.4 Model Parameters - Physical and Chemical Properties of Tyre Rubber

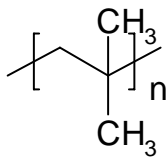
Besides steel and tread, TDF consist mainly of natural rubber, styrene-butadiene rubber and butyl-rubber (See Figure 4-21). These polymers are vulcanized in matrix with carbon black as filler [8,40].



Natural Rubber (NR)



Styrene Butadiene Rubber (SBR)



Butyl rubber (BR)

Figure 4-21: Structural units of common polymers used in manufacturing tyre rubber

Micro Thermo Gravimetric Analysis (TGA) and the corresponding derived mass-loss (DTGA) are used to investigate the thermal decomposition behaviour of the tested tyre rubber and to verify the employed kinetic scheme. The results of the experimental TGA as well as the derived DTGA, are shown in the lower part of Figure 4-22, together with a model fit with the applied Arrhenius parameters (see Table 4-3). The TGA model fit against temperature is obtained by substitution of the independent variable with temperature in (4-9) using the applied micro-TGA heating rate:

$$\frac{dx_i}{dT} = -\frac{1}{\text{Heating rate}} A_i \exp\left(-\frac{E_i}{R_g T}\right) x_i, \quad i = 1, 3 \quad (4-22)$$

and subsequently integrating the coupled set of differential equations using the initial mass fractions of Table 4-3 as initial conditions. The TGA and DTGA results are derived using:

$$TGA = x_{char} + x_{ash} + \sum_i x_i, \quad i = 1, 3 \quad (4-23)$$

$$DTGA = -\sum_i \frac{dx_i}{dt}, \quad i = 1, 3 \quad (4-24)$$

The upper part Figure 4-22 shows a Differential Scanning Calorimetric (DSC) curve for the tyre rubber tested. From the DTGA, at least three fractions are observed to decompose with three peaks in the mass-loss around 295°C, 380°C and 475°C, respectively. For temperatures exceeding approximately 510°C no more volatiles are observed to escape at the applied heating rate. It is also noted that the ultimate volatile content in Table 4-1, is identical to the ultimate value from the micro-TGA experiment. Yang et al. [8] have investigated the DTGA behaviour of straight pure elastomers of natural rubber (NR), styrene-butadiene-rubber (SBR) and butyl-rubber (BR). They found that each pure compound decomposed with two peaks in the TGA where the peak at the low temperature could be attributed to the processing oils for the respective polymer followed by a major peak representing the polymer. Yang et al. also observed that NR decomposed with a maximum mass-loss around 376°C, BR started to decompose around 350°C with a maximum mass-loss at approximately 465°C and SBR decomposed over a broad temperature interval with a maximal peak mass-loss at 450°C.

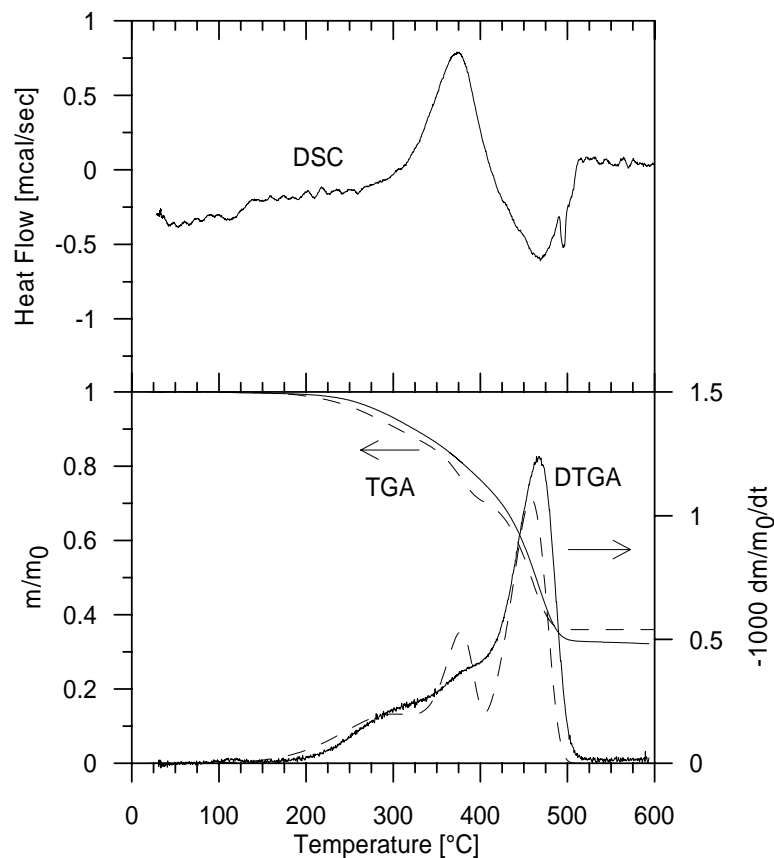


Figure 4-22: Differential Scanning Calorimetric (DSC), Thermo- (TGA) and Derivate (DTGA) Gravimetric results of the tested tyre rubber. Results are obtained at a heating rate of 10°C/min in inert atmosphere for an initial sample mass of 6.05 mg. The solid lines represent measured results and the dashed lines represent model fits.

Parameter		Model			Value(s)	Unit	Reference
		A	B	C			
Virgin fuel density	ρ_{vf}	√	√	√	1100	kg/m ³	Measured
	$x_{1,0}$		√		0.15	kg/kg	From TGA in present work
Initial mass fraction of volatile specie i.	$x_{2,0}$		√	√	0.13	kg/kg	do
	$x_{3,0}$		√		0.36	kg/kg	do
	A_1		√		100	1/s	Modified ^a value for oil fraction from [41] (original 668s ⁻¹)
Pre-exponential factors and Activation energies	E_1		√		49.1	kJ/mol	Value for oil fraction from [41]
	A_2		√	√	$3.93 \cdot 10^{14}$	1/s	Value for NR from [41]
	E_2		√	√	207	kJ/mol	do
	A_3		√		$1.05 \cdot 10^{13}$	1/s	Value for BR from [41]
	E_3		√		212	kJ/mol	Modified ^a value for BR from [41] (original 215 kJ/mol)
	ΔH_1			√	~0	kJ/kg	From DSC in this study
Reaction enthalpies	ΔH_2		√		-1200	kJ/kg	do
	ΔH_3		√		350	kJ/kg	do
	$c_{p,v}$		√		2400	J/kg/K	[15]
Specific heat capacity of volatile gas			√				
Specific heat capacity of virgin fuel	$c_{p,vf}$	√	√	√	2000	J/kg/K	[42]
Specific heat capacity of char	$c_{p,char}$		√		1800	J/kg/K	[15]
Conductivity of virgin fuel	k_{vf}	√	√	√	0.30	W/m/K	[41]
Conductivity of char	k_{char}		√		0.20	W/m/K	[15]
Devolatilization temperature(s)	T_D	√			400 or 500	°C	Estimated from TGA

Table 4-3: Physical and chemical parameters used in the model calculations. a) Modifications are made according to the model fit of the TGA/DTGA curve in Figure 4-22.

In this study, the observed temperatures for peak mass losses (see DTGA in Figure 4-22), suggest that the peak at approximately 475°C may be attributed to BR decomposition, whereas the peak observed at 380°C may be attributed to both NR and SBR decomposition. The chosen kinetic scheme in this study is observed to predict the TGA and DTGA for the fractions released at the low and high temperatures, whereas larger discrepancies exist for the middle fraction. Finally, the DSC curve reveals a heat release at 380°C, and heat consumption at 475°C. The two major peaks on the DSC curve are observed to be at temperatures coincident with the peaks in the DTGA curve, i.e. the heat effects can be regarded as effects of the decomposition reactions. The observed exothermic and endothermic reaction behaviour observed here is identical to the results of Yang et al. [15] and Chen and Qian [43]. Integration of the DSC curve yields the reaction enthalpies for the two reactions: -1200 kJ/kg and 350 kJ/kg for the second and third peaks, respectively.

A devolatilization temperature is needed for the Nusselt shrinking core model. From the TGA it is observed that at about 500°C, no more volatiles are present and this temperature may therefore be a suitable choice. However, conceivably the exothermic reaction just below 400°C may be sufficient to raise the temperature locally and induce the onset of reaction 3. It will later be shown using model B, that this is actually the case. Consequently, 400°C may also be a suitable choice for the devolatilization temperature of tyre rubber. For model C, the Arrhenius parameters of reaction 2 are applied as this exothermic reaction induces the onset of reaction 3 (see the sensitivity analysis of model B in appendix C). The remaining physical parameters used in the simulations as well as the data used in each particular model are shown in Table 4-3 (See appendix B for effective heat transfer coefficients).

4.5.5 Comparison of Model A, B and C with Flaming Devolatilization Exp. Results

Conversion Pathway E

The predicted devolatilization time using models A and B and a comparison with the experimental data are shown in Figure 4-23. Good agreement is observed between model A and the experimental data, for a surrounding temperature of 955°C and up to a particle height of 10mm. However, the models over-predict the devolatilization time for all other conditions. A slight effect of temperature on devolatilization time is predicted by the models, but not rediscovered in the experimental findings. Furthermore, the increase in devolatilization time is almost linear from the experimental results, whereas the models predict the devolatilization time to increase more than linearly with particle height.

The discrepancies between the models and the insulated experimental results, are most significant for the large particles, and may be attributed to the following:

- 1) *Unrealistic models*
- 2) *Flame radiation neglected in the model calculations.*
- 3) *Heating from side walls and bottom, i.e. the sample was not perfectly insulated.*

The effect of 1) is considered unimportant, due to the models being accurate in modeling of devolatilization behaviour loss in the macro-TGA experimental setup (see also section 4.5.6). The effect of 2) is most important for small particle heights, due to their being closer to the regime of external heat transfer control than for larger particles. It may be shown, using model calculations, that a high flame radiation intensity ($T_{\text{flame}} = 1500^{\circ}\text{C}$ and $\epsilon_{\text{flame}}=1$), cannot account for the observed discrepancies between the model and experimental data for particle sizes about 15 mm and above, i.e. the devolatilization process is almost exclusively controlled by internal heat transfer. Hence, neglecting of flame radiation cannot explain the discrepancies between the model and experimental data for particle heights above about 15 mm. For the particle height of 10mm, the neglecting of flame radiation can be shown to account for the discrepancies between model and experimental data. Finally, the effect of 3)

is most pronounced for higher times and may therefore partly be used to explain the observed discrepancies.

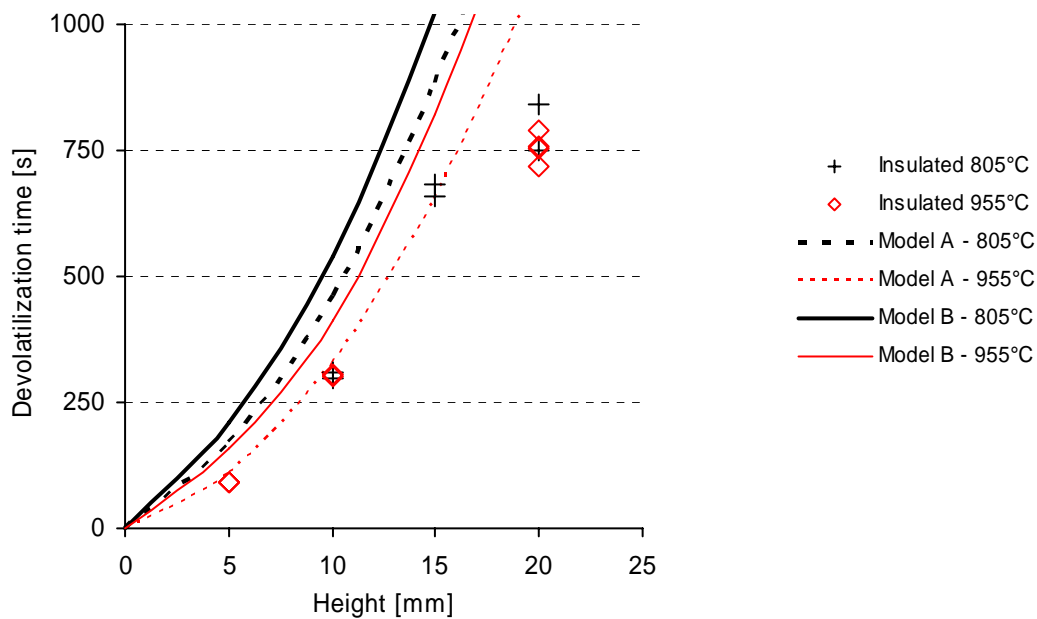


Figure 4-23: Results of flaming devolatilization experiments and comparison with model calculations of models A and B. The devolatilization time is assessed at 99% devolatilization conversion. A devolatilization temperature of 400°C is applied in Model A.

Conversion Pathway I

A comparison between experimental results and model C is shown in Figure 4-24. At a temperature of 805°C the model is observed to overpredict the devolatilization time, whereas at a temperature of 955°C, the model underpredicts the devolatilization time. The discrepancies between the experimental data and the model-predicted devolatilization time are most pronounced at 955°C.

The discrepancies between the model predictions and the experimental data is not a consequence of the neglected flame radiation, as the model predicts a shorter devolatilization time at 955°C and a longer devolatilization time at 805°C, than observed in the experiments. The discrepancies between the model and experimental data may be attributed to the following:

- 1) *The experimental uncertainties regarding heating from the sides*
- 2) *The model, and in particular the assumption of an infinitely thin reaction front*

In order to assess the effect of 1), a different experimental setup resembling a 1-dimensional specimen was to be used. This was sought in the experimental macro-TGA setup, but proved to yield other problems with the previously described loss of large char fragments. The effect of 2) may also influence the model results, as the devolatilization of large TDF particles

cracks at the outer surface rather than a continuous thin devolatilization front as assumed in the model.

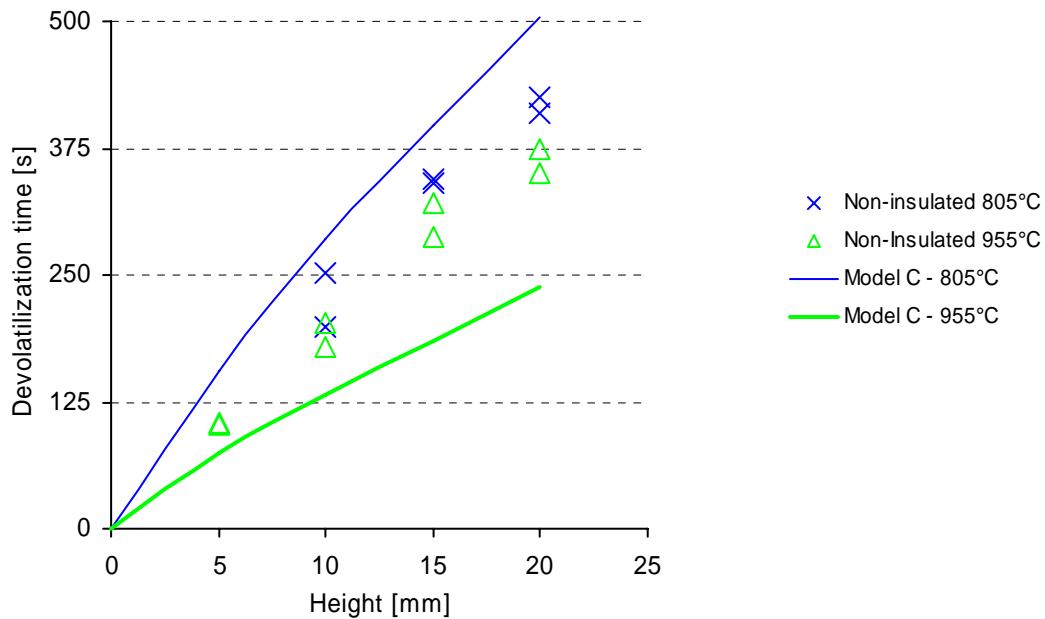


Figure 4-24: Results of flaming devolatilization experiments and comparison with results of model C. The devolatilization time is evaluated at 99% devolatilization conversion.

4.5.6 Comparison of Model A and B with Experimental Macro-TGA Results

This section contains a comparison between model predictions of models A and B with experimental macro-TGA data. No comparisons with model C are shown due to the lack of reliable data (see also section 4.4.2).

4.5.6.1 Mass Loss

Comparisons of the experimental mass loss and the results of models A and B are shown in Figure 4-25. Model A and $T_D = 400^\circ\text{C}$ results predict a mass loss against time that is shifted towards lower times than $T_D = 500^\circ\text{C}$. At a surrounding temperature of 840°C , both devolatilization temperatures predict the experimental mass loss well. At increasing particle size, however, the model results with $T_D = 500^\circ\text{C}$ deviate more from the experimental data than with $T_D = 400^\circ\text{C}$. This trend is even more pronounced for the 22mm particle and a surrounding temperature of 620°C , where significant discrepancies exist between model A ($T_D = 500^\circ\text{C}$) and the experimental results. Overall agreement exists between Model A and the experimental results using a devolatilization temperature of 400°C . The validity of model A with regard to mass loss prediction seems to increase with temperature. It should be noted that no results are obtained of model A with a devolatilization temperature (TD) of 500°C at a surrounding temperature of 490°C , due to the material never being heated above this temperature at these conditions.

For model B and a surrounding temperature of 840°C for the 14, 18.5 and 22 mm particles, the experimental and predicted scale mass losses are in good agreement, while at 620°C and for a diameter of 22 mm they are in excellent agreement. At 490°C and for particles with a diameter between 14-22 mm, the predicted mass loss is observed to initiate slightly faster than the experimental data. For prolonged times, the predicted mass loss curve is observed to cross the experimental curve. However, the predicted devolatilization time is seen to be in agreement with the experiments.

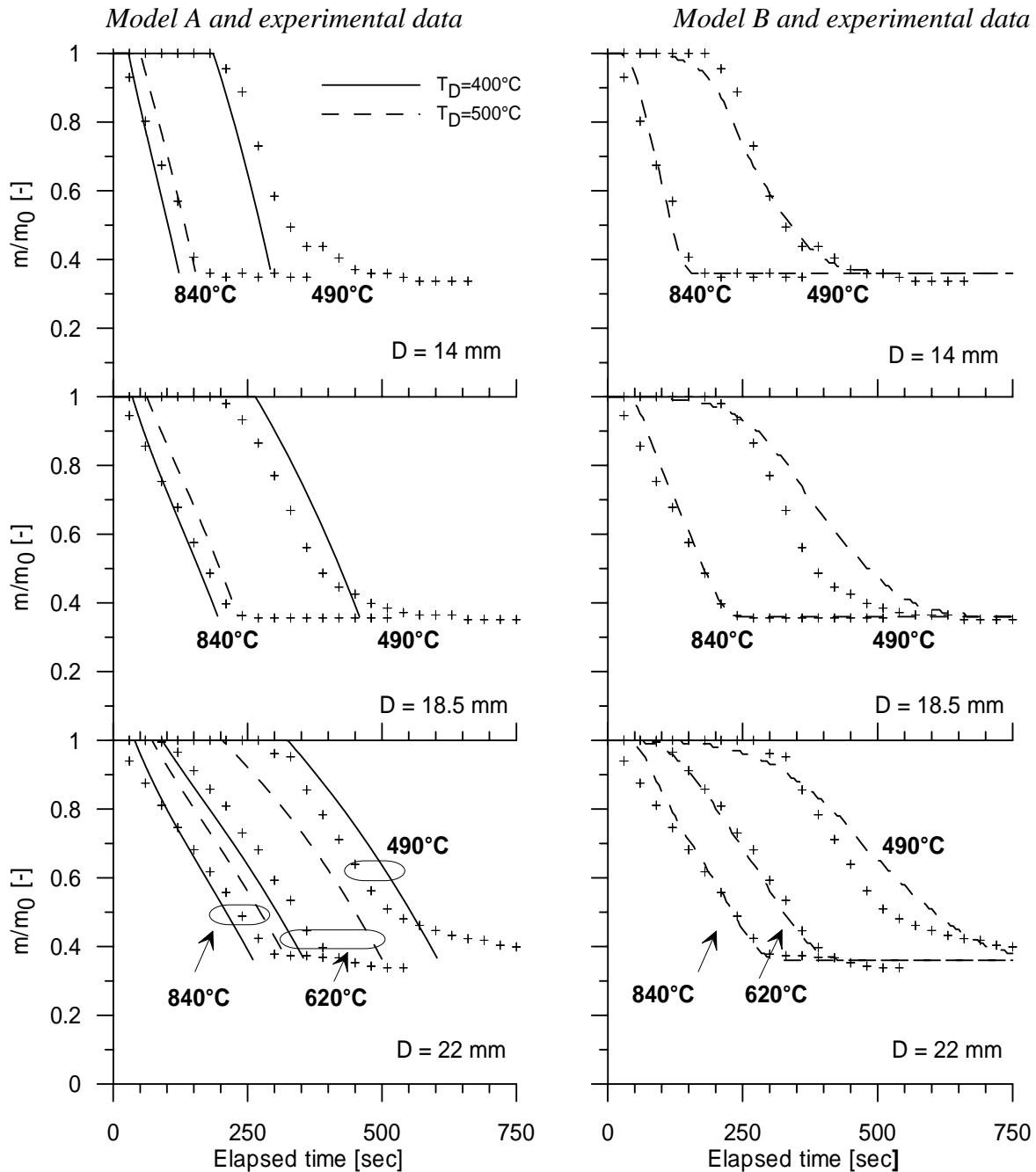


Figure 4-25: Comparison of measured (macro-TGA) and modelled mass loss for cylindrical tyre rubber cylinder particles at three particle sizes and three temperatures. Lines represent model results and symbols represent measured values.

4.5.6.2 Temperature Response

A comparison between the predicted and the measured temperature profiles at the particle centre and halfway between the centre and the surface is shown in Figure 4-26. Initially, both models predict the same temperature response, which is a consequence of the inert heating that initially takes place in model B. As expected, model A cannot predict the experimentally observed temperature rise initiating slightly below 400°C, due to the fact that it is a non reactive heat transport model.

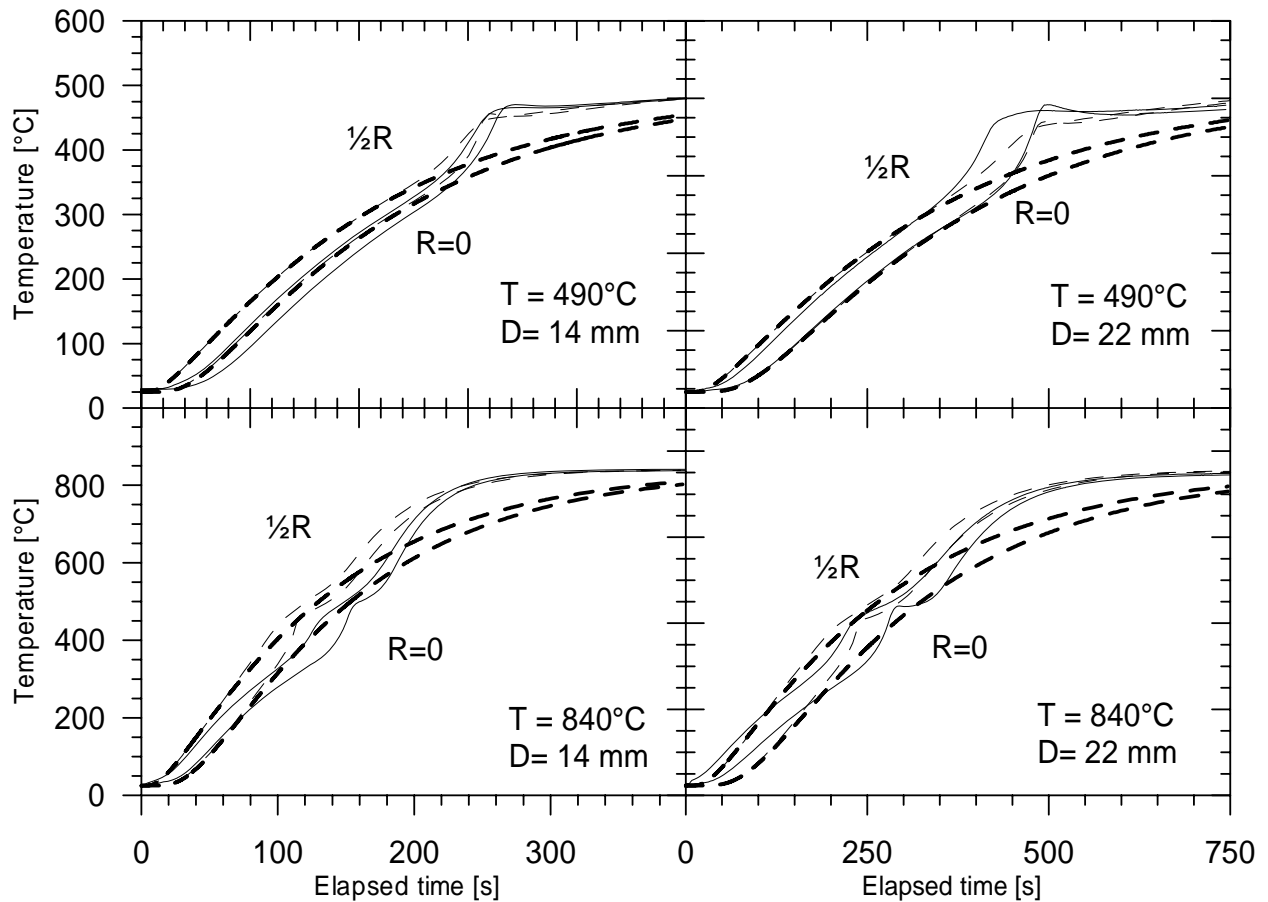


Figure 4-26: Comparison of modelled and experimentally measured transient temperature response for 2 particle diameters and 2 temperatures. Experimental results (full line), Model A (dashed) and Model B (bold dashed).

For model B, however, the predicted temperature response agrees with the experimental data for all four conditions. The model is also observed to be able to predict the experimentally observed peak in temperature initiating just below 400°C and reproduce the higher peak temperature response, in the centre, for all examined sizes.

Based on simulations using model B for a surrounding temperature of 490°C, the observed temperature rise initiating somewhere below 400°C, can be shown to be a consequence of the exothermic reaction enthalpy of reaction 2. The temperature rise is not a consequence of sudden changes in specific heat capacity of the solid material, when converted from virgin fuel to char. This can be shown in the model calculation by neglecting the reaction enthalpies and lowering the specific heat capacity for char to 1000 J/kg/K and observing that the

temperature peak is not present. For the surrounding temperature of 840°C, the resulting temperature rise caused by the exothermic reaction enthalpy is not as pronounced, because the driving force for external heat transfer is significantly higher than for a surrounding temperature of 490°C, causing the effect of the exothermic reaction enthalpy to diminish (this is also revealed in the sensitivity analysis to be presented later). This supports the fact that a devolatilization temperature of 400°C in model A yields better results with regard to mass loss than a devolatilization temperature of 500°C.

A sensitivity analysis of the predicted devolatilization time for a 14 mm tyre rubber particle was performed at 490°C and 840°C and revealed that the model predictions showed high sensitivity towards changes in the specific heat capacity of the virgin fuel and the activation energies of reactions 2 and 3 (See appendix C).

4.5.7 The Effect of Steel Wires on the Devolatilization Rate

The effect of steel wires on the devolatilization time was more pronounced in the flame devolatilization experiments than in the macro-TGA experiments. More precisely, the devolatilization time decreased by 35 and 12-17%, compared to without steel wires for the two experimental setups. These results are considered to be ambiguous and the two situations are therefore further analyzed in this section. Conceivably, the differences, with regard to effect of steel wires on devolatilization time, are due to the geometry of the investigated samples being different in the two cases and the fact that the steel wires are distributed differently (see Figure 4-10 and Figure 4-13).

In section 4.5.6, it was proved that Model A with $T_D=400^\circ\text{C}$ was capable of simulating the experimental mass loss obtained in the macro-TGA at 840°C, and this model is consequently considered valid. Therefore, analyses are performed to investigate the penetration of a 400°C front through tyre shape geometry with inclusion of steel wires, in order to simulate the conversion time of whole and shredded tyres with steel wires. However, the geometries cannot be modeled in 1D, as was the case without steel wires, and the Fluent software package is therefore applied for this purpose. Initially, symmetry and periodic planes are identified in the particular geometry, in order to save computational time (see Figure 4-27).

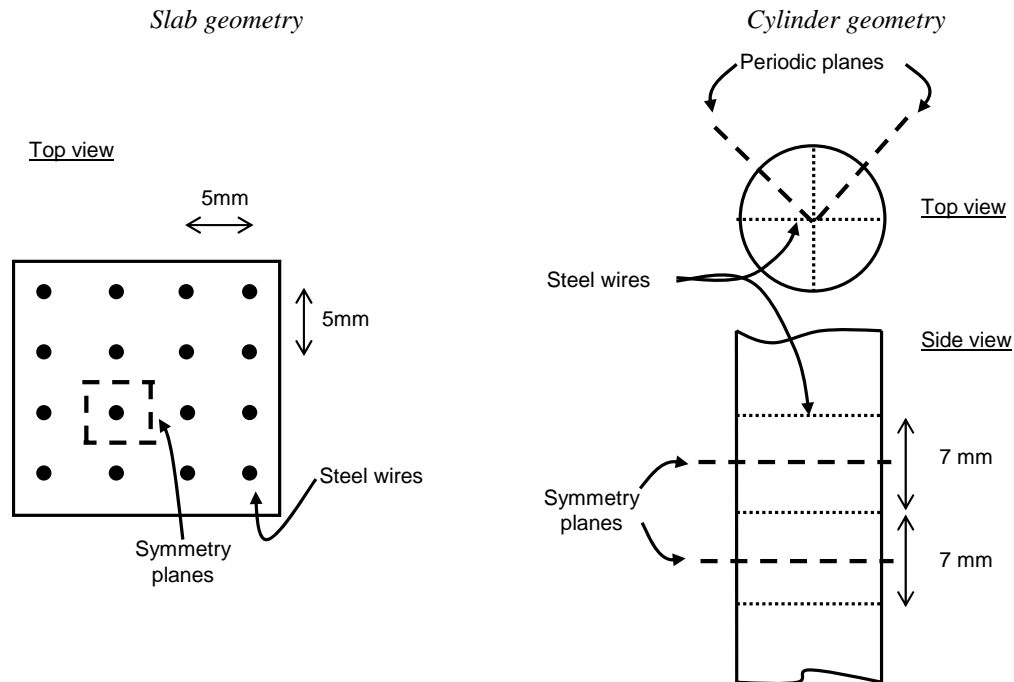


Figure 4-27: Symmetry and periodic planes applied in the modelling of transient heat transfer effects of steel wires in tyre rubber. Slab geometry (left) and cylinder geometry (right). Not to scale.

In the simulations, the external heat transfer boundary conditions are changed according to the respective experimental setup (see appendix B). The physical properties of the tyre rubber used here are identical to those applied in model B (see Table 4-3) and the physical properties of steel are obtained from Perry [42]: $\rho=7900 \text{ kg/m}^3$, $c_p= 502 \text{ J/kg/K}$ and $k=16 \text{ W/m/K}$. Selected results of the model calculations for four distinct times are shown in Figure 4-28 and Figure 4-29 for slab and cylinder geometry respectively. For both geometries, the presence of steel wires is initially observed to conduct heat faster into the interior of the particle than the tyre rubber. At prolonged times, when heated the steel wires serve as accelerators with regard to heating of the interior of the particle. This is considered to be the mechanism for the initial slower mass loss and the later fast mass loss for tyre rubber particles with steel wires compared to without steel wires that was experimentally demonstrated in section 4.4.

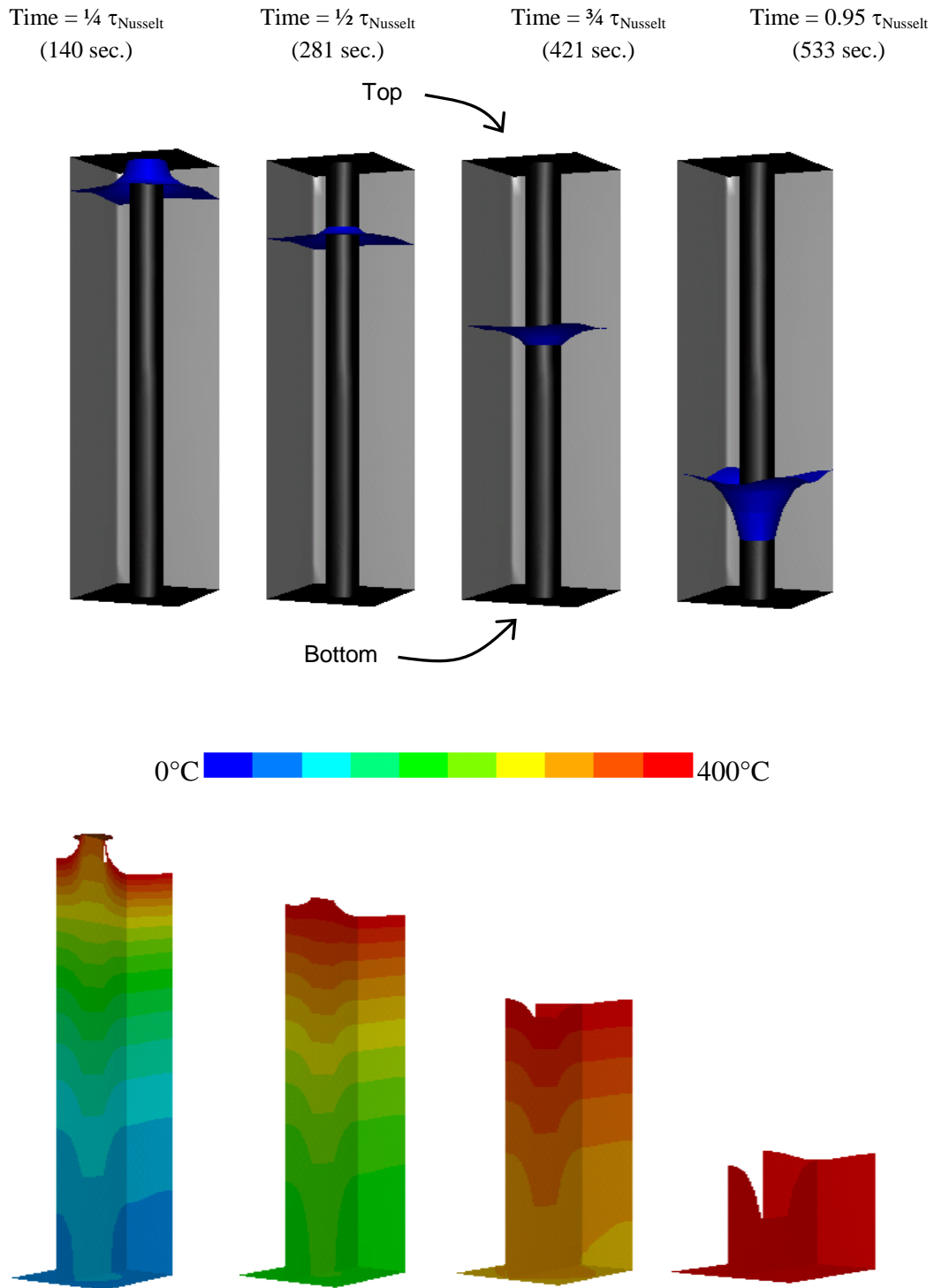


Figure 4-28: Results of 3D Nusselt shrinking core simulations for slab geometry with wires. Upper part shows the penetration of an iso-surface with a temperature of $T_D=400^{\circ}\text{C}$ through the tyre rubber at four distinct times and the lower part shows contour plots of temperature (only up to 400°C) at corresponding times. The steel wire is recognized as the dark rod in the middle (only upper).

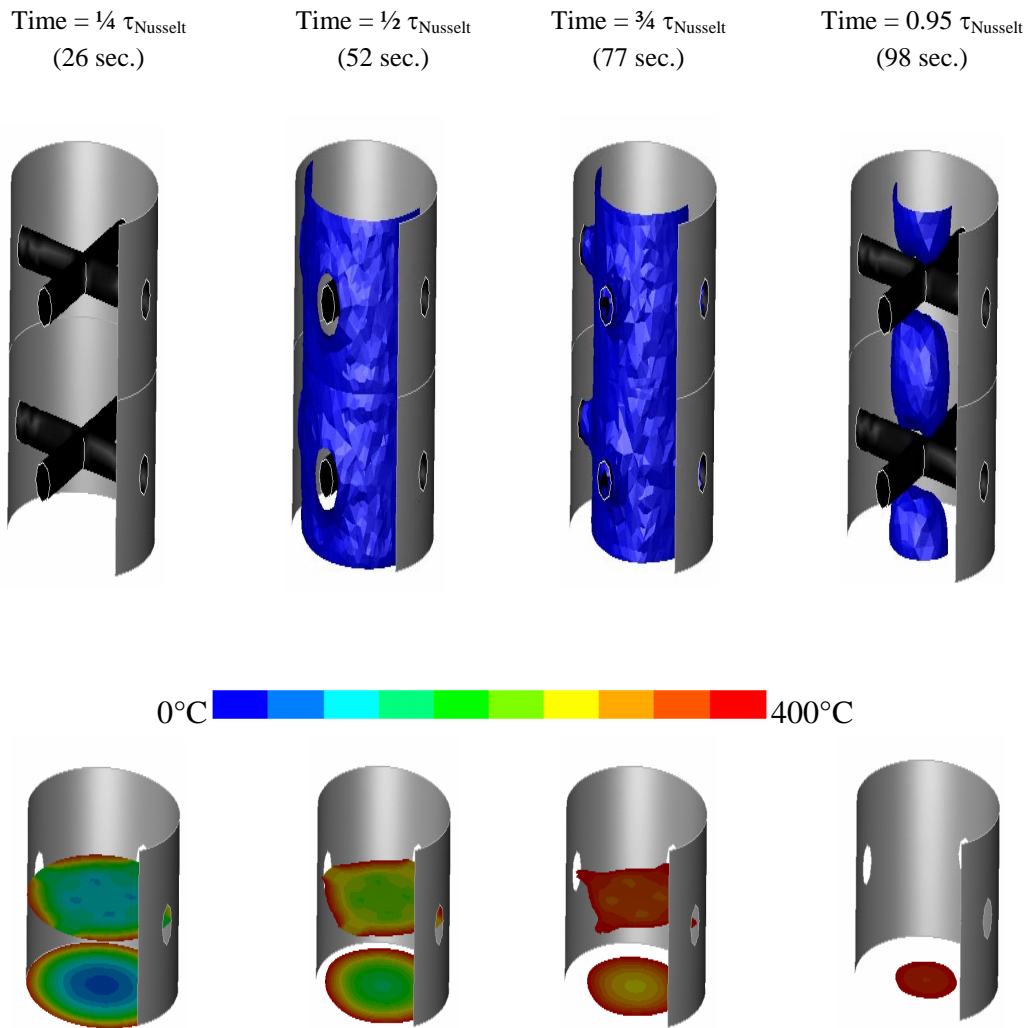


Figure 4-29: Results of 3D Nusselt shrinking core simulations for cylinder geometry ($D=14\text{mm}$) with wires. Upper part shows the penetration of an iso-surface with a temperature of $T_D=400^\circ\text{C}$ through the tyre rubber at four distinct times and the lower part shows contour plots of temperature (only up to 400°C) at corresponding times. The steel wires are recognized as the dark crosses (only upper) and as holes in the grey shell.

The devolatilization time for tyre rubber with steel wires may now be derived from the simulations as the time when the entire particle has a temperature of above 400°C . The derived devolatilization times are shown in Table 4-4. It also shows experimental results with and without steel wires, modeled devolatilization time without steel wires using model A and percentage decrease in devolatilization time.

Before conducting further data analysis, it should be noted that the Nusselt model is an engineering model and it is therefore not reasonable to compare exact levels, but rather to analyze tendencies in decrease in devolatilization time with inclusion of steel wires. For cylinder geometry, the model-predicted decreases in devolatilization time of 17 and 18% for

particle diameters of 14 and 22 mm are in good agreement with the experimental values of 17 and 12%. For slab geometry, an experimental decrease in devolatilization time of 34% is obtained compared to the modeled value of 50%. The larger discrepancy observed for slab geometry, may be a consequence of a too low experimentally determined devolatilization time, due to the possible sample heating from bottom and side walls in the flaming devolatilization experiments, as described in section 4.5.5. From these analyses, the observed effect of steel wires on devolatilization time is shown to be a function of 3D spatial heat transfer effects. Therefore, in order to assess the effect of steel wires on the devolatilization time of real tyres, the tyre geometry and the position of the steel wires as well as the sides exposed to external heating must be considered.

	<i>20 mm slab</i>		<i>14 mm cylinder</i>		<i>22 mm cylinder</i>	
	Exp.	Model	Exp.	Model	Exp.	Model
Without steel wires	736	1127 ^a	176	123 ^a	331	256 ^a
With steel wires	488	561 ^b	146	103 ^b	291	210 ^b
% Decrease	34	50	17	17	12	18

Table 4-4: Experimentally observed and modelled devolatilization time in seconds with and without steel wires and percentage decrease in devolatilization time. a) obtained using Fluent software and the approach described in this section, b) obtained using model A with $T_D=400^\circ\text{C}$.

4.5.8 Modeling Devolatilization Times of Whole and Shredded Car Tyres

Figure 4-4 showed a cross section of a real tyre and it is seen mainly to consist of tread rubber, sidewall rubber, steel and nylon. In this modeling study, the following assumptions have been made in order to simplify the modeling work:

- 1) *The devolatilization proceeds according to pathway E*
- 2) *The steel beads are assumed to be coherent, with a total diameter equal to that of the original outer diameter of the beads.*
- 3) *The steel belt is assumed to be coherent with outer dimensions equal to that of the original belt.*
- 4) *The hollows in the tread are neglected. Instead, the tread surface is modeled as a continuous surface with a thickness corresponding to the outer tread surface.*
- 5) *The presence of nylon is neglected.*
- 6) *No voidage between steel and tyre rubber contact points.*
- 7) *Sidewall and tread rubber are assumed to be identical.*
- 8) *Nusselt Shrinking Core model (Model B) with a devolatilization temperature of 400°C is assumed valid (assumptions described in section 4.3.1).*

With these assumptions, the geometry used for the model calculations is as shown in Figure 4-30.

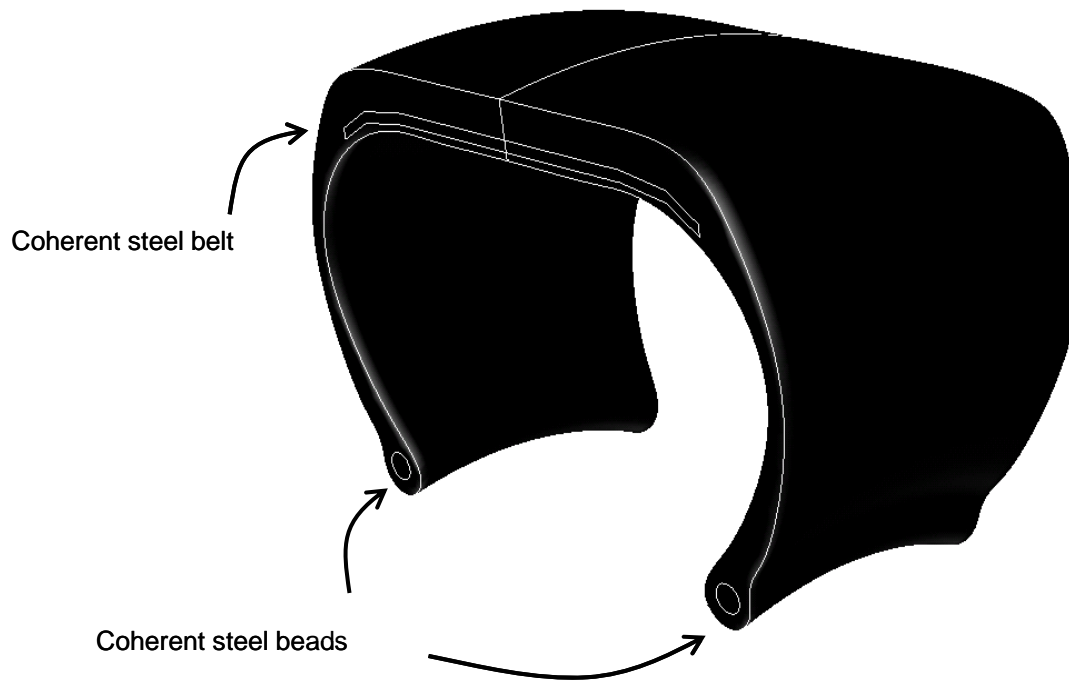


Figure 4-30: Outline of the geometry of a shredded car tyre used in the model calculations.

In the model calculations, the whole/shredded car tyre is injected into the preheated HOTDISC chamber in an environment assumed to have a temperature of 850°C. The difference in model calculations for whole and shredded car tyres stems from the fact that shredded tyres are susceptible to external heating from the shredded side (see also Figure 4-30), whereas whole tyres are only susceptible to heating on the inner and outer radial side. Using the Fluent software package to model and track the surface with a temperature of 400°C through the whole and shredded tyre, the devolatilization times of Table 4-5 are obtained. The predicted devolatilization times of whole and shredded tyre are seen to be about 295 seconds for both situations.

	<i>Whole tyre</i>	<i>Shredded tyre</i>
<i>Devolatilization time [s]</i>	295	295

Table 4-5: Modelled devolatilization times for whole and shredded car tyres with a tread thickness of 15mm at 850°C ($h_{\text{conv}} = 15 \text{ W/m}^2/\text{K}$ and $\epsilon = 0.25$).

A closer look at the predicted temperature distributions gives further insight into the devolatilization time of a whole tyre. In the upper part of Figure 4-31, the position of the core in model B is shown at four distinct times. With increasing time, the core is observed to shrink. From the time at 280s it is observed that the remaining virgin tyre part is in the thick tread. Consequently, devolatilization of this part is the rate determining process in the devolatilization of a whole car tyre.

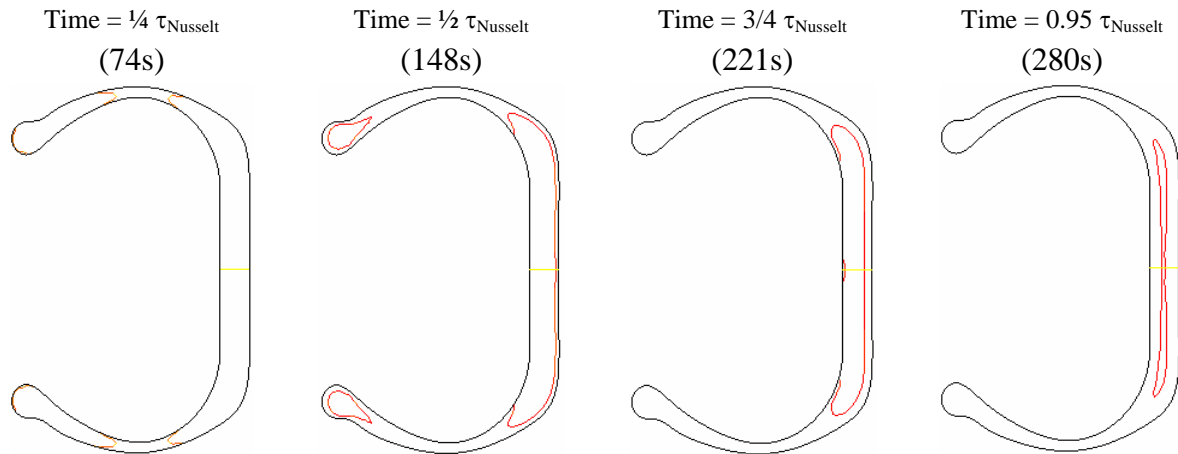


Figure 4-31: Cross section of tyre rubber (whole tyre model) and the movement of an iso temperature core of 400°C at four distinct times.

4.5.9 Tyres with Other Tread Thicknesses

In the previous section, it was shown that the thickest dimension of the tread was the rate controlling parameter for the devolatilization time of whole and shredded tyres with a tread thickness of 15 mm. However, it is relevant to analyze the impact of other tyre tread thicknesses on devolatilization times and to correlate these values to the simpler one-dimensional model B presented earlier, in order to produce a framework for predicting tyre devolatilization time for any tyre size without using detailed CFD calculations.

Figure 4-32 depicts the modelled devolatilization, using Model B and the whole tyre model, as a function of distance to centre line in slab geometry. It is evident that the devolatilization time using model B is about 12-14% higher than that predicted using the whole tyre model. This indicates that the devolatilization time of any whole or shredded tyre converted via conversion pathway E may be predicted by:

- 1) *Defining the thickest part of the tread,*
- 2) *Establishing external heat transfer characteristics,*
- 3) *Determining the devolatilization time using model B and subtracting 12-14%*

If the devolatilization conversion takes place via conversion pathway I, the devolatilization time obtained for the whole/shredded tyres should be adjusted accordingly. The experimental data of section 4.4 and calculations performed in the coming section 4.6 prove that a larger TDF particle converted via pathway I compared to E is converted approximately twice as fast.

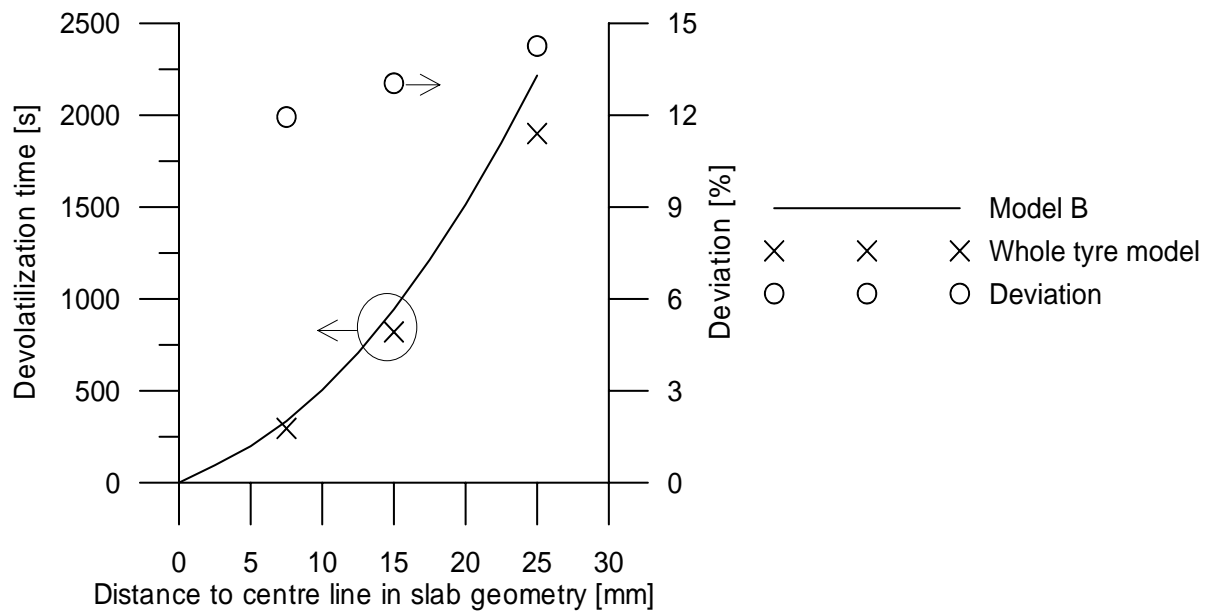


Figure 4-32: Modelled devolatilization time for whole tyres with steel wires using the model of 4.5.8.1 and the devolatilization for pure tyre rubber using model B as well as percentage deviation between these two. Conditions are equal to these described in the caption of Table 4-5 (except particle size).

4.5.10 Conclusions on Modeling Investigations

Two models for conversion via pathway E, were tested against the experimental results of the flaming devolatilization experiments and found to overpredict the devolatilization time observed. This was mainly attributed to the fact that the samples were possibly not completely insulated. A comparison between a model for conversion pathway I provided overall correct trends with regard to predicting the devolatilization time.

A comparison of the model predictions with experimental data obtained in the macro-TGA setup shows good agreement and demonstrates that the devolatilization process of large tyre rubber particles at temperatures above 490°C can be considered to be controlled mainly by heat transfer and reaction kinetics. The model analysis further shows that exothermic devolatilization reaction enthalpy effects cannot be neglected in the prediction of the intra particle temperature rise. This also explains the fact that model B is able to simulate the experimental mass loss results at a devolatilization temperature of 400°C.

Detailed modelling investigations were successfully used to explain mechanistic effects of steel wires on experimentally observed mass loss rate and devolatilization times. A framework for establishing the devolatilization time of a whole or shredded car tyre, converted according to pathway E, under conditions resembling those in the cement kiln system was developed. It was demonstrated that the thickest part of the tread is the rate controlling thickness for the devolatilization times of whole and shredded tyres.

4.6 Influencing Factors and Implications

When whole or shredded tyres are used as alternative fuel in the kiln system of a cement production system, the gas flow around the particles is often sufficient to remove the char layer during devolatilization and consequently promote conversion via pathway I rather than pathway E.

Despite the fact, that model C is not validated against reliable experimental data and it does not resemble the exact situation for TDF devolatilization via pathway I, it yields overall correct trends with regard to devolatilization conversion via this pathway. A comparison of results from model B (conversion pathway E) and model C (conversion pathway I) are shown in Figure 4-33 as a function of particle size and at two temperatures relevant to cement kiln systems. For a particle with a half thickness of 15 mm converted via pathway E, it is observed that the time of devolatilization is 694 to 887 seconds at 1100 and 850°C, respectively, whereas model C predicts conversion times of 265 and 127 seconds, respectively. For smaller particle sizes, the model predictions approach each other. The effect of an increased surrounding temperature is most significant for model C, where a predicted decrease in devolatilization time of about 52% for a particle with a half-thickness of 15mm is observed. For model B, the decrease is only about 22%. The less significant effect of an increased surrounding temperature on the results of model B compared to those of model C is due to the intra-particle heat transfer being more important in model B than in model C. Model B is close to the regime where the devolatilization process is dominated by internal heat transfer control. The implications of the result of the model analyses are:

- 1) Mechanical interaction (by gas or other means) of the TDF fuel particles should be enhanced in order to promote conversion during pathway I and consequently a reduced time of conversion.*
- 2) The outer particle surface should not be covered by other fuel and or raw material particles during devolatilization, as this promotes conversion via pathway E.*
- 3) When converted via pathway I, the devolatilization rate may be influenced by increasing the temperature.*

and these points may also be applicable to devolatilization of any solid alternative fuel applied in kiln systems in cement production.

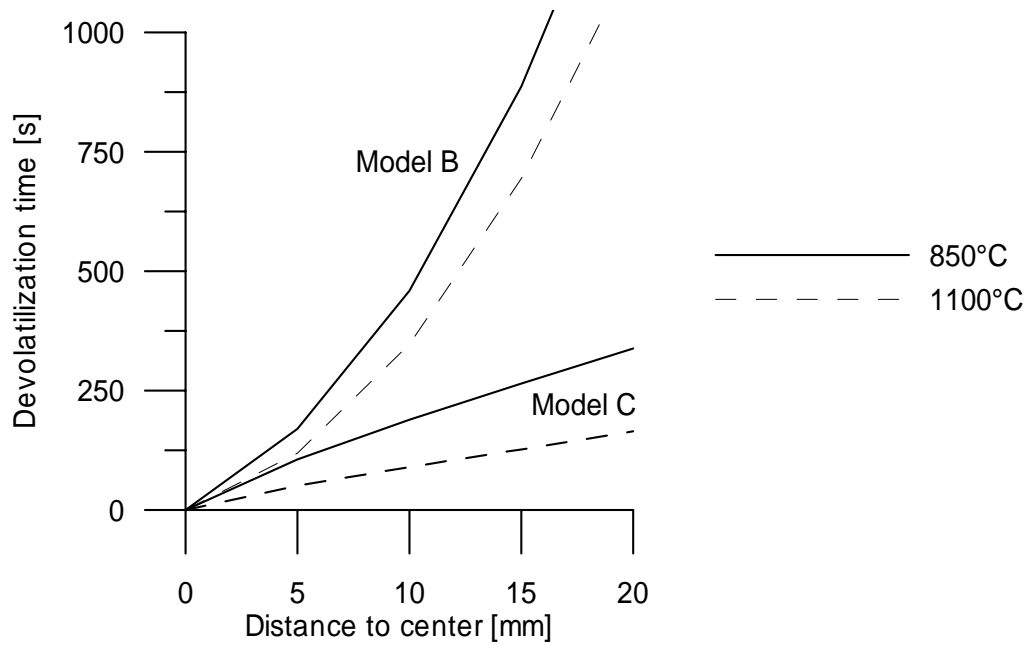


Figure 4-33: Modelled devolatilization time of large particles of tyre rubber without steel wires in slab geometry, as a function of conversion pathway. Model B represents the situation where the char layer is retained, and model C represents the situation where the char layer is removed continuously during devolatilization ($h_{\text{conv}} = 53 \text{ W/m}^2/\text{K}$, $\varepsilon=0.24$ with $T_{\text{rad}} = T_{\infty}$).

4.7 Other Alternative Fuels

It was demonstrated that heat transfer and kinetics are the rate controlling parameters in devolatilization of large particles of tyre rubber, in agreement with the literature regarding biomass and coal (see also section 4.5). It is expected that these parameters also control devolatilization rates of other alternative solid fuels. Mass transfer is merely considered to be the rate limiting parameter if a non-permeable char structure is formed during devolatilization pathway E, causing the devolatilization products to be trapped inside the fuel particle. Even for wood with a significantly less permeable char structure than e.g. TDF chars, heat transfer is still the devolatilization rate controlling parameter, c.f. section 4.5.

Under conditions resembling cement kiln systems, the important parameters controlling devolatilization rates and consequently the devolatilization conversion times for a given fuel are:

- 1) *Devolatilization conversion pathway*
- 2) *Heat transfer rate from surroundings to particle surface*
- 3) *Particle size/shape*
- 4) *Residence time*
- 5) *Intrinsic pyrolysis kinetics*

Re 1), it is clear that a particle converted via devolatilization pathway I is converted faster than pathway E, as demonstrated in sections 4.4 to 4.6 for TDF. In addition, for particles reshaping during heating (pathway K), a changed devolatilization time is expected compared to the particle retaining its shape. E.g. for plastic sheets reshaped to spheres, a longer conversion time is expected for the sphere than the sheet. Re 2), the external heat transfer rate is mainly influenced by radiation at temperatures resembling cement kiln systems (see also section 6.3). For large particles converted via pathway E, intra-particle heat transfer may be controlling, and the external heat transfer becomes of no influence. Intra-particle heat transfer limitations may be expected for a Biot number ($=h_{\text{eff}}r/k$) above 10. Re 3) as proved for TDF, it is clear that a larger particle increases the devolatilization time. Re 4), increased residence time increases the obtained devolatilization conversion level. Finally, re 5) intrinsic pyrolysis kinetics influence the temperature at which the pyrolysis reactions initiate. For all the fuels investigated in this chapter, the volatilization of the greatest part of the pyrolysis products occurs around 275 to 500°C (see Figure 4-6, Figure 4-7 and Figure 4-22).

4.8 Conclusions on Chapter 4

The devolatilization process of large solid fuel particles is initiated by external heating of the outer particle surface, causing intra-particle heating with spatial temperature gradients. The heating induces the decomposition at different spatial positions and the volatiles are transported towards the outer particle surface. In the surrounding gas, the volatiles may ignite in a flame front, if oxidizing conditions exist and the temperature is sufficiently high.

Few studies of devolatilization of large particles of plastics or TDF exist in the literature and no studies exist regarding devolatilization of large particles of MBM. In addition, the literature data is not clear with regard to the effect of particle and surrounding temperature on devolatilization rates and time. For sheets of the plastics of PE, PP and PS, a peculiar devolatilization behaviour was reported, as they were reshaped during heating and subsequently burned as droplets.

Two different experimental setups were used to investigate devolatilization of large particles of TDF with regard to the effect of size, surrounding temperature, steel wires and conversion pathway on the devolatilization rate and time. A significant effect of particle size and conversion pathway on devolatilization rate and time was found in both experimental setups and for both conversion pathways, where larger particle sizes and devolatilization via conversion pathway E increased the devolatilization time. A significant effect of temperature was found in the macro-TGA setup and for devolatilization via pathway I in the flaming devolatilization setup, whereas no effect was observed in the flaming devolatilization setup for devolatilization pathway E. Model analyses of the experimental data proved that devolatilization of large particles of TDF can be considered to be controlled by heat transfer and intrinsic pyrolysis kinetics.

Model analyses were applied in order to investigate the ambiguous effect of steel wires found in the experimental part. Indeed, this was demonstrated to be an effect of differences in spatial heat transfer effects. Analyses of whole/shredded tyre devolatilization via pathway E with steel wires confirmed that the thickest part of the tread was the rate determining part in the devolatilization process. Comparison with a one-dimensional model suggests that the devolatilization time of whole/shredded tyres with steel wires converted via pathway E may be derived from this relatively simpler model.

Analogies to devolatilization of other large alternative solid fuel particles under conditions relevant to cement kilns, indicate that their conversion rates are mainly controlled by 1) conversion pathway, 2) external heat transfer rate, 3) particle shape/size, 4) residence time and 5) intrinsic pyrolysis kinetics.

4.9 References

- ¹Schultz, L.; Pyrolysis of Tyre Rubber; M.Sc. Thesis; Dept. of Chem. Eng, Technical University of Denmark, June, 2005.
- ²Lecture notes from “High Temperature Chemistry in Action” held by Mikko Hupa, Dept. of Chem. Eng, Technical University of Denmark, Fall 2005.
- ³Levenspiel, O., Chemical Reaction Engineering 3rd ed., John Wiley & Sons, New York, 1999. ISBN 0-471-25424-X.
- ⁴Kim, S., Park, J.K., Chun, H.D., Devolatilization kinetics of scrap tyre rubbers. I: Using DTG and TGA, J. of Env. Eng., 121, 507-514, 1995
- ⁵Conesa, J.A., Font, R., Fullana, A. and Caballero, J.A., Kinetic Model for the combustion of tyre wastes, Fuel, 77, 1469-1478, 1998.
- ⁶Senneca, O., Salatino, P., Chirone, R., A Fast Heating-Rate Thermogravimetric Study of the Pyrolysis of Scrap Tyres, Fuel, 78, 1575-1581, 1999.
- ⁷Leung, D.Y.C. and Wang, L.C., Kinetic Study of scrap tyre devolatilization and combustion, J. Anal. Appl. Devolatilization, 45, 153-159, 1998.
- ⁸Yang, J., Kaliaguine, S., Roy, C., Improved Quantitative Determination of Elastomers in Tire Rubber by Kinetic Simulation of DTG curves. Rubb. Chem. Technol., 66, 213, 1993.
- ⁹Kyari, M. Cuncliffe, A. and Williams, P.T., Characterization of Oils, Gases, and Char in Relation to the Pyrolysis of Different Brands of Scrap Automotive Tires, Energy & Fuels, 19, 1165-1173, 2005.
- ¹⁰Ucar, S., Karagoz, S., Ozkan, A.R., Yanik, J., Evaluation of two different scrap tyres as hydrocarbon source by pyrolysis. Fuel, 84, 1884-1892, 2005.
- ¹¹Rodriguez, I.M., Laresgoiti, M.F., Cabrero, M.A., Torres, A., Chomon, M.J., Cabellero, B., Pyrolysis of Scrap Tires, Fuel Process. Technol., 72, 9-22, 2001.
- ¹²Giddings, D, Pickering S.J., Eastwick, C.N., Combustion and aerodynamic behaviour of car tyre chips in a cement works precalciner. J. Inst. Energy, 77, 91-99, 2002.
- ¹³Schmidthals, H., Luftvergasung von Altreifen zur integrierten stofflichen und energetischen Nutzung im Klinkerbrennprozess, Ph.D.-Thesis, Ruhr-Universität, Bochum, Germany, 2000
- ¹⁴Bouvier, J.M., Charbel, F. Gelus, M., Gas-Solid Pyrolysis of Tire Wastes - Kinetics and material balances of Batch Pyrolysis of used tyres. Resources Conservation, 15, 205-214, 1987.
- ¹⁵Yang, J., Tanguy, P.A., Roy, C., Heat transfer, Mass transfer and kinetics study of the vacuum pyrolysis of a large used tyre particle. Chem. Eng. Sci. 50,12,1909-1922, 1995.
- ¹⁶Senneca, O., Chirone, R. and Salatino, P., Oxidative Pyrolysis of Solid Fuels, J. Anal. Appl. Pyrolysis 71, 959-970,2004.

- ¹⁷Sørum, L., Grønli, M.G. and Hustad, J.E.; Pyrolysis characteristics and kinetics of municipal solid wastes; *Fuel*, 80, 1217-1227, 2001.
- ¹⁸Zevenhoven, R., Karlsson, M., Hupa, M. and Frankenhaeuser; Combustion and Gasification Properties of Plastic Particles; *J. Air & Waste Manage. Assoc.*, 47, 861-870, 1997.
- ¹⁹Turns, S.R.; *An introduction to Combustion*; McGraw-Hill, 2000. ISBN 0-07-230096-5,
- ²⁰Kanury, A.M.; *Introduction to Combustion Phenomena*; Gordon and Breach Science Publishers, 1975. ISBN 0-677-02690-0
- ²¹Franke, H.J.; Shimizu, T., Takano, Y., Hori, S., Strziga, M, Inagaki, M.and Tanaka, M.; Reduction of Devolatilization Rate of Fuel During Bubbling Fluidized Bed Combustion Using Porous Bed Material; *Chem. Eng. Technol.*, 24, 725-733, 2001.
- ²²Di Blasi, C.; Transition between regimes in the degradation of thermoplastic polymers; *Polymer Degradation and Stability*, 64, 359-367, 1999.
- ²³Salvador, S., Quintard, M and David, C.; Combustion of a substitution fuel made of cardboard and polyethylene: Influence of mix characteristics – experimental approach; *Fuel*, 83, 451-462, 2004.
- ²⁴Conesa, J.A., Fullana, A., and Font, R.; Thermal decomposition of of meat and bone meal; *J. Anal. Appl. Pyrolysis*, 70, 619-630, 2003.
- ²⁵Ayllon, M., Gea, G., Murillo, M.B., Sanchez, J.L., Arauzo, J.; Kinetic study of meat and bone meal decomposition: an evaluation and comparison of different possible kinetic models; *J. Anal. Appl. Pyrolysis*, 74, 445-453, 2005
- ²⁶Skodras, G., Grammelis, P., Basinas, P., Kakaras, E. and Sakellariopoulos, S.; Pyrolysis and Combustion Characteristics of Biomass and Waste Derived Feedstock; *Ind. Chem. Eng. Res.*, 45, 3791-3799, 2006.
- ²⁷Influence of temperature and heating rate on the fixed bed pyrolysis of meat and bone meal; Ayllon, M., Aznar, M., Sanchez, J.L., Gea, G., Arauzo, J.; *Chemical Engineering Journal*, 121, 85-96, 2006.
- ²⁸ Kanury, A.M., *Combustion Characteristics of Biomass Fuels*, *Combust. Sci. Tech.*, 97, 469-491, 1994.
- ²⁹ Goodman, T.R., *Application of integral methods to transient nonlinear heat transfer*. Advances in heat transfer. Academic Press, New York, 1964.
- ³⁰ Spearpoint J., Quintere, J.G., Predicting the burning of wood using an integral model. *Combustion and Flame*, 123:308-324, 2000.
- ³¹ Galgano, A., Di Blasi, C., Modelling wood degradation by the unreacted-core-shrinking approximation. *Ind. Eng. Chem. Res.*, 42, 2101-2111, 2003.
- ³² Galgano, A. and Di Blasi, C., Modeling the propagation of drying and decomposition fronts in wood. *Combustion Flame* 139, 16-27, 2004.
- ³³ Larfeldt, J., Leckner, B., Melaaen, M.C., Modelling and Measurement of Large Wood Particles. *Fuel*, 79, 1637-1643, 2000.

- ³⁴ Grønli, M.G., Melaaen, M.C., Mathematical model for wood pyrolysis - Comparisons of Experimental Measurements with Model Predictions. *Energy Fuels*, 14,791-800, 2000.
- ³⁵ Chern, J.-S., hayhurst, A.N.; A model for the devolatilization of a coal particle sufficiently large to be controlled by heat transfer; *Combustion and Flame*, 146, 553-571, 2006.
- ³⁶ Adesanay, B.A. and Pham, H.N., Mathematical modelling of devolatilization of large coal particles in a convective environment , *Fuel*, 74, 896-902, 1995.
- ³⁷ Wildegger-Gaismaier A.E. and Agarwal, P.K., Drying and devolatilization of large coal particles under combustion conditions. *Fuel*, 69, 44-62, 1990.
- ³⁸ Kanury, A.M.; *Introduction to Combustion Phenomena*; Gordon and Breach, Science Publishers; New York, 1994. ISBN 0-667-02690-0.
- ³⁹ Bird, R.B., Stewart, W.E., Lightfoot, E.N. *Transport Phenomena*, 2nd edition, Wiley, New York, 2002. ISBN 0-471-41077-2.
- ⁴⁰ Callister, D.W., *Materials Science and Engineering*. John Wiley, New York, 1996. ISBN: 0-471-13459-7,
- ⁴¹ Yang, J., Philippe, A.T., Roy, C., Numerical Model for the Vacuum Pyrolysis of Scrap Tires in Batch Reactors. *AIChE J.*, 41, 6, 1500-1512, 1995.
- ⁴² *Perry Chemical Engineers Handbook*, 7th edition, Mc-Graw Hill, 1999.
- ⁴³ Chen, F. & Qian, J., Studies of the thermal degradation of waste rubber. *Waste Management*, 23, 463-467, 2003.

Chapter 5 - Char Combustion

Char combustion is the final step in the combustion of most solid fuels, except those without a char content, and is therefore the main determining parameter with respect to prevention of 1) unburned carbon in the material kiln inlet which may induce kiln instabilities, and 2) unburned carbon dropping into the material charge of the rotary kiln which may induce problems with clinker chemistry (see also sections 3.2 and 3.3).

In chapter 6 it will be demonstrated that the HOTDISC is well suited for devolatilization of large fuel particles, e.g. TDF, and char combustion takes place both in the HOTDISC and in the subsequent calciner. Consequently, this chapter gives an understanding of TDF char burnout as well as a modelling study to predict burnout of TDF chars in the calciner.

The first part of this chapter provides literature data with respect to char combustion of the currently most important fuels used in the German cement industry, namely TDF and MBM – plastics are not considered due to their negligible char content. The following section describes fundamental combustion experiments performed in a laboratory reactor under well defined conditions as well as analyses of them in order to study the intrinsic kinetics of heterogeneous tyre char combustion. The experimental data in this section is obtained from a Master of Science project carried out parallel with this PhD study [1]. In the following sections, models for combustion of large TDF char particles in cement kiln systems are developed and the results are analyzed. In addition, analogies are drawn with respect to char burnout to chars from other fuels.

5.1 Literature Study on Char Conversion

This section reviews the literature regarding combustion kinetics of chars derived from the currently most used fuels in the German cement industry, namely TDF and MBM. See section 4.1 for an introduction to processes involved in char and solid fuel combustion.

Intrinsic char reactivity is commonly expressed as a function of temperature, oxygen concentration and intra-particle available surface area [2,3,4]:

$$\frac{dX}{dt} = A \cdot \exp\left(\frac{-E}{R_g T}\right) C_{O_2}^n \cdot \frac{S(X)}{S_0} \quad (5-1)$$

where the first part is the common Arrhenius dependence of the rate constant on temperature and the two latter factors describe the dependency of oxygen concentration and intra-particle surface area. For coal [5] and biomass chars [4], the reaction order of oxygen is between 0

and 1, approaching 0 for low temperatures and 1 for high temperatures. A similar behaviour may be expected for chars of TDF as identified by Masi et al. [2] ($n=0.68$) and Conesa et al. [6] ($n=0.69$).

The intra-particle surface area varies with conversion. Different models have been developed to account for this variation in available surface area with conversion. In the reported studies of combustion rates of TDF-char, the random pore model of Bhattia and Perlmutter [7] was employed by Masi et al. [2] ($\psi=16$), whereas the data of Conesa et al. [6] ($m=0.69$) and Leung and Wang [8] ($m=1$) is compatible with the power law model.

$$\frac{S(X)}{S_0} = (1-X) \sqrt{1-\psi \ln(1-X)} \quad \text{Random Pore Model} \quad (5-2)$$

$$\frac{S(X)}{S_0} = (1-X)^m \quad \text{Power law model} \quad (5-3)$$

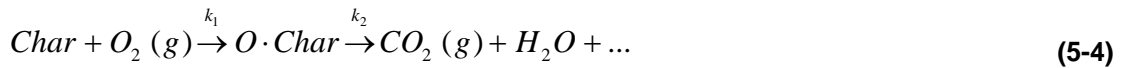
5.1.1 TDF Chars

To the author's knowledge studies of TDF to determine intrinsic reaction kinetics have been carried out by Masi et al. [2], Conesa et al. [6] and Leung and Wang [8]. Their studies were carried out in micro-TGA with a maximum temperature in the range of 500 to 600°C. A comparison of their results shows that the reported kinetic parameters of Conesa et al. [6] result in a rate that is 3 orders of magnitude lower than that of Masi et al. at 500°C and 5 orders of magnitude lower at 400°C (see also Figure 5-8). The kinetic scheme proposed for the char oxidation by Leung and Wang [8] does not include any dependence on oxygen concentration and is therefore only valid at conditions under which the kinetics were obtained (21 Vol.% O₂). Atal and Levendis [9] studied and compared the combustion characteristics of chars from TDF and a bituminous coal and concluded that TDF chars burned about 2-4 times faster than a bituminous coal char. They also reported that the bituminous coal swelled during devolatilization whereas the TDF char retained its original shape. Finally, Zabanitou and Stavrepoulos [10] studied the char gasification reactivity as a function of the temperature at which the char was prepared in the range of 350 to 900°C, and they reported that the most reactive char was that prepared at a temperature of 650°C.

5.1.2. MBM Chars

To the author's knowledge, only one study regarding MBM char combustion is presently available, namely that of Conesa et al. [11] who studied MBM devolatilization and char combustion in a micro-TGA reactor at three different heating rates and 21 Vol.% O₂. They applied a two step char combustion model, with a first step for the adsorption of oxygen onto the char followed by desorption of gaseous products^a:

^a Not stoichiometrically balanced, as in the original reference.



and fitted the experimental mass loss data to the following mathematical model to obtain Arrhenius parameters for the two rate constants k_1 and k_2 (1.9 is a reported yield coefficient):

$$\frac{d(\text{Char})}{dt} = -k_1 \text{Char} \quad (5-5)$$

$$\frac{d(\text{O} \cdot \text{Char})}{dt} = -k_2 \text{O} \cdot \text{Char} + 1.9 \cdot k_1 \text{Char} \quad (5-6)$$

The kinetic scheme does not include any dependence on oxygen concentration and is therefore only valid at conditions under which the kinetics were obtained (21 Vol.% O_2).

5.2 Experimental and Model Analysis of Intrinsic TDF Char Oxidation Kinetics

This section describes experimental investigations and mathematical modelling analyses that have been made to investigate the intrinsic kinetics of TDF char oxidation under combustion conditions.

5.2.1 Pre-experimental considerations

Char oxidation experiments may be divided into those performed at low temperatures in micro TGA reactors [2,4,6,11,12] or experiments performed at high temperatures pertinent to combustion in flow [12] or fixed bed reactors [3]. Experiments performed in micro-TGA systems are advantageous because the mass loss is measured directly, whereas experimental data from higher temperatures, gaseous concentrations in the effluent of the experimental combustion setup usually have to be analysed before the conversion can be determined. In addition, char particles combusted at higher temperature are more susceptible to mass transfer limitations compared to those combusted at low temperatures. However, one major drawback of the micro-TGA experiments is that the results obtained must be extrapolated to temperatures that are several hundred degrees higher than those under which they were obtained.

Contrary to many studies in the literature, the goal of the present experiments was to carry them out at temperatures relevant to combustion conditions. A micro-TGA reactor system is therefore inappropriate as the mass loss rates become too high. Instead, two other experiments were considered, 1) a fixed bed reactor system where the combusting char sample rests on a porous plate with or without sand, or 2) an entrained flow reactor system where char particles are fed continuously and combusted [12]. The advantage of 2) is that it

is a continuous system and that the conversion against e.g. residence time can be measured directly, whereas system 1) is a batch fed reactor susceptible to transient behaviour, which needs mathematical treatment before the conversion against time can be derived. The fixed bed reactor was chosen for the experiments, as this has previously been used successfully in the determination of char combustion kinetics [3].

5.2.2 Materials

Tyre rubber identical to that used in the devolatilization study in chapter 4 was also used in this study. The rubber was ground in a laboratory mill, and the resulting particle distribution was sieved in order to separate the different size fractions. The fraction with a particle size of 102-212 μm was used for the experiments (due to difficulties in milling the elastic tyre rubber material to smaller fractions). It was attempted to have as small a particle as possible in order to reduce mass transport resistance in the kinetic measurements.

5.2.3 Experimental Setup and Procedure

About 1-2 mg of tyre rubber particles were burned resting on a porous plate in a laboratory-scale reactor at temperatures of 750, 800 and 850°C at about 1 bar (see Figure 5-1). The reactor was made of quartz glass and designed to preheat gasses before they meet with the tyre rubber particles. This was accomplished by admission of gas in the bottom and preheating in the annulus outside the inner core, where reaction takes place. A gas-mixing panel upstream of the reactor consisting of mass flow controllers (MFC) ensures that the flow and composition of the gas entering the reactor remain constant. The reactor was placed in an electrically heated oven consisting of three heating-zones, where the temperature of each zone was independently controlled by an external PID-controller.

In each experimental run, tyre rubber particles were placed in the sample feeder with valve 1 closed (see Figure 5-1). Initially, valve 2 was opened and valve 4 was closed resulting in a slight overpressure inside the sample feeder chamber. Valve 1 was opened for a short while and via the solid feeding tube the overpressure carried the tyre rubber particles into the reactor, where they were captured resting on top of the porous plate. Valve 4 was opened and valves 1 and 2 were closed. The tyre rubber particles were initially exposed to pure N_2 with a flow of 2 NL/min for 60 seconds, whereby inert pyrolysis takes place leaving only char. Then, O_2 in N_2 (also 2 NL/min), with a nominal concentration of 10 Vol. %, was admitted to oxidize the remaining char. The effluent of the reactor was led to gas-analyzers, where profiles of CO , CO_2 and O_2 were measured and recorded for subsequent data-interpretation. At all times, the burning char particles experienced a gas flow coming from above ensuring that no fines were carried upward, and the porous plate was almost non permeable for fine particles. Consequently, the burning char particles and eventual fragments hereof were retained in the reaction zone just above the porous plate.

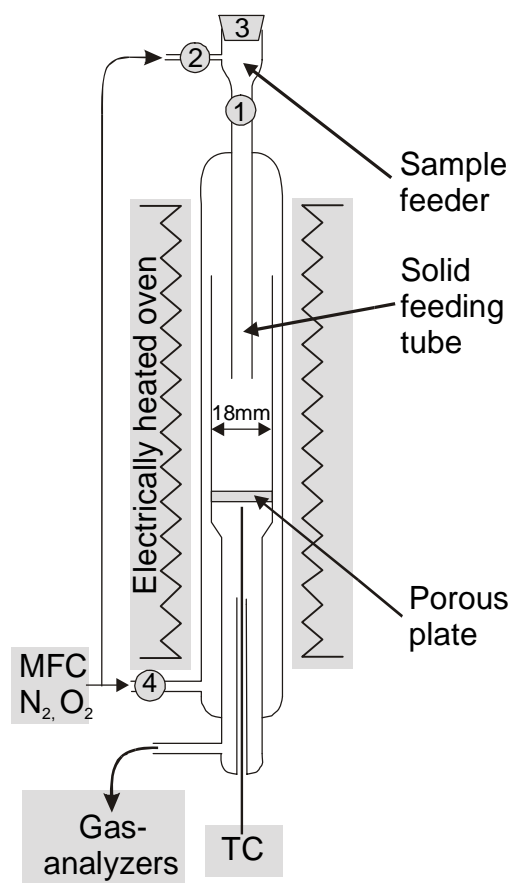


Figure 5-1: Experimental setup applied for kinetic studies of TDF char combustion.

Figure 5-2 shows an example of the measured effluent concentration for a particle converted at 750°C. It is observed that peaks of CO₂ and CO, with CO being the highest, develop about 17 seconds after the particles were injected, indicating pyrolysis. At this stage small amounts of O₂ as a consequence of entrainment into the sample feeder are also observed causing oxidation of pyrolysis products and partly char. The extent of char combustion is considered to be insignificant at the pyrolysis stage. This was quantified by a carbon mass balance over the char combustion stage, by integrating the CO and CO₂ signals, resulting in a closure of above 95%. Oxygen is switched on after 60 seconds resulting in an increased measured O₂-concentration slightly after 78 seconds increasing to the nominal concentration of about 10 Vol.%. Char was oxidized around 78-90 seconds resulting in peaks of CO₂ and CO, with the concentration of CO₂ now being the dominant peak. What should be particularly noted from the figure is the time delay from admission of particles or gaseous O₂ until a response is measured on the gas analyser. This time delay is a consequence of dispersion and residence time delays in the gas analyzers, pipes, condenser and mixing panel of the experimental setup. For the kinetic analysis, the concentration under char oxidation in the reaction zone is needed and signal deconvolution is therefore applied [13].

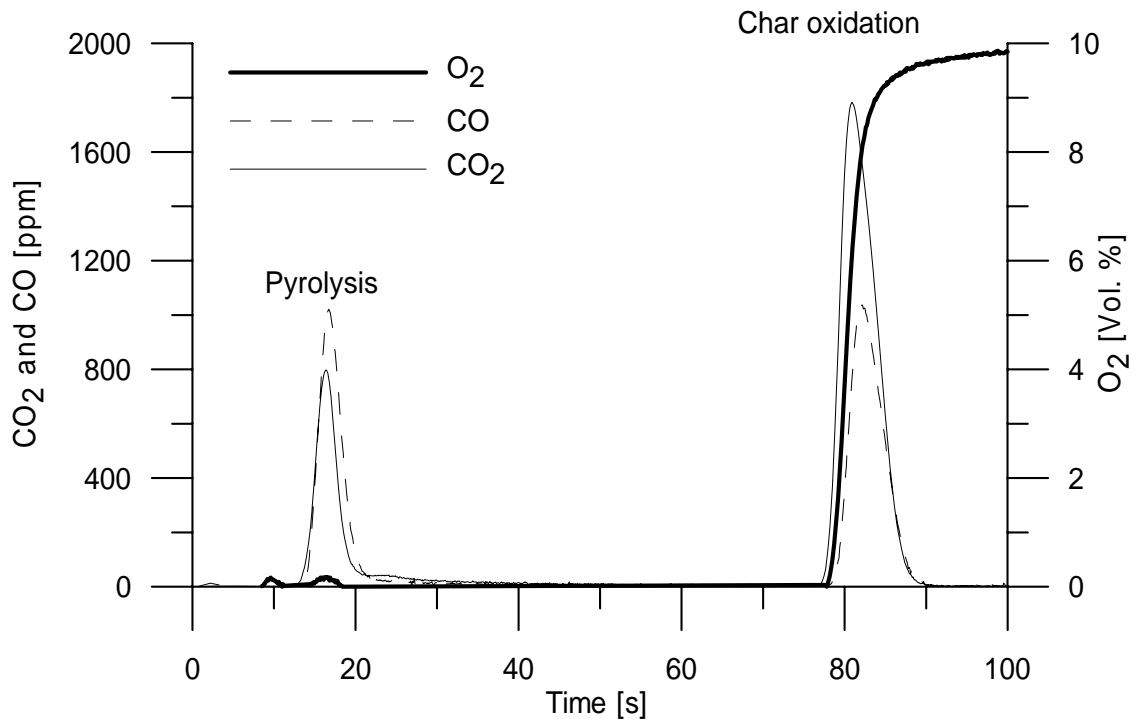


Figure 5-2: Measured effluent concentrations of O₂, CO₂ and CO for a TDF char particle converted at 750°C.

5.2.3.1 Deconvolution of Experimental Results

Deconvolution has previously been performed for a similar experimental setup, in order to study the decomposition and oxidation of Pyrite [14] and the char reactivity towards oxygen of different coals [3]. The in- and output signals are related to the residence time distribution in the following way [13]:

$$y_{i,out} = \int_0^t y_{i,in}(t-t') \cdot E_i(t') dt' \quad (5-7)$$

where $y_{i,in}$ and $y_{i,out}$ are the in- and output concentrations of specie i , and E_i is the residence time distribution of specie i in the system. For this experimental setup, $y_{i,out}$ is the concentration measured by the analyzer, and $y_{i,in}$ is the concentration of CO₂ or CO evolved at the position of the particle, or the concentration of O₂ which the char particle experiences. Fourier transformation on both sides of Figure 5-2 yields [14]:

$$F\{y_{i,out}\} = F\{y_{i,in}\} \cdot F\{E\} \quad (5-8)$$

from which the concentration $y_{i,in}$, which is needed for the kinetic analysis, may be derived by rearrangement followed by inverse Fourier transformation [14]:

$$y_{i,in} = F^{-1} \left\{ \frac{F \{ y_{i,out} \}}{F \{ E \}} \right\} \quad (5-9)$$

The Fourier and inverse Fourier transformations are calculated using the FFT and IFFT routines available in MATLAB 7.0. A filter equal to that used in the references [3,14] is applied in order to filter out noise in the frequency domain with frequencies above $17/64 \text{ s}^{-1}$ for CO and CO₂ and above $10/64 \text{ s}^{-1}$ for O₂.

The residence time distribution of the components CO, CO₂ and O₂ is determined by admitting a step response of the particular component, as closely to the reaction zone as possible, and subsequently recording the response on the gas analyser. The flows during the residence time distribution studies are equal to those used in the experiments. Figure 5-3 shows the normalised residence time curves for CO, CO₂ and O₂. The delays are about 11 seconds for O₂ and CO₂ and about 12 seconds for CO. The penetration increases from 0 to 1 in about 5 seconds indicating dispersion in the system. For an ideal plug-flow-reactor system exposed to a step response, the penetration should increase from 0 to 1 infinitely fast.

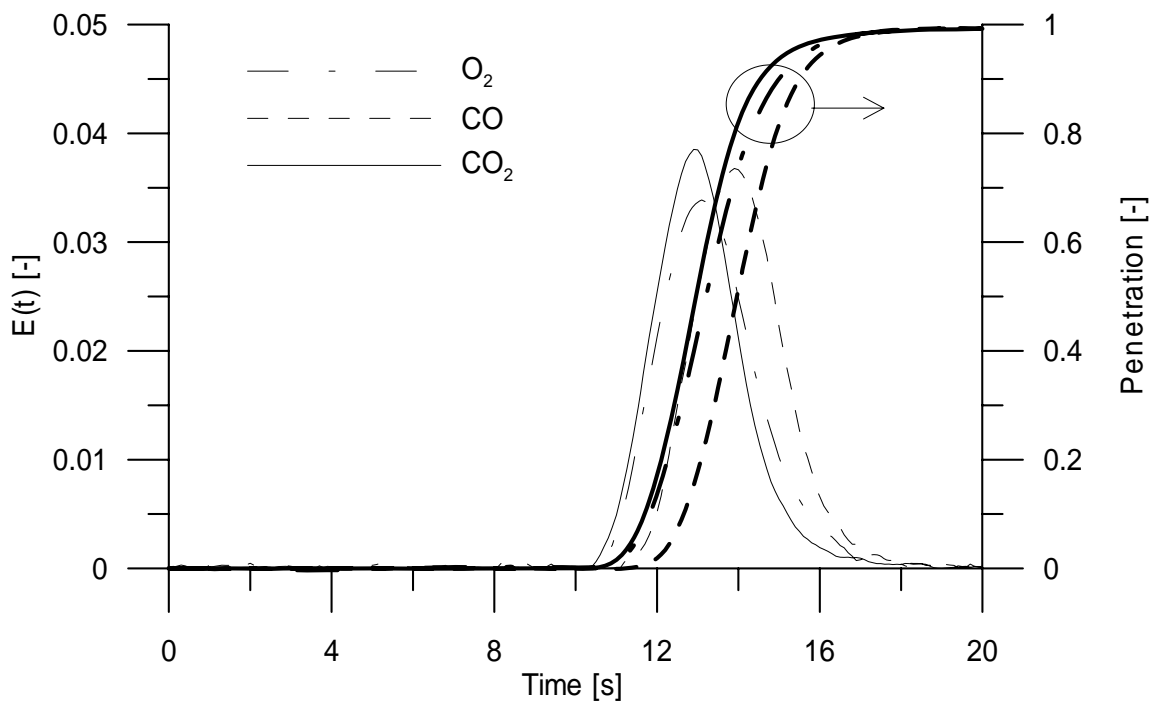


Figure 5-3: Normalised residence time distribution (E) and penetration based on step response experiments for CO, CO₂ and O₂.

The measured concentrations of CO and CO₂ may now be deconvoluted using the method outlined above. Figure 5-4 shows an example of deconvoluted concentrations of CO, CO₂ and O₂. It is observed that the measured concentrations are shifted about 11-12 seconds in accordance with the measured residence time distribution (see Figure 5-3). In addition, the deconvoluted peaks of CO and CO₂ are narrower than the measured profiles due to the fact

that the applied deconvolution method accounts for dispersion in the system. The deconvoluted O₂ profile shows a wave like profile for times above about 7 seconds which is due to the deconvolution method.

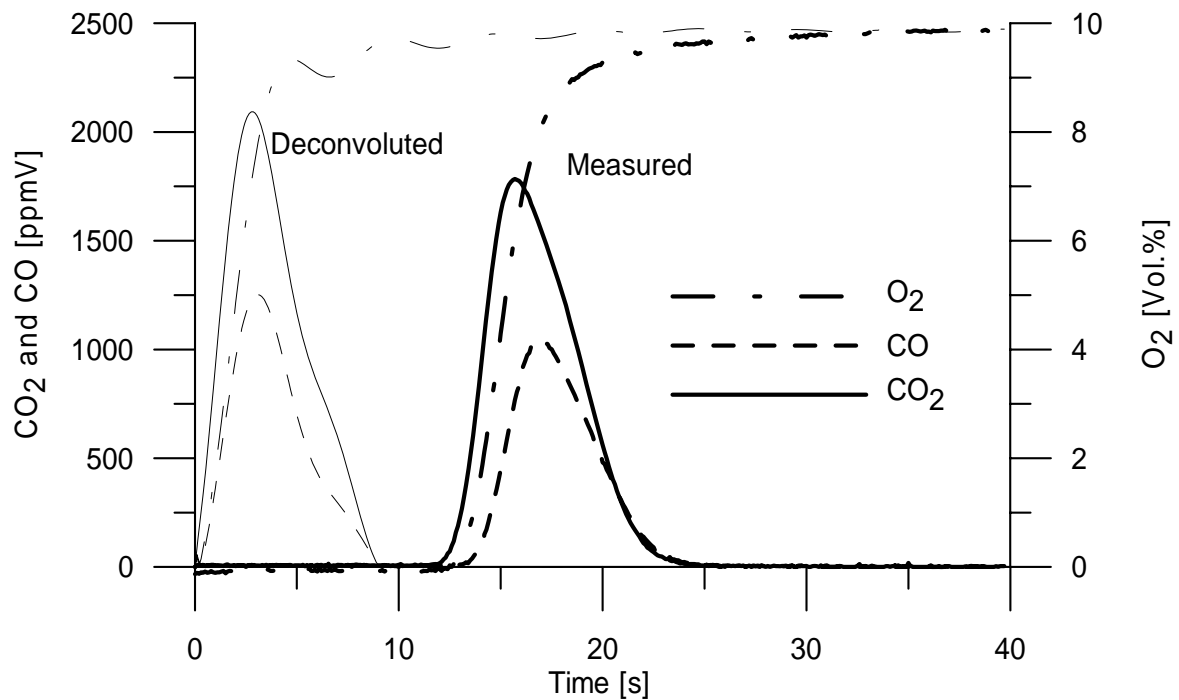


Figure 5-4: Deconvolution of measured gas species for a char oxidation experiment at 750°C (Only char oxidation stage shown).

5.2.3.2 Char conversion

The degree of char conversion against time may be derived, assuming that the char conversion is proportional to the carbon conversion, by integration of the deconvoluted concentration profiles of CO and CO₂:

$$X(t) = \frac{\int_0^t y_{CO} + y_{CO_2} dt}{\int_0^{\infty} y_{CO} + y_{CO_2} dt} \quad (5-10)$$

Figure 5-5 shows the derived conversions, using the method outlined in the last section, for the temperatures of 750, 800 and 850°C. The repeatability is seen to be good. At a temperature of 750°C, the conversion time is about 9 seconds. At 800 and 850°C, the conversion times is about 4.8 and 4.1 seconds respectively. The distance between the curves for 800 and 850°C is significantly smaller than the distance between 800 and 750°C, indicating that conditions are approaching a regime where mass transfer has an influence. At all temperatures, the derived conversion against time forms s-shaped curves.

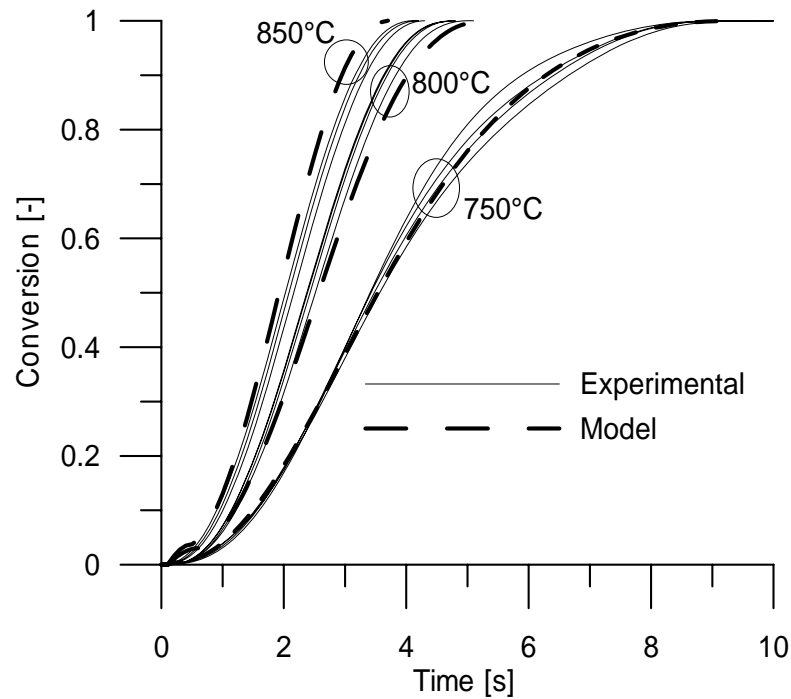


Figure 5-5: Conversion against time at temperatures of 750, 800 and 850°C. See section 5.2.4 for model.

5.2.3.3 Char oxidation products

The oxidation products from the char combustion have been investigated by integrating the measured CO and CO₂ signals in the following way:

$$\Pi = 1 + \frac{\int_0^{\infty} y_{CO} dt}{\int_0^{\infty} y_{CO} + y_{CO_2} dt} \quad (5-11)$$

Consequently, $\Pi \rightarrow 2$ if the product of the char combustion is CO or $\Pi \rightarrow 1$ if the product is CO₂. Intermediate values may be obtained for mixtures of CO and CO₂. Figure 5-6 shows the values of Π determined as a function of temperature. Π is observed to be about 1.36 to 1.38.

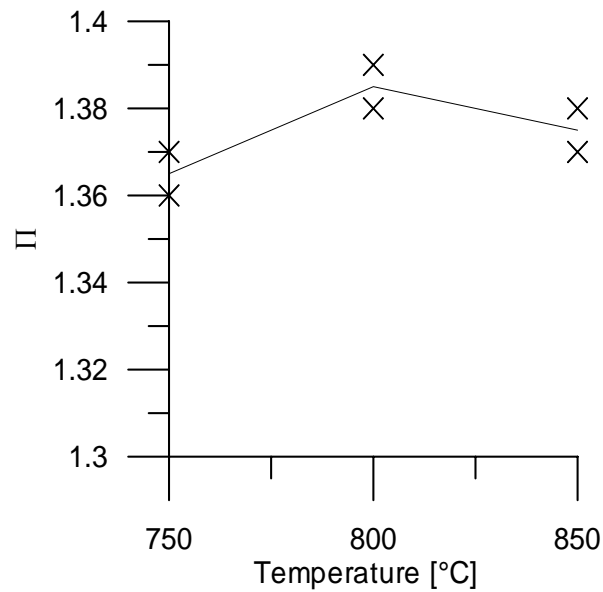


Figure 5-6: Values of Π as a function of combustion temperature where points represent results and the line represents an average value. Note the y-axis range.

5.2.4 Interpretation of combustion kinetics

From the experimental results, mass transfer was observed to have an influence at higher temperatures. To analyze the effect of simultaneous intrinsic kinetics and mass transfer, a mathematical model for diffusion and reaction inside the char particle is developed, and an iterative fitting procedure is applied in order to determine intrinsic kinetic parameters. In agreement with experimental observations (see also section 5.3.1.3), the conversion of the char particle is assumed to follow a constant size progressive conversion model, where O_2 enters and reacts with solid carbon throughout the particle at all times. Consequently, the particle size remains almost constant during conversion. For sake of simplicity, the following model assumptions have been made:

- 1) *The char particle is assumed to be spherical*
- 2) *The particle temperature is assumed to be uniform and identical to the surroundings*
- 3) *The effective intra-particle diffusion coefficient of O_2 is assumed to be constant*
- 4) *A change of char reactivity with carbon conversion is neglected, and the reaction rate is evaluated using the power law model (5-3) evaluated at 50% conversion*

For spherical geometry a differential mass balance of O_2 inside the particle becomes:

$$\frac{1}{r^2} \frac{d}{dr} \left(r^2 D_{O_2,eff} \frac{dC_{O_2}}{dr} \right) - R(C_{O_2}(r)^n) = 0 \quad (5-12)$$

The first term governs diffusion of O₂ inside the particle and the second term regards the reaction of O₂ with the char inside the particle. The corresponding boundary conditions are shown in (5-13) and (5-14) and represent film resistance at the outer particle surface and symmetry in the particle center respectively.

$$D_{O_2,eff} \left. \frac{dC_{O_2}}{dr} \right|_{r=r_p} = k_g (C_{O_2,\infty} - C_{O_2,r=r_p}) \quad (5-13)$$

$$\left. \frac{dC_{O_2}}{dr} \right|_{r=0} = 0 \quad (5-14)$$

The diffusion reaction model represents a non-linear model for $n \neq 1$ and must therefore be solved numerically, and the solution is further complicated by the convection boundary condition (5-13). Introduction of the dimensionless position $x = r/r_p$ and the dimensionless concentration $Y = C_{O_2}/C_{O_2,\infty}$ transforms the differential equation and its boundary conditions into the following:

$$\frac{1}{x^2} \frac{d}{dx} \left(x^2 \frac{dY}{dx} \right) - Y^n \phi^2 = 0 \quad (5-15)$$

$$\left. \frac{dY}{dx} \right|_{x=1} = \frac{r_0 k_g}{D_{O_2,eff}} (1 - Y_{x=1}) \quad (5-16)$$

$$\left. \frac{dY}{dx} \right|_{x=0} = 0 \quad (5-17)$$

where the Thiele modulus, ϕ , is obtained assuming that the reaction proceeds according to (5-1) and the power law model evaluated at 50% char conversion:

$$\phi^2 = \frac{r_p^2 \cdot A \cdot \exp\left(\frac{-E}{R_g T}\right) y_{O_2,\infty}^{n-1} \cdot (1-0.5)^m \cdot \rho_C / M_{w(C)}}{D_{O_2,eff} \cdot \left(\frac{P}{R_g T}\right) \cdot \Pi} \quad (5-18)$$

The dimensionless model is solved using orthogonal collocation [15], and the effectiveness factor is obtained by the ratio of reaction inside the particle to that of reaction outside the particle:

$$\eta = \frac{\int_0^1 R(Y(x)) x^2 dx}{\int_0^1 R(Y_\infty) x^2 dx} \quad (5-19)$$

Application of the power law model, the global reaction rate as measured in the experiments may be derived from (5-1) and (5-3) multiplied by the effectiveness factor:

$$\frac{dX}{dt} = \eta \cdot A \cdot \exp\left(\frac{-E}{R_g T}\right) y_{O_2}^n \cdot (1-X)^m \quad (5-20)$$

It is clear from the above equations, that mass transfer and intrinsic kinetics are linked and that the intrinsic rate parameters may only be determined considering both effects.

5.2.4.1 Physical parameters

The effective diffusivity of O₂ inside the tyre char particle is reported to vary between 2.3-3.3·10⁻⁶ m²/s [2] and an average value of 2.8·10⁻⁶ m²/s is used here. An average virgin fuel particle diameter of 150µm is used (see also section 5.2.2) and the resulting char is assumed to have the same particle size [9]. The char density of carbon is calculated from the volatile and ash content (see section 4.3.2), a virgin fuel density of 1100 kg/m³ (see section 4.5.4), a carbon content in the char of about 95 wt% [16] and the assumption of constant particle size [9]: ρ_C=1100·(1-Volatiles-Ash)·0.95. The molar ratio between carbon and oxygen is assumed to be constant and equal to Π=1.37 (see Figure 5-6). Finally, the mass transfer coefficient at the outer particle surface is calculated from a Sherwood correlation [17]:

$$Sh = \frac{k_g \cdot (2 \cdot r_p)}{D_{O_2}} = 2 + 0.69 Re^{1/2} \cdot Sc^{1/3} \quad (5-21)$$

5.2.5 Results of model analyses

The approach taken here is to initially assign an effectiveness factor of 1 for all temperatures and then fit the experimental data to equation (5-20) to obtain first set of A, E, n and m in equation (5-20). The derived kinetic parameters are subsequently applied in the effectiveness factor calculation, and new estimates of effectiveness factors at each temperature are obtained. The new effectiveness factors are used for another fit to obtain a second set of kinetic parameters from which a new set of effectiveness factors is recalculated. The iterative procedure continues until the effectiveness factors for each temperature converge to a single value. The fitting procedure is performed using a non-linear least squares method on the experimental data and the intrinsic kinetic parameters obtained are shown in (5-22). The

converged effectiveness factors from the calculation ranged from 0.76 to 0.37 at 750 and 850°C respectively confirming that the char combusted at these temperatures experienced mass transfer resistances, in accordance with the experimental results of Figure 5-5.

$$\frac{dX}{dt} = (1.5 \pm 5.1) \cdot 10^{10} \cdot \exp\left(\frac{-(193 \pm 28) \text{ kJ/mol}}{R_g T}\right) y_{O_2}^{0.66 \pm 0.1} \cdot (1-X)^{0.63 \pm 0.07} \quad [s^{-1}] \quad (5-22)$$

The effect of mass transfer limitations is also demonstrated from the predicted intra-particle O_2 -concentration profiles shown in Figure 5-7. The predicted O_2 -concentration profile at 850°C decreases sharply at the surface to a nearly zero concentration in the particle centre. The O_2 -concentration profile for a char particle combusted at 600°C shows that only slight mass transfer resistance exists at this temperature (calculated $\eta=0.99$) in agreement with Masi et al. [2] who conclude that the onset of mass transfer resistance occurs at about 600°C for TDF char particles in this size range. Finally, it may be observed from the concentration profiles that the dimensionless surface concentration is close to 1 indicating little resistance of external mass transfer.

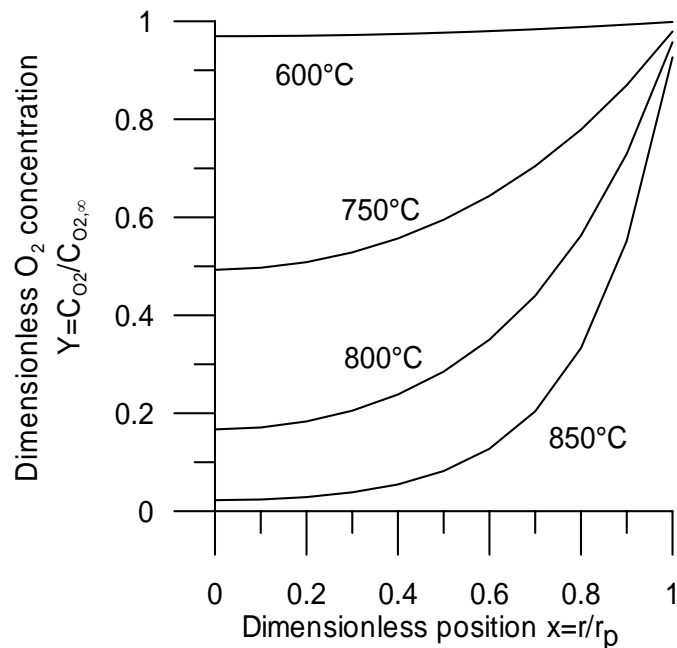


Figure 5-7: Predicted intra-particle dimensionless O_2 -concentration profiles through the char particles against dimensionless position at different temperatures (physical data provided above).

5.2.6 Comparison of Estimated Intrinsic Kinetics with Literature data

Figure 5-8 shows a comparison of the TDF char reactivity determined in this study with results from the literature. The three sets of kinetic data obtained at the low temperature represent those from the literature, and the kinetic data determined in this study is shown at higher temperatures. Fair agreement is observed between the low temperature data of Masi et

al [2] and Leung and Wang [8]. Significant discrepancies exist between the data reported by Conesa et al. [6] and those of Masi et al [2] and Leung and Wang [8]. The difference is about 5 orders of magnitude at low temperatures, decreasing to about 3 orders of magnitude at higher temperatures. Extrapolation of the kinetic data of Masi et al. [2] and Leung and Wang [8] to higher temperatures reveals that the intrinsic kinetics estimated in this work is in fairly good agreement with literature data. Extrapolation of low temperature data from Conesa et al. [6] to higher temperatures results in better agreement with data of Masi et al. [2], Leung and Wang [8] and the kinetics derived in this study, than at lower temperatures. This, however, is due to the significantly higher activation energy reported by Conesa et al. [6] (223 kJ/mol) compared to Masi et al. (133 kJ/mol) and Leung and Wang [8] (145 kJ/mol).

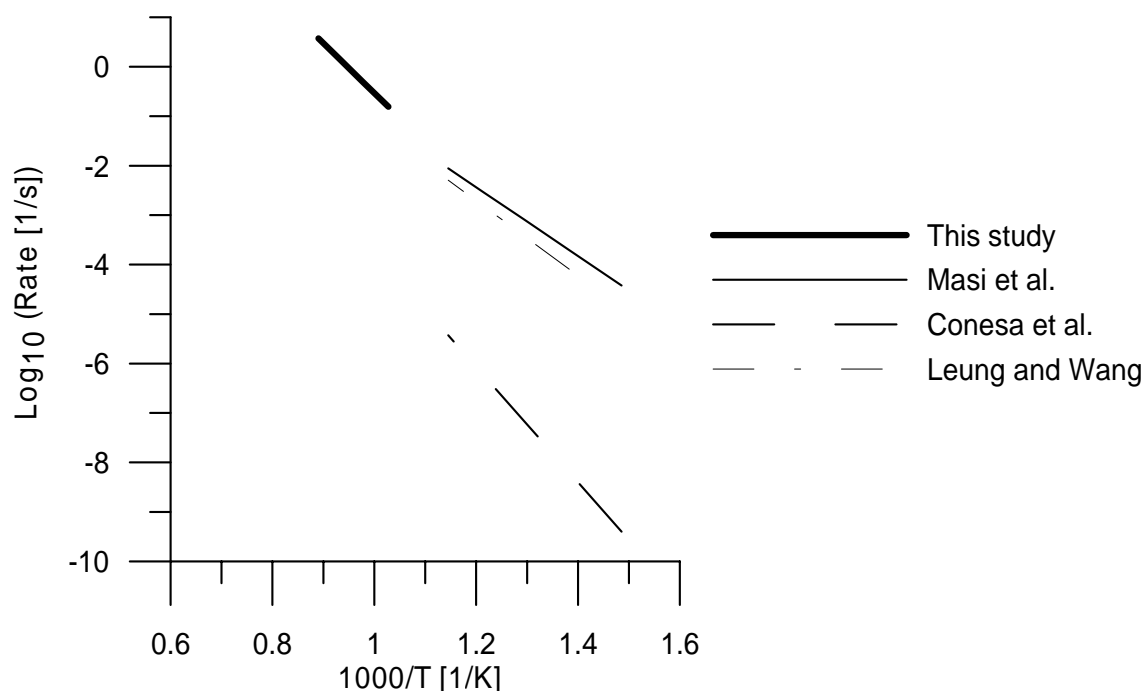


Figure 5-8: Arrhenius plot showing estimated TDF char reactivity and those from the literature (Masi et al. [2], Conesa et al. [6] and Leung and Wang [8]). Rate determined at 21 Vol. % O₂ in order to compare with the data of [8] and X=0.5 to compensate for the applied pore model (same trend obtained with X=0.25 and 0.75).

5.2.7 Conclusions

Combustion experiments have been performed in a fixed bed reactor at 750-850°C with tyre rubber masses of about 1-2 mg in up to 10 vol.% O₂ and particle sizes between 102-212 μm. The results show that for these particle sizes, a char conversion time of about 9 and 4.1 seconds can be expected at 750 and 850°C, respectively, and that mass transfer mass transport effects were influencing the measured rates at the investigated conditions. Considering the mass transfer of O₂ through the boundary layer, diffusion in the char matrix and chemical reaction, a mathematical model was developed and a scheme for the intrinsic kinetics was proposed. A comparison of the derived kinetics with those from the literature showed fair agreement.

5.3 Modeling TDF Char Combustion in the Kiln System

The aims of this section are to 1) develop an understanding of TDF char conversion in calciner systems, 2) to elucidate controlling factors for char conversion and 3) to discuss what can be done to enhance char conversion, and 4) to develop a realistic in-line-calciner model in order to study co-firing of a traditional calciner fuel and conversion of large TDF char particles discharged from the HOTDISC and into the calciner.

5.3.1 Pre Modeling Considerations

5.3.1.1 Char Particle size Distribution

It was observed experimentally, that TDF forms a crackling char structure under devolatilization with particle sizes in the mm range (see also section 4.3), which are expected to disintegrate once discharged from the HOTDISC table and into gas phase of the HOTDISC and/or the calciner. Consequently, for precise prediction of char burnout, the particle size distribution of the resulting char particles must be known.

In order to quantify the resulting char particle size distribution, a char batch prepared from a single piece of lump tyre rubber was subjected to sieving. However, the sieving process could erode the outer particle surface or break the particles, and consequently produce a *false* size distribution shifted towards lower particle sizes. In order to investigate these phenomena, it was decided to produce two sieving analyses with durations of 3 and 10 minutes. The investigated tyre rubber was identical to that described in section 4.3 and the char batch was prepared at 840°C in inert conditions in the macro-TGA described in section 4.3.4.

The results of the sieve analyses are shown in Figure 5-9. It is observed that the measured particle size distribution is identical for the sieving analyses performed with duration of 3 and 10 minutes, indicating that the char particles are very rigid with regard to erosion or breakup. The particle size distribution shows that about 75 wt. % of the TDF char particles have a particle size above about 1 mm, about 50 wt. % above 2 mm, and about 25 wt. % of the particles have a particle size above about 3.2 mm. Comparisons with literature data of Li S.Q. et al. [16] for TDF char particles prepared in a laboratory rotary kiln at a temperature of 650°C show good agreement up to a particle size of about 3 mm. The discrepancies for larger particle sizes may be a consequence of differences in char preparation conditions.

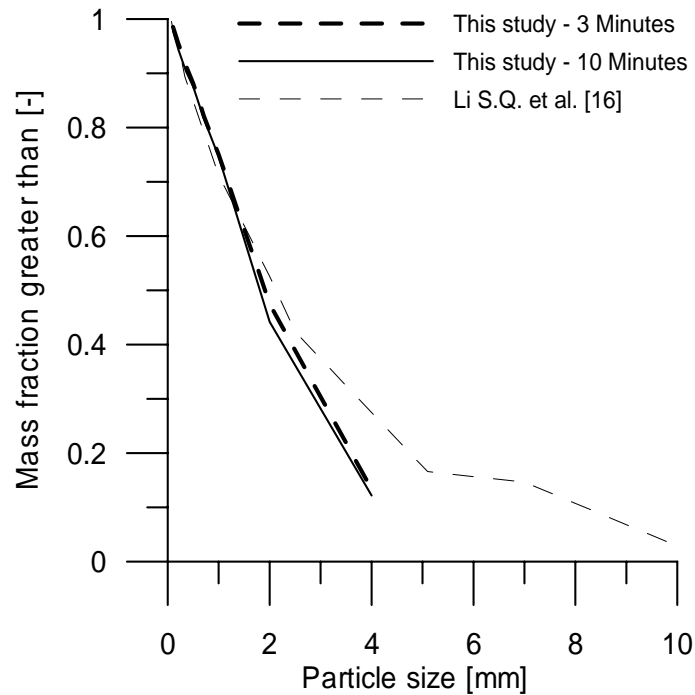


Figure 5-9: Measured TDF char particle size distribution for a char prepared at 840°C in inert conditions and comparison with literature data.

5.3.1.2 TDF char particle movement

Raw material particles and fine coal particles are known to have a residence time in suspension calciners which is about 4 times larger than the gas residence time, which was attributed to the clustering of small particles (see also section 2.4). However, as the TDF char particles are significantly larger than raw material particles, they may not behave as small particles, and as the residence time is important for predicting TDF char burnout, brief analyses of TDF char particle behaviour in a suspension calciner is made in this section.

The forces acting on a large TDF char particle suspended in the calciner are the gravitational force and the drag forces of gas and solid raw material particles (see Figure 5-10). Regarding the drag force from raw material particles, it is known from fluidized bed experiments that particles with terminal settling velocities higher than the upward gas velocity may be carried upward [18]. The drag force of solid raw material particles in calciner systems is also expected to influence particle dynamics of larger char particles.

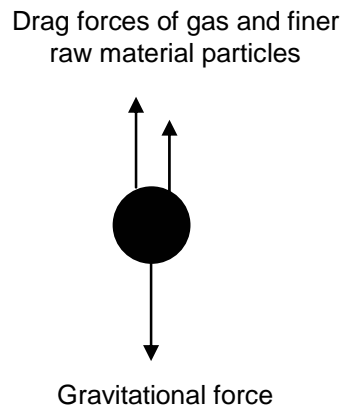


Figure 5-10: Forces acting on a large char particle in a suspension calciner system.

If the drag force of raw material particles is disregarded and the char particles are assumed to be spherical, the calculated terminal settling velocity for TDF chars with relevant particle sizes is shown in Figure 5-11. With these assumptions, it is observed that TDF char particles with sizes above about 3.5 mm have a terminal settling velocity higher than the upward gas velocity of about 8 m/s. They are consequently carried downwards to the riser (between the rotary kiln and calciner system), where the gas velocity is significantly higher causing them to re-circulate in the lower part of the calciner until they are small enough to be entrained with the gas.

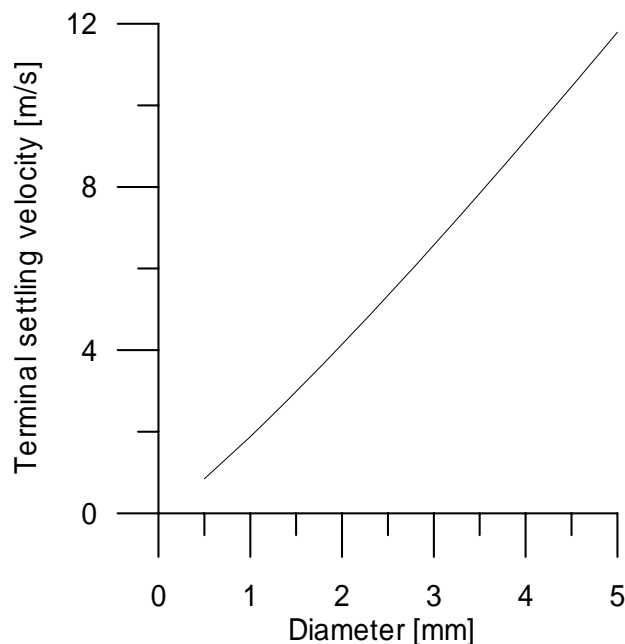


Figure 5-11: Calculated terminal settling velocities of large TDF char particle sizes at conditions relevant to a suspension calciner.

In fluidized bed systems, the solid movement typically shows a core annulus flow, where particles are transported upwards in the centre of the flow and downward close to the wall, and this flow behaviour may also be a possibility for suspension calciners (see also CFD

simulations described in section 2.4.3.1). A model, including the gravitational force and the drag force exerted by finer particles, for upward transport of larger particles in the centre of the flow is shown in equation (5-23) [18].

$$v_{p,upward} = v_{suspension,upward} - \rho_{particle}^{0.5} \cdot D_{particle}^{0.573} \cdot \sqrt{\frac{9.82 \text{ m/s}^2}{0.7 \cdot \rho_{suspension}}} \quad (5-23)$$

This model is used to analyze the effect from drag of fine raw material particles on the upward transport of large TDF char particles in the centre of a suspension calciner. Figure 5-12 shows the mean upward velocity determined against particle size at two suspension concentrations. The upward velocity is observed to decrease with particle size. No negative upward velocity is found, under the investigated conditions, indicating that TDF char particles are carried upward in the transport zone. In addition, it is observed that lowering the density of the suspension by assuming a similar gas and solid residence time results in a lower upward particle velocity as a consequence of a lowered drag force of fine raw material particles on the TDF char particles. Finally, as the drag force of the gas is not included in the model, a slightly higher upward particle velocity is to be expected.

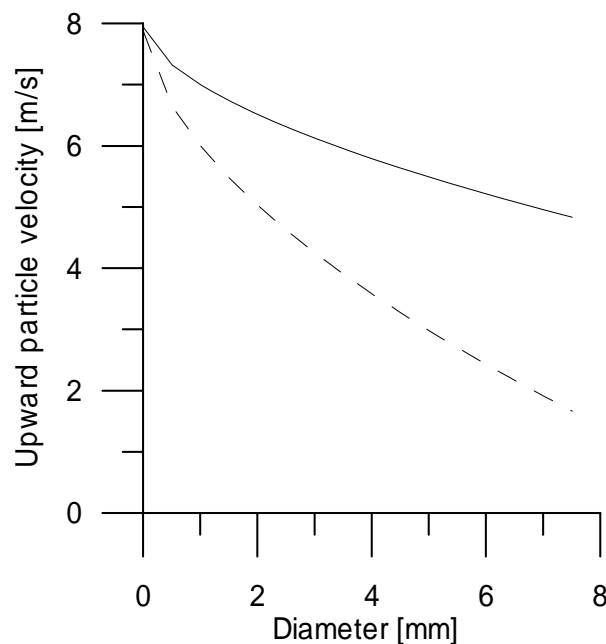


Figure 5-12: Calculated mean upward TDF char particle velocity in the centre of the suspension calciner. The upper curve represents the situation where the raw material particles have a residence 4 times greater than the gas, and the lower curve represents the limiting situation where the raw material and gas residence time is identical, i.e. differences in suspension density.

From these simple analyses it is shown that disregarding the drag force of finer raw material particles may result in wrong predictions of upward velocity of large particles in the centre of the calciner.

The model approaches used here to describe the movement of large solid TDF char particles through the calciner are:

- a) *As the mass fraction of large TDF char particles is significantly lower than the mass fraction of raw material particles in the suspension calciner (below about 0.5 wt.%), the large char particles are assumed to move with the clusters of raw material particles. Consequently, the residence time of all solids becomes four times the gas residence time (see also section 2.4), with a mean slip velocity between gas and particles of $8\text{ m/s} \cdot (1-1/4) = 6\text{ m/s}$ to be used for calculation of external mass transfer coefficients.*
- b) *The large solid TDF char particles travel upward with a velocity according to that of equation (5-23), where the upper curve of Figure 5-12 is applied as this is closest to real conditions. The slip velocity between gas and individual TDF char particles are calculated as the difference between the gas and upward particle velocity,*

Figure 5-13: Model approaches to simulate TDF char particle movement in suspension calciner.

5.3.1.3 Conversion pathway

The model analyses performed in section 5.1 demonstrated that TDF chars are very reactive, at temperatures relevant to the calciner of 850°C and higher. As a consequence of this high reactivity, the intra particle oxygen diffusion was shown to be very limited due to oxygen being consumed near the outer particle surface. For larger particle sizes equal to those of Figure 5-9, the limited intra-particle oxygen diffusion, may be expected to be more prominent (remember that the analysis in section 5.2 was for an average particle size of about 150µm). A simple combustion experiment, where a 4 mm TDF char particle was partially combusted, supported the theoretical analyses, as an intra-particle char structure was observed to be surrounded by an outer ash layer (see Figure 5-14).

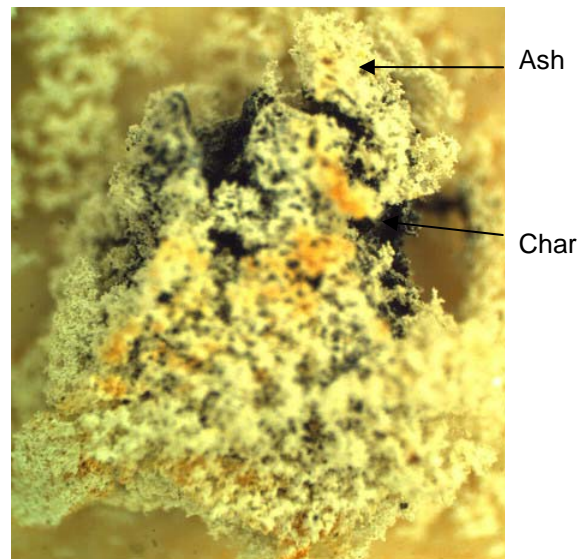


Figure 5-14: TDF char particle size of about 4 mm partially combusted at 800°C and atmospheric conditions

In addition, the ash layer was observed to be very porous, and consequently easily removed by slight mechanical interaction of the particle with tweezers. In the kiln system, the mechanical action of suspended raw material particles is expected to remove the ash layer in

a similar manner, leaving an almost unconverted char particle. Consequently, the model to be used in order to describe the conversion of large TDF char particles in a suspension calciner should be a shrinking particle model, identical to pathway G of section 4.1.

5.3.2 Single Particle Model for TDF char combustion

As identified above, a shrinking particle model should be adequate to simulate the conversion of TDF char particles in calciner systems. Consequently, the steps in the model are:

- 1) *Transport of O_2 from the surrounding gas through the boundary layer to the outer particle surface.*
- 2) *Reaction of solid carbon and O_2 at the outer particle surface.*

In addition, the single particles are assumed to be spherical and isothermal with a temperature equal to the surrounding gas. The isothermal assumption may be questionable in the case of larger particles that are susceptible to over-temperatures during combustion. However, it will be demonstrated in the next section, that the presence of an over-temperature will not change the model result under conditions relevant to a cement kiln system.

The transport of O_2 to the outer particle surface may be written as the mass transfer coefficient multiplied by the driving force:

$$r = -k_g \frac{p}{R_g T} (y_{O_2, \infty} - y_{O_2, surf}) \quad \left[\frac{\text{mol } O_2}{\text{m}^2 \text{ s}} \right] \quad (5-24)$$

The reaction at the particle surface may be written as the intrinsic volumetric kinetics derived in section 5.1 multiplied by the volume/surface ratio and the molar carbon density according to Laurendau [5] (may also be derived from equation (4-19) with the assumption of an isothermal particle). The product distribution ratio between CO and CO_2 , Π (see also section 5.2), is used to convert between molar rates of carbon and O_2 . The reaction rate is calculated at $X=0.5$.

$$r = -\frac{r_p \rho_c}{3 \Pi} \cdot A \cdot \exp\left(\frac{-E_A}{R_g T}\right) y_{O_2, surf}^n \cdot (1-0.5)^m \quad \left[\frac{\text{mol } O_2}{\text{m}^2 \text{ s}} \right] \quad (5-25)$$

At pseudo steady state, the external O_2 flux balances the consumption at the particle surface and differential movement of the outer surface may be shown to yield:

$$\frac{d r_p}{dt} = - \frac{\Pi \cdot r}{\rho_c} \quad (5-26)$$

or expressed in terms of conversion for a particle with an initial diameter $r_{p,0}$:

$$\frac{dX}{dt} = 3 \frac{r_p^2}{r_{p,0}^3} \frac{\Pi \cdot r}{\rho_c} \quad (5-27)$$

The differential equation (5-26) or (5-27) is easily solved for $n=1$ by solving for the unknown surface oxidizer concentration and rate in (5-24) and (5-25). However, for $n \neq 1$, a numerical solution procedure must be applied before the differential equation(s) can be integrated (A Newton iteration is applied here). In addition, the external mass transfer coefficient is influenced by the changing particle size, and that must also be included in the algorithm. The differential equation is integrated using the numerical integration routine Siruke [15].

The physical and chemical parameters applied are identical to those of section 5.2 and the external mass transfer coefficient is calculated using (5-21) with the approaches for the gas-particle slip velocity in Figure 5-13. The remaining parameters are the initial particle size, temperature and the concentration of oxidizer.

5.3.3 Analysis of Single Particle Model

Initially, the developed char combustion model is solved for single particles at different conditions in order to study important effects of external mass transfer rate (slip velocity between particles and gas), surrounding oxygen concentration, particle size and temperature. This initial model study is performed, because it 1) increases the understanding of behaviour of large particles, and 2) eases the interpretation of the more detailed in-line-calciner model to be presented in section 5.3.4.

Figure 5-15 shows the simulated results for conversion against time of single TDF char particles with initial diameters of 0.5, 2 and 4 mm at two different oxygen concentrations at 850°C. For all particle sizes and both model approaches, it is observed that the conversion time is almost inversely proportional with the oxygen concentration. For instance, the model predictions using approach a) for an initial particle diameter of 4mm, yields a conversion time of about 246 seconds at 2.5 vol.% O₂ decreasing to 123 at 5 Vol.% O₂. The almost inverse proportionality is due to the surface reaction being faster than the O₂ transport through the boundary layer, and as a result the surface concentration approaches zero (verified by the model simulations). Consequently, the conversion is controlled almost exclusively by external mass transfer rate causing the inverse proportionality between oxidizer concentration and conversion time. The external mass transfer controlled conversion

is also observed when comparing the conversion times between approach a) and b), where the lower slip velocity in approach b) lowers the external mass transfer coefficient and consequently the conversion rate, i.e. prolonged conversion time (see also section 5.4.4). The profile of the conversion again shows a curved shape at higher conversions. This is due to the particle being almost completely consumed ($D_p \rightarrow 0$), which enhances the external mass transfer, and the surface kinetics therefore also become important, as indicated by an increasing surface oxidizer concentration. The effect of particle size is also evident from Figure 5-15. For instance in model approach a), the conversion time increases from 5.1 to 39.7 to 123 seconds for particles of initial diameters of 0.5, 2 and 4 mm respectively at 5 vol.% O_2 .

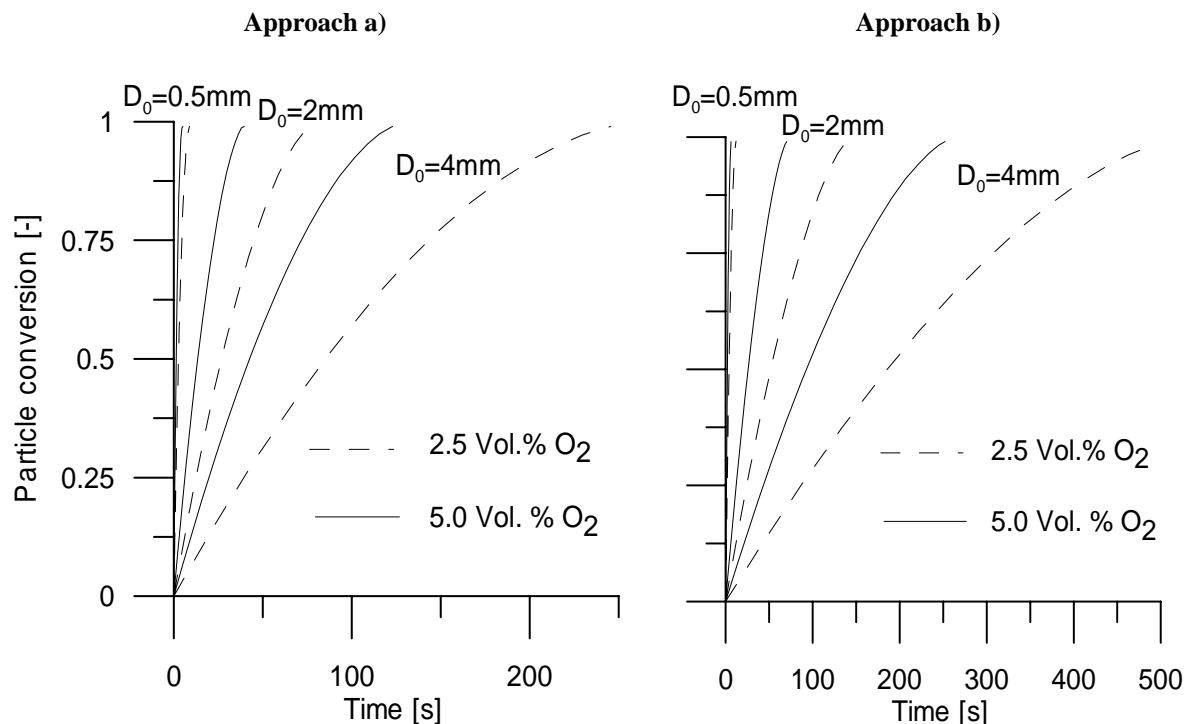


Figure 5-15: Results of single particle model for conversion at 850°C at different oxygen concentrations and different initial particle diameters for the slip velocities according to the model approaches in Figure 5-13. Note the difference in time scale.

The effect of temperature on conversion rates/times is demonstrated in Figure 5-16 for three initial particle diameters of 0.5, 2 and 4 mm combusted at 850°C or 1150°C and 5 Vol.% O_2 . For model approach a) and an initial particle diameter of 0.5 mm, the simulated conversion time decreases from 5.1 to 3.1 seconds when increasing the temperature from 850 to 1150°C at 5 vol.% O_2 , or equivalent to a decrease in conversion time of 39%. A similar trend is observed for model approach b) corresponding to a decrease in conversion time of 31%.

For the initial particle diameters of 2 and 4 mm, no significant effect of increased temperature on conversion time is observed. The observed differences in effect of temperature on conversion between the 0.5 mm particle and the larger particles are due to the 0.5 mm particle being both under kinetic and mass transfer control, whereas the larger

particles are almost exclusively influenced by external mass transfer. The mass transfer controlled conversion of the larger particles may also be observed from the almost perfect overlap of the conversion curves initially. At larger conversions, the curves for different temperatures separate as chemical kinetics become of higher influence, and the higher surrounding temperature yields a slightly faster conversion. The negligible demonstrated effect of temperature in the investigated temperature interval on the conversion of larger particles indicates that the assumption of an isothermal particle is good.

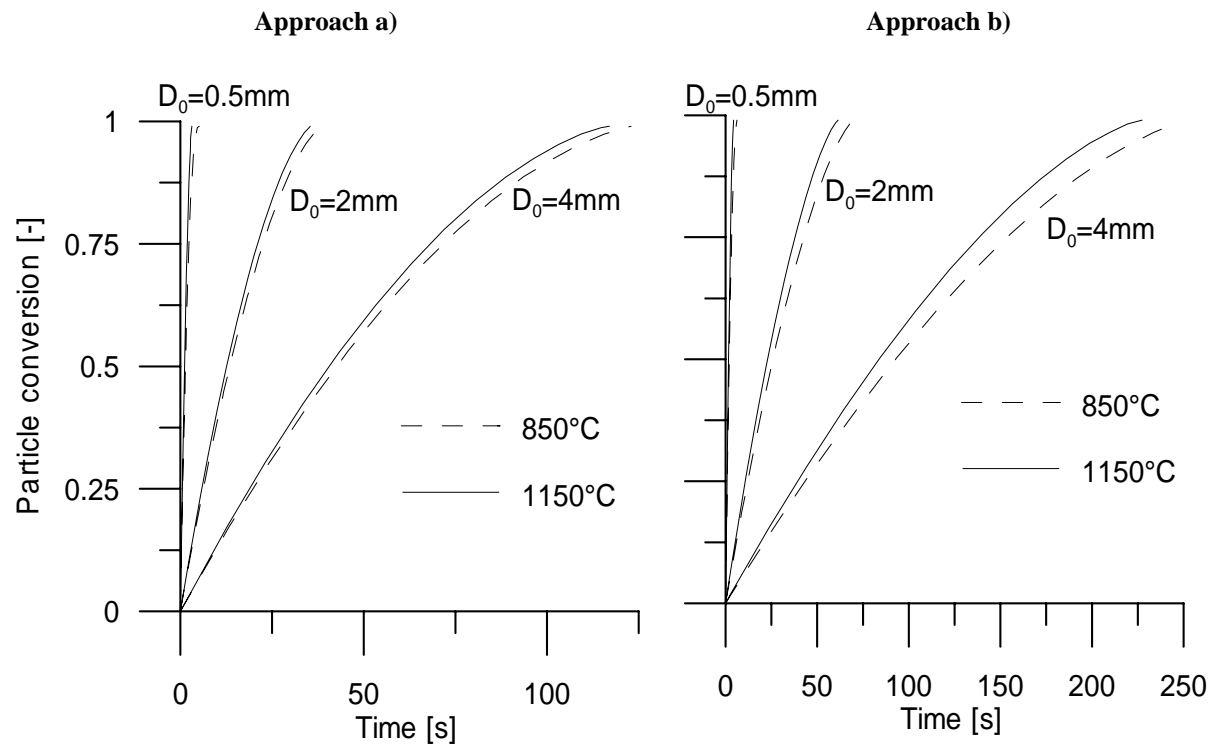


Figure 5-16: Results of single particle model for conversion at 850 and 1150°C at 5 Vol.% O₂ to illustrate effect of temperature and particle size for the slip velocities according to the model approaches in Figure 5-13. Note the difference in time scale.

From the analyses of the single particle model, it may be concluded that the conversion rate of TDF char may be enhanced by increasing the oxidizer concentration, increasing external mass transfer rate coefficient or reducing the particle size. However, if the particle size is reduced to very small sizes, the char conversion rate may also be expected controlled by chemical kinetics and consequently influenced by a higher combustion temperature.

5.3.4 In-Line-Calciner Model

The aim of this section is to develop a model in order to 1) simulate the conversion of large TDF char particles discharged from the HOTDISC and into the In-Line-Calciner, and 2) improve the understanding of conversion of large TDF char particles in ILC systems. The system to be simulated can be seen from the figures 2-4 and 3-7. The assumptions made in the simulation are as follows:

- 1) 37 % fuel substitution of calciner fuel in the HOTDISC in conjunction with measurements at plant B (see also chapter 6).
- 2) Devolatilization of calciner fuel takes place instantaneously after admission. The devolatilization products are oxidized completely and instantaneously.
- 3) Devolatilization of the large TDF particles takes place in the HOTDISC (see also chapter 6). The devolatilization products are oxidized completely and instantaneously.
- 4) No char oxidation takes place in the HOTDISC.
- 5) The gasses from the HOTDISC and the lower part of the calciner are mixed instantaneously and completely.
- 6) The gas moves upward in plug flow inside the calciner. The gas residence time from this point and up to the bend of the CO-eliminating duct (see figure 2-5) is assumed to be about 3.3 seconds.
- 7) The gasses move downward in plug flow in the downcomer. The gas residence time in this section is assumed to be 1 second.
- 8) The residence time of pulverized coal particles and raw meal is assumed to be 4 times the gas residence time in the calciner (see also section 2.4).
- 9) The movement of larger TDF char particles entrained from the HOTDISC is assumed to follow model approach a) or b) of Figure 5-13 and up to the bend of the CO-eliminating duct. The particles follow the gas in the downcomer.
- 10) The conversion of calciner fuel char under kinetic control is modeled by an expression of bituminous coal char conversion [3]:

$$\frac{dX}{dt} = 3.6 \cdot 10^6 \left[\frac{\text{cm}^{1.62}}{\text{mol}^{0.54} \cdot \text{s}} \right] \cdot \exp\left(\frac{-83.2 \text{kJ/mol}}{R_g T}\right) \cdot (1-X)^{1.15} \cdot C_{O_2}^{0.54} \quad (5-28)$$

- 11) The conversion of TDF char particles follows the model developed in section 5.3.2. A discrete particle size distribution is used to simulate the initial particle size variation:

\widetilde{D}_0 [mm]	Weight fraction [kg/kg]
0.43	0.25
1.5	0.28
3	0.34
4	0.13

Table 5-1: Discrete particle size distribution of TDF char used in the calciner model.

- 12) The concentration of O_2 is determined at all positions from mass balances considering O_2 consumed in combustion and dilution of CO_2 from calcination.

The complete ILC model results in 5 coupled differential equations: (5-28) and 4 equations for each discrete TDF char particle size which is solved using the Fortran subroutine Siruke [15]. The initial conditions for the system are a zero conversion for the four TDF fractions and the bituminous coal. As for the single particle model, a numerical solution method is applied in order to resolve the surface concentration at the four different discrete TDF char particle sizes. Algebraic equations are used to determine the concentration of O₂ and mass transfer coefficients for each particle size in the distribution. Finally, two temperature profiles in the calciner have been simulated in order to investigate the situation with or without a high temperature oxidation zone (see also section 2.4): 1) Gas temperature of 850°C throughout the calciner reflecting the equilibrium temperature of CaCO₃ decomposition, and 2) a high temperature zone with 1100°C in the first 1.65 seconds (half the calciner residence time) followed by 850°C for the remaining time.

5.3.4.1 Results of ILC Model

The results of the ILC model simulations are shown in Figure 5-17 in terms of conversion against *gas* residence time. The left part shows results using model approach a) of Figure 5-13, and the right part shows the results using approach b).

The upper parts of the figures show the total char conversion determined from the HOTDISC fuel substitution ratio and the char fractions of calciner and HOTDISC fuel respectively. For both investigated model approaches, the rates of total char conversion are faster with the presence of a high temperature zone than without. In addition, the total char conversion in the downcomer - which is the parameter of interest with regard to preventing unburned carbon in the material inlet of the rotary kiln (see also sections 3.2 and 3.3) – is slightly higher with the presence of a high temperature oxidation zone in the calciner. A similar trend is observed for the coal char conversion. The determined total char conversion is linked to the total carbon burnout in the calciner and HOTDISC system shown in Table 5-2.

	<i>approach a)</i>	<i>approach b)</i>
<i>With a high temperature zone</i>	91.3	88.9
<i>Without a high temperature zone</i>	86.3	83.0

Table 5-2: Model predicted carbon burnout (in %) for an ILC with HOTDISC.

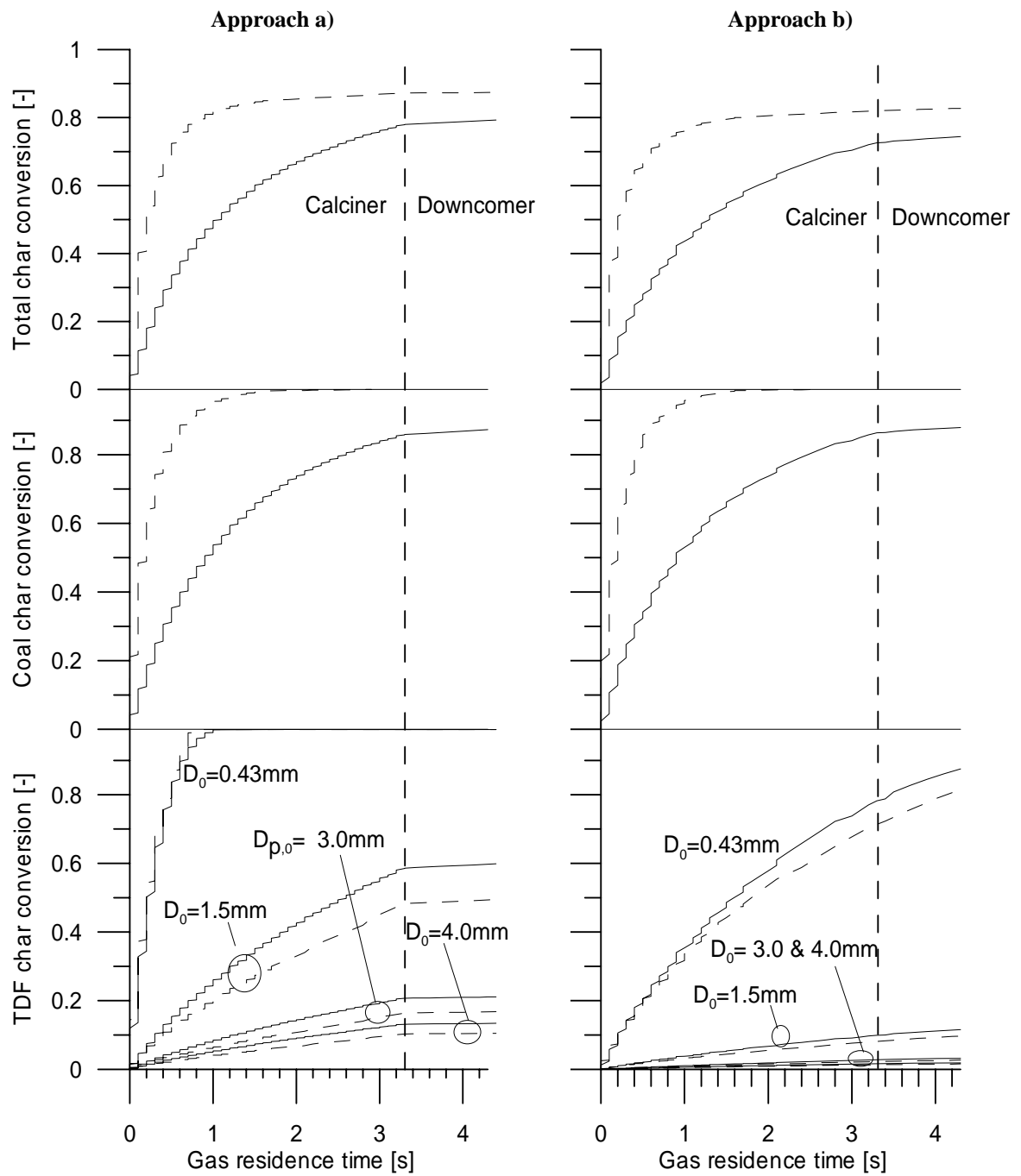


Figure 5-17: Results of ILC model for char burnout as a function of solid residence time. The full lines represent 850°C throughout and the dashed lines represent a high temperature zone of 1100°C half the calciner residence time (excluding downcomer).

For model *approach a*), the predicted conversion of the four discrete initial TDF char particles is seen from the lower part of Figure 5-17. The initial particle diameter of 0.43 mm is seen to be slightly influenced by the presence of a high temperature oxidation zone, due to this particle size being susceptible to kinetic control. This particle size is seen to be converted after about 1 second (gas residence time) with or without a high temperature oxidation zone. For the larger particle sizes, limited char conversion is observed from the model simulations. The TDF char particles with an initial size of 1.5 mm is predicted to be about 49 and 59% converted with and without high temperature oxidation zone,

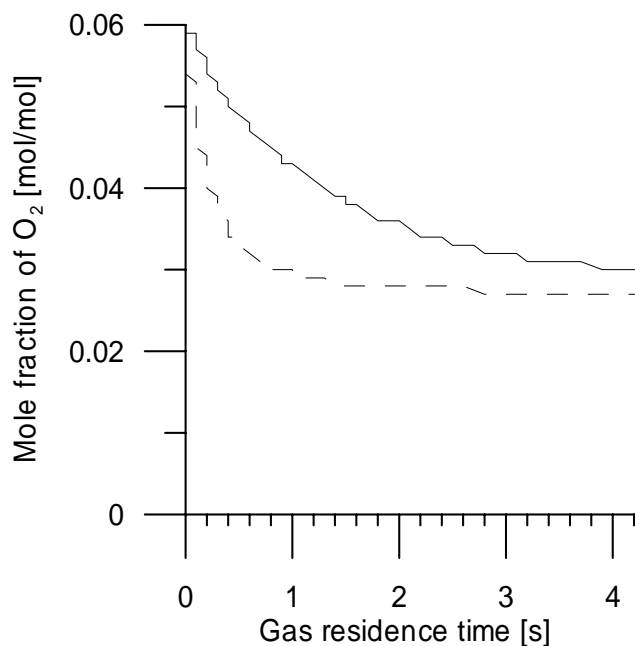


Figure 5-18: Oxygen profile for calciner model approach a) for with (dashed) or without (full) a high temperature oxidation zone as a function of solid residence time. Note the y-axis range

respectively. The larger particles with initial diameters of 3.0 and 4.0 mm are observed to be converted only about 10-20 %. For the three largest particle fractions of TDF char, the presence of a high temperature oxidation zone yields lower char conversion. This is due to the high temperature zone favoring the oxidation of calciner coal under kinetic control, as seen in the middle part of Figure 5-17, which consequently consumes a higher amount of oxidizer. The increased oxygen usage lowers the O₂ concentration (see Figure 5-18), and thus reduces the conversion rate of TDF char particles, as a consequence of the conversion of these particle sizes being controlled by external mass transfer as demonstrated in section 5.3.3. For model *approach b*), similar trends are observed, except that the obtained TDF char conversion is significantly lower than that for model approach a) and consequently also a lower total carbon burnout in Table 5-3. This is due to the fact that the TDF char particles travel faster through the calciner in model approach b) than a), which decreases the solid residence time and the slip velocity between gas and TDF particles (lower external mass transfer rate).

Despite the presence of a high temperature zone reducing burnout of large TDF char particles, the highest total char carbon conversion is still obtained with a high temperature oxidation zone. This is a consequence of the char fraction of the calciner fuel being significantly higher than in the alternative fuel (62.9 wt.% compared to 21.6 wt.%) and due to the fact that 37% of the total calciner and HOTDISC fuel originates from the alternative fuel.

5.3.4.2 Comparison of Calciner Model with Plant Data and Discussion

The only available data from an industrial cement plant equipped with a HOTDISC for comparison with the calciner model is the overall degree of carbon burnout in the calciner system. Data from an industrial plant, operated under the same conditions as in the calciner model and with a high temperature zone, yields a carbon burnout of above 99%, i.e. significantly more than the model predicted values of 88.9-91.3% (see Table 5-2). The reasons for the lower burnout in the model are caused by insufficient burnout of the larger TDF char particles, which may be attributed to the following model assumptions:

- 1) *Initial char burnout in the HOTDISC is not considered.*
- 2) *The gas from the HOTDISC is assumed to mix instantaneously with the gas from the rotary kiln and riser.*
- 3) *Possible attrition and fragmentation phenomena of TDF chars in the calciner are ignored.*
- 4) *The movement of larger TDF char particles is not adequately described*

Re 1): If the devolatilization process occurs according to pathway I in the HOTDISC, with a simultaneous production of smaller char particles entrained into the gas, these particles may combust in the gas phase. A model calculation for combustion of TDF char particles entrained into the gas stream of the HOTDISC yields the conversions at the end of the HOTDISC as shown in Table 5-3. The small particle fraction with an initial diameter of 0.43 mm is seen to be almost completely converted, whereas the other particle fractions are only slightly converted. In order to simulate the possible initial char burnout in the gas phase of the HOTDISC, the previous full ILC model may be applied with the figures of Table 5-3 as new initial conditions. This yields a total carbon conversion in the calciner system of 91.7% and 89.5% for model approach a) and b) respectively, i.e. only slightly higher than the original calciner model, but not sufficient to explain the discrepancies. Consequently, the effect char oxidation in the HOTDISC cannot explain the differences between modeled carbon conversion and measured data.

D_0 [mm]	Conversion in HOTDISC [-]
0.43	0.80
0.85	0.081
3.0	0.022
4.0	0.012

Table 5-3: Predicted conversion of TDF char particles entrained into the gas stream of the HOTDISC using the developed model. Parameters are: $y_{O_2}=0.15$ mol/mol (measured average value), residence time of 1 sec. (see section 3.2.2.1), relative velocity of 0 m/s between gas and particles (particles are entrained) and a temperature of 900°C.

If the devolatilization process of the TDF utilized in the HOTDISC follows pathway E, limited char oxidation takes place in the HOTDISC (see also chapter 6) and this cannot explain the differences between modeled carbon conversion and measured data either.

Re 2): In industrial systems, a more gradual mixing of these two streams may occur as depicted in the CFD simulation of Figure 5-19. A slow mixing of the gasses, may cause the char particles from the HOTDISC to be entrained into a gas stream with a significantly higher O_2 concentration of initially about 15 Vol.%, compared to about 6.2 Vol.% when the kiln and HOTDISC gasses are mixed instantaneously. And, as shown in section 5.3.3, the TDF char conversion rate is almost directly proportional to the oxygen concentration, and a significant increase in TDF char conversion rate may consequently be expected. This, however, implies that the calciner coal is to be combusted in a more oxygen deficient atmosphere, but as the oxygen dependency of the calciner fuel char conversion is usually significantly below 1 (0.54 in this case – see equation (5-28)), the effect is not directly proportional to the oxygen concentration as for the large TDF char particles. A more detailed study of these effects may be carried out using CFD including combustion and the models developed in this chapter for combustion of large TDF char particles. The discrepancies between the model and the measured data may partly be explained by the assumption of instantaneous mixing.

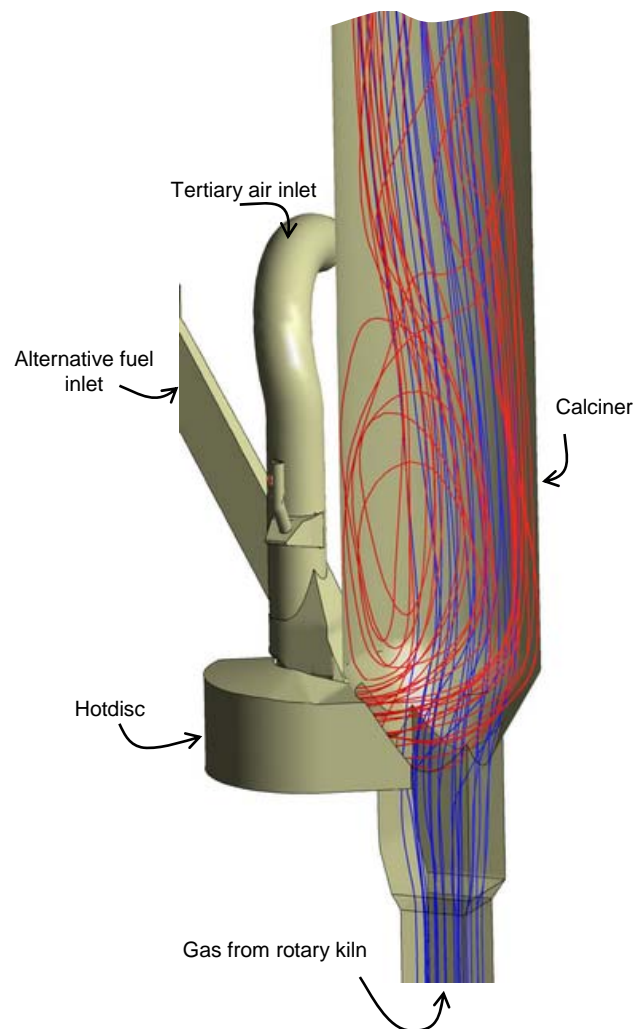


Figure 5-19: CFD simulated path-lines illustrating mixing of gas flows from the HOTDISC (red) and the rotary kiln (blue) in the calciner. Only lower part of calciner shown and combustion not simulated.

Re 3): Attrition and fragmentation phenomena of TDF char under conditions pertinent to fluidized bed combustion are reported by Arena et al. [19,20], whereas the sieve investigations demonstrated that the virgin char particles are almost non-susceptible to attrition and fragmentation under these conditions (see also section 5.3.1). If attrition and

fragmentation take place under conditions in the calciner, large TDF chars are expected to be converted significantly faster. A quantitative estimate of the conversion time reduction may be obtained from Figure 5-15, from which it may be observed that the conversion time decreases by a factor of about 3, when decreasing the particle size from 4 to 2 mm at 850°C and 2.5 Vol. % O₂, and a factor of 9 when decreasing the particle size from 2 to 0.5 mm.

Re 4): The movement of large char particles in the ILC system influences 1) the residence time and 2) the slip velocity between the particle and gas. A prolonged residence time as well as increased slip velocity between gas and char particles both increase TDF char burnout. Consequently, this may also explain the differences between the measured and modeled carbon conversion in the system.

5.3.5 Conclusions

A model for conversion of single TDF char particles converted according to a shrinking particle mechanism was developed. Analyses at single particle level showed that the conversion of large TDF char particles is almost exclusively controlled by external mass transfer under conditions relevant to cement kiln systems. Consequently, the conversion is almost insensitive to an increased temperature, whereas the conversion rate is almost proportional to the oxidizer concentration and external mass transfer coefficient.

An in-line-calciner model showed that the presence of a high temperature region lowered the degree of TDF char burnout for large particles, as O₂ was consumed by combustion of the calciner coal. Comparison of calciner model and available experimental data revealed that the model under-predicted the measured carbon burnout. This was attributed to 1) attrition and fragmentation of the large TDF char particles may take place in the calciner, 2) combustion of larger chars from the HOTDISC may take place in a gas stream of higher O₂ concentration, and 3) the movement of larger TDF char particles is not adequately described.

5.4 Chars from Other Alternative Fuels

The preceding sections treated conversion of large TDF chars. The aim of this section is to systemize the parameters influencing the burnout of chars from any alternative fuel under conditions relevant to the kiln system.

The solid fuel of first choice in the cement industry has, for many years, been finely pulverized coal or petcoke. The char conversion rate of these fuels, under conditions relevant to cement kilns, is mainly determined by 1) intrinsic kinetics, 2) temperature, 3) surrounding oxidizer concentration, and 4) residence time. However, with the introduction of chars from alternative fuels, which differ from fine coal particles in terms of physical properties, other parameters may also influence fuel char conversion rate. The parameters involved in the conversion of any char particle (irrespective of origin) are:

- 1) *Intrinsic kinetics*
- 2) *Surrounding / particle temperature*
- 3) *Structural changes during conversion*
- 4) *Size / shape*
- 5) *Oxidizer concentration in bulk gas*
- 6) *Mass transfer rates*
- 7) *Particle residence time*

Figure 5-20: Parameters influencing burnout of chars from alternative fuels.

5.4.1 Intrinsic Kinetics

In Figure 5-21, the TDF char reactivity estimated in section 5.2 and that of Masi et al. [2] is compared with char reactivity of a broad range of other chars. Zolin [12] made a study at low temperatures in micro TGA of coal char reactivity from 7 different coal chars. From that study, rates from the least and most reactive chars have been extracted for comparison purposes. The Lower Kittaning coal is seen to be less reactive than the TDF rate reported by Masi et. al. [2] with about two orders of magnitude, whereas the Dietz coal is slightly more reactive than the TDF char reactivity reported by Masi et al. [2]. Kinetic data for chars of petcoke, anthracite and a bituminous coal produced at high temperatures have been obtained from Jensen [3], and their reactivity are all seen to be below the reactivity of TDF char estimated in this study.

Char reactivity for a refuse derived fuel (RDF) from Masi et al. [2], a pine char from Janse et al. [4] and a wheat straw from Zolin [21], obtained in micro-TGA at low temperatures, have also been included for reactivity ranking purposes. It is evident from Figure 5-21, that the reported reactivity of pine is significantly higher than the TDF rate reported by Masi et al. [2], whereas the rate of RDF and leached wheat straw is located approximately in between the two.

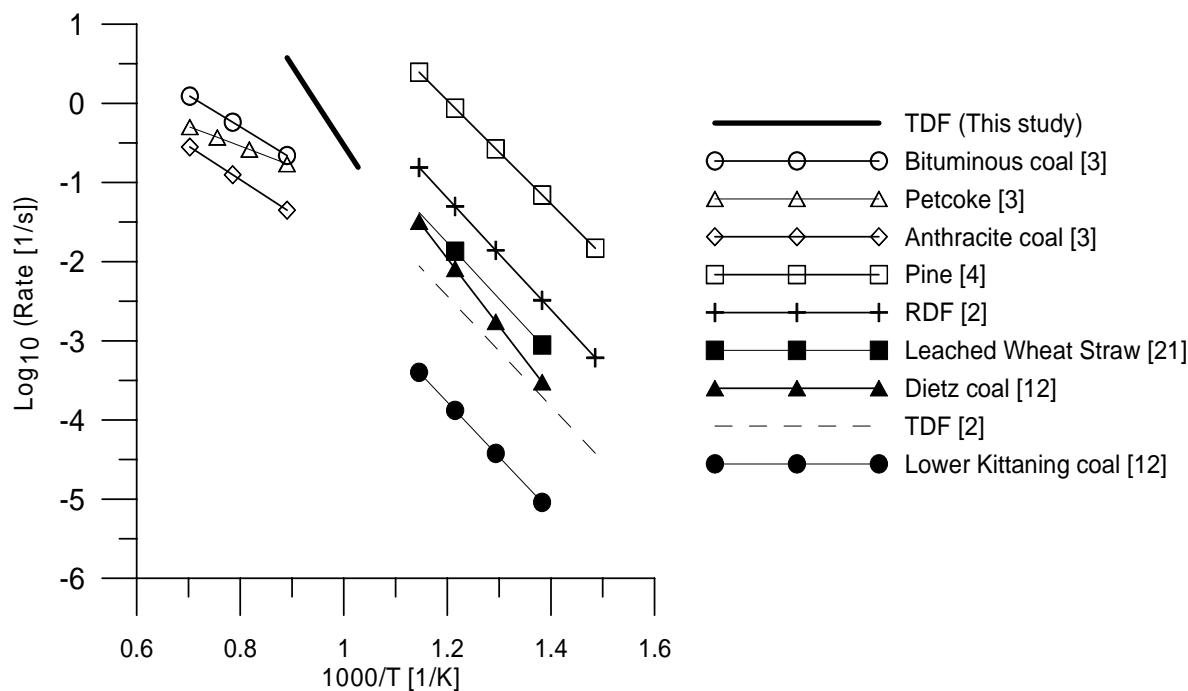


Figure 5-21: Arrhenius plot showing comparison of char reactivities (only TDF char data from this study and Masi et. al [2] included). Rate determined at 10 Vol. % O₂ and X=0.5 to compensate for applied pore model (same trend obtained with X=0.25 and 0.75).

For all investigated coal chars, the reactivity is seen to increase with the volatile content of the virgin fuel. For the rates obtained at the high temperatures by Jensen [3], the bituminous coal with a volatile content of 38.9 wt.% dry shows the highest reactivity, petcoke medium reactivity (11.5 wt.% dry volatiles) and anthracite the lowest reactivity (5.9 wt.% dry volatiles) acknowledging the increasing reactivity with increasing volatile content. For the coal char reactivity obtained at low temperatures the same trend is observed, where the low volatile bituminous Lower Kittanning coal shows a lower reactivity than the sub-bituminous Dietz coal.

The TDF char reactivity determined in this study at high temperatures is higher than the bituminous coal char reactivity determined by Jensen [3]. This is in accordance with the significantly higher volatile content of TDF (64.9 wt.% dry volatiles) than in the bituminous coal (38.9 wt.% dry volatiles). Consequently, there seems to be a correlation between reactivity and volatile content among different fuels. This is also verified by comparison of coal and TDF char reactivity investigations in micro TGA at low temperatures, the TDF char of Masi et al. [2] being about as reactive as the Dietz coal [12], which may be attributed to the volatile content of the sub-bituminous coal being close to that of TDF. Finally, pine, RDF and wheat straw with volatile contents of about 92 [22], 75 [2] and 81 (wt.% dry volatiles) [21] respectively, show the highest reactivity of all the investigated fuels.

For a broad range of fuels including coals, secondary fuels and biomass, it is indicated that increasing volatile content increases the char reactivity. Consequently, typical alternative

fuels used in cement production are also expected to have high intrinsic char reactivity, as these fuels typically have a high volatile content (see also table 3-2).

It was demonstrated in section 5.3 that conversion of TDF char particles was almost exclusively controlled by external mass transfer, and as a result the char conversion is practically insensitive to changes in temperature, under conditions relevant to cement kiln systems. Usually, the char particles formed from other alternative fuels are also in the mm size rather than the μm size, and the conclusions for TDF chars may also be applied to these other alternative fuel chars. Consequently, conversion of large char particles derived from an alternative fuel is nearly independent of intrinsic kinetics and, consequently, temperature changes under conditions relevant to the kiln system. Consequently 3) to 7) of Figure 5-20 are the important characteristics determining fuel burnout of large chars from alternative fuels.

5.4.2 Structural Changes and Effect of Particle Size

Four different pathways were identified to be responsible for char conversion (see also section 4.1). Pathway H2, however, may be rejected for large particles of alternative fuel chars, due to their high reactivity. For large spherical particles converted via pathway G under external mass transfer control, the conversion time is proportional to $D_{p,0}^{1.5-2}$ - the model results of section 5.3 also show this dependency. For char particles converted via pathways H1 or F, diffusion through the ash layer is usually the rate determining parameter, due to the external mass transport being faster. For these pathways, the conversion times are proportional to D_p^2 (applicable to sphere, cylinder or plate geometry) [13].

A significant reduction in char conversion time may be achieved by decreasing the particle size.

5.4.3 Oxidizer Bulk Concentration

The rate of char conversion for a large particle controlled by mass transport is directly proportional to the oxidizer concentration. In this regime, a doubling of the O_2 concentration results in a doubling of the external mass transfer rate and consequently halves the conversion time. Consequently, a significant reduction in conversion time may be achieved by increasing the bulk O_2 concentration.

5.4.4 Mass Transfer Rates

Mass transfer characteristics may be divided into external and intra-particle diffusion. The latter is governed by the effective intra-particle diffusion coefficient, which is an intrinsic fuel property that cannot be altered. The external mass transfer, however, may be increased by changing the fluid-particle interactions.

Correlations for external mass transfer typically contain the particle Reynolds and Schmidt numbers, as well as the particle size and the effective oxygen diffusivity. For spherical particles with diameters of 1 to 8 mm, under conditions relevant to the calciner, the slip velocity between the particle and gas influences the external mass transfer coefficient significantly. For instance, for a particle with a diameter of 2 mm, the mass transfer coefficient increases by about 276% when the slip velocity is increased from 0 m/s to 6 m/s (calculated with equation (5-21)), and it is further increased by 28% when increasing the slip velocity from 6 to 12 m/s. The significant effect of slip velocity on external mass transfer rate was also observed when comparing the results using model approach a) or b) in all model results of section 5.3.

Consequently, for chars combusted under external mass transfer control, a significant increase in char conversion rate may be achieved by increasing the slip velocity between particle and gas.

5.4.5 Particle Residence Time

It is clear that longer particle residence time in an oxidizing atmosphere increases burnout. Consequently, measures to increase particle residence should be promoted.

5.4.6 Conclusions

In order to increase burnout of chars derived from alternative fuels, the following process options are available:

- 1) *Increase bulk oxidizer concentration*
- 2) *Increase external mass transfer rate*
- 3) *Increase particle residence time*

In addition, it was identified that the particle size and the conversion pathway are also important. However, these are intrinsic fuel specific properties that is not to be altered.

5.5 Conclusions on Chapter 5

Char oxidation is the last step in the combustion of solid fuels and therefore has a decisive influence on the degree of fuel burnout in the calciner system as well as in the rotary kiln burner.

An experimental study supported by mathematical modeling showed that TDF chars are very reactive, under conditions relevant to a cement kiln system. Based on the experimental data coupled with a diffusion reaction model a kinetic scheme was proposed and comparison with literature data revealed fair agreement.

A shrinking particle model for realistically sized TDF char particles was developed, and the main conclusion from the model analyses was that the rate of TDF char conversion is almost exclusively controlled by external mass transfer rates. Based on the shrinking particle model, an In-line-calciner model was developed in order to study the conversion of large TDF char particles discharged from the HOTDISC table and into the in-line-calciner. Comparison of model predictions with experimental data showed that the model underpredicted the degree of carbon conversion in the calciner system compared to plant measurement data. This was attributed to the following 1) fragmentation and attrition of char particles neglected in the model, 2) too idealized flow patterns in the model, and 3) the movement of larger TDF char particles is not adequately described.

Analogies are drawn to other alternative fuels, and the rate determining factors, for conversion of large char particles derived from high volatile fuels, are provided. An increased O₂-level, increased external mass transfer rate and increased solid residence time may be used to improve char burnout in the calciner system or rotary kiln burner.

5.6 References

- ¹Hansen, M.L.; Combustion Reactivity of Secondary Fuels in Cement Production; M.Sc. Thesis, Technical University of Denmark, Dept. of Chem. Eng.; June 30th, 2006.
- ²Masi, S., Salatino, P. and Senneca, O.; Combustion Rates of Chars from High Volatile Fuels for FBC Application; Fluidized Bed Combustion, Volume, ASME, 135-143, 1997.
- ³ Jensen, L.S.; NO_x from cement production – Reduction from primary measures; PhD Thesis, Department of Chemical Engineering, DTU, Denmark, 1999. ISBN 87-90142-55-1.
- ⁴ Janse, A.M.C., Jonge, H.G., Prins, W. and Swaaij, W.P.M.; Combustion Kinetics of Char Obtained by Flash Pyrolysis of Pine Wood; Ind. Eng. Chem. Res., 37, 3909-3918, 1998.
- ⁵ Laurendau, N.M.; Heterogenous Kinetics of Coal Char Gasification and Combustion; Prog. Energy Combust. Sci., 4, 221-270, 1978.
- ⁶Conesa, J.A., Font, R., Fullana, A. and Caballero, J.A., Kinetic Model for the combustion of tyre wastes, Fuel, 77, 1469-1478, 1998.
- ⁷Bhatia, S.K., Perlmutter, D.D.; A Random Pore Model For Fluid Solid Reactions: I. Isothermal, kinetic control; AIChE J. Vol. 26, 379, 1980.
- ⁸Leung, D.Y.C. and Wang, L.C., Kinetic Study of scrap tyre devolatilization and combustion, J. Anal. Appl. Devolatilization, 45, 153-169, 1998.
- ⁹Atal, A., Levendis, Y.I.; Comparison of the combustion behaviour of pulverized waste tyres and coal; Fuel, Vol.74, 111 1570-1581, 1995.
- ¹⁰Zabaniotou, A.A., Stavrepoulos; Pyrolysis of used automobile tires and residual char utilization; J. Anal. Appl. Pyrolysis, 70, 711-722, 2003.
- ¹¹Conesa, J.A., Fullana, A. and Font, R.; Thermal decomposition of Meat and Bone Meal; J. Anal. Appl. Pyrolysis, 70, 619-630, 2003.
- ¹² Zolin, A.; Reactivity of Solid Fuels; PhD Thesis, Department of Chemical Engineering, DTU, Denmark, 2001. ISBN 87-90142-66-7.
- ¹³ Levenspiel, O., Chemical Reaction Engineering 3rd ed., John Wiley & Sons, New York, 1999. ISBN 0-471-25424-X.
- ¹⁴ Hansen, J.P., Skaarup-Jensen, L., Wedel, S., Dam-Johansen, K.; Decomposition and Oxidation of Pyrite in a Fixed-Bed Reactor; Ind. Eng. Chem. Res., 42,4290-4295, 2003.
- ¹⁵Villadsen, J. and Michelsen, M.L.; Solution of Differential Equation Models by Polynomial Approximation; Prentice-Hall, 1978; ISBN 013-822205-3.
- ¹⁶Li S.Q., Yao, Q., Chi, Y., Yan, J.H. and Cen, K.F.; Pilot Scale Pyrolysis of Scrap Tires in a continous Rotary Kiln Reactor; Ind. Eng.Chem. Res., 43, 5133-5145, 2004,

¹⁷ Perry Chemical Engineers Handbook, 7th edition, Mc-Graw Hill, 1999.

¹⁸ Weinell, C.E., Dam-Johansen, K. and Johnsson, J.E.; Single-particle behaviour in circulating fluidized beds; Powder Technol., 92, 241-252, 1997.

¹⁹ Arena, U., Cammarota, A. and Chirone, R.; Fragmentation and Attrition During the Fluidised Bed Combustion of two Waste Derived Fuels; Fluidization VIII, Engineering Foundation, 437-444, New York, 1995.

²⁰ Arena, U., Chirone, R and Salatino, P.; The fate of Fixed Carbon During the Fluidized-Bed Combustion of a Coal and Two Waste Derived Fuels; Twenty-Sixth Symposium (International) on Combustion. The Combustion Institute, 3243-3251, 1996.

²¹ Zolin, A., Jensen, A.D., Jensen, P.A., Dam-Johansen, K.; Experimental study of char thermal deactivation; Fuel, 81, 1064-1075, 2002.

²² Saeed, L.; Tohka, A.; Haapala, M.; Zevenhoven, R.; Pyrolysis and combustion of PVC, PVC-wood and PVC-coal mixtures in a two-stage fluidized bed process; Fuel Processing Technology, Vol. 85, 1565-1583, 2004

Chapter 6 - Analyses of Industrial Scale HOTDISCs

This chapter summarises analyses that have been made in order to elucidate the controlling factors for conversion of solid alternative fuel used in the FLSmidth HOTDISC. The focus is on whole and shredded tyres, because they were used as fuel during measurement programmes at two industrial scale HOTDISCs.

Initially, a simplified plug-flow-reactor model is developed to simulate solid fuel conversion in the HOTDISC and to interpret the data from the two measurement programmes. Secondly, a detailed measurement and analysis programme for two industrial HOTDISCs using shredded and whole tyres as alternative fuel is described. The model predictions and the measured data are compared. From the conclusions and comparisons of the model and measurement studies, analogies are drawn to other types of alternative fuels with regard to fuel conversion in the HOTDISC.

The aim of this chapter is to provide insight into the combustion mechanisms responsible for conversion of solid alternative fuels in the HOTDISC.

6.1 Model for Conversion of Whole and Shredded Tyres in the HOTDISC

In this section, a simplified plug flow reactor model for predicting conversion of whole and shredded tyres in the HOTDISC is developed. The aims of the model are:

- 1) *To predict degree of fuel conversion as a function of:*
 - a. *Angular position*
 - b. *fuel feed rate*
 - c. *disc size and rotational speed*
 - d. *shape and kinetics of the alternative fuel used*
- 2) *To analyze experimental data obtained at two industrial HOTDISCs in order to elucidate controlling factors for solid fuel conversion*

Besides the well-known plug-flow-reactor assumption from chemical engineering, the following additional simplifying assumptions are made:

- 1) *The HOTDISC chamber is “unfolded” and approximated by a duct (see Figure 6-1) with a bottom surface area equal to that of the HOTDISC table.*
- 2) *The gas velocity profile is assumed to be uniform with an average gas velocity equal to the average velocity of the HOTDISC.*

- 3) The drying stage is ignored. Moisture from the fuel is instead released at the same rate as volatiles.
- 4) Char is assumed to consist of pure carbon, in agreement with data for TDF char of Karlsson et al. [1].
- 5) Instantaneous and complete oxidation of devolatilization products in the gas phase once released from the solid fuel.
- 6) Raw material particles added to the HOTDISC are assumed to be completely suspended in the gas phase and not to cover the surfaces of the solid fuel.
- 7) The temperature is assumed constant, as heat released by combustion is absorbed by the endothermic calcination process.

Alternative fuel, raw material. & tertiary air

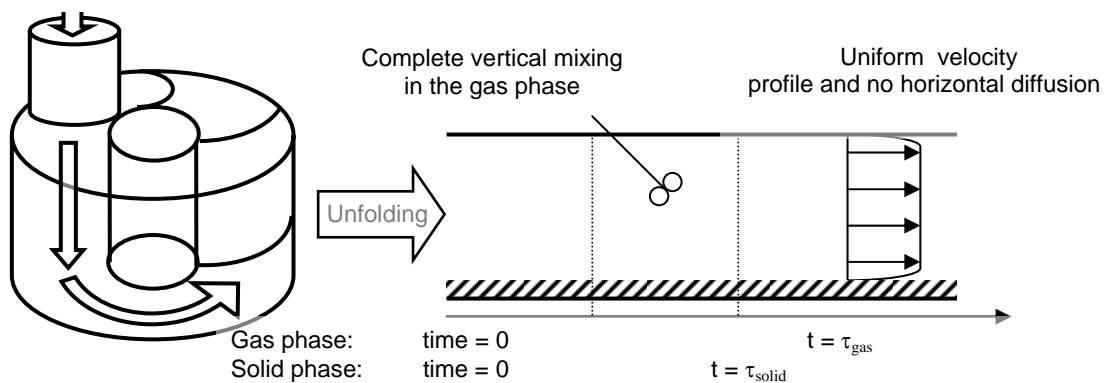


Figure 6-1: Approximation of the HOTDISC chamber with a duct. Note that the solids resting on the disc-floor travel at a velocity that is significantly lower than that of the gas.

In order to simulate the two limiting conversion pathways that may be encountered when using TDF as alternative fuel in the HOTDISC the devolatilization process of TDF is assumed to proceed either according to pathway I (see section 4.1), with a simultaneous production of smaller char particles that are entrained in the gas phase and combusted, or pathway E with no entrainment of char in the gas phase. In the latter situation, the char oxidation is assumed to start when the devolatilization is 90% complete, as the flame from the volatile combustion effectively prevents oxygen diffusing to the char surface.

Before sub-models are developed for the steps in the combustion, a recapitulation is made of the two different situations when using shredded and whole tyres as a fuel in the HOTDISC. When using whole tyres (see Figure 6-2), it is possible for the gas to pass through the voidage of the tyres and consequently sweep a significant part of the outer surface tyre area. Only the contact points between tyres and disc and the contact points between adjacent tyres are not easily accessible for gas contact (see also Figure 6-4). However, shredded tyre particles behave more like a compact mass, where the gas contact is primarily on the upper surface.

Qualitatively, the two situations differ in that a relatively larger surface area of the whole tyres is swept by the gas than is the case with the shredded tyre particles.

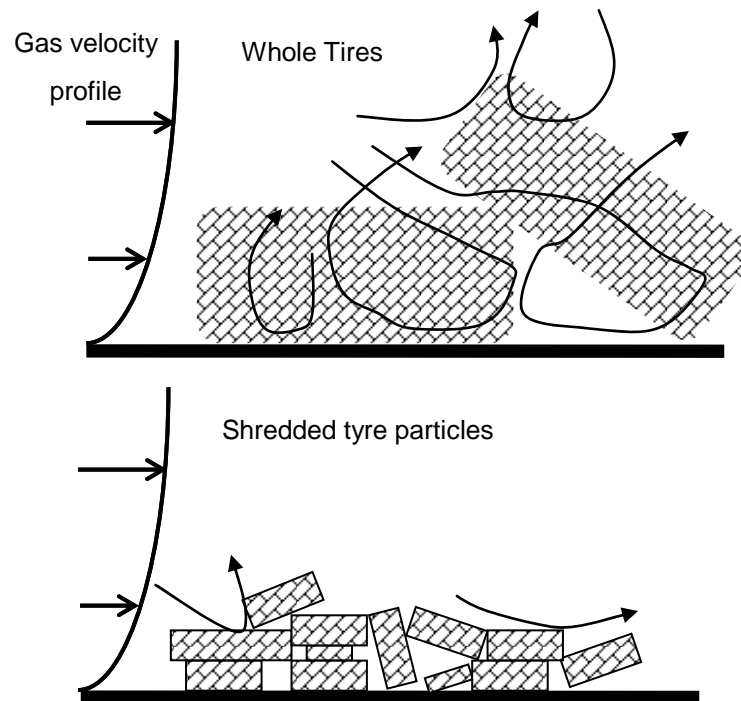


Figure 6-2: Illustration of situations when using whole and shredded tyres as a fuel in the HOTDISC.

6.1.1 Devolatilization

In this model, a controlling particle size or thickness as well as external heat transfer characteristics are defined and applied in devolatilization model B or C, presented in chapter 4, to simulate devolatilization conversion pathway I or E, respectively. The output of model B or C is used as input to the HOTDISC model in this section. The controlling thicknesses for whole and shredded tyres are defined in the following sections.

6.1.1.1 Shredded Tyres

Here it is assumed that the shredded tyre particles pack without voidage and that the corresponding layer height determines the controlling thickness for the devolatilization time:

$$\text{Layer height} = \frac{m_f \tau_{disc}}{\rho_{fuel} A_{disc}} \quad (6-1)$$

In the calculation of the convective heat transfer coefficient, a correlation is available for mass transfer between a turbulent gas and a flat plate, which is approximately the situation for shredded tyres resting on the HOTDISC. The assumption of analogy between mass and heat transfer is used to convert to energy transfer (Sh is replaced with Nu in (6-7)) [2]. The radiative heat transfer coefficient is calculated with (A-23) in appendix B with $T_\infty=900^\circ\text{C}$ and

$\varepsilon=0.25$. Another approach might have been to define variable external radiative heat transfer, in order to simulate for instance the ignition of a volatile flame. This would mainly have affected the devolatilization rate during pathway I, because devolatilization via pathway E is mainly controlled by internal heat transfer (see also section 4.6).

6.1.1.2 Whole Tyres

It was shown in section 4.5, that the thickest part of the tread determines the devolatilization time of a whole tyre. A first approach would then just be to select the half of the thickest dimension of the tread of the whole tyres (see Figure 6-3-A) and then use that dimension to determine the devolatilization time using models B and C of chapter 4. However, when the thickest part of the tyre rests against the HOTDISC table, this part is only susceptible to heating on one side, and consequently the entire tread thickness should be used as the controlling thickness (see Figure 6-3-B). Besides, connection points between the tyres may also be shielded for heating, and here again the entire tread thickness should be used (see Figure 6-3-C). The approach used here to model devolatilization kinetics of whole tyres, is to use $\frac{3}{4}$ of the thickest part as the controlling thickness.

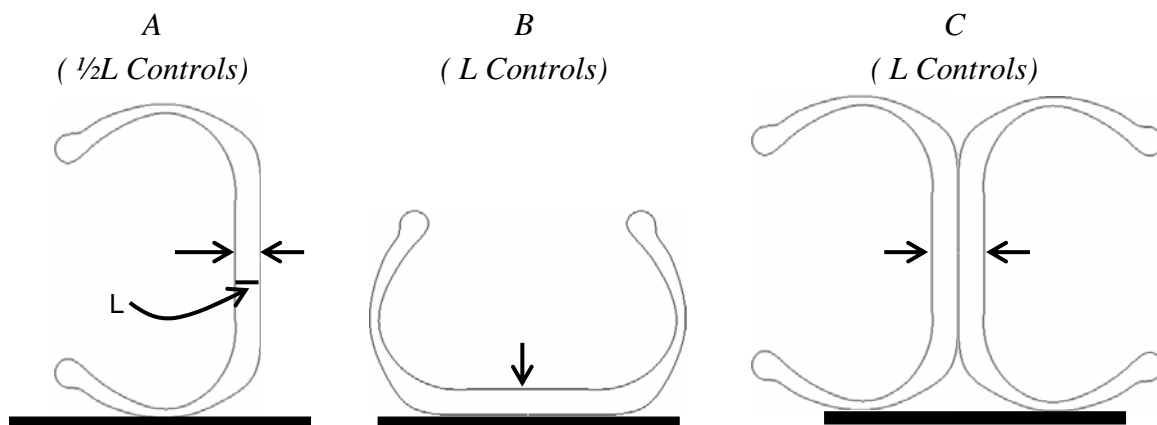


Figure 6-3: Controlling thickness (distance to symmetry line) for devolatilization time of whole tyres in three different situations.

A similar radiative external heating, as for shredded tyres, is used here. With regard to convective heating, no correlation is available for turbulent flow around tyre shaped objects. Instead, efforts were made to resolve the velocity boundary layer for turbulent flow around tyre shaped objects using computational fluid dynamics, and consequently use that to determine the local heat transfer coefficients. However, it was a difficult task because the solutions turned out to be very grid dependent with no stable solution, and the method was consequently rejected (It worked fine for well defined geometries of spheres cylinders and plates). Instead, the assumption of analogy between mass and heat transfer is used and (6-12) is applied with Sh and Sc replaced by Nu and Pr respectively [2].

6.1.2 Char Oxidation

6.1.2.1 Shredded Tyres Converted according to Devolatilization Pathway E

In this situation the char is not entrained in the gas phase, and the upper surface of the shredded tyres is only swept by the gas. Consequently, the outer area of the char may be assumed equal to the HOTDISC surface area. It was shown in chapter 5 that the conversion rate of large particles of TDF char is almost exclusively controlled by external mass transfer at conditions corresponding to cement kiln systems. This may also be expected to be the situation here, and in particular because the outer surface compared to its mass, is significantly lower in this situation than for the suspended spherical particles treated in chapter 5. Therefore, the rate of char conversion of shredded tyres may be written as a function of the mass transfer coefficient multiplied by the driving force, which in this case is the concentration difference of oxygen. The product distribution between CO and CO₂ (II, see also section 5.2), is used to correlate between molar rates of O₂ and C

$$r_{char} = -k_{g,shredded} \frac{P}{R_g T} (y_{O_2,\infty} - y_{O_2,s}) \Pi \quad \left[\text{mol C} / \text{m}^2 \text{disc} / \text{s} \right] \quad (6-2)$$

A stationary Lagrangian mass balance is developed for the control volume shown in the right part of Figure 6-1:

$$\begin{aligned} In &= n_{char,0} (1 - X_{Char}) \Big|_t, & Out &= n_{char,0} (1 - X_{Char}) \Big|_{t+\Delta t} \\ Prod &= r_{char} \Delta t \end{aligned} \quad (6-3)$$

Setting up the balance ($Out - In = Prod$) yields:

$$\frac{dX_{char}}{dt} = - \frac{r_{char}}{n_{char,0}} \quad (6-4)$$

where $n_{char,0}$ is the initial char loading calculated as:

$$n_{char,0} = \frac{m_f \frac{FC}{M_{w(C)}}}{A_{disc} / \tau_{disc}} \quad \left[\text{mol C} / \text{m}^2 \text{disc} \right] \quad (6-5)$$

Oxygen is consumed at the char surface and the surface concentration of O₂ therefore becomes 0. Substituting (6-2) and (6-5) into (6-4) and introducing the dimensionless position $\eta = t / \tau_{disc}$ the following equation is obtained:

$$\frac{dX_{char}}{d\eta} = \frac{k_{g,shredded} A_{disc} \frac{P}{R_g T} y_{O_2,\infty}}{m_f \frac{FC}{M_{w(C)}}} \Pi \quad (6-6)$$

An analysis of the parameters in this differential equation reveals that the qualitative effect of changing the parameter values agrees with what is intuitively expected. Increasing the mass transfer coefficient, HOTDISC area or oxygen concentration accelerates the char conversion rate, whereas increasing the fuel feed rate and fixed carbon content decreases the char conversion rate. A higher fuel feed rate decreases the char conversion rate, as the fuel layer height increases.

The mass transfer coefficient is obtained according to a Sherwood correlation for a turbulent flow over a flat plate [3], which is approximately the situation with shredded tyres:

$$Sh = \frac{k_{g,shredded} L}{D_{O_2}} = 0.0365 Re_L^{0.8}, \quad Re_L \geq 10^5 \quad (6-7)$$

where Re_L is the Reynolds number based on the equivalent plate length, which in this case is the length of the unfolded HOTDISC. Finally, the degree of fuel conversion on mass basis is calculated according to the proximate analysis:

$$X_{Fuel} = \frac{FC}{FC+V} X_{char} + \frac{V}{FC+V} X_D \quad (6-8)$$

6.1.2.2 Shredded Tyres Converted according to Devolatilization Pathway I

Here char particles are entrained into the gas phase, with the size distribution of section 5.3.1, and combusted according to the model presented in that section. For the sake of simplicity to avoid population balances, it is assumed that all char particles are released to the gas phase at the onset of the devolatilization. This approach yields a higher degree of char conversion than if the char particles were released continuously with devolatilization. However, it will be demonstrated later that devolatilization according to this model takes place over a relatively short interval (see also Figure 6-5), and the assumption of instantaneous char release is considered fair. In addition, the obtained degree of char conversion for particles entrained to the gas phase is also relatively low, c.f. Table 5-3.

6.1.2.3 Whole Tyres Converted according to Devolatilization Pathway E

Assuming, based on the same arguments as earlier, that the char conversion rate is controlled by external mass transfer, the reaction rate for conversion of whole tyres based on the outer tyre surface area becomes:

$$r_{char} = -k_{g,whole} \frac{P}{RT} (y_{O_2,\infty} - y_{O_2,s}) \Pi \quad \left[\text{mol C} / \text{m}^2 \text{ tyre} / \text{s} \right] \quad (6-9)$$

The available outer surface area of the tyres per HOTDISC area is used to transform the char reaction rate to be a function of HOTDISC surface area in order to be equivalent to (6-2). In the limiting case, the total outer surface area of the tyres is equal to the total outer surface area. However, as the tyres pack, parts of the area may be covered. The outer surface area for closely packed tyres stacked on top of each other (shown in the left part of Figure 6-4) is approximately 2/3 of the total outer surface area. This figure is because the radial contact points cover a very little part of the outer area, whereas the axial contact points cover both axial outer sides (except the upper tyre). Assuming that the inner and outer radial axial surfaces have equal areas, 2/3 is obtained. The right part of Figure 6-4 shows another possibility for the whole tyres to pack. The available surface area in this situation, however, is larger than 2/3 of the total surface area.

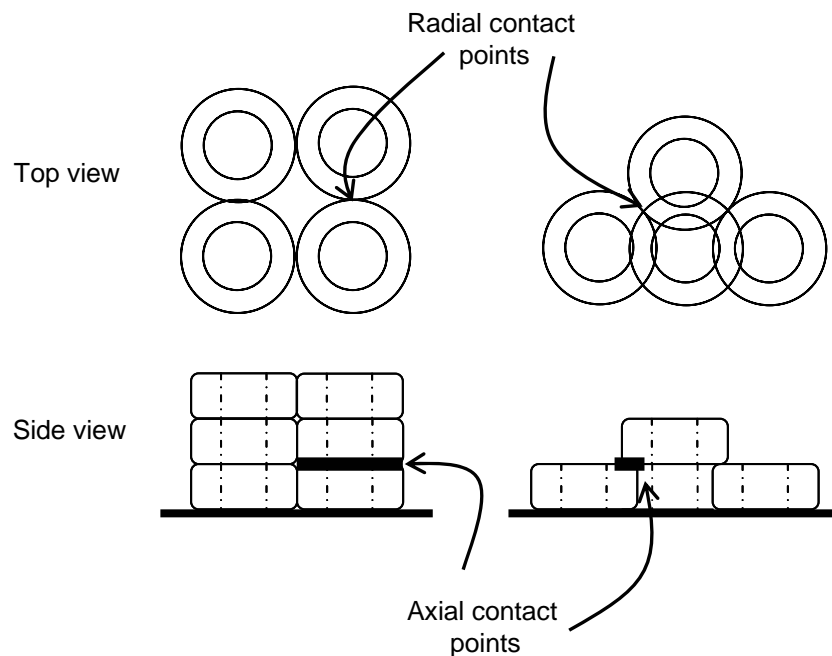


Figure 6-4: “Worst case” stacking of tyres on the HOTDISC in two different ways and indication of contact points preventing immediately interaction from gas.

Assuming that 2/3 of the outer surface area of the tyres “see” the gas, the total outer surface of the tyres may be expressed in the following way:

$$\frac{m_f \cdot \tau_{disc}}{A_{disc}} \left[\frac{\text{kg tyre}}{\text{m}^2 \text{ disc}} \right] \cdot \frac{2}{3} \cdot A_{tyre} \left[\frac{\text{m}^2}{\text{kg tyre}} \right] \quad (6-10)$$

Introducing (6-10) into (6-9) and substituting into (6-4) with (6-5) and introducing the dimensionless position, the following expression for the rate of char conversion for whole tyres is obtained:

$$\frac{dX_{char}}{d\eta} = \frac{\frac{2}{3} \cdot k_{g,whole} \tau_{disc} A_{tyre} \frac{P}{R_g T} y_{O_2,\infty}}{\frac{FC}{M_{w(C)}}} \Pi \quad (6-11)$$

Again, the differential equation is in agreement with what is intuitively expected. Increasing the mass transfer coefficient, solid residence time, specific outer surface area or oxygen concentration all increases the char conversion rate. Increased fixed carbon content in the denominator decreases the rate of conversion. An interesting observation in this model is the fact that the char conversion rate is independent of the fuel feed rate of tyres, in contrast to the model of shredded tyres (see (6-6)). This is due to the fact that increasing fuel feed rate at fixed residence time increases the height of stacked tyres, but the available outer surface area also increases and hence there is no decrease in char conversion rate. However, another effect of an increased fuel feed rate, which is not immediately observed from (6-11), is an increased oxygen consumption and consequently lower reaction rate.

The mass transfer coefficient is calculated using a Sherwood correlation for flow past submerged “other” objects [3], as this correlation was estimated to be the most suitable for the current situation. An accuracy of $\pm 15\%$ may be expected.

$$Sh = \frac{k_{g,whole} L}{D_{O_2}} = 0.692 Re^{0.514} \cdot Sc, \quad 500 \leq Re_{ch} \leq 5000 \quad (6-12)$$

where Re is calculated on the length based from the ratio between the total surface area and the perimeter normal to flow.

6.1.2.4 Whole Tyres Converted according to Devolatilization Pathway I

This situation is treated in a similar manner as shredded tyres.

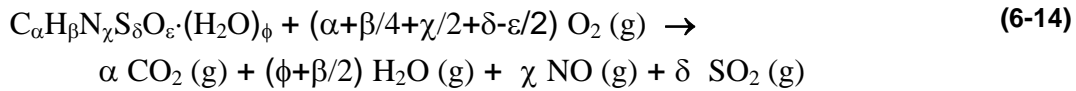
6.1.3 Calcination

Heat released from the combustion process is mainly absorbed by calcination of limestone. Consequently, the degree of calcination may be expressed as a function of devolatilization and char conversion in the following way.

$$X_{calcination} = \frac{X_{Fuel} \cdot LHV \cdot m_f}{\Delta H_{Calcination} \cdot n_{CO_2,meal}} \quad (6-13)$$

6.1.4 Gas Phase Calculations

The following stoichiometric equation is adopted for combustion of the devolatilization products:



where the stoichiometric coefficients for the devolatilization are calculated from the proximate and ultimate fuel analysis and the following equations:

$$\alpha = \frac{V - H - S - N - O}{M_{w(C)}} \quad (6-15)$$

$$\beta = \frac{H}{M_{w(H)}} \quad (6-16)$$

$$\chi = \frac{N}{M_{w(N)}} \quad (6-17)$$

$$\delta = \frac{S}{M_{w(S)}} \quad (6-18)$$

$$\varepsilon = \frac{O}{M_{w(O)}} \quad (6-19)$$

$$\phi = \frac{M}{M_{w(H_2O)}} \quad (6-20)$$

} for $C \geq FC$

A prerequisite for these calculations is the carbon content being equal to or greater than the char content, which is fulfilled for tyres (see Table 6-2). Molar balances in the gas phase yield information about amount of moles present as a function of devolatilization, char and calcination conversion as shown in Table 6-1. It may be observed that N_2 is inert and that only O_2 is consumed. The components CO_2 , NO , SO_2 and H_2O are produced.

The total molar flow of gas may for any degree of conversion be derived by summing the contributions in the row “End”. The molar fraction of component i may subsequently be derived from the ratio between the mole flows of component i evaluated at “End” and the total mole flow.

	<i>Initial</i>	<i>Produced</i>	<i>End = Initial + Produced</i>
N_2	$n_{tert} \cdot 0.79$	0	$n_{tert} \cdot 0.79$
O_2	$n_{tert} \cdot 0.21$	$-m_f \left(X_D \left(\alpha + \frac{\beta}{4} + \frac{\chi}{2} + \delta - \frac{\varepsilon}{2} \right) + X_{Char} \frac{FC}{M_{w(C)}} \right)$	$n_{tert} \cdot 0.21 - m_f \left(X_D \left(\alpha + \frac{\beta}{4} + \frac{\chi}{2} + \delta - \frac{\varepsilon}{2} \right) + X_{Char} \frac{FC}{M_{w(C)}} \right)$
CO_2	0	$m_f \left(X_D \alpha + X_{Char} \frac{FC}{M_{w(C)}} \right) + n_{CO_2,meal} \cdot X_{calcination}$	$m_f \left(X_D \alpha + X_{Char} \frac{FC}{M_{w(C)}} \right) + n_{CO_2,meal} \cdot X_{calcination}$
H_2O	0	$m_f X_D \left(\frac{\beta}{2} + \phi \right)$	$m_f X_D \left(\frac{\beta}{2} + \phi \right)$
NO	0	$m_f X_D \chi$	$m_f X_D \chi$
SO_2	0	$m_f X_D \delta$	$m_f X_D \delta$

Table 6-1: Molar balances for gas phase species as a function of devolatilization and char conversion, as well as calcination degree.

6.1.5 Solution Procedure

The set of algebraic equations and the differential equation(s) for the char conversion(s) are handled in Fortran with the use of the subroutine *Siruke* [4]. The initial conditions are zero for all char conversion and the fuel analysis for the species balances in Table 6-2.

		Unit	
Proximate analysis	Moisture - M	wt. %	5.7
	Volatiles - V	wt. %	51.3
	Ash	wt. %	21.4
	Fixed C – FC (Calculated)	wt. %	21.6
Ultimate analysis	C	wt. %	60.4
	H (Excl. H ₂ O)	wt. %	5.3
	S	wt. %	1.3
	N	wt. %	0.42
	O (Calculated Excl. H ₂ O)	wt. %	5.48
	Mineral matter	wt. %	21.4
LHV		MJ/kg	26.9

Table 6-2: Proximate, ultimate analysis and lower heating value for a car tyre used in the model calculations (see also table 3-3). Determined according to British Standard Methods (BS 1016-1018) and the heating value was determined using the ISO 1928 standard.

6.1.6 Results of Model Calculations

Figure 6-5 shows model predicted total fuel conversion and the contribution of devolatilization to the total fuel conversion for the two investigated industrial HOTDISCs, using the devolatilization pathway I or E. The x-axis indicates the dimensionless position, ranging between 0 and 1 for the start and the end of the HOTDISC respectively.

For the HOTDISC at plant A, it is observed that the devolatilization initiates at about $\eta=0.1$ minute for both pathways, which is due to the particles needing to be heated at the outer surface to initiate the devolatilization reactions. The devolatilization rate is faster when converted according to pathway I than according to pathway E in agreement with data of chapter 4 – and what is intuitively expected. For devolatilization pathway E, little devolatilization conversion and no char oxidation are obtained. The latter is due to the flame shielding the outer surface during devolatilization in this model. Pathway I predicts occurrence of char oxidation, which is due to particles being entrained in the gas phase and combusted with a higher outer specific surface area. The model for devolatilization pathway I predicts a total degree of fuel conversion of about 0.75 at the end of the HOTDISC, with devolatilization being responsible for about 92% of the total fuel conversion.

For the HOTDISC at plant B using whole tyres, it is observed that the devolatilization rates for the two models are faster than the situations with shredded tyres, and that a significantly higher char oxidation is obtained for devolatilization pathway E. The latter is mainly a consequence of a higher degree of devolatilization with a resulting flame extinction allowing transport of O_2 to the char surface. The predicted total fuel conversions are 0.75 and 0.8 for devolatilization pathways E and I, respectively, of which the devolatilization contributions are 82 and 88% respectively.

A comparison of the two situations using whole or shredded tyres reveals that if devolatilization takes place according to pathway E, a significant difference with regard to fuel burnout may be expected in these two situations. If conversion takes place according to pathway I, less difference between the two situations may be expected.

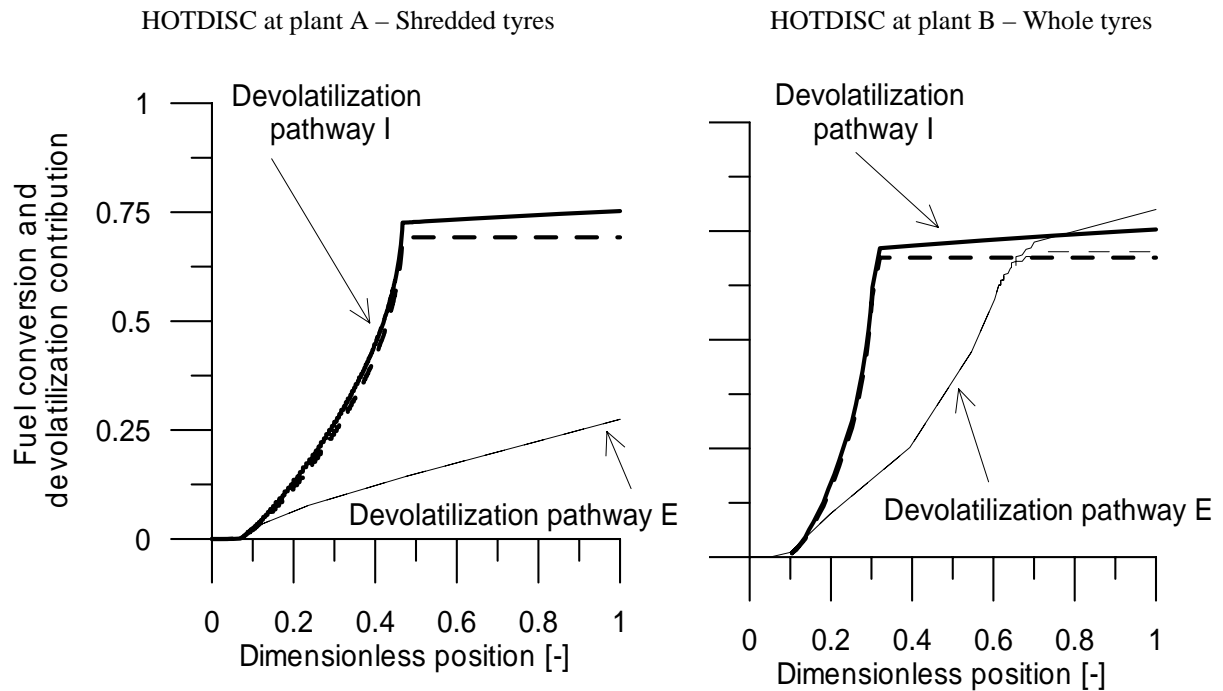


Figure 6-5: Modelled fuel conversion for industrial HOTDISCs. Captions are: Total fuel conversion (—), devolatilization contribution (---).

6.1.7 Conclusions on Model Investigations

A model for devolatilization and char combustion of whole and shredded tyres fed to the HOTDISC has been developed. The model is based on previously presented sub-models for two different devolatilization pathways and char oxidation. The aim of the model was to simulate the fuel conversion as a function of relevant parameters and to use the model in the interpretation of experimental data.

The main conclusions of the model are that 1) almost exclusively devolatilization takes place on the HOTDISC whereas char oxidation also takes place in the calciner, and 2) if the devolatilization proceeds according to pathway E, the fuel conversion rate is significantly faster for whole than for shredded tyres.

6.2 Plant Measurements and Analyses

In order to be able to test the conclusions from the model study, a detailed plant measurement programme at two industrial HOTDISCs was carried out. The HOTDISC at plant A used shredded tyres during the measurement campaign, whereas the HOTDISC at plant B used whole tyres. This section describes how the measurements were performed, how the data was analysed and the results of the analyses.

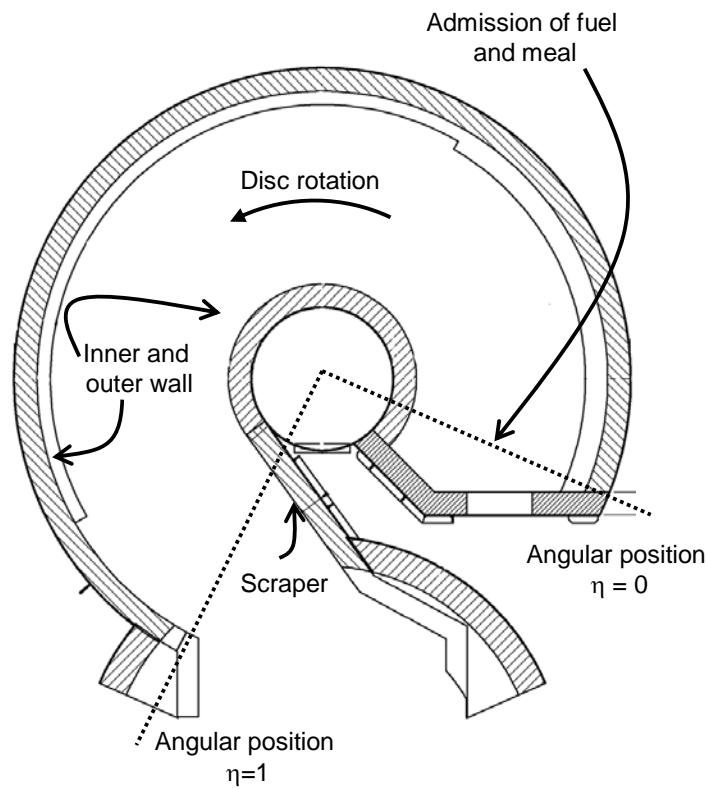
The aims of the measurement programmes were mainly to determine the degree of fuel conversion as a function of angular position. The fuel conversion may be determined either from analyses of fuel particles and solid material extracted from the disc table, or from analyses of species concentrations in the gas phase. The first approach was initially tested, but was found unsuitable primarily due to it being difficult to extract a representative sample from the HOTDISC table. However, with gas measurements it is possible to measure species concentrations over a continuous period and thereby gain better average values. Consequently, this method is used and described here.

6.2.1 Procedures for Measurements

Angular gas measurement positions were established on the two HOTDISCs at different angles from the tertiary air inlet. Their location was chosen on the basis of equipment accessibility (surrounding walls etc.) and in order to get a representative characterization of the HOTDISC. The upper part of Figure 6-6 shows a top view of a HOTDISC and the nomenclature of the angular positions. They are shown as a dimensionless position in order to correspond to the model calculations, in which the start and the end of the disc correspond to $\eta=0$ and 1, respectively. At the HOTDISC at plant A, three angular measurement positions were established at positions of $\eta \approx 0.42$, 0.54 and 0.78 and two angular positions were established at the HOTDISC at plant B at $\eta \approx 0.22$ and 0.60.

For each angular position, measurement holes were made at three different heights as shown in the lower part of Figure 6-6. In each measurement hole, gas measurements were performed at two (plant B HOTDISC) or three measurement depths (plant A HOTDISC). Consequently, nine gas measurements are obtained for each angular position at the plant A HOTDISC and six gas measurements for each angular position at the plant B HOTDISC.

Top view:



Angular cross sectional view:

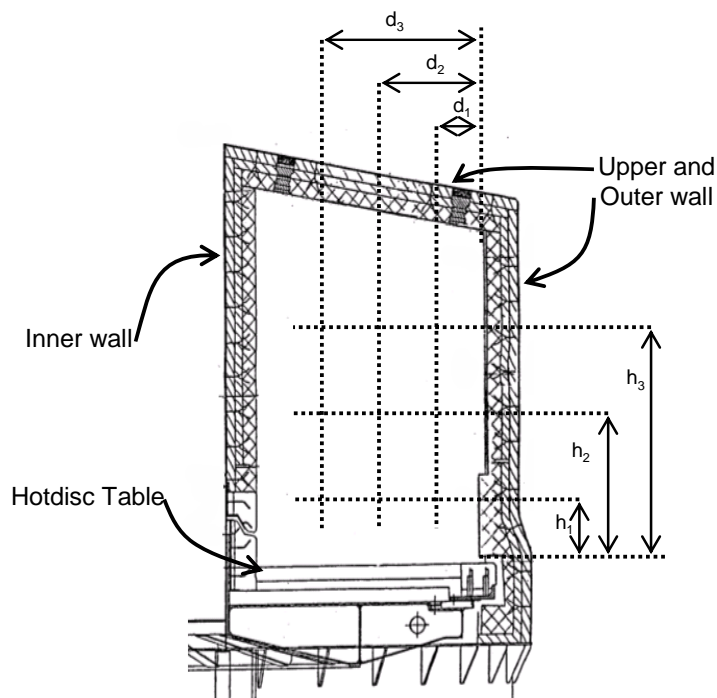


Figure 6-6: Upper part: Top view of the HOTDISC with indication of limiting angular positions. Lower part: angular cross section and indication of heights and depths of measurement positions from HOTDISC table and inner side wall, respectively.

A schematic illustration of the gas measurement setup is shown in Figure 6-7. A water-cooled probe is connected to a cyclone for removal of rough particulates, and a gas conditioning unit and a continuous gas measurement device (URAS 14) are connected to a PC for simultaneous data collection. The purpose of the gas-conditioning unit is to remove fine particulates not removed in the cyclone and to cool the flue gas thereby removing the water vapour from the flue gas. Furthermore, the gas conditioning unit generates the suction needed to extract the gas from the HOTDISC and transport it to the gas measurement device.

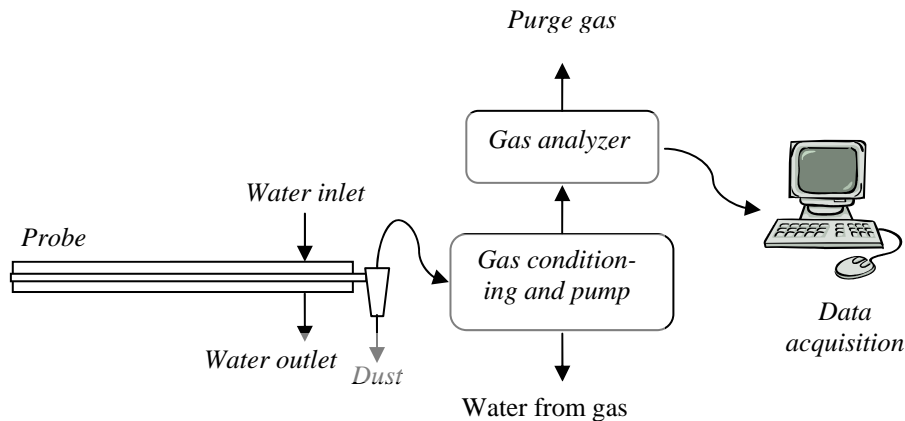


Figure 6-7: Schematic illustration of gas measurement setup

Preferably, the duration of a gas measurement at a single point should be as long as possible, to observe transient phenomena. However, a very long measurement is not possible, since up to nine measurement positions need to be evaluated under the same operating conditions to gain consistency between the gas measurements. Preferably, a stable period of 20-30 minutes was sought for each measurement position; this period, however, may have been prolonged if significant deviations in the measured gas concentrations were observed in the continuously monitored signal.

6.2.2 Analysis Method of Plant Measurement Data

6.2.2.1 Degree of Fuel Conversion

The solid fuel conversion is determined from an average concentration in each cross section determined from the measured concentrations. The approach used here exploits the fact that the ratio between the overall excess air ratio for complete combustion and the instantaneous air excess ratio, yields the fuel conversion:

$$X_{Fuel} = \frac{\lambda}{\lambda_{inst.}} \quad (6-21)$$

For combustion in atmospheric air, the instantaneous air excess ratio may be determined in the following way [5]:

$$\lambda_{inst.} = 1 + \frac{1}{\frac{21}{79} \left(\frac{1 - \widetilde{y_{O_2}} - \widetilde{y_{CO_2}} - \widetilde{y_{CO}}}{\widetilde{y_{O_2}} - \frac{1}{2}\widetilde{y_{CO}}} \right) - 1} \quad (6-22)$$

where the average molar fractions are on a dry basis. The advantage of this method to determine fuel conversion stems from the fact that carbon dioxide from the calcination process does not influence the results compared to a carbon mass balance, where the degree of calcination is needed to determine the degree of fuel conversion (CO₂ from calcination enters the balance). This is due to the amount of oxygen consumed in combustion being related to the amount of inert N₂, as demonstrated in the derivation of a similar expression (without CO) in appendix D.

The overall excess air ratio for the complete combustion is determined based on ultimate fuel analysis assuming that all species are evenly distributed between char and volatile fraction. The decomposition of the solid fuel is assumed to be according to (6-14), where α is the molar carbon content, β is the molar hydrogen content calculated from (6-16) to (6-20) and (6-23).

$$\alpha = \frac{C}{M_{w(C)}} \quad (6-23)$$

The stoichiometric molar air consumption per mass of fuel is then determined by:

$$n_{air} = \frac{(\alpha + \beta/4 + \chi/2 + \delta - \varepsilon/2)}{y_{O_2}} \quad (6-24)$$

The ratio between the tertiary air flow and the determined molar air consumption derived from (6-24) with data from Table 6-2, yields air excess ratios of 2.6 and 3.1 for the HOTDISCs at plant A and B, respectively.

6.2.2.2 Weighting Method for Average Species Concentrations

Average species concentrations in each cross section are needed in order to determine the degree of fuel conversion. Two weighting methods are used throughout the analysis to determine average concentrations of CO₂, CO and O₂ in each cross section. In weighting method A, the concentrations are weighted according to temperature, since the molar volume of a gas changes with temperature, and the weighting factor, $\mu_{i,A}$, in point i becomes:

$$\mu_{i,A} = \frac{\frac{T^\theta}{T_i}}{\sum_{i=1}^n \frac{T^\theta}{T_i}} \quad (6-25)$$

where T_i is the temperature in point i , n is the number of measurement points in the cross section and $T^\theta = 273.15$ K. In weighting method B, the weighting is according to gas velocity and temperature at that particular measurement point. The weighting factor, $\mu_{i,B}$, at point i becomes:

$$\mu_{i,B} = \frac{v_i \frac{T^\theta}{T_i}}{\sum_{i=1}^n v_i \frac{T^\theta}{T_i}} \quad (6-26)$$

where v_i is the linear velocity at point i . The average molar fraction, \widetilde{y}_j , of species, j , in each cross section is then calculated as:

$$\begin{aligned} \widetilde{y}_{j,A} &= \sum_{i=1}^n \mu_{i,A} y_{j,i} && \text{for weighting method A} \\ \widetilde{y}_{j,B} &= \sum_{i=1}^n \mu_{i,B} y_{j,i} && \text{for weighting method B} \end{aligned} \quad (6-27)$$

The temperature weighting is based on the experimental measurements inside the HOTDISC, where it was found that the temperature varies between 800°C and 1200°C, whereas the velocity weighting is based on Computational Fluid Dynamics simulations of the flow inside the two chambers (see Figure 6-8).

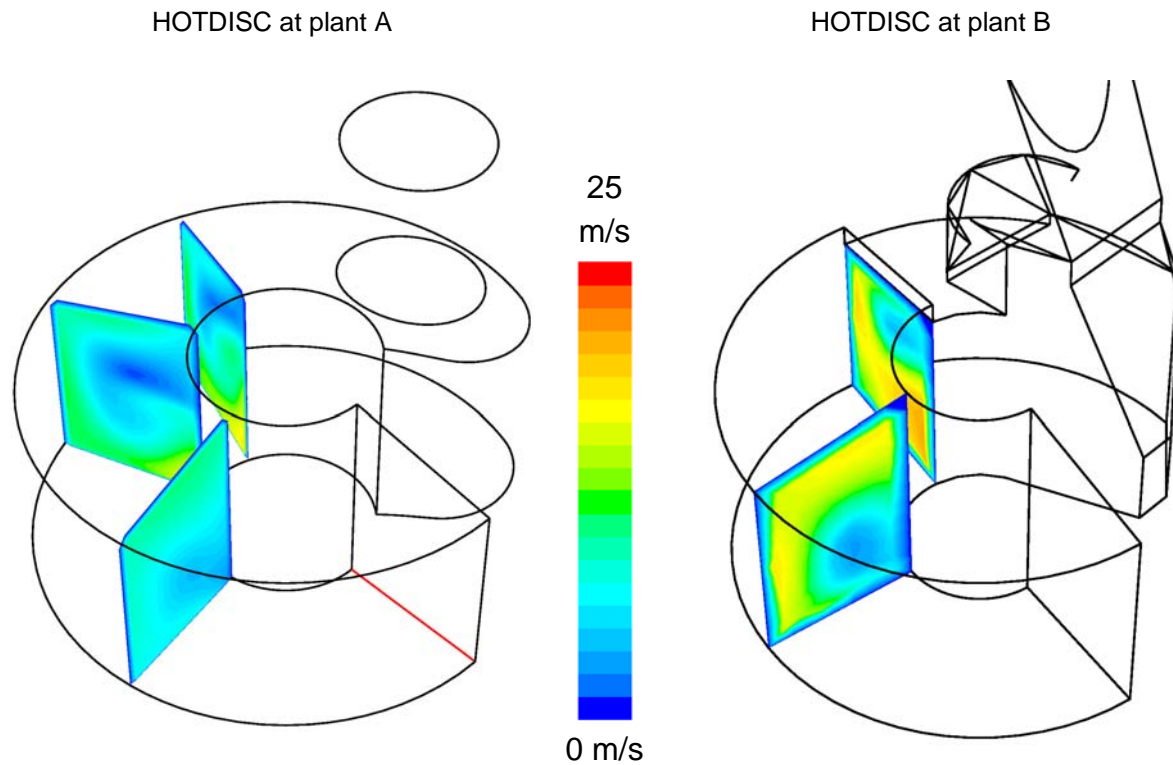


Figure 6-8: Isothermal Computational Fluid Dynamics simulation of linear gas velocity at the measurement positions of the two industrial HOTDISCs. Results are obtained with the Reynolds Stress Model and effects of combustion, calcination and interaction between solid raw material particles and gas are not included.

6.2.3 Uncertainties

An uncertainty analysis of the determined degree of fuel conversion using the methods in this section is presented in appendix E. An uncertainty of $\pm 12\%$ (absolute) may be expected with regard to the degree of fuel conversion.

6.2.4 Results of Plant Measurements

Using the outlined data analysis method on the measured species concentrations, the degree of fuel conversion is determined at each angular measurement position. In the following sections, the results of the analysis are shown as graphs with degree of fuel conversion against dimensionless angular location on disc.

6.2.4.1 HOTDISC at Plant A

The fuel conversion determined by weighting methods A and B are shown in Figure 6-9. Weighting method A is seen to yield fuel conversion in the range 39-50% regardless of position. In the case of weighting method B, it is observed that the predicted degree of fuel conversion is in the range 37-58%, i.e. a larger spread than in the case of weighting method A. Furthermore, it is observed that weighting method A predicts a nearly flat fuel conversion profile throughout the disc, whereas weighting method B predicts a slightly falling conversion

throughout the HOTDISC. The difference in measured fuel conversion between two measurement programmes at $\eta=0.42$ and 0.78 , is seen to be within each of the accumulated uncertainties. Consequently, there is no statistical difference between the predicted fuel conversions at $\eta=0.42$ and 0.78 .

The additional data point at $\eta=0.42$ shows a fuel conversion of about 63%, which is slightly higher than the data points of this study. However, considering the accumulated uncertainties, the data point with highest fuel conversion of this study cannot be separated from the data point carried out by others. The additional data points at $\eta=0.78$ show a significantly higher fuel conversion than the data points of this study, as the error bars are separated.

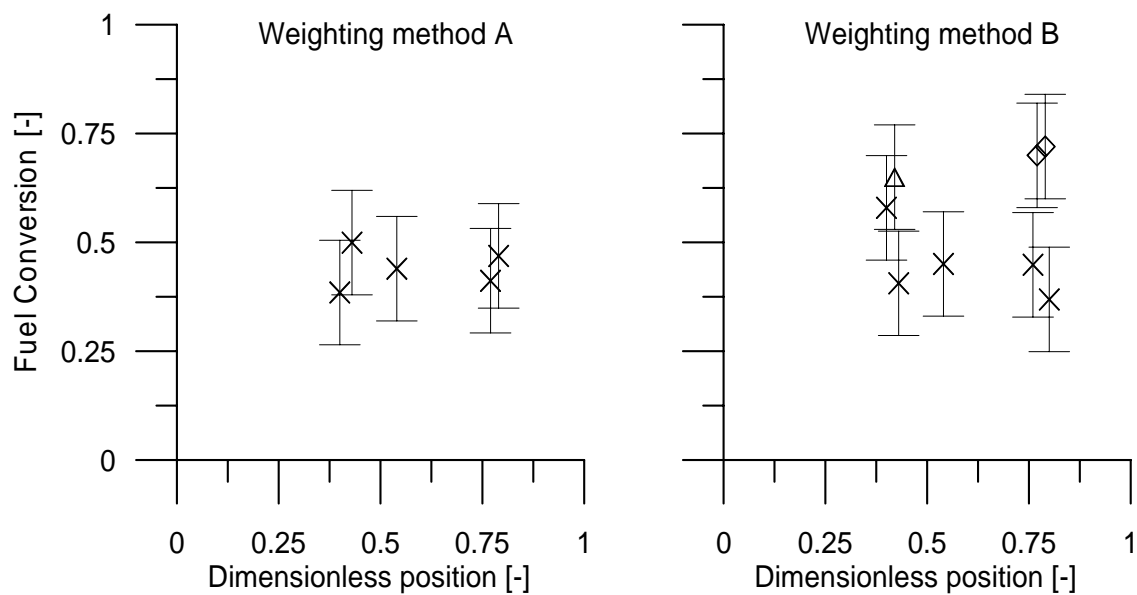


Figure 6-9: Determined fuel conversion in the measurement positions of the HOTDISC at plant A, using weighting methods A and B on measured gas species (x). The magnitude of the error bars shown corresponds to that of section 6.2.3. Data points designated \diamond and Δ represent data obtained from additional measurements and analyses performed in a similar way by other people from FLSmidth. For positions where more than one measurement has been performed, the data points are moved slightly on the x-axis for the sake of clarity.

6.2.4.2 HOTDISC at Plant B

The predicted degree of fuel conversion in the HOTDISC at plant B is shown in Figure 6-10. For weighting method A, it is observed that the predicted degree of fuel conversion increases from approximately 0.18 at $\eta=0.22$ to 0.60 and 0.89 at $\eta=0.60$. The two determined values at $\eta=0.60$ reflect first and second measurement programme respectively, whereas only one data set was obtained for the measurement at the position at $\eta=0.22$. For weighting method B, the same trend is observed, where the predicted fuel conversion increases from about 0.23 at $\eta=0.22$ to 0.60 and 0.78 at $\eta=0.60$ for first and second measurement programme, respectively. The two weighting methods applied are observed to yield approximately equal predicted fuel conversion at $\eta=0.22$. At $\eta=0.60$, the predicted fuel conversion between the

two measurement programmes is observed to vary. Weighting method A is furthermore observed to yield the highest variation between the predicted fuel conversions in the two measurement programmes. No statistical difference is found when using weighting method B at $\eta=0.60$, whereas a statistical difference exists using weighting method A.

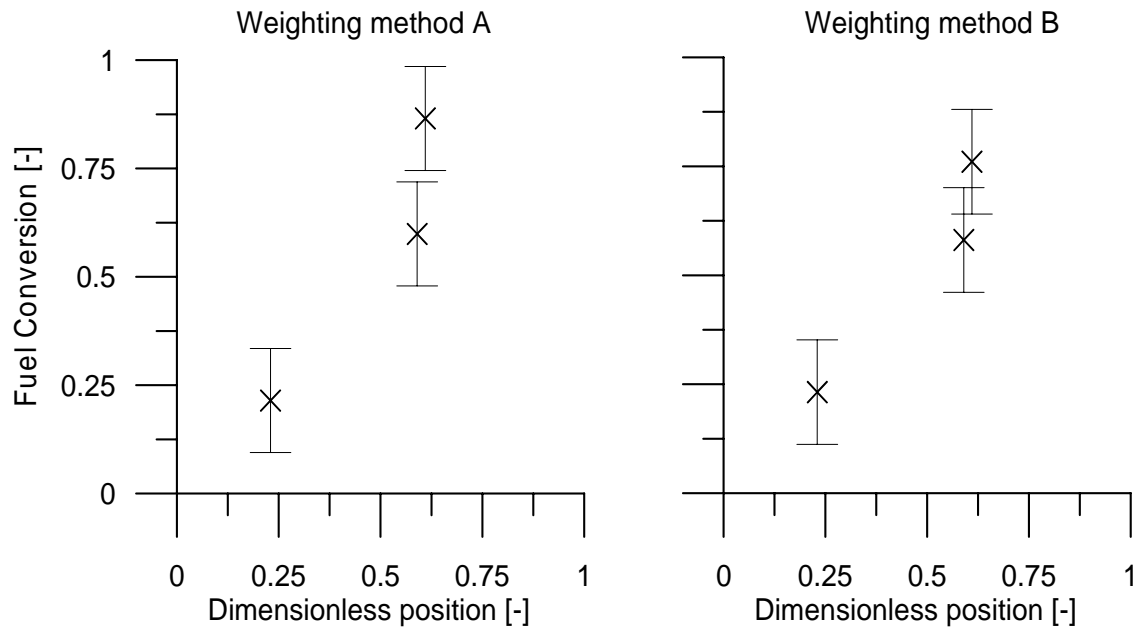


Figure 6-10: Determined fuel conversion in the measurement positions of the HOTDISC at plant B, using weighting methods A and B on measured gas species. For positions where more than one measurement has been performed, the data points are moved slightly on the x-axis for the sake of clarity.

6.2.5 Conclusion on Plant Measurements and Analyses

Detailed gas measurement programmes have been carried out at two industrial HOTDISCs using whole and shredded tyres, respectively. Measured species of CO, CO₂ and O₂ were transformed into average concentrations using two weighting methods and used to determine the degree of fuel conversion.

The predicted fuel conversion on the HOTDISC at plant A using shredded tyres showed a nearly flat fuel conversion profile throughout the HOTDISC. The absolute fuel conversion level was slightly below 50% for four out of five measurement programmes. However, other measurement programmes determined degree of fuel conversions in a similar way yielding 65% at $\eta=0.42$ and 70% at $\eta=0.78$, where the latter was shown to be significantly higher than the fuel conversion determined in this study.

The predicted fuel conversion profile on the HOTDISC at plant B using whole tyres, showed an increase in fuel conversion from about 20% at $\eta=0.22$ and up to 62-89% at $\eta=0.60$.

6.3 Comparison of Measured and Modelled Fuel Conversion

The degree of fuel conversion is an important parameter with regard to the performance of the HOTDISC. This is due to the fact that unconverted fuel in the HOTDISC is delivered to the calciner and must subsequently be converted here in order to avoid kiln instability and reduced clinker quality (see also section 3.2 and 3.3). A comparison of this parameter from the model simulations and the measured value is therefore performed here in order to analyze the behaviour of the HOTDISC when using shredded and whole tyres. Results obtained with weighting method B are used exclusively in the comparisons, because this method is considered to be the most accurate due to the inclusion of the gas velocity in the weighting procedure.

Figure 6-11 and Figure 6-12 show a comparison between the modelled and measured fuel conversion for the two HOTDISC's using shredded tyres or whole tyres respectively.

6.3.1 HOTDISC at Plant A

At the position of $\eta=0.42$, fair agreement between the model for devolatilization pathway I and the fuel conversions determined in this study is observed. The model prediction for pathway I is just at the lower limit of the measured data point *others #1*, considering the magnitude of the error bars. For $\eta=0.54$ and 0.7 , the model for conversion pathway I significantly over-predicts the measured fuel conversions from this study. However, at $\eta=0.78$, good agreement between the model for pathway I and the fuel conversions obtained by *others #2* is observed. For all positions, the model predicted fuel conversions via devolatilization pathway E are significantly lower than all measured fuel conversions.

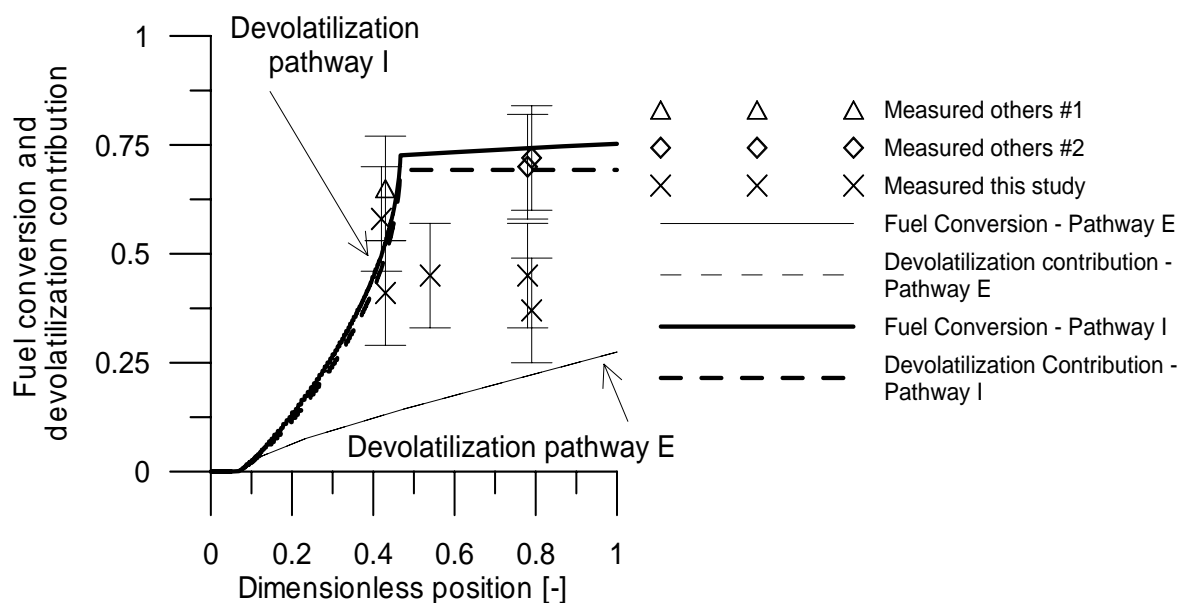


Figure 6-11: Comparison between modelled and measured fuel conversion obtained using weighting method B at plant A. For positions where more than one measurement has been performed, the data points are moved slightly on the x-axis for the sake of clarity.

6.3.2 HOTDISC at Plant B

At a position of $\eta=0.22$, good agreement between the model predicted fuel conversion via pathway I and the experimental data is observed. The predicted fuel conversion of pathway E is observed to be just at the lower limit of the measured fuel conversion. For $\eta=0.6$, the model predictions via pathway I are observed to be approximately the average of the measured fuel conversions. At this position, devolatilization pathway E agrees well with the lowest of the measured fuel conversions.

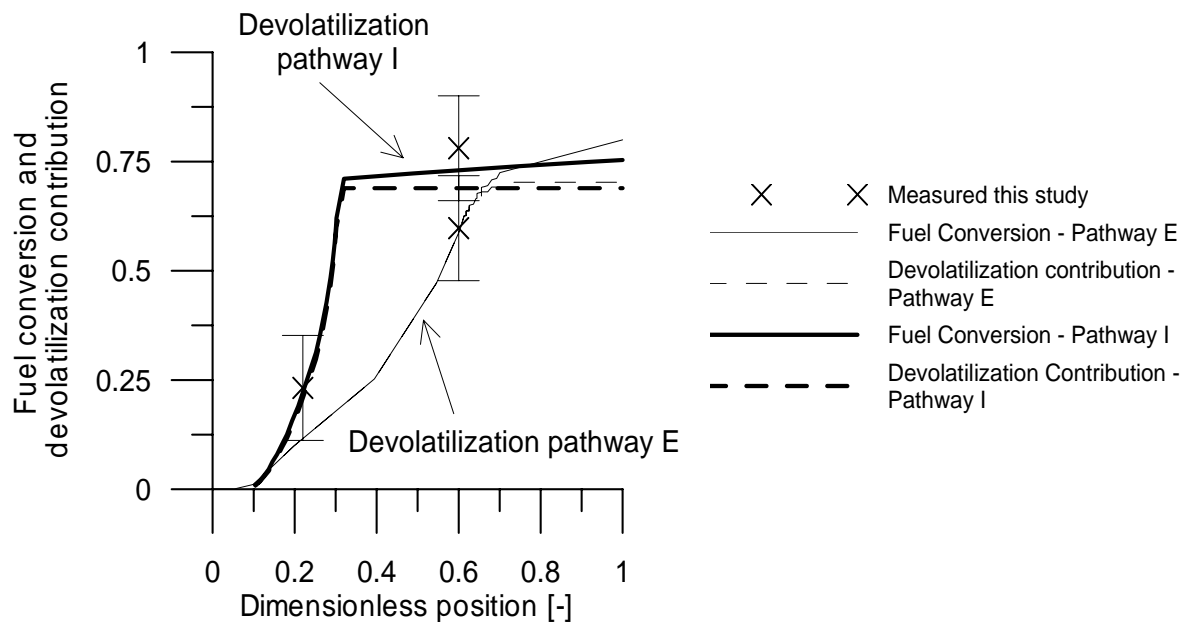


Figure 6-12: Comparison between modelled and measured fuel conversion obtained using weighting method B at plant B.

6.3.3 Discussion of Discrepancies between Modelled and Measured Fuel Conversion

6.3.3.1 HOTDISC at plant A

For the HOTDISC at plant A, overall agreement between the measured data and model predictions via devolatilization pathway I exists for all positions, except for the measured fuel conversions in this study at $\eta=0.54$ and 0.78 . In order to analyze these discrepancies, two points of view are applied:

- 1) *All measured fuel conversions are correct, and the discrepancies are therefore a consequence of differences in HOTDISC operating conditions*
- 2) *One of the two measurement programmes have been influenced by unknown systematic error(s).*

Re 1) This might be a consequence of different amounts of raw material particles covering the fuel in the HOTDISC in the two situations. For instance, if a high amount of raw material covers the solid fuel, devolatilization conversion pathway E is promoted rather than pathway I

which prolongs devolatilization time. Consequently, a partial coverage of fuel particles with meal may explain the fact that the measured fuel conversions are situated in between the model predicted fuel conversions at $\eta=0.54$ and 0.78 .

Re 2) A systematic error at one of the measurement programmes may have caused the discrepancies between the measured fuel conversions at $\eta=0.54$ and 0.78 . The fuel conversions at $\eta=0.78$ obtained by *others #2*, are in agreement with the model predictions of devolatilization pathway I and the modelled and measured fuel conversion at plant B at the end of the disc. Conceivably, the measured fuel conversions in this study at $\eta=0.54$ and 0.78 may have been influenced by a systematic error.

If the measured fuel conversions of this study at $\eta=0.54$ and 0.78 are neglected, overall agreement between the measured and the model predicted fuel conversion via pathway I is observed. Both the model for devolatilization conversion pathway I and the experimental measurements show that almost exclusively devolatilization takes place in the HOTDISC, whereas char oxidation also takes place in the calciner.

6.3.3.1 HOTDISC at plant B

For the HOTDISC at plant B, good agreement between the modelled and measured fuel conversions are observed, with the tendency that devolatilization via conversion pathway I seems better able to explain the measured data. Both the model for devolatilization conversion pathway I and the experimental measurements show that almost exclusively devolatilization takes place in the HOTDISC, whereas char oxidation also takes place in the calciner.

6.3.4 Conclusions on Comparison between Modelled and Measured Data

A comparison between measured fuel conversions and the model predicted conversion via devolatilization pathway I, reveals that this mechanism may be responsible for devolatilization of whole and shredded tyres in the HOTDISC. The models and measurements prove that devolatilization takes place in the HOTDISC and that char oxidation takes place both in the HOTDISC and in the subsequent calciner.

6.4 Use of Other Alternative Fuels in the HOTDISC

It was shown in the previous section that devolatilization takes place in the HOTDISC and char oxidation takes place both in the HOTDISC and in the calciner. In addition, the model calculations and experimental data show that the outer available particle surface also influences the rate of conversion. From these conclusions, the following clear guidelines for fuel selection for the HOTDISC may therefore be drawn up:

- 1) The fuel should be high in volatile content.*
- 2) The fuel should possess a non uniform shape that does not pack easily.*
- 3) Any char should be of the crackling type in order to produce small char particles that are easily converted when suspended in the gas stream of the HOTDISC or calciner.*

In the following sections, each of the above points is considered briefly with regard to the use of different types of alternative fuels in the HOTDISC. Please see Table 3-2 for detailed data for each fuel.

6.4.1 Liquids

1) The volatile content of liquid fuels approaches 100%. They evaporate and subsequently burn as a gaseous fuel. 2) Liquid fuels may be interpreted as “uniform objects” which pack closely. However, these fuels typically evaporate at temperatures below the intra particle devolatilization temperatures associated with solid fuels (see also chapter 4). 3) Since the volatiles content approaches 100%, char combustion is not an issue.

1) and 3) favour the use of liquid fuels in the HOTDISC, whereas 2) may limit their use.

6.4.2 Paper and Cardboard

1) These fuels have a relatively high volatile content in the range 73.6-88.5 wt.% dry. 2) The packing tendency of these fuels depends on the shape and size in which they are delivered to the system. Pre-treatment before admission to the HOTDISC may be an advantage in order to decrease the packing tendency. 3) The char content is in the range 6.2-10.9 wt.% dry and measures must be taken to ensure that the remaining char is sufficiently suspended as small particles.

1) Favour use in the HOTDISC, whereas 2) and 3) must be evaluated based on the input to the HOTDISC.

6.4.3 Plastics

1) The volatile content of plastics approaches 100%. 2) As with paper and cardboard, the packing tendency of plastics, also depends on size and shape. 3) Since the volatile content approaches 100%, char combustion is not an issue.

1) and 3) favours the use of plastic fuels in the HOTDISC, whereas 2) may limit their use.

6.4.4 Refuse Derived Fuel

Primarily a mixture of plastics, paper and cardboard and the guidelines of these fuels must also be applied here.

6.4.5 Meat and Bone Meal

1) The volatile content is in the range of 65-74 wt. % dry. 2) It is considered to pack due to its granular structure. 3) The char content is in the range of 7.2-10.6 wt. % dry. Meat and bone meal has a tendency to form agglomerated chars, i.e. pathway J of Figure 4-3.

1) Favours use in the HOTDISC, whereas 2) and 3) must be evaluated based on the input to the HOTDISC.

6.5 Conclusions on Chapter 6

Measured fuel conversions from measurement programmes at two industrial HOTDISC's were compared to the predictions of a plug-flow-reactor model and were used to identify controlling factors for solid fuel combustion in the HOTDISC. It was demonstrated that the HOTDISC is capable of devolatilizing difficult fuels, whereas char oxidation takes place both in the HOTDISC and in the calciner.

Based on the analyses performed, clear guidelines for selection of alternative fuel for use in the HOTDISC were made. These were briefly applied on alternative fuels typically used in cement production.

6.6 References

¹ Karlsson, M., Zevenhoven, R., Hupa, M.; Laboratory Characterisation of Waste Tyre Particles for Combustion in a Cement kiln; Finnish-Swedish Flame Days, Naantali, Finland, 1996.

² Bird RB, Stewart WE, Lightfoot EN. Transport phenomena. 2nd ed. New York: Wiley; 2002, p. 681. ISBN 0-471-41077-2.

³Perry Chemical Engineers Handbook, 7th edition, Mc-Graw Hill, 1999. ISBN 0-07-049841-5

⁴.Villadsen, J., Michelsen, M.L; Solution of differential equations models by polynomial approximation. Prentice-Hall, 1978; ISBN 013-822205-3.

⁵Jensen, L.S.; Analysis and improvement of ILC and SLC-D; Internal FLSmidth memo, January 2003.

Chapter 7 – Final Conclusions

An improved understanding of the combustion mechanism of alternative fuels used in cement production has been gained in this thesis. This has been achieved through literature studies, experimental studies under well-defined conditions and mathematical modelling as well as plant measurements on an industrial scale. In addition, the literature regarding process issues relevant to the use of alternative fuels in modern cement kiln systems was systematically reviewed. Rather than addressing only one of the points in detail, it was decided within the available time frame to work with all elements.

7.1 Concluding Trends

This section provides the important conclusions to be derived from this thesis. The important trends to be acknowledged from the literature review are:

- 1) The substitution rate of alternative fuels in cement production has been increasing significantly in the recent years, and the currently most used alternative fuels are in the solid state. Notably, plastics, meat and bone meal and tyre derived fuel covered 22, 17 and 18 energy-%, respectively, of all alternative fuels used in the German cement industry in 2004. In addition, alternative fuels typically have a higher volatile content than traditional coals and their physical and chemical properties may be significantly different from traditional fossil solid fuels.
- 2) The use of alternative fuels may influence clinker chemistry or induce process instabilities caused by restrictions of gas and solids flows in the kiln system. The clinker chemistry may be affected by minor components from the fuel ashes (e.g. zinc from TDF or phosphorous from MBM or other elements from other ashes), or from unburned carbon from the fuel in the material charge of the rotary kiln. Process instabilities causing restriction of gas and solids flows are significantly influenced by reducing conditions in the material inlet of the rotary kiln, mainly caused by unburned carbon in the calciner system, which induces formation of low melting sticky eutectics that may form deposits.
- 3) The gaseous emissions when using alternative fuels seem not to have been affected compared to traditional fossil fuels used up until now, and even a decrease in some emissions is reported to be a consequence of the increasing alternative fuel substitution rate. Care should be taken when considering new alternative fuels or equipment with regard to CO emissions.

The important trends to be emphasized with regard to combustion mechanisms of alternative fuels are:

- 1) With the increasing use of alternative fuels, larger fuel particles than traditionally used in pulverized fuel combustion are inevitably introduced to the kiln system, and mechanisms valid for small particles are therefore not sufficiently adequate to describe the combustion of them. Consequently, it has been a major technical issue to understand mechanisms controlling combustion conversion of large particles under conditions relevant to cement kiln systems.
- 2) With the typically high volatile content of alternative fuels, combustion of volatiles becomes responsible for a significant part of the fuel heating value. It was proved that devolatilization kinetics of large particles cannot be ignored, due to the conversion time being in the order of minutes. The devolatilization kinetics of large solid fuel particles is mainly controlled by heat transfer and kinetics. Consequently, the important parameters controlling the devolatilization kinetics are 1) devolatilization conversion pathway (e.g. constant size or shrinking particle), 2) external heat transfer rate from surroundings to particle, 3) particle size/shape, 4) residence time and 5) intrinsic pyrolysis kinetics.
- 3) Char oxidation is the final step in the solid fuel combustion process and therefore has a decisive influence on the degree of fuel burnout in the calciner system and/or rotary kiln burner. It was demonstrated that intrinsic char oxidation kinetics of typically alternative fuels are faster than intrinsic kinetics of traditionally used coals and petcoke char combustion kinetics. Combined with the fact that alternative fuels typically produce a char with relative large particle size, mass transfer becomes the rate limiting factor in the char conversion process, under conditions relevant to cement kiln systems. Consequently, the temperature is of less importance than for chars combusted under kinetic control. The important parameters controlling char oxidation are 1) conversion pathway, 2) the oxygen concentration in the bulk gas and transfer rate to particle surface, 3) particle size/shape, and 4) residence time.
- 4) The HOTDISC from FLSmidth is capable of devolatilizing difficult fuels, while char oxidation takes place both in the HOTDISC and in the subsequent calciner. When considering new fuels for use in the HOTDISC, the important parameters are 1) fuel conversion pathway, 2) volatile compared to char content, and 3) particle shape.

7.2 Suggestions for Further Work

It was identified that the solids residence time is an important factor for controlling the degree of fuel burnout in suspension calciners. Presently, the knowledge regarding residence time of solids in SLC and ILC systems is limited to small particles. Consequently, quantification of solids residence times for particle sizes/shapes relevant to alternative fuel utilization could be useful information in the prediction of fuel burnout as well as development of existing/new equipment. An increased understanding of solids residence time might be achieved either

through simple models, detailed flow models (CFD or other) or experiments, or a combination of the three.

It was also proved that the fuel conversion pathway is an important parameter that may vary between different fuels. Consequently, laboratory methods should be developed in order to characterize fuel conversion pathway under realistic conditions relevant to cement kiln systems.

Appendixes

Appendix A: Solution of Devolatilization Model A and C

Devolatilization models A and C are solved using orthogonal collocation (See [1] for further details). The solution presented here is that for model C, whereas the solution to the transient temperature profile in model A may be derived in a similar way by omitting the surface movement of model C.

A-1: Dimensionless Model

The model is made dimensionless by introducing a number of variables selected to fit the system in the best possible way. The dimensionless temperature, θ , is selected in such a way that the dimensionless temperature ranges between 0 and 1.

$$\theta = \frac{T - T_0}{T_0^\infty - T_0} \quad (\text{A-1})$$

The dimensionless time chosen is often used with transient heat conduction problems. However, for this moving boundary problem the time is scaled according to a fixed size, namely the initial distance from the surface to the centre. The dimensionless time, τ , is given by:

$$\tau = \frac{\frac{k}{\rho c_p} t}{r_0^2} \quad (\text{A-2})$$

The dimensionless position within the particle is scaled so that the moving surface is always located at 1 and the centre of the particle is located at 0, yielding the dimensionless location x :

$$x = \frac{r}{r_{surf}(t)} \quad (\text{A-3})$$

To satisfy the symmetry boundary condition at the centre, the following variable substitution is used:

$$u = x^2 \quad (\text{A-4})$$

To track the position of the surface in time, a dimensionless position, η , is introduced:

$$\eta = \frac{r_{surf}(t)}{r_0} \quad (\text{A-5})$$

A dimensionless activation energy, γ , is also introduced based on the initial temperature:

$$\gamma = \frac{E}{R_G T_0} \quad (\text{A-6})$$

The dimensionless variables are introduced into the original equations using substitution when changing the dependent variable and the chain rule when changing the independent variable. The conservation of energy in the solid particle becomes:

$$\frac{\partial \theta}{\partial \tau} \eta^2 = 2 \left(s + 1 + u \eta \frac{\partial \eta}{\partial \tau} \right) \frac{\partial \theta}{\partial u} + 4u \frac{\partial^2 \theta}{\partial u^2} \quad (\text{A-7})$$

with corresponding initial and boundary conditions :

$$\left. \frac{\partial \theta}{\partial u} \right|_{u=1} = \frac{1}{2} \frac{h_{eff} r_{surf}}{k} (\theta^\infty - \theta|_{u=1}) = \frac{Bi(r_{surf})}{2} (\theta^\infty - \theta|_{u=1}) \quad (\text{A-8})$$

or

$$\left. \frac{\partial \theta}{\partial u} \right|_{u=1} = \frac{1}{2} \frac{h_{eff} r_{surf}}{k} (\theta^\infty - \theta|_{u=1}) = \frac{Bi(r_0)}{2} \eta (\theta^\infty - \theta|_{u=1}) \quad (\text{A-9})$$

$$\theta(t = 0, u) = 0 \quad (\text{A-10})$$

where it is noted that the Biot number(= $h_{eff} r/k$), a characteristic dimensionless group in transient heat conduction problems, is introduced. Initially, the movement of the surface is also made dimensionless yielding:

$$\frac{d\eta}{d\tau} = - \frac{r_0^2 A}{2 \frac{k}{\rho c_p}} \eta \int_0^1 u^{\frac{s-1}{2}} \exp \left(- \frac{\gamma}{\left(\frac{T_0^\infty}{T_0} - 1 \right) \theta(u) + 1} \right) du \quad (\text{A-11})$$

with the initial condition:

$$\eta(\tau = 0) = 1 \quad (\text{A-12})$$

A-2: Collocation Equations

Trial functions of Lagrange polynomials based on $N+1$ points ($N_0=0$ and $N_1=1$, due to the boundary condition at the surface) are used, where N is the number of interior collocation points. As collocation points, the zeros of the following Jacobi polynomial are used:

$$p_{N+1}(u) = p_N^{(\alpha,\beta)} u^{N_0} (1-u)^{N_1} \quad (\text{A-13})$$

where $\alpha=0$ and $\beta=(s-1)/2$ are chosen so that the collocation points become equivalent to the quadrature points needed for the integration of the reaction rate expression of section 4.5.3. A solution of the following form is used for the transient temperature profile:

$$\theta(\tau, u) = \sum_{i=1}^{N+1} l_i(u) \theta_i(\tau) \quad (\text{A-14})$$

and when this expansion is inserted in the original heat transfer equation the following relation is obtained:

$$\eta^2 \sum_{i=1}^{N+1} l_i(u) \frac{\partial \theta_i}{\partial \tau} = 2 \left(s+1 + u\eta \frac{\partial \eta}{\partial \tau} \right) \sum_{i=1}^{N+1} \frac{dl_i}{du} \theta_i(\tau) + 4u \sum_{i=1}^{N+1} \frac{d^2 l_i}{du^2} \theta_i(\tau) \quad (\text{A-15})$$

from which the residual is derived:

$$R_N = -\eta^2 \sum_{i=1}^{N+1} l_i(u) \frac{\partial \theta_i}{\partial \tau} + 2 \left(s+1 + u\eta \frac{\partial \eta}{\partial \tau} \right) \sum_{i=1}^{N+1} \frac{dl_i}{du} \theta_i(\tau) + 4u \sum_{i=1}^{N+1} \frac{d^2 l_i}{du^2} \theta_i(\tau) \quad (\text{A-16})$$

The collocation procedure demands that the residual in each collocation point (u_j) should be zero ($R_N(u_j)=0$), yielding:

$$\eta^2 \frac{\partial \theta_j}{\partial \tau} = 2 \left(s+1 + u_j \eta \frac{\partial \eta}{\partial \tau} \right) \sum_{i=1}^{N+1} \frac{dl_i}{du} \Big|_{u_j} \theta_i(\tau) + 4u_j \sum_{i=1}^{N+1} \frac{d^2 l_i}{du^2} \Big|_{u_j} \theta_i(\tau) \quad (\text{A-17})$$

where it has been utilized that $l_i(u_j)=1$ for $j=i$ and $l_i(u_j)=0$ for $j \neq i$. By introducing the discretization matrices \mathbf{A} and \mathbf{B} , obtained by application of the subroutines JCOBI and DFOPR, and expansion of the sums the following expression is obtained:

$$\frac{\partial \theta_j}{\partial \tau} = \frac{1}{\eta^2} \left(2 \left(s+1 + u_j \eta \frac{\partial \eta}{\partial \tau} \right) \left(\sum_{i=1}^N A_{ji} \theta_i(\tau) + A_{j,N+1} \theta_{u=1}(\tau) \right) + 4u_j \left(\sum_{i=1}^N B_{ji} \theta_i(\tau) + B_{j,N+1} \theta_{u=1}(\tau) \right) \right) \quad (\text{A-18})$$

It is observed that the unknown boundary temperature at $u=1$ is now no longer part of the sum and the value of the dimensionless surface temperature can be found by treating the boundary condition at the surface in a similar manner yielding the following expression for the surface temperature.

$$\theta_{u=1} = \frac{\frac{Bi}{2}\theta^\infty - \sum_{i=1}^N \theta_i A_{N+1,i}}{\frac{Bi}{2} + A_{N+1,N+1}} \quad (\text{A-19})$$

Inserting (A-19) into (A-18) yields N coupled differential equations and integration of these N equations with the equation for the movement of the surface, yields the solution to the system.

The reaction rate expression (A-11) is integrated using Gauss integration with $\alpha=0$ and $\beta=(s-1)/2$:

$$\frac{d\eta}{d\tau} = -\frac{r_0^2 A}{k} \eta \sum_{i=1}^N \frac{w_i}{(s+1)} \exp\left(-\frac{\gamma}{\left(\frac{T_0^\infty}{T_0} - 1\right)\theta(u_i) + 1}\right) \quad (\text{A-20})$$

Where w_i are the normalized weight factors derived using the DFOPR subroutine. Integration of the coupled differential equations is performed using the semi-implicit Runge-Kutta integration routine SIRUKE.

A-3: References

¹ Villadsen, J., Michelsen, M.L. Solution of Differential Equation Models by Polynomial Approximation. Prentice-Hall, New Jersey, USA, 1978

Appendix B: Determination of External Heat Transfer Coefficients

These sections show how the external heat transfer characteristics for the experimental setups of chapter 4 are derived.

B-1: Flame Devolatilization Experimental Setup

The effective heat transfer coefficient to the surface of the large particle is influenced by radiation from the surroundings and by convection. Radiation stems mainly from wall and gas:

$$h_{eff} = h_{conv} + h_{rad,wall} + h_{rad,gas} \quad (\text{A-21})$$

Gas radiation is limited to gas species that are asymmetric, such as CO₂ and H₂O. Gas radiation is therefore only considered in the preliminary experimental setup, because the macro-TGA experiments were performed in an N₂-atmosphere.

The convective heat transfer coefficient is estimated using a Nusselt correlation for flow around a sphere [1]:

$$Nu = \frac{h \cdot D_{eq}}{k_{gas}} = 2 + 0.6 \cdot Re_{D_{eq}}^{1/2} \cdot Pr^{1/3} \quad Re_{D_{eq}} < 70.000 \quad (\text{A-22})$$

The equivalent sphere diameter of the sample holder was applied and the results shown in Table A-1 were obtained.

	D_{eq} [mm]	\tilde{v} [m/s]	Re [-]	Nu [-]	h_{conv} [W/m ² /K]
$T_{\infty} = 805^{\circ}\text{C}$	70	2.2	1102	33	32
$T_{\infty} = 955^{\circ}\text{C}$	70	6.1	2597	49	53

Table A-1: Determined convective heat transfer coefficients for conditions pertinent to the preliminary experimental setup.

The radiation to the surface follows Stefan Boltzmann's law, where the emitted radiation is proportional with the absolute temperature raised to 4th power. Correspondingly, a radiative heat transfer coefficient is calculated according to [2]:

$$h_{rad,i} = \varepsilon_i \sigma (T_{\infty}^2 + T_{r=r_0}^2) (T_{\infty} + T_{r=r_0}) \quad (\text{Temperatures in Kelvin}) \quad (\text{A-23})$$

The effective emissivity for the walls and the gaseous species was estimated using a rigorous method, including geometry of chamber as well as concentrations of oxygen and carbon dioxide. The magnitude of radiation from the gas and wall to the surface of the particle is calculated as:

$$Q_{SS} + Q_{GS} = (F_{SS} + F_{GS}) \sigma (T_{\infty}^4 - T_{Surface}^4) = \varepsilon \sigma (T_{\infty}^4 - T_{Surface}^4) \quad (\text{A-24})$$

where F_{GS} and F_{SS} are the total exchange areas for radiation exchange between gas to surface (GS) and surface to surface (SS). The total exchange areas are dependent on geometry and radiation properties. For infinite parallel planes, with the view factor of unity, the total exchange areas are calculated as [1], where index 1 indicates fuel surface and index 2 indicates surroundings.

$$F_{SS} = \frac{a\varepsilon_1\varepsilon_2}{\zeta} - \frac{(1-a)\varepsilon_1\varepsilon_2}{1-\rho_1\rho_2} \quad (\text{A-25})$$

$$F_{GS} = \frac{\varepsilon_1\varepsilon_g \left(\frac{1}{1-\varepsilon_g/a} + \rho_2 \right)}{\zeta} \quad (\text{A-26})$$

where

$$\zeta = \frac{1}{1-\varepsilon_g/a} - (1-\varepsilon_g/a)\rho_1\rho_2 \quad (\text{A-27})$$

The emissivity of the gas mixture is dependent on a characteristic length as well as the concentration of carbon dioxide and water. The height of the reaction chamber is 0.4 m and the concentrations of carbon dioxide and water were both approximately 8 vol.% in the experiments. Based on the method outlined here and information given in [1] regarding determination of gas emissivity, the results of Table A-2 are obtained.

T_{∞}	$T_{r=r0}$	a	ε_g	F_{GS}	F_{SS}	$F_{GS}+F_{SS}$	$\overline{F_{SS} + F_{GS}}$ = ε
$^{\circ}C$	$^{\circ}C$	-	-	-	-	-	-
805	250	0.28	0.14	0.12	0.17	0.29	
805	500	0.20	0.14	0.12	0.13	0.25	0.25
805	750	0.15	0.14	0.11	0.11	0.22	
955	250	0.27	0.12	0.11	0.17	0.28	
955	500	0.19	0.12	0.10	0.13	0.23	0.23
955	750	0.15	0.12	0.10	0.10	0.20	
955	900	0.13	0.12	0.10	0.09	0.19	

Table A-2: Derivation of applied effective emissivity used in the interpretation of the flaming devolatilization experiments.

The outflow of volatile gases from the particle surface, however, may reduce the convective heat transfer coefficient [3,4], and in order to compensate for this effect, the correlation given by Bird et al. [5] is applied (A-28) (Only for model B).

$$\frac{h_{conv}}{h_{conv,0}} = \frac{m_{v,r=r_0} c_{p,v} / h_{conv,0}}{\exp(m_{v,r=r_0} c_{p,v} / h_{conv,0}) - 1} \quad (\text{A-28})$$

B-2: Macro-TGA setup

In this setup, the convective heat transfer coefficient is estimated using a Nusselt correlation for laminar external flow in a vertical tube [1], as is the case in this experimental setup:

$$Nu = \frac{h_{conv,0} r_{r=r_0}}{k_{gas}} = \frac{1.02}{2} Re^{0.45} Pr^{0.5} \left(\frac{D_H}{L} \right)^{0.4} \left(\frac{r_{reactor}}{r_{r=r_0}} \right)^{0.8} Gr^{0.05} \quad (\text{A-29})$$

The results using this correlation are shown in Figure A-1 as a function of particle radius. The convective heat transfer coefficient is observed to be very dependent on particle radius, decreasing from about 38-45 W/m²/K at a radius of 5mm to slightly above 10 W/m²/K at a particle radius of 25mm. The effect of gas temperature on convective heat transfer coefficient is not as significant as the particle size.

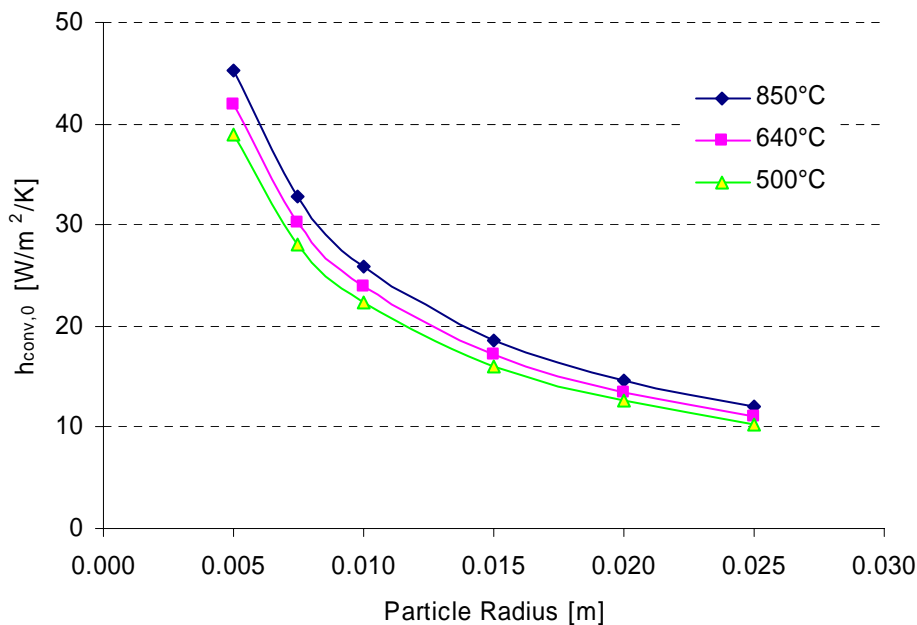


Figure A-1: Calculated convective heat transfer coefficient in the experimental macro-TGA setup at conditions relevant to the experimental conditions as a function of particle radius.

As described, gas radiation is neglected in the macro-TGA setup, due to the fact that experiments were performed in N₂. Moreover, the distance between the reactor wall and fuel

sample is short compared to the preliminary experimental setup, and the radiation exchange is therefore calculated using (A-23) with a wall emissivity of 0.35 [2].

B-3: References

¹ Perry Chemical Engineers Handbook, 7th edition, Mc-Graw Hill, 1999.

² Szekely, J., Ewans, J.W., Sohn, H.Y., Gas-Solid Reactions, Academic Press, New York, 1976.

³ Thunman, H., Principles and Models of Solid Fuel Combustion, PhD Thesis, Chalmers University of Technology, 2001.

⁴ Thunman, H., Davidsson, K., Leckner, B., Separation of drying and devolatilization during conversion of solid fuels, Combustion and Flame, 137, 242-250, 2004.

⁵ Bird, R.B., Stewart, W.E., Lightfoot, E.N. Transport Phenomena, 2nd edition, Wiley, New York, 2002. ISBN 0-471-41077-2.

Appendix C: Sensitivity Analysis on Devolatilization Model B

Since model B contains many parameters, it is relevant to assess the parameters that have significant influence on the output of the model calculation. In order to assess the influence of each parameter in the model, a sensitivity analysis is performed by changing each parameter $\pm 25\%$ while keeping the other parameters constant. As described, the devolatilization time is an important parameter and therefore the sensitivity analysis is performed on the devolatilization time. The analysis is performed for a 14mm tyre rubber particle at temperatures of 490°C and 840°C, and the resulting change in devolatilization time, compared to the time computed with standard parameters of section 4.5.3, is reported in Table A-3. A negative number indicates that the conversion time is lower compared to standard parameters while a positive number means the conversion time is higher.

The results of the sensitivity analysis show that increasing the heat capacity of virgin fuel, char or volatile gas, results in a prolonged conversion time. If the conductivity of either char or virgin fuel is lowered, the conversion time is also prolonged. Regarding the devolatilization reaction enthalpy effects, an increased exothermicity is observed to decrease the devolatilization time and the opposite is observed for the endothermic reaction. For the kinetic parameters of reactions 1 and 3, an increase in activation energy or decrease in pre exponential factor increases the time of devolatilization. The observed increase in devolatilization time, when increasing the activation energy is a consequence of the reaction being shifted towards higher temperatures. For reaction 2, however, the devolatilization time is observed to increase regardless of the $\pm 25\%$ change tested in the activation energy of reaction 2 and this behaviour is especially pronounced at a surrounding temperature of 490°C. The increase in devolatilization time when increasing the activation energy is again a consequence of the reaction been shifted towards higher temperatures as was the case for reactions 1 and 3. However, the increase in devolatilization time when decreasing the activation energy can be explained, based on model calculations, by the fact that the exothermic reaction enthalpy increases the temperature locally and induces the onset of reaction 3. If the exothermic reaction is shifted to lower temperatures (lowering E_2), the heat evolved from the reaction is not sufficient to increase the local temperature to initiate reaction 3 and therefore the devolatilization time is prolonged.

The highest sensitivity is found for the activation energies for the decomposition reactions 2 and 3, indicating that chemical kinetics are important in the prediction of the devolatilization times. However, it is noted that a $\pm 25\%$ change in activation energy causes significant changes in the kinetics, because the activation energy enters inside an exponential term. For the heat transfer model the specific heat capacity of the virgin fuel yields the highest sensitivity on the predicted devolatilization time at both 490°C and 840°C. At 490°C, the second highest sensitivity in the heat transfer parameters is found for the effective heat transfer coefficient, whereas for 840°C the conductivity of the virgin fuel and effective heat transfer coefficient have equally important impact on the prediction of devolatilization time. The conductivity and specific heat capacity of the char and the specific heat capacity of the

volatile gas have little influence on the predicted devolatilization time. The influence of devolatilization reaction enthalpy on the predicted devolatilization time, is found to be most significant for reaction 2 (e.g. the exothermic reaction) and for the temperature of 490°C.

<i>Parameter</i>	$T_{\infty}=490^{\circ}\text{C}$		$T_{\infty}=840^{\circ}\text{C}$	
	-25%	+25%	-25%	+25%
<i>Heat transfer parameters</i>				
$c_{p,v}$	-1.8 %	1.8	-4.4	4.2
$c_{p,vf}$	-22.0	19.7	-20.5	19.4
$c_{p,char}$	-3.6	3.5	-2.3	2.2
k_{vf}	9.2	-5.4	15.7	-9.6
k_{char}	0.1	-0.1	-0.2	0.9
h_{eff}	16.0	-9.7	15.1	-8.9
<i>Devolatilization reaction enthalpy</i>				
ΔH_1	0	0	0	0
ΔH_2	8.4	-9.3	4.7	-4.8
ΔH_3	-2.6	2.5	-1.4	1.4
<i>Devolatilization reaction kinetics</i>				
A_1	0.9	-0.6	1.0	-0.7
E_1	-5.4	18.9	-4.0	12.6
A_2	-1.0	0.7	-0.2	0.1
E_2	9.6	96.5	1.9	14.5
A_3	6.8	-4.5	1.4	-1.1
E_3	-40.3	96.5	-15.8	53.3

Table A-3: Calculated sensitivities in percentage change in conversion time (90%) for a $\pm 25\%$ change in model parameter while keeping the other parameters constant. The calculation is performed for a 14 mm tyre rubber cylinder.

As revealed in the sensitivity analysis, the most important heat transfer parameter is the specific heat capacity of the virgin fuel. In the literature, the reported heat capacities of tyre rubber are found to deviate significantly (see Figure A-2). The employed heat capacity of 2000 J/kg/K from [1] was observed to give the best correlation between the model and the experimental results with regard to mass loss and intra-particle temperature profiles.

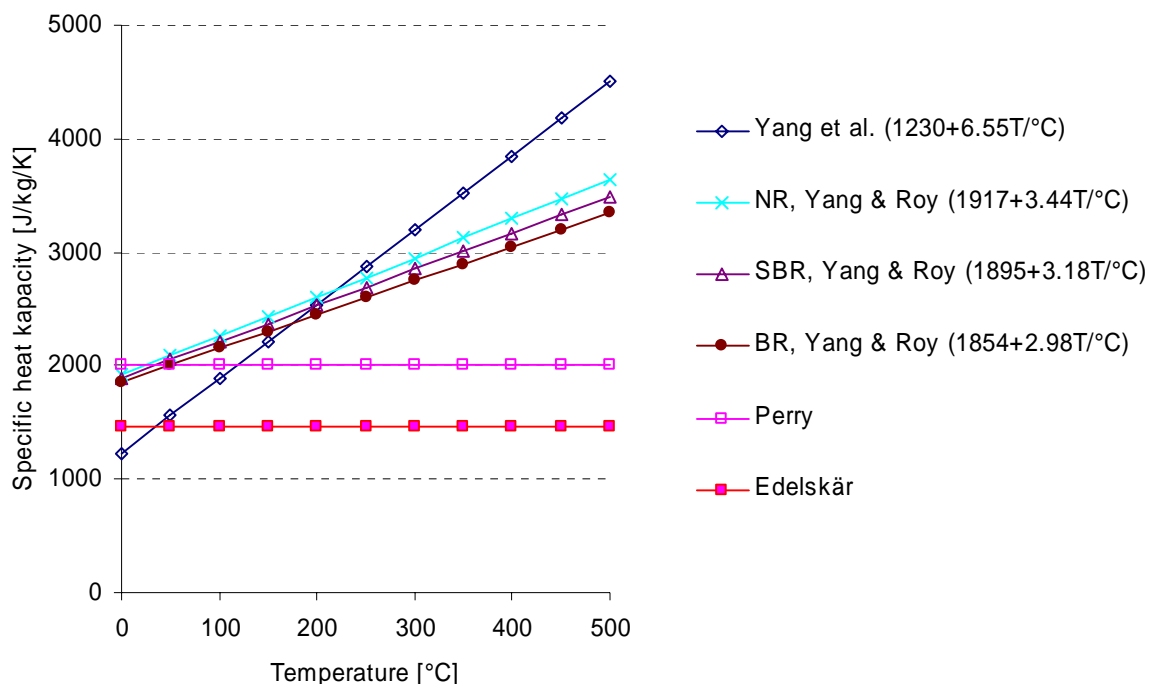


Figure A-2: Comparison of specific heat capacity of tyre rubber constituents obtained from the literature. Vulcanized tyre rubber reported by Perry [1], Yang et al. [2,3] and Edelskär [4] whereas Yang and Roy reports for the pure rubber compounds [5].

C-1: References

¹Perry Chemical Engineers Handbook, 7th edition, Mc-Graw Hill, 1999.

²Yang, J., Tanguy, P.A., Roy, C., Heat transfer, Mass transfer and kinetics study of the vacuum pyrolysis of a large used tyre particle. Chem. Eng. Sci. 50,12,1909-1922, 1995.

³Yang, J., Philippe, A.T., Roy, C., Numerical Model for the Vacuum Pyrolysis of Scrap Tires in Batch Reactors. AIChE J., 41, 6, 1500-1512, 1995.

⁴ Edelskär, T., Technical and Environmental Properties of Tyre Shreds Focusing on Ground Engineering Applications, Technical Report, Luleå University of Technology, May, 2004.

⁵ Yang, J, Roy, C., A new method for DTA measurements of enthalpy change during the pyrolysis of rubbers. Thermochemica Acta 288, 155-168, 1996.

Appendix D: Instantaneous Air Excess Ratio

This appendix shows how an expression for the instantaneous air excess ratio for systems without CO may be derived.

$$\lambda_{inst.} = \frac{O_2 \text{ consumed in combustion} + O_2 \text{ remaining}}{O_2 \text{ consumed in combustion}}$$

$$\lambda_{inst.} = 1 + \frac{O_2 \text{ remaining}}{O_2 \text{ consumed in combustion}}$$

$$\lambda_{inst.} = 1 + \frac{O_2 \text{ remaining}}{O_2 \text{ at start} - O_2 \text{ remaining}}$$

$$\lambda_{inst.} = 1 + \frac{O_2 \text{ remaining}}{\frac{21}{79} \text{ Inert } N_2 \text{ at start} - O_2 \text{ remaining}} \quad \text{(A-30)}$$

$$\lambda_{inst.} = 1 + \frac{\text{mole flow} \cdot \%O_2}{\frac{21}{79} \text{mole flow} \cdot \% \text{Inert } N_2 - \text{mole flow} \cdot \%O_2}$$

$$\lambda_{inst.} = 1 + \frac{1}{\frac{21}{79} \left(\frac{1 - \widetilde{y}_{O_2} - \widetilde{y}_{CO_2} - \widetilde{y}_{CO}}{\widetilde{y}_{O_2}} \right) - 1}$$

Appendix E: Uncertainties on Estimated Degree of Fuel conversion

Errors may be systematic or random. In this case the former is mainly entrainment of atmospheric air into the gas measurement system, thereby increasing the measured concentration of O₂ and decreasing CO₂ and CO (false air). However, efforts were made to reduce this systematic error, where leak tests were made several times a day and other preventive measures were taken. Random errors include fluctuations in fuel feed rates, gas flows, uncertainties in measured gas species, and these cannot be avoided. The impact of accumulated random errors on the predicted degree of fuel conversion is examined here.

The degree of fuel conversion is estimated from a series of calculated and measured values and may hence be expressed as a function of these values:

$$X_{Fuel} = X_{Fuel} \left(Q_{tert}, m_f, n_{air}, \widetilde{y}_{O_2}, \widetilde{y}_{CO_2}, \widetilde{y}_{CO} \right) \quad (\text{A-31})$$

In order to determine the uncertainty on the determined fuel conversion, the accumulation law of uncertainties is applied [1]:

$$\Delta(X_{Fuel}) = \sqrt{\left(\frac{\partial X_{Fuel}}{\partial Q_{tert}} \Delta(Q_{tert}) \right)^2 + \left(\frac{\partial X_{Fuel}}{\partial m_f} \Delta(m_f) \right)^2 + \dots + \left(\frac{\partial X_{Fuel}}{\partial y_{CO}} \Delta(y_{CO}) \right)^2} \quad (\text{A-32})$$

In the estimation of the total uncertainty, the tertiary air flow is assumed to fluctuate $\pm 5\%$ of the total flow, the fuel feed rate is assumed to fluctuate $\pm 10\%$ and the stoichiometric combustion air amount is assumed to fluctuate $\pm 5\%$. The uncertainties regarding measured gas species are $\pm 2\%$ of total span range for each specie, due to the fact that the analyzer is calibrated daily during the measurement campaign.

Applying relevant figures, the uncertainty analysis demonstrates that a total deviation on the determined fuel conversion can be expected to be $\pm 12\%$ (absolute). It also demonstrates that the measured O₂ concentration has the highest impact on overall uncertainty. It accounts for about 60% of the total uncertainty.

E-1:References

¹ Larsen, M.O.; Statistik 1, Institut for Anvendt Kemi, 3. Udgave, 1998. (In danish)

Devolatilization characteristics of large particles of tyre rubber under combustion conditions

Morten Boberg Larsen ^{a,b,*}, Lars Schultz ^b, Peter Glarborg ^b, Lars Skaarup-Jensen ^a,
Kim Dam-Johansen ^b, Flemming Frandsen ^b, Ulrik Henriksen ^c

^a FLSmith A/S, Vigerslev Allé 77, DK-2500 Valby, Denmark

^b CHEC Research Centre, Department of Chemical Engineering, Technical University of Denmark, (DTU), DK-2800 Lyngby, Denmark

^c Department of Mechanical Engineering, Technical University of Denmark (DTU), Building 403, DK-2800 Lyngby, Denmark

Received 5 October 2005; received in revised form 13 December 2005; accepted 13 December 2005

Available online 19 January 2006

Abstract

A systematic experimental study has been performed in order to investigate the effect of particle size and temperature on the devolatilization rate of large tyre rubber particles. Cylindrical tyre particles with diameters between 7.5 and 22 mm were devolatilised in a macro-TGA reactor, at temperatures between 490 and 840 °C in an inert atmosphere. The effect of particle size and surrounding temperature on the rate of devolatilization was observed to be significant, i.e. larger particle diameters and lower temperatures increased the devolatilization time. A detailed mathematical model for the devolatilization process including internal and external heat transfer, three parallel independent devolatilization reactions and reaction enthalpy effects has been developed and solved using an implicit finite difference method. Comparison of the model predictions with experimental data, reveals that the devolatilization process of large tyre rubber particles at temperatures above 490 °C can be considered to be controlled mainly by heat transfer and reaction kinetics. The model analysis further shows that exothermic devolatilization reaction enthalpy effects cannot be neglected in the prediction of the intra particle temperature rise. A sensitivity analysis of the model parameters, demonstrates that the specific heat capacity of the virgin fuel and the activation energies of the devolatilization reactions is the most important model parameters in the prediction of devolatilization times of large tyre rubber particles.

© 2006 Elsevier Ltd. All rights reserved.

Keywords: Devolatilization; Large particles; Tyre rubber

1. Introduction

The number of scrap tires produced each year amounts to 2.0–2.5 million tonnes in Europe, 2.5 million tonnes in North America, 0.5–1 million tonnes in Japan and more than one million tonnes in China [1]. For many years, tyres have been stockpiled in open dumps with the risk of catching fire which may result in toxic emissions and these fires are furthermore, difficult to extinguish once ignited [2]. In addition, stockpiled tyres, containing small amounts of rain water are also outstanding breeding sites for mosquitoes [2]. In the European Union, the EC Waste Landfill Directive bans land filling of

tyres by 2006 [3]; this poses great challenges for the reuse of tyres for various purposes in Europe.

Typically, a tyre consists of vulcanised rubber with reinforcing steel or fabric belts and reinforcing textile cords. The rubber is a blend of natural and synthetic rubber, where carbon black has been added to increase the strength and abrasion resistance. The exact composition of tyres depends on brand, age, and type, e.g. car tyre vs. truck tyre, and the composition and processing may often be held secret by the different tyre producers. Several techniques for reuse or disposal of used tyres are currently under development or in use. One of these techniques is the pyrolysis process, where tyres typically are heated to approximately 400–700° in an inert atmosphere, causing the rubber polymers to degrade into a complex mixture of gaseous, solid and liquid hydrocarbons, which may be processed in different ways, thereby producing chemical feedstock, fuel or activated carbon. Steel may also be reused. Another viable technique is direct combustion of the tyre, and subsequent usage of the released energy. The heating value of tyres is comparable to high rank coals,

* Corresponding author. Address: CHEC Research Centre, Department of Chemical Engineering, Technical University of Denmark, (DTU), DK-2800 Lyngby, Denmark. Tel.: +45 45252842.

E-mail address: mbl@kt.dtu.dk (M.B. Larsen).

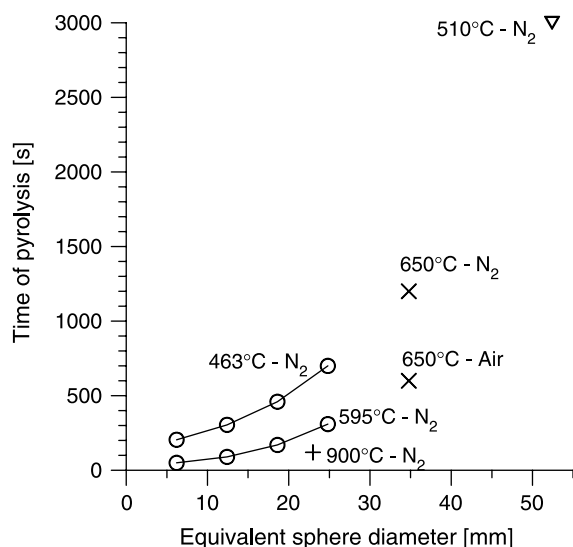


Fig. 1. Comparison of devolatilization times for large particles of tyre rubber from the literature with temperature as discrete variable. The captions are: (○) Bouvier et al. [14], (▼) Yang et al. [15], (+) Giddings et al. [13] and (×) Schmidthals [4].

atmosphere (flame enveloping the particle), particle size and temperature on the rate of devolatilization of large tyre rubber particles is not clear in the literature.

The present study emphasizes the mass-loss vs. time, rather than devolatilization product distributions or yields. The aims of the present work are (1) to investigate systematically the effect of size and temperature on the devolatilization of large tyre rubber particles under inert conditions, and (2) to validate a mathematical model against the experimental results.

2. Experimental

In this study, tyre rubber is cut into cylindrical particles with a diameter between 7.5 and 22 mm and a height of approximately 35 mm. Since tyre is an inhomogeneous material, containing tread and steel it is unsuitable for systematic experiments, due to the difficulties in producing identical samples. Consequently, new tyre rubber from the wearing face of a truck tyre without tread and steel wires were obtained from *PointS*, Denmark, and used for the experiments. Proximate and ultimate analyses were determined according to British Standard Methods (BS 1016-1018) and the heating value was determined using ISO 1928 standards (Table 1).

The Macro-TGA setup used for the experiments is depicted in Fig. 2. It consists of a vertical cylindrical reactor with four electrical heating elements. A valve and a mass flow controller (MFC) are used for addition of a well defined flow of pure N₂ to the bottom of the reactor. All experimental results herein are obtained with a gas flow of 17.5 Nl/min. Preheating of the gas takes place in the bottom of the reactor and experimental temperature measurements in the centre of the reactor for different set point temperatures of the heating elements gives the temperature that the sample experiences in the reactor. Two cylindrical tyre rubber samples are placed axially on top of each other, in order to ensure a high length to diameter ratio for

Table 1
Proximate, ultimate analysis and lower heating value for the tested tyre rubber

		Unit	Truck tyre rubber
Proximate analysis	Moisture	wt%	1.2
	Volatiles	wt%	64.1
	Ash	wt%	5.0
	Fixed C (calculated)	wt%	29.7
Ultimate analysis	C	wt%	82.0
	H	wt%	6.71
	S	wt%	1.35
	N	wt%	0.32
	O (calculated)	wt%	3.42
Lower heating value	MJ/kg	35.0	

the later data interpretation, and inserted into a holder prepared in the same diameter as the tyre sample. The holder is made of a stainless steel mesh where the wires have a diameter of approximately 0.5 mm and a quadratic clearance of approximately 0.5 × 0.5 mm. The purpose of the net is to retain the char layer during the devolatilization process and thereby secure well defined conditions, i.e. swelling and removal of the char layer is inhibited. Each experiment is initiated by immersing the sample holder with tyre rubber into the preheated reactor under continuous gas flow, i.e. the tyre rubber particle experiences the same environment as a piece of tyre rubber under combustion conditions or continuous pyrolysis processes. A precision balance measures the weight of the sample, and a data acquisition program records the signal on a computer for later data interpretation.

Additional experiments for measuring the temperature profiles in the tyre rubber during the devolatilization were made. Thermocouples were placed in the axial direction at

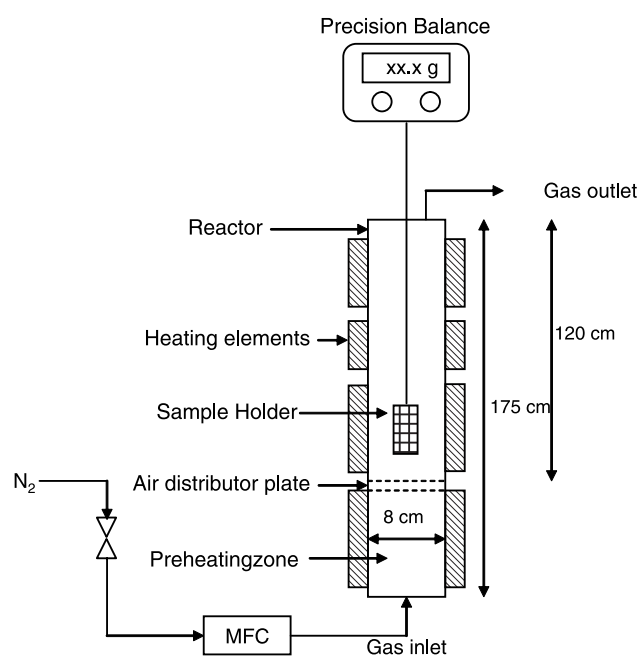


Fig. 2. Experimental setup.

the centre of the cylindrical particle, i.e. $r=0$, and at the halfway distance between the surface and the centre, i.e. $r=\frac{1}{2}r_0$. The signal from the temperature measurements as a function of time was then logged on a computer during an experiment. Mass-loss measurements were not made simultaneously with measuring the transient temperature profiles, because the thermocouples could disturb the mass-loss measurement.

3. Mathematical model

The aim of the mathematical model is to predict devolatilization mass-loss behaviour for large tyre rubber particles, under conditions pertinent to combustion. Several mathematical models for the devolatilization of large particles have been published; however, most of these models concern the devolatilization of biomass or coal. To the authors' knowledge only Yang et al. [15] consider modelling of devolatilization of large tyre rubber particles. Mathematical models for the devolatilization of large particles include coupled, non-linear, ordinary and partial differential equations, which are not easily solved. The modelling approaches found in the literature may be divided into three classes (the latter approach is used in the model solution presented in this work):

1. Via suitable assumptions and reductions of the original equations, the resulting equation(s) may be solved analytically, e.g. see Kanury [17].
2. Integral models [18] where heat transfer is assumed to be the rate controlling parameter and the spatial transient temperature profile is assumed to be a known function, e.g. polynomial or linear, which upon substitution into the original partial differential equation reduces to a system of ordinary differential equations [19–21].

3. Solution of ordinary and partial differential equations via finite approximation methods [22,23].

The devolatilization of a large tyre rubber particle may be subdivided into a number of physical and chemical processes. Fig. 3 depicts a simplified drawing of a partially devolatilised solid fuel particle, where the devolatilization is driven by external heating. The heat is transported into the material by conduction through the char, reacting and virgin fuel layers, where radiative heat transfer may have a role in the char and reacting layers. In the reacting layer, the rubber polymers are depolymerised and evaporated, and as a consequence of the volatile-production, an outward mass transport through the particle is induced. Independent reactions may be endo or exothermic and may also include secondary reactions. The outward mass-flow may also cool the hotter solid when the cooler gas flows from the interior. In an oxidizing atmosphere, the devolatilization products may ignite in a flame front above the outer surface, enhancing the external heat transfer to the surface. Finally, the outflow of devolatilization products may cause the solid to swell.

In the model presented in this work, heat transfer and chemical reaction kinetics are assumed to be the rate controlling parameters for the devolatilization process, whereas resistance to mass transport is assumed negligible. In the literature, these assumptions are also successfully used in the modelling of devolatilization mass-loss rates and conversion times by Adesanya and Pham [24] and Wildegger-Gaissmaier and Agarwall [25] in their modelling of coal devolatilization and by Galgano and Di Blasi to model devolatilization of both dry [20] and wet [21] biomass. Grønli and Melaan [23] argue that the internal mass transfer during the devolatilization has negligible influence on the

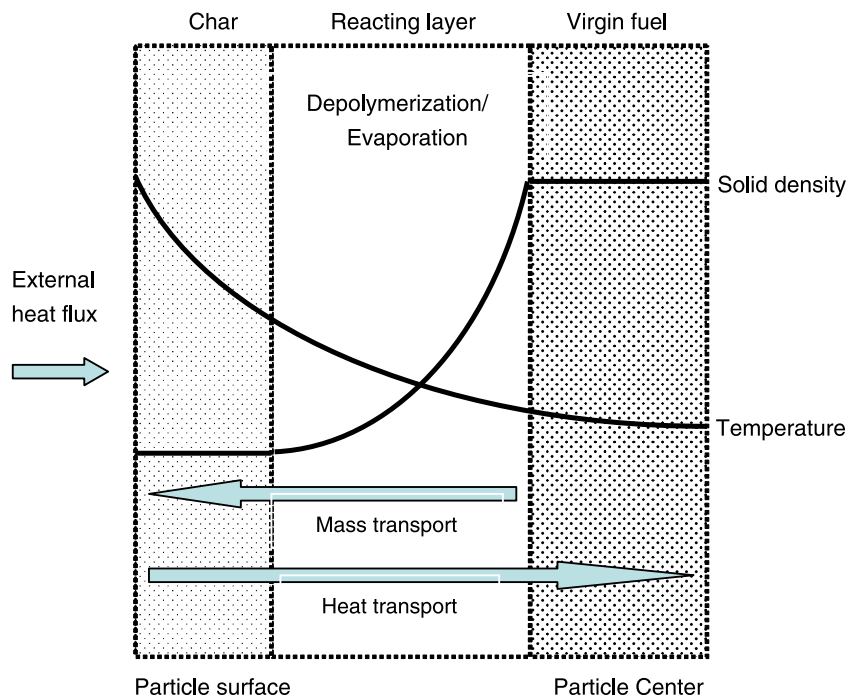


Fig. 3. Schematic illustration of the devolatilization of a large tyre particle.

spatial temperature profile for biomass. The mass transport has influence on the residence time distribution of out flowing gasses, i.e. it has only influence on the secondary reactions.

In the current model, the solid matrix is assumed to consist of constant char and ash fractions as well as a varying volatile part made up of three sub fractions. The reaction scheme for the devolatilization process is assumed to consist of three independent parallel reactions where the solid is depolymerised and evaporated forming gas in a single step according to (1). The gas produced during the solid decomposition of the different fractions is assumed to behave identical and to have same specific heat capacity.



where the solid is decomposed according to the following first order volumetric Arrhenius decomposition rate:

$$R_i = \frac{dx_i}{dt} = -A_i \exp\left(-\frac{E_i}{R_g T}\right) x_i, \quad i = 1,3 \quad (2)$$

where x_i is the mass fraction of the volatile component, i , based on initial mass (see nomenclature). Because the temperature may vary radially in the large tyre rubber particle, the rate of decomposition may be different in the particle centre from a position closer to the surface. Therefore, an energy balance is needed to account for the temperature variation. If the outflow of volatile gasses is in thermal equilibrium with the surrounding solid, the complete energy balance for a cylinder with heat transport in the radial direction becomes:

$$\begin{aligned} & (\rho_{\text{solid}} c_{p,\text{solid}} + \rho_{\text{gas}} c_{p,\text{gas}}) \frac{\partial T}{\partial t} + c_{p,v} m_v \frac{\partial T}{\partial r} \\ & - \frac{1}{r} \frac{\partial}{\partial r} \left(k r \frac{\partial T}{\partial r} \right) - \rho_{\text{vf}} \sum_{i=1}^3 R_i \Delta H_i = 0 \end{aligned} \quad (3)$$

The first term represents accumulation of energy, the second term convective transport of energy, the third term conduction of energy and fourth term heat effects of reactions. A reduction of (3) can safely be performed acknowledging that $\rho_{\text{solid}} c_{p,\text{solid}} \gg \rho_{\text{gas}} c_{p,\text{gas}}$ which yields:

$$\begin{aligned} & \rho_{\text{solid}} c_{p,\text{solid}} \frac{\partial T}{\partial t} + c_{p,v} m_v \frac{\partial T}{\partial r} - \frac{1}{r} \frac{\partial}{\partial r} \left(k r \frac{\partial T}{\partial r} \right) \\ & - \rho_{\text{vf}} \sum_{i=1}^N R_i \Delta H_i = 0 \end{aligned} \quad (4)$$

The initial and boundary conditions for (4) are as follows, where (6) states that heat transferred to the outer particle surface is conducted into the material and (7) states that the particle is symmetric around the centre:

$$T(r, t = 0) = T_0 \quad (5)$$

$$\left. \frac{\partial T}{\partial r} \right|_{r=r_0, t>0} = h_{\text{eff}} (T_\infty - T_{r=r_0}) \quad (6)$$

$$\left. \frac{\partial T}{\partial r} \right|_{r=0} = 0 \quad (7)$$

h_{eff} is the effective overall heat transfer coefficient including both convective and radiative heat transport. The outflow of volatiles accumulates towards the particle surface, since volatiles released closer to the particle centre flows towards the particle surface where decomposition reactions may further contribute to the volatile flux. A differential mass balance for cylinder geometry yields:

$$-\frac{d}{dr} (r m_v) = r \rho_{\text{vf}} \sum_{i=1}^3 R_i \quad (8)$$

Upon integration, the volatile flux at a given radial position, r' , is:

$$m_v(r') = -\frac{\rho_{\text{vf}}}{r'} \sum_{i=1}^3 \int_0^{r'} r R_i dr \quad (9)$$

During the progress of the devolatilization, the physical structure of the solid changes, and therefore, the thermal conductivity and the specific heat capacity also changes. In order to describe the change of physical parameters, a local devolatilization conversion is introduced:

$$X_{\text{local}}(r) = 1 - \frac{\rho(r) - (1-V)\rho_{\text{vf}}}{V\rho_{\text{vf}}} \quad (10)$$

and from the local devolatilization conversion, the effective thermal conductivity and effective heat capacity of solid is obtained:

$$k(r) = (1 - X_{\text{local}})k_{\text{vf}} + X_{\text{local}}k_{\text{char}} \quad (11)$$

$$c_{p,\text{solid}}(r) = (1 - X_{\text{local}})c_{p,\text{vf}} + X_{\text{local}}c_{p,\text{char}} \quad (12)$$

The total devolatilization conversion, X , is determined by:

$$\begin{aligned} X(t) &= 1 - \frac{\text{mass of volatiles at } t}{\text{mass of volatiles at } t = 0} \\ &= 1 - \frac{2 \int_0^{r_0} r(\rho(r) - (1-V)\rho_{\text{vf}}) dr}{r_0^2 V \rho_{\text{vf}}} \end{aligned} \quad (13)$$

and from the devolatilization conversion the normalized (or scaled) mass-loss, m/m_0 , for comparison with the experimental results is derived:

$$\frac{m(t)}{m_0} = 1 - X(t)V \quad (14)$$

Eq. (4) is discretized and solved together with the remaining equations using an implicit finite difference method. The obtained solution was tested and found to be independent of applied spatial discretization points and time step.

The model for devolatilization of large tyre particles presented by Yang et al. [15] uses a similar heat transport model in two dimensions (radial and axial in cylinder geometry), a reaction scheme of independent parallel reactions for both polymer decomposition and evaporation, and they

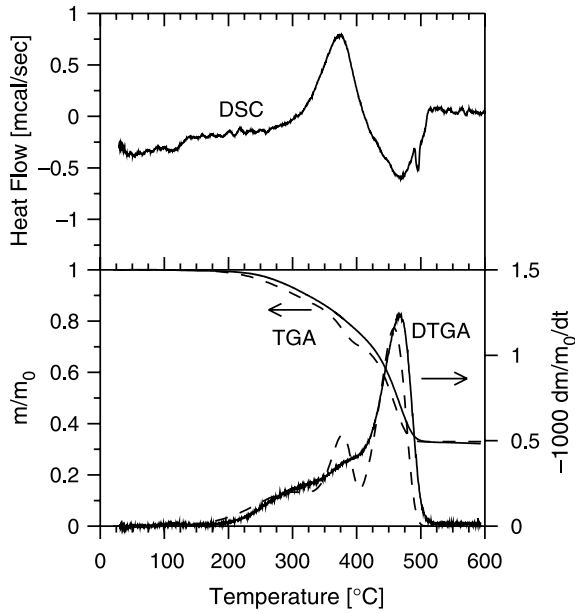


Fig. 4. Differential scanning calorimetric (DSC), Thermo (TGA) and Derivate (DTGA) Gravimetric results of the tested tyre rubber. Results are obtained at a heating rate of 10 °C/min in inert atmosphere for a sample mass of 6.05 mg. The solid lines represent measured results and the dashed lines represent model fits.

included mass transfer via a bubble-transfer mechanism. Therefore, the major differences between the model presented in this work and the model of Yang et al., is that the model presented here uses one step for the polymer decomposition forming a gas that is transported immediately towards the particle surface with no resistance to mass transfer.

The simplifications of the model presented here is motivated by the fact that the length to diameter ratios for the performed experiments are in the range of 2.2 for the particles with a diameter of 22 mm to 6.7 for a diameter of 7.5 mm. It is therefore assumed that heat transfer is mainly in the radial direction. In the experiment of Yang et al. [15] the length to diameter ratio is 1.5. The one step reaction is observed to be in agreement with the TGA and DTGA in Fig. 4. Finally, the resistance of mass transfer is neglected in the current model, because the tyre rubber particles were visually observed to produce a crackling surface with little resistance to mass transfer during the devolatilization process.

3.1. Chemical kinetic and physical parameters

Micro Thermo Gravimetric Analysis (TGA) and the corresponding derived mass-loss (DTGA) are used to investigate the thermal devolatilization behavior of the tested tyre rubber and to verify the employed kinetic scheme. The results of the experimental TGA, and the derived DTGA, are shown in the lower part of Fig. 4, together with a model fit with the applied Arrhenius parameters (see Table 2), whereas the upper part shows a Differential Scanning Calorimetric (DSC) curve for the tested tyre rubber. From the TGA and DTGA, at least three fractions are observed to decompose with three peaks in the mass-loss around 295, 380 and 475 °C, respectively, and for temperatures exceeding approximately 510 °C no more volatiles are observed to escape for the applied heating rate. It is further noted that the ultimate volatile content in Table 1, is identical to the ultimate value from the micro-TGA experiment. Yang et al. [10] have investigated

Table 2
Physical and chemical parameters used in the model calculation

Parameter		Value	Unit	Reference
Virgin fuel density	ρ_{vf}	1100	kg/m ³	Measured
Initial mass fraction of volatile specie i	$x_{1,0}$	0.15	kg/kg	From TGA in present work
	$x_{2,0}$	0.13	kg/kg	From TGA in present work
	$x_{3,0}$	0.36	kg/kg	From TGA in present work
Pre-exponential factors and activation energies	A_1	100	1/s	Modified value for oil fraction from [32] (original 668 s ⁻¹)
	E_1	49.1	kJ/mol	Value for oil fraction from [32]
	A_2	3.93×10^{14}	1/s	Value for NR from [32]
	E_2	207	kJ/mol	Value for NR from [32]
	A_3	1.05×10^{13}	1/s	Value for BR from [32]
	E_3	212	kJ/mol	Modified value for BR from [32] (original 215 kJ/mol)
Reaction enthalpies	ΔH_1	~0	kJ/kg	From DSC in this study
	ΔH_2	-1200	kJ/kg	From DSC in this study
	ΔH_3	350	kJ/kg	From DSC in this study
Specific heat capacity of volatile gas	$c_{p,v}$	2400	J/kg/K	[15]
Specific heat capacity of virgin fuel	$c_{p,vf}$	2000	J/kg/K	[27]
Specific heat capacity of char	$c_{p,char}$	1800	J/kg/K	[15]
Conductivity of virgin fuel	k_{vf}	0.30	W/m/K	[32]
Conductivity of char	k_c	0.20	W/m/K	[15]

Modifications are made according to the model fit of the TGA/DTGA curve in Fig. 4.

the DTGA behaviour of straight pure elastomers of natural rubber (NR), styrene–butadiene-rubber (SBR) and butyl-rubber (BR) which are the common polymers used in tyre rubber. They found that each pure compound decomposed with two peaks in the TGA where the peak at the low temperature could be attributed to the processing oils for the, respectively, polymer following by a major peak representing the polymer. Yang et al. further observed that NR decomposed with a maximum mass-loss around 376 °C, BR started to decompose around 350 °C with a maximum mass-loss at approximately 465 °C and SBR decomposed over a broad temperature interval with a maximal peak mass-loss at 450 °C.

In this study, the observed temperatures for peak mass losses (see DTGA in Fig. 4), suggest that the peak at approximately 475 °C may be attributed BR decomposition, whereas the peak observed at 380 °C may be attributed to both NR and SBR decomposition. The chosen kinetic scheme in this study is observed to predict the TGA and DTGA for the fractions released at the low and high temperature, whereas larger discrepancies exist for the middle fraction. Finally, the DSC curve reveals a heat release at 380 °C, and heat consumption at 475 °C. The two major peaks on the DSC curve are observed to be at temperatures coincident with the peaks in the DTGA curve, i.e. the heat effects can be regarded as effect of the decomposition reactions. The observed exothermic and endothermic reaction behavior observed here is identical to results of Yang et al. [15] and Chen [26]. Integration of the DSC curve yields the reaction enthalpies for the two reactions: –1200 and 285 kJ/kg for the second and third peaks, respectively.

The effective heat transfer coefficient to the surface of the tyre rubber particle is influenced by radiation from the gas and surrounding walls, as well as by convection:

$$h_{\text{eff}} = h_{\text{conv}} + h_{\text{rad}} \quad (15)$$

where the convective heat transfer coefficient is estimated using an Nusselt correlation [27] for laminar external flow in a vertical tube, as is the case in the experimental setup:

$$\frac{h_{\text{conv},0} r_{r=r_0}}{k_{\text{gas}}} = \frac{1.02}{2} Re^{0.45} Pr^{0.5} \left(2r_{r=r_0} - \frac{1}{2} \frac{r_{r=r_0}^2}{r_{\text{reactor}}} \right)^{0.4} \times \left(\frac{r_{\text{reactor}}}{r_{r=r_0}} \right)^{0.8} Gr^{0.05} \quad (16)$$

The outflow of volatile gases from the particle surface may however, reduce the convective heat transfer coefficient [28,29], and in order to compensate for this effect the correlation given by Bird et al. [30] is applied:

$$\frac{h_{\text{conv}}}{h_{\text{conv},0}} = \frac{m_{v,r=r_0} c_{p,v} / h_{\text{conv},0}}{\exp(m_{v,r=r_0} c_{p,v} / h_{\text{conv},0}) - 1} \quad (17)$$

The radiation to the surface follows Stefan Boltzmanns law, and correspondingly a radiative heat transfer coefficient is

calculated as [31] with the temperatures in Kelvin:

$$h_{\text{rad}} = \varepsilon \sigma (T_{\infty}^2 + T_{r=r_0}^2)(T_{\infty} + T_{r=r_0}) \quad (18)$$

4. Experimental and model results

In the following sections, the devolatilization mass-loss behaviour is interpreted by use of graphs showing the scaled mass-loss against time. For all experiments, double determinations were performed, showing good repeatability. However, for clarity the double determinations are not shown.

Fig. 5 shows the scaled mass-loss for four different particle sizes at different temperatures in inert atmosphere.

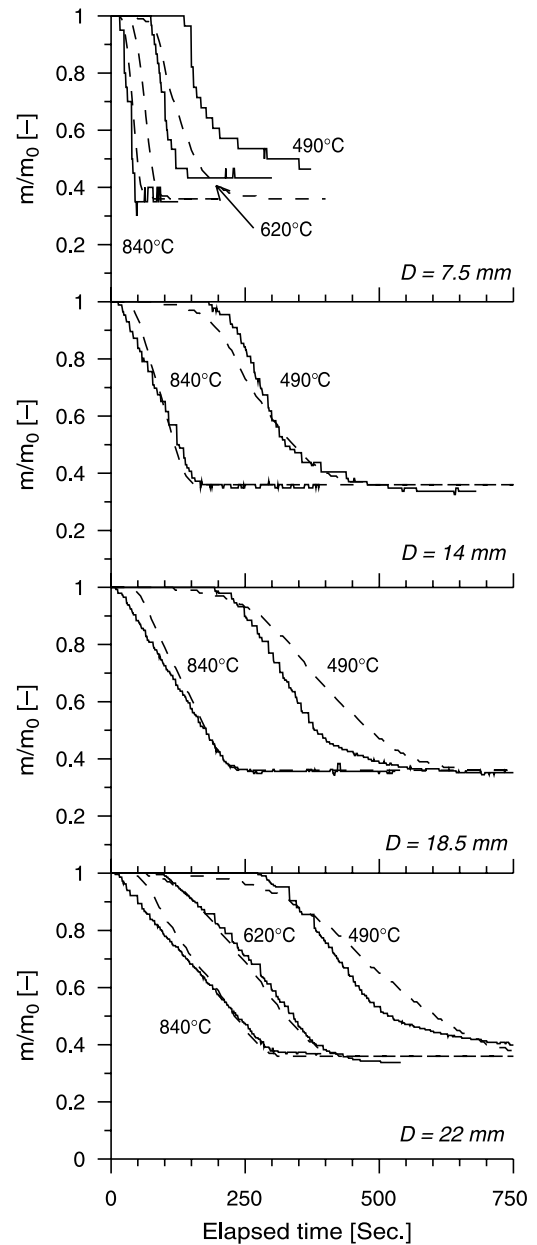


Fig. 5. Measured and predicted scaled mass-losses for tyre rubber cylinders as a function of size and temperature in inert atmosphere. The dashed and solid lines represent the model calculation and measured values, respectively.

The discontinuities observed in the experimental mass-loss curves are a consequence of the balance, which has an accuracy of ± 0.1 g. Since the weight of a rubber sample can be down to 3.4 g, a small variation in the scale readout may cause significant changes in the calculated scaled mass-loss. For the larger particles, the discontinuity diminishes as the particles have larger masses. The ultimate mass-loss observed in the macro-TGA experiments is observed to be approximately 0.65 independent of particle size, i.e. a volatile content of approximately 65 wt% which is in agreement with the proximate analysis (Table 1). For the 7.5 mm particle, the ultimate mass-loss is observed to vary in the range 0.50–0.70, with a temperature of 840 °C yielding the highest amount of volatiles and these variations are attributed to experimental uncertainties for the small sample masses. If the devolatilization time is defined as the time where the first derivative of the scaled mass-loss curve against time approaches zero, the effect of the surrounding temperature on devolatilization time is seen to be very significant for all particle diameters. For a particle with a diameter of 22 mm, the devolatilization time is observed to increase from approximately 300 s for a surrounding temperature of 840 °C to approx. 400 s at 620 °C and approx. 750 s at 490 °C. The effect of particle size on the time of devolatilization is also significant. At 840 °C, the time of devolatilization is observed to increase from approximately 75 to 300 s when increasing the particle diameter from 7.5 to 22 mm. The shape of the mass-loss vs. time is observed to behave similarly. For the temperature of 840 °C, the shape of the mass-loss curve is seen to be close to a straight line for all sizes, whereas the shape for the results at 490 °C is seen to be more curved, and this behaviour is especially pronounced against the end of the devolatilization process. Apparently each

particle size seems to yield approximately the same slope of the mass loss against time independent of temperature.

Comparisons between the predicted and measured mass-loss are made for all particle sizes and surrounding temperatures are also found in Fig. 5. At a surrounding temperature of 840 °C for the 14, 18.5 and 22 mm rubber particle, the agreement between the experimental and predicted scaled mass losses is good, while at 620 °C and for a diameter of 22 mm it is excellent. At 490 °C and for particles with a diameter between 14 and 22 mm, the predicted mass loss is observed to initiate slightly faster than the experimental data. For prolonged times, the predicted mass loss curve is observed to cross the experimental curve. The predicted devolatilization time is however, observed to be in agreement with the experiments. For the particle with a diameter of 7.5 mm, discrepancies arise between the predicted and measured mass loss for longer times, and this is mainly caused by that the model uses a fixed volatile content whereas the experimental results yields varying ultimate mass loss (caused by uncertainties). However, the shape of the modelled mass loss curves for the 7.5 mm rubber particles is in agreement with the experimental findings.

Fig. 6 shows the measured temperature profiles at the particle centre and halfway between the centre and the particle surface during devolatilization for two particle sizes and surrounding temperatures of 490 and 840 °C. The graphs in the left part shows results for particles with a diameter of 14 mm and the graphs to the right represent particles with a diameter of 22 mm. It is observed that a higher surrounding temperature causes the intra-particle temperature to rise faster, and for all four conditions, the temperature is asymptotically approaching the surrounding temperature for increasing time. The effect of

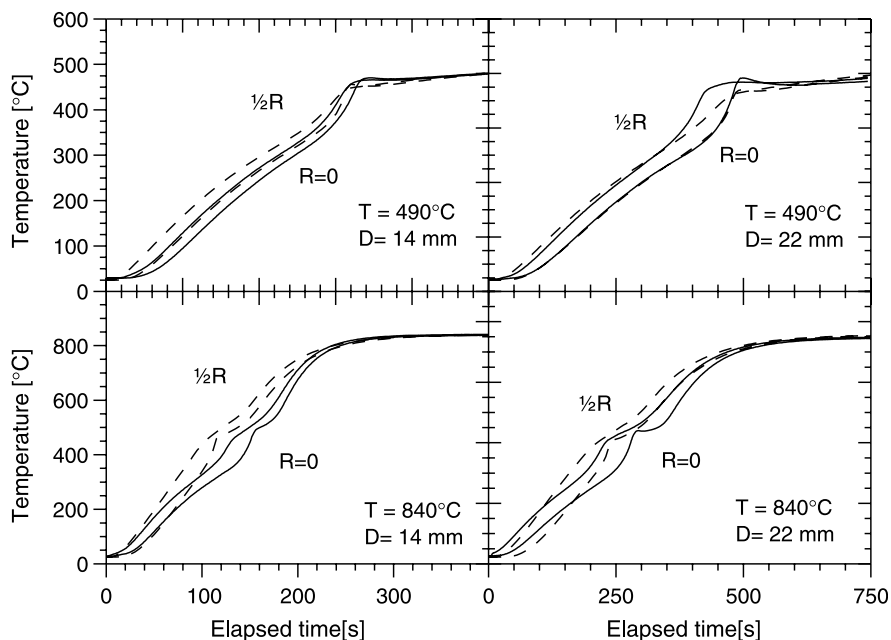


Fig. 6. Measured and predicted intra particle temperatures for two particle sizes and two surrounding temperatures at the centre of the particle ($R=0$) and halfway between the centre and the surface ($\frac{1}{2}R$). The dashed and solid lines represent the model calculation and measured values, respectively.

size and surrounding temperature is also recognized in the temperature measurements via the penetration time, i.e. how long time it does take before the thermocouple in the centre feels the external heat flux. For both particle sizes, it is observed that increasing the surrounding temperature decreases the penetration time and for increasing particle size, at constant surrounding temperature, the penetration time also increases. A temperature difference is observed between the two measurement positions for all sizes and surrounding temperatures, demonstrating a presence of an intra-particle temperature gradient. Finally, an interesting observation from all the transient temperature measurements is the temperature rise initiating when the local temperature approaches 400 °C. This temperature rise is especially pronounced at the centre of the particle. Comparison between the predicted and the measured temperature profiles at the particle centre and halfway between the centre and the surface is also found in Fig. 6. The predicted temperature response is observed to be in agreement for all four conditions. The model is furthermore, observed to be able to predict the experimentally observed peak in temperature initiating just below 400 °C and that the model is capable of reproducing the higher peak temperature response, in the centre, for all investigated sizes.

The observed temperature rise initiating somewhere below 400 °C, can based on model calculations for a surrounding temperature of 490 °C be shown to be a consequence of the exothermic reaction enthalpy of reaction 2. The temperature rise is not a consequence of sudden changes in specific heat capacity of the solid material, when converted from virgin fuel to char. This can be shown in the model calculation by neglecting the reaction enthalpies and lower the specific heat capacity for char to 1000 J/kg/K and observe that the temperature peak is not present. For the surrounding temperature of 840 °C, the resulting temperature rise caused by the exothermic reaction enthalpy is not as pronounced, because the driving force for external heat transfer is significantly higher than for a surrounding temperature of 490 °C, causing the effect of the exothermic reaction enthalpy to diminish (this is also revealed in the sensitivity analysis presented in Section 4.1).

4.1. Sensitivity analysis of model

Since the mathematical model contains many parameters, it is difficult to assess, which parameters that are of significant influence for the output of the model calculation. In order to assess the influence of each parameter in the model, a sensitivity analysis is performed by changing each parameter $\pm 25\%$ while keeping the other parameters constant. As described, the devolatilization time is an important parameter in designing of combustion and devolatilization reactors and therefore the sensitivity analysis is performed on the devolatilization time. The analysis is performed for a 14 mm tyre rubber particle at temperatures of 490 and 840 °C, and the resulting change in devolatilization time, compared to the time computed with standard parameters (Table 2), are reported in Table 3. A negative number indicates that the conversion time

Table 3

Calculated sensitivities in percentage change in conversion time (90%) for a $\pm 25\%$ change in model parameter while keeping the other parameters constant

Parameter	$T_{\infty} = 490\text{ }^{\circ}\text{C}$		$T_{\infty} = 840\text{ }^{\circ}\text{C}$	
	-25%	+25%	-25%	+25%
<i>Heat transfer parameters</i>				
$c_{p,v}$	-1.8%	1.8	-4.4	4.2
$c_{p,vf}$	-22.0	19.7	-20.5	19.4
$c_{p,char}$	-3.6	3.5	-2.3	2.2
k_{vf}	9.2	-5.4	15.7	-9.6
k_{char}	0.1	-0.1	-0.2	0.9
h_{eff}	16.0	-9.7	15.1	-8.9
<i>Devolatilization reaction enthalpy</i>				
ΔH_1	0	0	0	0
ΔH_2	8.4	-9.3	4.7	-4.8
ΔH_3	-2.6	2.5	-1.4	1.4
<i>Devolatilization reaction kinetics</i>				
A_1	0.9	-0.6	1.0	-0.7
E_1	-5.4	18.9	-4.0	12.6
A_2	-1.0	0.7	-0.2	0.1
E_2	9.6	96.5	1.9	14.5
A_3	6.8	-4.5	1.4	-1.1
E_3	-40.3	96.5	-15.8	53.3

The calculation is performed for a 14 mm tyre rubber cylinder.

is lowered compared to standard parameters while a positive number means the conversion time is raised.

The results of the sensitivity analysis are in agreement with common sense, e.g. when increasing the heat capacity of virgin fuel, char or volatile gas, the sensitivity analysis yields a prolonged conversion time, or if the conductivity of either char or virgin fuel is lowered, the conversion time is also prolonged. Regarding the devolatilization reaction enthalpy effects, an increased exothermicity is observed to decrease the devolatilization time and the opposite is observed for the endothermic reaction. For the kinetic parameters of reaction 1 and 3, an increase in activation energy or decrease in pre exponential factor increases the time of devolatilization. The observed increase in devolatilization time, when increasing the activation energy is a consequence of the reaction is shifted towards higher temperatures. For reaction 2 however, the devolatilization time is observed to increase regardless of the tested $\pm 25\%$ change in the activation energy of reaction 2 and this behaviour is especially pronounced at the surrounding temperature of 490 °C. The increase in devolatilization time when increasing the activation energy is again a consequence of the reaction been shifted towards higher temperatures as the case for reaction 1 and 3. However, the increase in devolatilization time when decreasing the activation energy can be explained, based on model calculations, by the fact that the exothermic reaction enthalpy increases the temperature locally and induces the onset of reaction 3. If the exothermic reaction is shifted to lower temperatures (lowering E_2), the evolved heat from the reaction is not sufficient to increase the local temperature to initiate reaction 3 and therefore the devolatilization time is prolonged.

The highest sensitivity is found for the activation energies for the decomposition reactions 2 and 3, indicating that chemical kinetics are important in the prediction of

the devolatilization times. It is however noted, that a $\pm 25\%$ change in activation energy is causing significant changes in the kinetics, because the activation energy enters inside an exponential term (see Eq. (2)). For the heat transfer model, the specific heat capacity of the virgin fuel yields the highest sensitivity on the predicted devolatilization time at both 490 and 840 °C. At 490 °C, the second highest sensitivity in the heat transfer parameters is found for the effective heat transfer coefficient, whereas for 840 °C the conductivity of the virgin fuel and effective heat transfer coefficient have equally important impact on the prediction of devolatilization time. The conductivity and specific heat capacity of the char and the specific heat capacity of the volatile gas have little influence on the predicted devolatilization time. The influence of devolatilization reaction enthalpy on the predicted devolatilization time, is found to be most significant for reaction 2 (e.g. the exothermic reaction) and for the temperature of 490 °C.

As revealed in the sensitivity analysis, the most important heat transfer parameter is the specific heat capacity of the virgin fuel. In the literature, the reported heat capacities of tyre rubber are found to deviate significantly. Yang et al. [15,32] report a linear correlation with temperature ($c_{p,vf} = 1230 + 6.55 T/^\circ\text{C}$ in J/kg/K) for the vulcanized tyre rubber, while constant values of 2000 and 1470 J/kg/K are reported by [27] and [33], respectively. For the pure rubber compounds the following linear correlations are reported by Yang and Roy [34] ($c_{p,NR} = 1917 + 3.44 T/^\circ\text{C}$, $c_{p,SBR} = 1895 + 3.18 T/^\circ\text{C}$ and $c_{p,BR} = 1854 + 2.98 T/^\circ\text{C}$ in J/kg/K) for natural rubber, styrene butadiene rubber and butyl rubber, respectively. The employed heat capacity of 2000 J/kg/K from [27] was observed to give the best correlation between the model and the experimental results with regard to mass loss and intra-particle temperature profiles.

4.2. Devolatilization time as a function of size and temperature

In dimensioning and designing combustion and devolatilization reactors, the devolatilization time as a function of size and external heat transfer characteristics is an important parameter, since it informs about the needed residence time in a given reactor system. As indicated in Section 1, it is difficult to extract precise results regarding devolatilization times and therefore, the developed and validated model is now used to interpret the devolatilization time of large cylindrical tyre rubber particles under combustion conditions; in this case the devolatilization time is defined to be when 90% of the volatiles have been released. Fig. 7 shows the model predicted devolatilization time for surrounding temperatures of 750 and 1000 °C, respectively, and for three different external heat transfer coefficients: 25, 100 and 1000 W/m²/K where the first two represent typical ranges found in combustion systems and the latter represents a limiting case where only internal heat transfer becomes significant, i.e. the external heat transfer is approaching infinitely fast. As in the experimental findings, it is observed that the devolatilization time increases with diameter and decreases with temperature. For the applied heat transfer coefficients of 25 and 100 W/m²/K and fixed temperature,

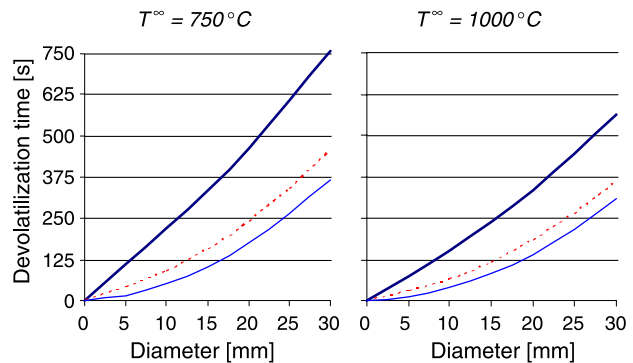


Fig. 7. Model predicted devolatilization time (90% release of volatiles) for two temperatures and three external heat transfer coefficients. The solid thick line represent $h_{\text{eff}} = 25 \text{ W/m}^2/\text{K}$, the dotted line represent $h_{\text{eff}} = 100 \text{ W/m}^2/\text{K}$ and the solid thin line represent $h_{\text{eff}} = 1000 \text{ W/m}^2/\text{K}$.

significant differences in the predicted devolatilization time is observed indicating that external heat transfer characteristics is important. The effect of external heat transfer is observed to be most significant for smaller particle diameters. The tested increase in heat transfer coefficient from 25 to 100 W/m²/K decreases the devolatilization time with a factor of approximately 2.7–2.8 for both temperatures for a diameter of 5 mm, whereas for a diameter of 30 mm the factor is 1.6–1.7 for both temperatures. It is furthermore, observed that the devolatilization time with a heat transfer coefficient of 100 W/m²/K is near the limiting case where only internal heat transfer controls the devolatilization process.

5. Conclusion

The devolatilization of large tyre rubber particles with diameters between 7.5 and 22 mm has been investigated in a macro-TGA reactor, at temperatures of 490–840 °C. The emphasis of the study has been on the effect of the particle size and the surrounding temperature on the mass-loss behaviour. A significant effect of the surrounding temperature on the mass-loss behaviour was found for all particle sizes where the time of devolatilization increased from approximately 300 s, for a tyre rubber particle with a diameter of 22 mm to approximately 400 s, at 620 °C, and 750 s, at 490 °C. The same experimental trend is also observed for other particle sizes. Finally, the effect of the particle diameter on the mass-loss behaviour was observed to be significant, e.g. the devolatilization time increased from 75 to 300 s when increasing the particle diameter from 7.5 to 22 mm at 840 °C.

Assuming that heat transfer and devolatilization decomposition kinetics are the rate controlling parameters; a detailed mathematical model was developed. The model includes external heat transfer, heat conduction in a physically changing solid layer, convective outward transport of energy, devolatilization and related enthalpy effects and accumulation of energy. A comparison between predictions and experimental results showed that the model was capable of simulating the mass-loss vs. time profile for all temperatures. The model was further validated against experimental temperature

measurements at two radial positions and it was found that the model was capable of simulating the experimental findings. The observed temperature rise initiating below 400 °C was shown to be an effect of exothermic reaction enthalpy effects of the thermal tyre rubber decomposition. The coincidence between the model predictions and experimental results indicates that heat transfer and chemical kinetics are the rate controlling parameters for devolatilization of large tyre rubber particles under combustion conditions. A sensitivity analysis on the predicted devolatilization time for a 14 mm tyre rubber particle was performed, at 490 and 840 °C, which revealed that the model predictions showed high sensitivity towards changes in the specific heat capacity of the virgin fuel and the activation energies of reaction 2 and 3.

References

- [1] Lin SQ, Yao Q, Chi Y, Yan JH, Cen KF. Pilot-scale pyrolysis of scrap tires in a continuous rotary kiln reactor. *Ind Eng Chem Res* 2004;43: 5133–45.
- [2] Manugian David. Tires-to-energy facility cost issues. *Trans Am Assoc Cost Eng* 1994;TR.2.1–TR.2.4.
- [3] European Commission, Landfill of waste, Council Directive 1999/31/EC. Brussels, Belgium: European Commission; 1999.
- [4] Schmidthals H. Luftvergasung von Altreifen zur integrierten stofflichen und energetischen Nutzung im Klinkerbrennprozess, PhD thesis, Ruhr-Universität, Bochum, Germany; 2000.
- [5] Kyari M, Cuncliffe A, Williams PT. Characterization of oils, gases, and char in relation to the pyrolysis of different brands of scrap automotive tires. *Energy Fuels* 2005;19:1165–73.
- [6] Kim S, Park JK, Chun HD. Devolatilization kinetics of scrap tyre rubbers. I: using DTG and TGA. *J Environ Eng* 1995;121:507–14.
- [7] Conesa JA, Font R, Fullana A, Caballero JA. Kinetic model for the combustion of tyre wastes. *Fuel* 1998;77:1469–78.
- [8] Senneca O, Salatino P, Chirone R. A fast heating-rate thermogravimetric study of the pyrolysis of scrap tyres. *Fuel* 1999;78:1575–81.
- [9] Leung DYC, Wang LC. Kinetic study of scrap tyre devolatilization and combustion. *J Anal Appl Devolatilization* 1998;45:153–9.
- [10] Yang J, Kaliaguine S, Roy C. Improved quantitative determination of elastomers in tyre rubber by kinetic simulation of dtg curves. *Rubber Chem Technol* 1993;66:213.
- [11] Ucar S, Karagoz S, Ozkan AR, Yanik J. Evaluation of two different scrap tyres as hydrocarbon source by pyrolysis. *Fuel* 2005;84:1884–92.
- [12] Rodriguez IM, Laresgoiti MF, Cabrero MA, Torres A, Chomon MJ, Caballero B. Pyrolysis of scrap tires. *Fuel Process Technol* 2001;72:9–22.
- [13] Giddings D, Pickering SJ, Eastwick CN. Combustion and aerodynamic behaviour of car tyre chips in a cement works precalciner. *J Inst Energy* 2002;77:91–9.
- [14] Bouvier JM, Charbel F, Gelus M. Gas–solid pyrolysis of tyre wastes—kinetics and material balances of batch pyrolysis of used tyres. *Resour Conserv* 1987;15:205–14.
- [15] Yang J, Tanguy PA, Roy C. Heat transfer, mass transfer and kinetics study of the vacuum pyrolysis of a large used tyre particle. *Chem Eng Sci* 1995; 50(12):1909–22.
- [16] Senneca O, Chirone R, Salatino P. Oxidative pyrolysis of solid fuels. *J Anal Appl Pyrolysis* 2004;71:959–70.
- [17] Kanury AM. Combustion characteristics of biomass fuels. *Combust Sci Technol* 1994;97:469–91.
- [18] Goodman TR. Application of integral methods to transient nonlinear heat transfer. *Advances in heat transfer*. New York: Academic Press; 1964.
- [19] Spearpoint J, Quintere JG. Predicting the burning of wood using an integral model. *Combust Flame* 2000;123:308–24.
- [20] Galgano A, Di Blasi C. Modelling wood degradation by the unreacted-core-shrinking approximation. *Ind Eng Chem Res* 2003;42:2101–11.
- [21] Galgano A, Di Blasi C. Modeling the propagation of drying and decomposition fronts in wood. *Combust Flame* 2004;139:16–27.
- [22] Larfeldt J, Leckner B, Melaaen MC. Modelling and measurement of large wood particles. *Fuel* 2000;79:1637–43.
- [23] Grønli MG, Melaaen MC. Mathematical model for wood pyrolysis—comparisons of experimental measurements with model predictions. *Energy Fuels* 2000;14:791–800.
- [24] Adesanay BA, Pham HN. Mathematical modelling of devolatilization of large coal particles in a convective environment. *Fuel* 1995;74:896–902.
- [25] Wildegger-Gaismaier AE, Agarwal PK. Drying and devolatilization of large coal particles under combustion conditions. *Fuel* 1990;69:44–62.
- [26] Chen F, Qian J. Studies of the thermal degradation of waste rubber. *Waste Manage* 2003;23:463–7.
- [27] Perry chemical engineers handbook, 7th ed. NY, USA: Mc-Graw Hill; 1999.
- [28] Thunman H. Principles and models of solid fuel combustion. PhD thesis, Chalmers University of Technology; 2001.
- [29] Thunman H, Davidsson K, Leckner B. Separation of drying and devolatilization during conversion of solid fuels. *Combust Flame* 2004; 137:242–50.
- [30] Bird RB, Stewart WE, Lightfoot EN. *Transport phenomena*. 2nd ed. New York: Wiley; 2002 p. 705.
- [31] Szekeley J, Ewans JW, Sohn HY. *Gas–solid reactions*. New York: Academic Press; 1976.
- [32] Yang J, Philippe AT, Roy C. Numerical model for the vacuum pyrolysis of scrap tires in batch reactors. *AIChE J* 1995;41(6):1500–12.
- [33] Edeskär T. Technical and environmental properties of tyre shreds focusing on ground engineering applications. Technical Report, Luleå University of Technology; May 2004.
- [34] Yang J, Roy C. A new method for DTA measurements of enthalpy change during the pyrolysis of rubbers. *Thermochim Acta* 1996;288:155–68.



Kinetics of tyre char oxidation under combustion conditions

Morten Boberg Larsen ^{a,b,*}, Morten Linde Hansen ^b, Peter Glarborg ^b,
Lars Skaarup-Jensen ^a, Kim Dam-Johansen ^b, Flemming Frandsen ^b

^a *FLSmidth A/S, Vigerslev Allé 77, DK-2500 Valby, Denmark*

^b *Department of Chemical Engineering, CHEC Research Centre, Technical University of Denmark (DTU), DK-2800 Lyngby, Denmark*

Received 6 September 2006; received in revised form 11 January 2007; accepted 11 January 2007

Available online 15 February 2007

Abstract

Combustion of tyre char particles with diameters between 102 and 212 μm was performed in an experimental laboratory reactor, at temperatures between 750 and 850 $^{\circ}\text{C}$, in an oxidative atmosphere with up to 10 vol.% O_2 at 1 bar. The observed char combustion time varied from about 9 s at 750 $^{\circ}\text{C}$ to about 4 s at 850 $^{\circ}\text{C}$. Under these conditions the experimental data indicated increasing mass transfer resistance with temperature. A diffusion reaction model was employed to study the effects of simultaneous mass transfer and kinetics in the experiments. An intrinsic reaction rate for tyre char combustion was estimated and comparison with literature data revealed good agreement.

© 2007 Elsevier Ltd. All rights reserved.

Keywords: Tyre derived fuel; Char; Reactivity

1. Introduction

Tyre derived fuel (TDF) is an important fuel in cement production. The utilization amounted to about 550×10^3 tons in Europe in 2001, equalling about 23% of the total disposal [1]. TDF has a calorific value of about 28 MJ/kg, which is comparable to that of high quality coals. In addition, iron from the steel reinforcement of the TDF is replacing iron raw materials needed for cement production, and consequently natural resources are saved through recycling. One major drawback, however, is that TDF is energy expensive to reduce in size due to its content of steel wires and rubber [2].

Despite the fact that TDF is an important fuel, only limited investigations exist regarding its char reactivity. Several investigations have been performed in micro-TGA in order to determine the kinetics and reaction mechanisms

[3–5] for the pyrolysis decomposition pattern. A recent study investigated the effect of particle size and surrounding temperature on devolatilization mass loss of large tyre rubber particles between 7.5 and 22 mm under well defined conditions [6]. Studies of intrinsic char oxidation reaction kinetics of TDF have been carried out by Masi et al. [7], Conesa et al. [8] and Leung and Wang [5] in micro-TGA with a maximum temperature in the range of 500–600 $^{\circ}\text{C}$. The reported kinetic parameters of Conesa et al. [8] result in a rate that is 3 orders of magnitude lower than that of Masi et al. at 500 $^{\circ}\text{C}$ and 5 orders of magnitude lower at 400 $^{\circ}\text{C}$ (see also Fig. 8). The kinetic scheme proposed for the char oxidation by Leung and Wang [5] does not include any dependence on oxygen concentration and is therefore only valid at conditions under which the kinetics were obtained (21 vol.% O_2). Atal and Levendis [9] concluded that TDF chars burned about 2–4 times faster than a bituminous coal char. They also reported that TDF char retained its original shape during devolatilization. Finally, Zabanitou and Stavrepoulos [10] studied the char gasification reactivity as a function of the temperature at which the char was prepared in the range of 350–900 $^{\circ}\text{C}$, and they

* Corresponding author. Address: FLSmidth A/S, Vigerslev Allé 77, DK-2500 Valby, Denmark. Tel.: +45 36182357.

E-mail address: MBL@FLSmidth.com (M.B. Larsen).

Nomenclature

A	pre-exponential factor, 1/s	S	surface area, m ²
C	molar concentration, mol/m ³	Sc	Smith number, –
D_{O_2}	diffusion coefficient of O ₂ , m ² /s	Sh	Sherwood number, –
E	residence time distribution, –	t	time, s
E_A	activation energy, J/mol	T	temperature, K or °C
k_g	mass transfer coefficient, m ³ /m ² /s	x	dimensionless position, –
m	power law model parameter, –	X	conversion, –
$M_{w(i)}$	molecular weight of specie i , kg/mol	y	mole fraction, mol/mol
n	reaction order in oxygen, –	Y	dimensionless concentration, –
r	radial position, m	σ	standard deviation
R	volumetric reaction rate, mol O ₂ /m ³ /s	ρ	density, kg/m ³
Re	Reynolds number, –	ψ	structure parameter, –
R_g	universal gas constant, 8.314 J/mol/K	Π	molar ratio, –
r_p	particle radius, m		

reported that the most reactive char was that prepared at a temperature of 650 °C.

Intrinsic char reactivity is commonly expressed as a function of temperature, oxygen concentration and intra-particle available surface area [7,11,12]:

$$\frac{dX}{dt} = A \cdot \exp\left(\frac{-E_A}{R_g T}\right) C_{O_2}^n \cdot \frac{S(X)}{S_0} \quad (1)$$

where the first part is the common Arrhenius dependence of the rate constant on temperature and the two latter factors describe the dependency of oxygen concentration and intra-particle surface area. For coal [13] and biomass chars [12], the reaction order of oxygen is between 0 and 1, approaching 0 for low temperatures and 1 for high temperatures. A similar behaviour may be expected for chars of TDF as identified by Masi et al. [7] ($n = 0.68$) and Conesa et al. [8] ($n = 0.69$).

The intra-particle surface area varies with conversion. Different models have been developed to account for this variation in available surface area with conversion. In the reported studies of combustion rates of TDF-char, the random pore model of Bhattia and Perlmutter [14] was employed by Masi et al. [7] ($\psi = 16$), whereas the data of Conesa et al. [8] ($m = 0.69$) and Leung and Wang [5] ($m = 1$) are compatible with the power law model.

$$\frac{S(X)}{S_0} = (1 - X) \sqrt{1 - \psi \ln(1 - X)} \quad \text{Random pore model} \quad (2)$$

$$\frac{S(X)}{S_0} = (1 - X)^m \quad \text{Power law model} \quad (3)$$

Char oxidation experiments may be divided into those performed at low temperatures in micro-TGA reactors [7,8,12,15] or experiments performed at high temperatures pertinent to combustion in flow [15] or fixed bed reactors [11]. Experiments performed in micro-TGA systems are advantageous because the mass loss is measured directly,

whereas experimental data from higher temperatures, gaseous concentrations in the effluent of the experimental combustion setup usually have to be analysed before the conversion can be determined. In addition, char particles combusted at higher temperature are more susceptible to mass transfer limitations compared to those combusted at low temperatures. However, one major drawback of the micro-TGA experiments is that the results obtained must be extrapolated to temperatures that are several hundred degrees higher than those under which they were obtained.

Contrary to many studies in the literature, it was important that the present experiments were carried out at temperatures relevant to combustion conditions. A micro-TGA reactor system was therefore inappropriate as the mass loss rates become too high. Instead, two other experiments were considered: (1) a fixed bed reactor system where the combusting char sample rests on a porous plate with or without sand, or (2) an entrained flow reactor system where char particles are fed continuously and combusted. The advantage of (2) is that it is a continuous system and that the conversion against e.g. residence time can be measured directly, whereas system (1) is a batch fed reactor susceptible to transient behaviour, which needs mathematical treatment before the conversion against time can be derived. The fixed bed reactor was chosen for the experiments, as this has previously been used successfully in the determination of char combustion kinetics [11].

2. Experimental

New tyre rubber from the wearing face of a truck tyre without steel wires was obtained from *PointS*, Denmark, and used for the experiments (identical to tyre rubber of [6]). Proximate and ultimate analyses were determined according to British Standard Methods (BS 1016–1018) and the heating value was determined using the ISO 1928 standard (see Table 1).

Table 1
Proximate-, ultimate analysis and lower heating value for the tested tyre rubber

		Unit	Truck tyre rubber
Proximate analysis	Moisture	wt.%	1.2
	Volatiles	wt.%	64.1
	Ash	wt.%	5.0
	Char (calculated)	wt.%	29.7
Ultimate analysis	C	wt.%	82.0
	H ^a	wt.%	6.71
	S	wt.%	1.35
	N	wt.%	0.32
	O ^a (calculated)	wt.%	3.42
Lower heating value		MJ/kg	35.0 ^b

^a H₂O from moisture excluded.

^b This value is for pure tyre rubber whereas the lower heating value of 28 MJ/kg from the introduction is the as fired value with steel wires, gravel, etc.

The rubber was ground in a laboratory mill, and the resulting particle distribution was sieved in order to separate the different size fractions. The fraction with a particle size of 102–212 μm was used for the experiments (due to difficulties in milling the elastic tyre rubber material to smaller fractions). It was attempted to have as small a particle as possible in order to reduce mass transport resistance in the kinetic measurements.

About 1–2 mg of tyre rubber particles were burned resting on a porous plate in a laboratory-scale reactor at temperatures of 750, 800 and 850 $^{\circ}\text{C}$ at about 1 bar (see Fig. 1). The reactor was made of quartz glass and designed to pre-

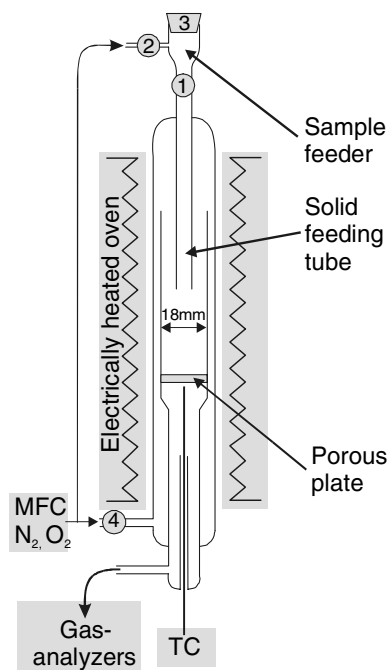


Fig. 1. Experimental setup applied for kinetic studies of TDF char combustion.

heat gasses before they meet with the tyre rubber particles. This was accomplished by admission of gas in the bottom and pre-heating in the annulus outside the inner core, where reaction takes place. A gas-mixing panel upstream of the reactor consisting of mass flow controllers (MFC) ensures that the flow and composition of the gas entering the reactor remain constant. The reactor was placed in an electrically heated oven consisting of three heating-zones, where the temperature of each zone was independently controlled by an external PID-controller.

In each experimental run, tyre rubber particles were placed in the sample feeder with valve 1 closed (see Fig. 1). Initially, valve 2 was opened and valve 4 was closed resulting in a slight overpressure inside the sample feeder chamber. Valve 1 was opened for a short while and via the solid feeding tube the overpressure carried the tyre rubber particles into the reactor, where they were captured resting on top of the porous plate. Valve 4 was opened and valves 1 and 2 were closed. The tyre rubber particles were initially exposed to pure N₂ with a flow of 2 NL/min for 60 s, whereby inert pyrolysis takes place leaving only char. Then, O₂ in N₂ (also 2 NL/min), with a nominal concentration of 10 vol.%, was admitted to oxidize the remaining char. The effluent of the reactor was led to gas-analyzers, where profiles of CO, CO₂ and O₂ were measured and recorded for subsequent data-interpretation. At all times, the burning char particles experienced a gas flow coming from above ensuring that no fines were carried upward, and the porous plate was almost non-permeable for fine particles. Consequently, the burning char particles and eventual fragments hereof were retained in the reaction zone just above the porous plate.

Fig. 2 shows an example of the measured effluent concentration for a particle converted at 750 $^{\circ}\text{C}$. It is observed that peaks of CO₂ and CO, with CO being the highest, develop about 17 s after the particle is injected, indicating pyrolysis. At this stage small amounts of O₂ as a consequence of entrainment into the sample feeder are also observed causing partial oxidation of pyrolysis products

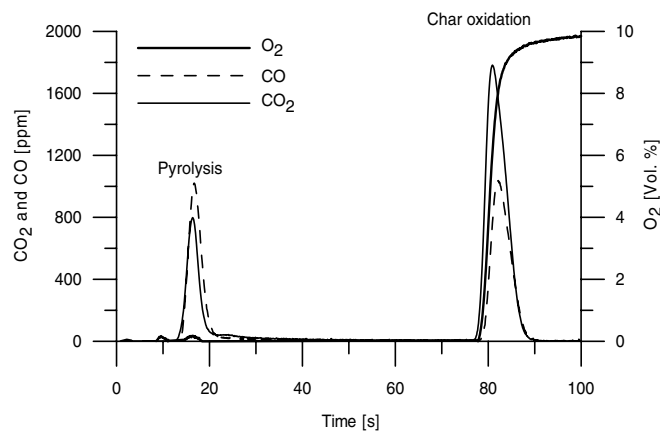


Fig. 2. Measured effluent concentrations of O₂, CO₂ and CO for a TDF char particle converted at 750 $^{\circ}\text{C}$.

and char. The extent of char combustion is considered to be insignificant at the pyrolysis stage. This was quantified by preliminary carbon mass balances over the char combustion stage, by integrating the CO and CO₂ signals. Oxygen is switched on after 60 s resulting in an increased measured O₂-concentration slightly after 78 s increasing to the nominal concentration of about 10 vol.%. Char is oxidized around 78–90 s resulting in peaks of CO₂ and CO, with the concentration of CO₂ now being the dominant peak. What should be particularly noted from the figure is the time delay from admission of particles or gaseous O₂ until a response is measured on the gas analyser. This time delay is a consequence of dispersion and residence time delays in the gas analyzers, pipes, condenser and mixing panel of the experimental setup. For the kinetic analysis, the concentration under char oxidation in the reaction zone is needed and signal deconvolution is therefore applied [16].

2.1. Deconvolution of experimental results

Deconvolution has previously been performed for a similar experimental setup, in order to study the decomposition and oxidation of Pyrite [17] and the char reactivity towards oxygen of different coals [11]. The in- and output signals are related to the residence time distribution in the following way [16]:

$$y_{i,\text{out}} = \int_0^t y_{i,\text{in}}(t-t') \cdot E_i(t') dt' \quad (4)$$

where $y_{i,\text{in}}$ and $y_{i,\text{out}}$ are the in- and output concentrations of specie i , and E_i is the residence time distribution of specie i in the system. For this experimental setup, $y_{i,\text{out}}$ is the concentration measured by the analyzer, and $y_{i,\text{in}}$ is the concentration of CO₂ or CO evolved at the position of the particle, or the concentration of O₂ which the char particle experiences. Fourier transformation on both sides of (4) yields [17]:

$$F\{y_{i,\text{out}}\} = F\{y_{i,\text{in}}\} \cdot F\{E\} \quad (5)$$

from which the concentration $y_{i,\text{in}}$, which is needed for the kinetic analysis, may be derived by rearrangement followed by inverse Fourier transformation [17]:

$$y_{i,\text{in}} = F^{-1} \left\{ \frac{F\{y_{i,\text{out}}\}}{F\{E\}} \right\} \quad (6)$$

The Fourier and inverse Fourier transformations are calculated using the FFT and IFFT routines available in MATLAB 7.0. A filter equal to that used in the Refs. [11,17] is applied in order to filter out noise in the frequency domain with frequencies above 17/64 s⁻¹ for CO and CO₂ and above 10/64 s⁻¹ for O₂.

The residence time distribution of the components CO, CO₂ and O₂ is determined by admitting a step response

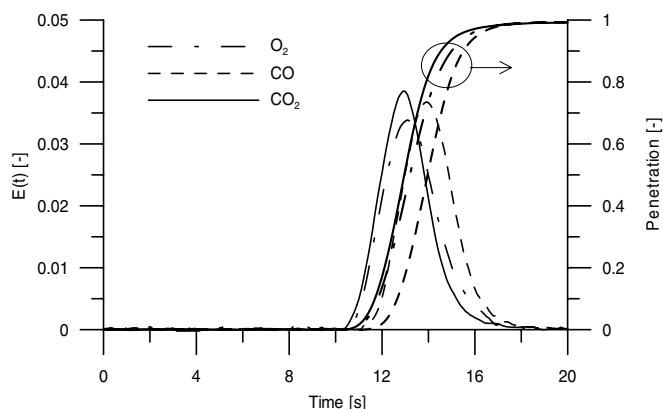


Fig. 3. Normalised residence time distribution (E) and penetration based on step response experiments for CO, CO₂ and O₂.

of the particular component, as closely to the reaction zone as possible, and subsequently recording the response on the gas analyser. The flows during the residence time distribution studies are equal to those used in the experiments. Fig. 3 shows the normalised residence time curves for CO, CO₂ and O₂. The delays are about 11 s for O₂ and CO₂ and about 12 s for CO. The penetration increases from 0 to 1 in about 5 s indicating dispersion in the system. For an ideal plug-flow-reactor system exposed to a step response, the penetration should increase from 0 to 1 infinitely fast.

The measured concentrations of CO and CO₂ may now be deconvoluted using the method outlined above. Fig. 4 shows an example of deconvoluted concentrations of CO, CO₂ and O₂. It is observed that the measured concentrations are shifted about 11–12 s in accordance with the measured residence time distribution (see Fig. 3). In addition, the deconvoluted peaks of CO and CO₂ are narrower than the measured profiles due to the fact that the applied deconvolution method accounts for dispersion in the system. The deconvoluted O₂ profile shows a wave like profile for times above about 7 s which is due to the deconvolution method.

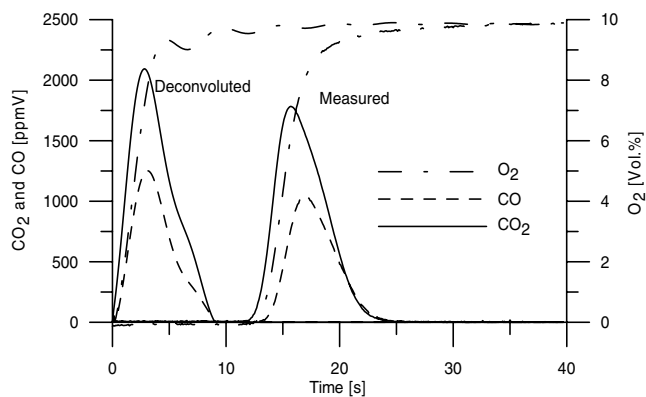


Fig. 4. Deconvolution of measured gas species for a char oxidation experiment at 750 °C (only char oxidation stage shown).

2.2. Char conversion

The degree of char conversion against time may be derived, assuming that the char conversion is proportional to the carbon conversion, by integration of the deconvoluted concentration profiles of CO and CO₂ over the char combustion stage:

$$X(t) = \frac{\int_0^t y_{\text{CO}} + y_{\text{CO}_2} dt}{\int_0^\infty y_{\text{CO}} + y_{\text{CO}_2} dt} \quad (7)$$

Fig. 5 shows the derived conversions, using the method outlined in the last section, for the temperatures of 750, 800 and 850 °C. The repeatability is seen to be good. At a temperature of 750 °C, the conversion time is about 9 s. At 800 and 850 °C, the conversion times are about 4.8 and 4.1 s, respectively. The distance between the curves for 800 and 850 °C is significantly smaller than the distance between 800 and 750 °C, indicating that conditions are approaching a regime where mass transfer has an influence. At all temperatures, the derived conversion against time forms s-shaped curves.

2.3. Char oxidation products

The oxidation products from the char combustion have been investigated by integrating the measured CO and CO₂ signals in the following way:

$$\Pi = 1 + \frac{\int_0^\infty y_{\text{CO}} dt}{\int_0^\infty y_{\text{CO}} + y_{\text{CO}_2} dt} \quad (8)$$

Consequently, $\Pi \rightarrow 2$ if the product of the char combustion is CO or $\Pi \rightarrow 1$ if the product is CO₂. Intermediate values may be obtained for mixtures of CO and CO₂. Fig. 6 shows the values of Π determined as a function of temperature. Π is observed to be about 1.36–1.38.

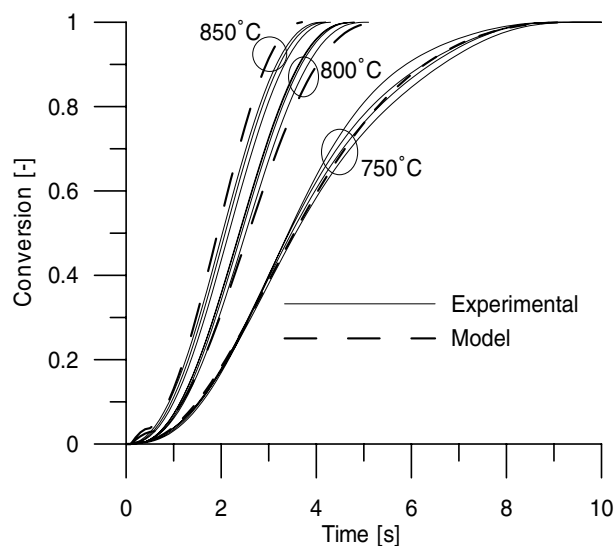


Fig. 5. Conversion against time at temperatures of 750, 800 and 850 °C. See Section 3 for model details.

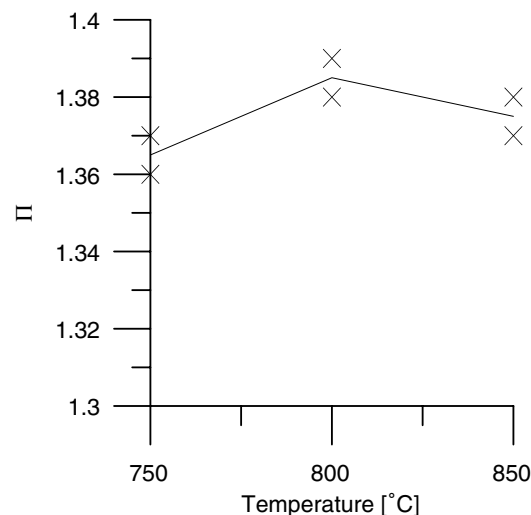


Fig. 6. Values of Π as a function of combustion temperature where points represent results and the line represents an average value. Note the y-axis range.

3. Interpretation of combustion kinetics

From the experimental results, mass transfer was observed to have an influence at higher temperatures. To analyze the effect of simultaneous intrinsic kinetics and mass transfer, a mathematical model for diffusion and reaction inside the char particle is developed, and an iterative fitting procedure is applied in order to determine intrinsic kinetic parameters. In agreement with preliminary combustion experiments performed in a muffle furnace under conditions relevant to this experimental setup, the conversion of the char particle is assumed to follow a constant size progressive conversion model, where O₂ enters and reacts with solid carbon throughout the particle at all times [16]. For sakes of simplicity, the following model assumptions have been made:

- (1) The char particle is assumed to be spherical.
- (2) The particle temperature is assumed to be uniform and identical to the surroundings.
- (3) The effective intra-particle diffusion coefficient of O₂ is assumed to be constant.
- (4) A change of char reactivity with carbon conversion is neglected, and the reaction rate is evaluated using the power law model (3) evaluated at 50% conversion.

For spherical geometry a differential mass balance of O₂ inside the particle becomes:

$$\frac{1}{r^2} \frac{d}{dr} \left(r^2 D_{\text{O}_2, \text{eff}} \frac{dC_{\text{O}_2}}{dr} \right) - R(C_{\text{O}_2}(r)^n) = 0 \quad (9)$$

The first term governs diffusion of O₂ inside the particle and the second term regards the reaction of O₂ with the char inside the particle. The corresponding boundary conditions are shown in (10) and (11) and represent film resis-

tance at the outer particle surface and symmetry in the particle center respectively.

$$D_{O_2, \text{eff}} \left. \frac{dC_{O_2}}{dr} \right|_{r=r_p} = k_g (C_{O_2, \infty} - C_{O_2, r=r_p}) \quad (10)$$

$$\left. \frac{dC_{O_2}}{dr} \right|_{r=0} = 0 \quad (11)$$

The diffusion reaction model represents a non-linear model for $n \neq 1$ and must therefore be solved numerically, and the solution is further complicated by the convection boundary condition (10). Introduction of the dimensionless position $x = r/r_p$ and the dimensionless concentration $Y = C_{O_2}/C_{O_2, \infty}$ transforms the differential equation and its boundary conditions into the following:

$$\frac{1}{x^2} \frac{d}{dx} \left(x^2 \frac{dY}{dx} \right) - Y^n \phi^2 = 0 \quad (12)$$

$$\left. \frac{dY}{dx} \right|_{x=1} = \frac{r_0 k_g}{D_{O_2, \text{eff}}} (1 - Y_{x=1}) \quad (13)$$

$$\left. \frac{dY}{dx} \right|_{x=0} = 0 \quad (14)$$

where the Thiele modulus, ϕ , is obtained assuming that the reaction proceeds according to (1) and the power law model evaluated at 50% char conversion:

$$\phi^2 = \frac{r_p^2 \cdot A \cdot \exp\left(\frac{-E_A}{R_g T}\right) Y_{O_2, \infty}^{n-1} \cdot (1 - 0.5)^m \cdot \rho_C / M_{w(C)}}{D_{O_2, \text{eff}} \cdot \left(\frac{p}{R_g T}\right) \cdot \Pi} \quad (15)$$

The dimensionless model is solved using orthogonal collocation [18], and the effectiveness factor is obtained by the ratio of reaction inside the particle to that of reaction outside the particle:

$$\eta = \frac{\int_0^1 R(Y(x)) x^2 dx}{\int_0^1 R(Y_\infty) x^2 dx} \quad (16)$$

Application of the power law model, the global reaction rate as measured in the experiments may be derived from (1) and (3) multiplied by the effectiveness factor:

$$\frac{dX}{dt} = \eta \cdot A \cdot \exp\left(\frac{-E_A}{R_g T}\right) Y_{O_2}^n \cdot (1 - X)^m \quad (17)$$

It is clear from the above equations, that mass transfer and intrinsic kinetics are linked and that the intrinsic rate parameters may only be determined considering both effects.

3.1. Physical parameters

The effective diffusivity of O_2 inside the tyre char particle is reported to vary between 2.3 and $3.3 \times 10^{-6} \text{ m}^2/\text{s}$ [7] and an average value of $2.8 \times 10^{-6} \text{ m}^2/\text{s}$ is used here. An average virgin fuel particle diameter of $150 \mu\text{m}$ is used (see Section 2) and the resulting char is assumed to have the same particle size [9]. The char density of carbon is calculated from the volatile and ash content (see Table 1), a virgin fuel

density of 1100 kg/m^3 [6], a carbon content in the char of about 95 wt.% [19] and the assumption of constant particle size [9]: $\rho_C = 1100 \cdot (1 - \text{Volatiles-Ash}) \cdot 0.95$. The molar ratio between carbon and oxygen is assumed to be constant and equal to $\Pi = 1.37$ (see Fig. 6). Finally, the mass transfer coefficient at the outer particle surface is calculated from a Sherwood correlation [20] using the particle radius:

$$Sh = \frac{k_g \cdot (2 \cdot r_p)}{D_{O_2}} = 2 + 0.69 Re^{1/2} \cdot Sc^{1/3} \quad (18)$$

3.2. Results of model analyses

The approach taken here is to initially assign an effectiveness factor of 1 for all temperatures and then fit the experimental data to Eq. (17) to obtain first set of A , E_A , n and m in Eq. (17). The derived kinetic parameters are subsequently applied in the effectiveness factor calculation, and new estimates of effectiveness factors at each temperature are obtained. The new effectiveness factors are used for another fit to obtain a second set of kinetic parameters from which a new set of effectiveness factors is recalculated. The iterative procedure continues until the effectiveness factors for each temperature converge to a single value. The fitting procedure is performed using a non-linear least squares method on the experimental data and the intrinsic kinetic parameters obtained are shown in (19). The converged effectiveness factors from the calculation ranged from 0.76 to 0.37 at 750 and 850 °C respectively confirming that the char combusted at these temperatures experienced mass transfer resistances, in accordance with the experimental results of Fig. 5.

$$\frac{dX}{dt} = (1.5 \pm 5.1) \times 10^{10} \cdot \exp\left(\frac{-(193 \pm 28) \text{ kJ/mol}}{R_g T}\right) Y_{O_2}^{0.66 \pm 0.1} \cdot (1 - X)^{0.63 \pm 0.07} [\text{s}^{-1}] \quad (19)$$

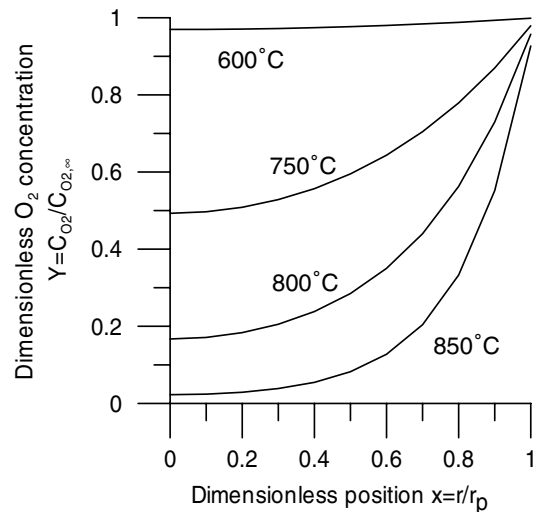


Fig. 7. Predicted intra-particle dimensionless O_2 -concentration profiles through the char particles against dimensionless position at different temperatures (physical data provided in Section 3.1).

The effect of mass transfer limitations is also demonstrated from the predicted intra-particle O_2 -concentration profiles shown in Fig. 7. At 850 °C it decreases sharply at the surface to a nearly zero concentration in the particle centre. The calculated profile at 600 °C shows that only slight mass transfer resistance exists at this temperature (calculated $\eta = 0.99$). This is in agreement with Masi et al. [7] who conclude that the onset of mass transfer resistance occurs at about 600 °C for TDF char particles in this size range. Finally, it may be observed that the dimensionless surface concentration is close to 1 indicating little resistance of external mass transfer.

4. Comparison of estimated intrinsic kinetics with literature data

Fig. 8 shows a comparison of the TDF char reactivity determined in this study with results from the literature. The three sets of kinetic data obtained at the low temperature represent those from the literature, and the kinetic data determined in this study is shown at higher temperatures. Fair agreement is observed between the low temperature data of Masi et al. [7] and Leung and Wang [5]. Significant discrepancies exist between the data reported by Conesa et al. [8] and those of Masi et al. [7] and Leung and Wang [5]. The difference is about 5 orders of magnitude at low temperatures, decreasing to about 3 orders of magnitude at higher temperatures. Extrapolation of the kinetic data of Masi et al. [7] and Leung and Wang [5] to higher temperatures reveals that the intrinsic kinetics estimated in this work is in fairly good agreement with literature data. Extrapolation of data from Conesa et al. [8] to higher temperatures results in better agreement with extrapolated data of Masi et al. [7], Leung and Wang [5]

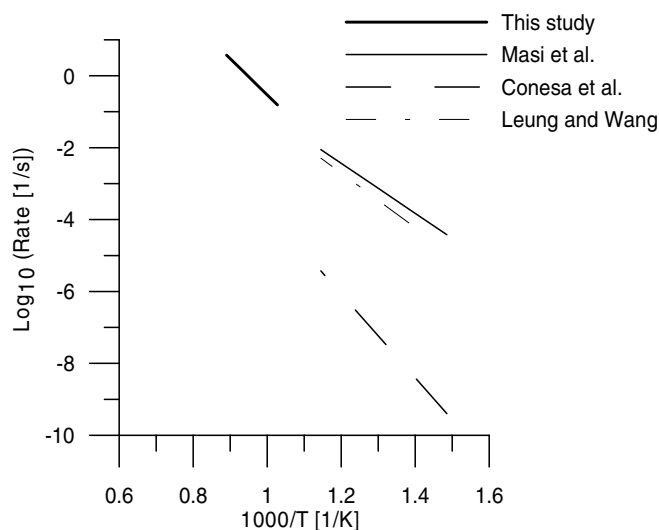


Fig. 8. Arrhenius plot showing estimated TDF char reactivity and those from the literature [7,8,5]. Rate determined at 21 vol.% O_2 in order to compare with the data of Leung and Wang [5] and $X = 0.5$ to compensate for the applied pore model (same trend obtained with $X = 0.25$ and 0.75).

and the kinetics derived in this study. This, however, is due to the significantly higher activation energy reported by Conesa et al. [8] (223 kJ/mol) compared to Masi et al. (133 kJ/mol) and Leung and Wang [5] (145 kJ/mol).

5. Conclusion

Combustion experiments have been performed in a fixed bed reactor at 750–850 °C with tyre rubber masses of about 1–2 mg in up to 10 vol.% O_2 and particle sizes between 102 and 212 μm . The results show that for these particle sizes, a char conversion time of about 9 and 4.1 s can be expected at 750 and 850 °C, respectively, and that mass transfer mass transport effects were influencing the measured rates at the investigated conditions. Considering the mass transfer of O_2 through the boundary layer, diffusion in the char matrix and chemical reaction, a mathematical model was developed and a scheme for the intrinsic kinetics was proposed. A comparison of the derived kinetics with those from the literature showed fair agreement.

Acknowledgements

We would like to thank Stig Wedel and Jan Erik Johnson from Department of Chemical Engineering, Technical University of Denmark for good discussions regarding the diffusion reaction model.

References

- [1] Lorea C, Van Lo W. Energy recovery from used tyres in the European cement industry. In: Proceedings of the international conference on sustainable waste management, 2004. p. 234–5.
- [2] Schrama H, Blumenthal H, Weatherhead EC. A survey of tire burning technology for the cement industry. In: IEEE cement industry technical conference, San Juan, Puerto Rico, 1995. p. 206–83.
- [3] Kim S, Park JK, Chun HD. Devolatilization kinetics of scrap tyre rubbers. I: Using DTG and TGA. *J Env Eng* 1995;121:507–14.
- [4] Senneca O, Salatino P, Chirone R. A fast heating-rate thermogravimetric study of the pyrolysis of scrap tyres. *Fuel* 1999;78:1575–81.
- [5] Leung DYC, Wang LC. Kinetic study of scrap tyre devolatilization and combustion. *J Anal Appl Devolatilization* 1998;45:153–69.
- [6] Larsen MB, Schultz L, Glarborg P, Skaarup-Jensen L, Dam-Johansen K, Frandsen F, et al. Devolatilization characteristics of large particles of tyre rubber under combustion conditions. *Fuel* 2006;85:1335–45.
- [7] Masi S, Salatino P, Senneca O. Combustion rates of chars from high volatile fuels for FBC application. *Fluidized bed combustion*, volume, ASME, 1997. p. 135–43.
- [8] Conesa JA, Font R, Fullana A, Caballero JA. Kinetic model for the combustion of tyre wastes. *Fuel* 1998;77:1469–78.
- [9] Atal A, Levendis YI. Comparison of the combustion behaviour of pulverized waste tyres and coal. *Fuel* 1995;74(111):1570–81.
- [10] Zabaniotou AA, Stavropoulos. Pyrolysis of used automobile tires and residual char utilization. *J Anal Appl Pyrol* 2003;70:711–22.
- [11] Jensen LS. NO_x from cement production – Reduction from primary measures. PhD thesis, Department of Chemical Engineering, DTU, Denmark. 1999, ISBN 87-90142-55-1.
- [12] Janse AMC, Jonge HG, Prins W, Swaaij WPM. Combustion kinetics of char obtained by flash pyrolysis of pine wood. *Ind Eng Chem Res* 1998;37:3909–18.

- [13] Laurendau NM. Heterogenous kinetics of coal char gasification and combustion. *Prog Energy Combust Sci* 1978;4:221–70.
- [14] Bhatia SK, Perlmutter DD. A random pore model for fluid solid reactions: I. Isothermal, kinetic control. *AIChE J* 1980;26:379.
- [15] Zolin A. Reactivity of solid fuels. PhD thesis, Department of Chemical Engineering, DTU, Denmark. 2001, ISBN 87-90142-66-7.
- [16] Levenspiel O. Chemical reaction engineering. 3rd ed. John Wiley & Sons; 1999, ISBN 0-471-25424-X.
- [17] Hansen JP, Skaarup-Jensen L, Wedel S, Dam-Johansen K. Decomposition and oxidation of pyrite in a fixed-bed reactor. *Ind Eng Chem Res* 2003;42:4290–5.
- [18] Villadsen J, Michelsen ML. Solution of differential equation models by polynomial approximation. Prentice-Hall; 1978, ISBN 013-822205-3.
- [19] Li SQ, Yao Q, Chi Y, Yan JH, Cen KF. Pilot scale pyrolysis of scrap tires in a continuous rotary kiln reactor. *Ind Eng Chem Res* 2004;43:5133–45.
- [20] Perry chemical engineers handbook, 7th ed. Mc-Graw Hill, 1999.